Universidad Autónoma de Madrid

Theoretical description of radiative heat transfer: Exploring the limits of Planck's law

Víctor Fernández Hurtado

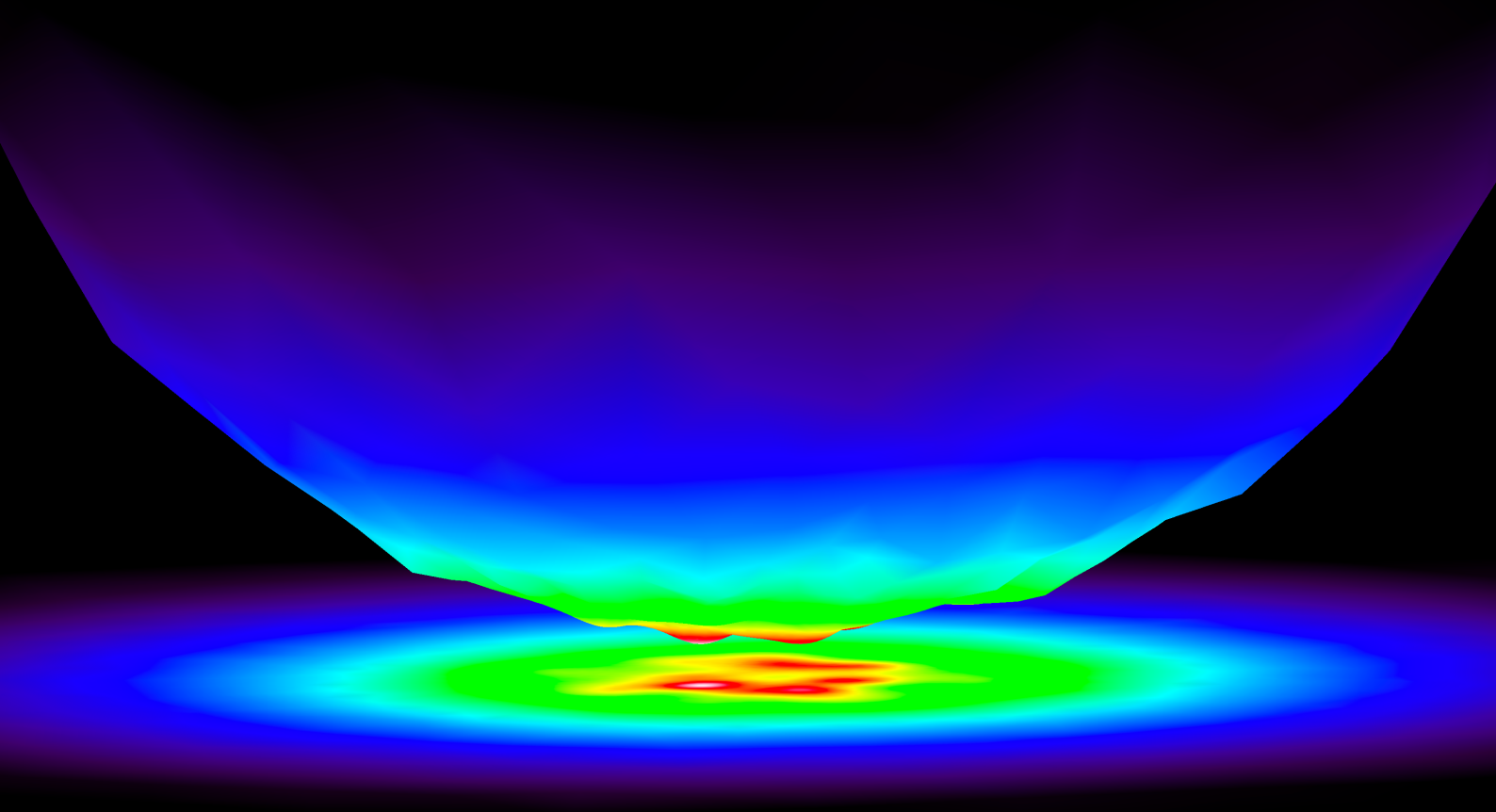

Universidad Autónoma de Madrid

Departamento de Física Teórica de la Materia Condensada

Condensed Matter Physics Center (IFIMAC)

Tesis doctoral dirigida por:

Juan Carlos Cuevas Rodríguez
Francisco José García Vidal

Miembros del tribunal:

Yannick De Wilde
Javier García de Abajo
Ceferino López Fernández
Esteban Moreno Soriano
Alejandro Rodríguez

Madrid, June 2018

Physics is like sex. Sure, it may give some practical results, but that's not why we do it.

R. Feynman

Contents

Abstract

English

This thesis is devoted to the theoretical study of the radiative heat transfer between two objects. Thermal radiation is a ubiquitous physical phenomenon that plays a crucial role in many fields of science and engineering. Until recently, our knowledge of the thermal radiation was largely based on Planck's famous law and the concept of black body, which is an ideal body that absorbs all the radiation that hits on it. In particular, Planck's law establishes an upper limit for the thermal energy that can be transferred between two objects via radiation. However, as acknowledged by Planck's himself, this fundamental law of physics has known limitations and, in principle, it is only valid when all the dimensions involved in the problem are larger than the so-called thermal wavelength (λ_{Th}), which is around 10 microns at room temperature. This thesis work aims at exploring the limits of Planck's law and it focuses on two situations in which this law is no longer valid. First of all, we study the radiative heat transfer between two objects in a variety of situations in which they are separated by a distance smaller than λ_{Th}. In this case, it is well-known that the radiative heat transfer can be dominated by the so-called near field in the form of evanescent waves, and the Planckian limit can be largely overcome by bringing the two objects sufficiently close. On the other hand, we also study here the radiative heat transfer between objects whose characteristics dimensions are smaller than λ_{Th}. In this limit, Planck's law, which is based on ray optics, is also expected to fail even in the far-field regime, *i.e.*, when the separation between the objects is larger than λ_{Th}. In this sense, we present in this thesis a thorough analysis of the radiative heat transfer between small objects in the far-field regime and show for the first time that the Planckian limit can also be overcome in this regime.

The first Chapter of this thesis presents a general introduction to the research field of radiative heat transfer. It includes a brief historical review and outlines the state of the art of this research area. In Chapter 2 we study the thermal radiation of a silica

(SiO_2) thin film in the near-field regime, *i.e.*, when the separation between the film and another body is smaller than λ_{Th}. For this purpose, we have carried out a fundamental study in collaboration with the experimental group of professors Pramod Reddy and Edgar Meyhofer (University of Michigan, Ann Arbor, USA) that demonstrates that a submicron SiO_2-layer is able to transfer as much radiative energy as a bulk SiO_2 sample as long as the gap is smaller than the film thickness. In Chapter 3, we present a theoretical analysis of how the near-field radiative heat transfer between doped semiconductors is modified when an external magnetic field is applied. Our study shows, in particular, that the radiative power transferred between two infinite parallel plates can be reduced up to a factor of 7 upon application of a magnetic field of a few Teslas.

We investigate in Chapter 4 the radiative heat transfer between two silicon-based metasurfaces featuring two-dimensional periodic arrays of holes. We demonstrate theoretically that the near-field thermal conductance between these two metasurfaces is larger than the one between any other unstructured materials. In Chapter 5 we proceed to analyze, in collaboration with the aforementioned experimental group, the radiative heat transfer in the extreme near-field regime, *i.e.*, when the separation distance between two objects is smaller than 10 nm. We show for the first time that the so-called fluctuational electrodynamics theory is able to describe the radiative heat transfer between metals and polar dielectrics in this regime. Moreover, our study suggests that the large thermal conductance values reported in previous experiments that strongly disagree with the predictions of this theory are due to the existence of surface contamination in the employed devices.

In Chapter 6 and 7 we analyze the radiative heat transfer between objects whose dimensions are smaller than λ_{Th} and we focus on the far-field regime. To study this problem, we first derive in Chapter 6 a relation between the far-field radiative heat transfer and the directional absorption efficiency of the individual objects involved. Subsequently, we demonstrate the dramatic failure of the standard thermal radiation theories to predict the far-field radiative heat transfer between micro- and nano-devices. Moreover, we show for the first time that the far-field radiative heat transfer can overcome the Planckian limit by orders of magnitude. In Chapter 7 we explore the limits of the violation of Planck's law in the far-field regime with the help of two-dimensional materials such as graphene and single-layer black phosphorus. In particular, we show in this chapter that the radiative heat transfer between two coplanar systems with a one-atom-thick geometrical cross section can be more than 7 orders of magnitude larger than the theoretical limit set by Planck's law for black bodies. Finally, we present in Chapter 8 the general conclusions of the thesis and a brief outlook about the future directions of the field.

Español

Esta tesis está dedicada al estudio teórico de la transferencia radiativa de calor entre dos objetos. La radiación térmica es un fenómeno físico universal que juega un papel crucial en muchas áreas de la ciencia y la ingeniería. Hasta hace poco, el análisis de la radiación térmica estaba basado fundamentalmente en la famosa ley de Planck y en el concepto de cuerpo negro, que es un cuerpo ideal capaz de absorber toda la radiación que incide en él. En concreto, la ley de Planck establece una cota superior para la energía térmica que pueden intercambiar dos objetos por radiación. Sin embargo, como el propio Planck reconoció, esta ley fundamental tiene limitaciones y, en principio, sólo es válida cuando todas las dimensiones del problema son mayores que la denominada longitud de onda térmica (λ_{Th}), que es alrededor de 10 micras a temperatura ambiente. Esta tesis tiene el propósito de explorar los límites de la ley de Planck y está centrada en analizar dos regímenes en los que esta ley no es válida. En primer lugar, estudiamos la transferencia radiativa de calor entre dos objetos en distintas situaciones en las que la distancia de separación entre ellos es menor que λ_{Th}. En este caso, es bien conocido que la transferencia radiativa de calor puede estar dominada por el llamado campo cercano en forma de ondas evanescentes, y el límite Planckiano puede ser ampliamente sobrepaso acercando lo suficiente los dos objetos. Por otro lado, estudiamos también la transferencia radiativa de calor entre objetos cuyas dimensiones características son más pequeñas que λ_{Th}. En este límite, la ley de Planck, que se basa en la óptica de rayos, también se espera que falle incluso en el campo lejano, es decir, cuando la separación entre los objetos es mayor que λ_{Th}. En este sentido, presentamos en esta tesis un análisis exhaustivo de la transferencia radiativa de calor entre objetos pequeños en el campo lejano y mostramos por primera vez que el límite Planckiano puede ser también superado en este régimen.

El primer Capítulo de esta tesis presenta una introducción general al campo de la transferencia radiativa de calor. Incluye un breve repaso histórico y explica en términos generales el estado del campo. En el segundo Capítulo, estudiamos la radiación térmica de una lámina delgada de sílice (SiO_2) en el campo cercano, es decir, cuando la distancia entre la lámina y otro cuerpo es menor que λ_{Th}. Para ello, hemos llevado a cabo un estudio fundamental en colaboración con los grupos experimentales de los profesores Pramod Reddy y Edgar Meyhofer (Universidad de Míchigan, Ann Arbor, EEUU) que demuestra que una lámina de grosor nanométrico de SiO_2 es capaz de transferir la misma energía radiativa que una muestra del material en volumen siempre y cuando la distancia que la separa de otro objeto sea menor que el grosor de la lámina. En el siguiente Capítulo, presentamos un análisis teórico sobre cómo se modifica la transferencia de calor en el

campo cercano cuando se aplica un campo magnético. En concreto, nuestro estudio muestra que la energía radiativa transferida entre dos placas paralelas puede reducirse hasta un factor 7 debido a la aplicación de un campo magnético de unos pocos Teslas.

En el cuarto Capítulo investigamos la transferencia radiativa de calor entre dos metasuperficies de silicio dopado que contienen una red periódica bidimensional de agujeros. Demostramos teóricamente que la conductancia térmica en el campo cercano entre estas metasuperficies es mucho mayor que la de cualquier otro material sin estructurar. El quinto Capítulo está centrado en analizar, en colaboración con el grupo experimental mencionado anteriormente, la transferencia radiativa de calor en el régimen de campo cercano extremo, es decir, cuando la distancia entre dos objetos es menor a 10 nm. Mostramos por primera vez que la teoría denominada "fluctuational electrodynamics" es capaz de describir la transferencia radiativa de calor entre tanto metales como dieléctricos polares en este régimen. Además, nuestro estudio sugiere que las altas conductancias térmicas medidas por experimentos previos y que muestran grandes diferencias con las predicciones de esta teoría surgen debido a la presencia de contaminación superficial en los dispositivos empleados.

En los últimos capítulos del manuscrito, analizamos la transferencia de calor entre objetos cuyas dimensiones son menores que λ_{Th}, centrándonos en el régimen de campo lejano. Para ello, en el sexto Capítulo derivamos una relación entre la transferencia radiativa de calor en el campo lejano y la eficiencia de absorción direccional de los objetos involucrados. Utilizando este resultado, demostramos que las teorías estándar de radiación térmica son incapaces de predecir correctamente el intercambio radiativo de calor en el campo lejano entre micro- y nanoestructuras. Es más, mostramos por primera vez que la transferencia radiativa de calor en el campo lejano puede sobrepasar el límite Planckiano en órdenes de magnitud. En el séptimo Capítulo exploramos los límites de la transferencia radiativa súper Planckiana en el campo lejano con la ayuda de materiales bidimensionales como el grafeno y las monocapas de fósforo negro. En concreto, mostramos que la transferencia radiativa de calor entre sistemas de grosor atómico puede ser más de 7 órdenes de magnitud mayor que el límite teórico establecido por la ley de Planck para cuerpos negros. Finalmente, en el octavo Capítulo presentamos las conclusiones generales de la tesis y una breve perspectiva sobre el futuro del campo.

List of acronyms

BEM	Boundary element method
CSPhPs	Cavity surface phonon polaritons
DDA	Discrete dipole approximation
EM	Electromagnetic
EMT	Effective medium theory
eNFRHT	Extreme near-field radiative heat transfer
FE	Fluctuational electrodynamics
FFRHT	Far-field radiative heat transfer
FSC	Fluctuating-surface-current
FTDT	Finite-difference time-domain
HMs	Hyperbolic modes
HTC	Heat transfer coefficient
MO	Magneto-optical
NFRHT	Near-field radiative heat transfer
RCWA	Rigorous coupled wave analysis
RHT	Radiative heat transfer
SEM	Scanning electron microscope
SLBP	Single-layer black phosphorus
SPhPs	Surface phonon polaritons
SPPs	Surface plasmon polaritons
SThM	Scanning thermal microscopy
TDDA	Thermal discrete dipole approximation
TE	Transverse electric
TM	Transverse magnetic
TPV	Thermophotovoltaic

1 | General introduction

1.1. Planck's law for black-body radiation

Thermal radiation is probably one of the most ubiquitous physical phenomena. Any object at a non-zero temperature emits a broadband spectrum of incoherent electromagnetic (EM) radiation. At temperatures lower than 600 °C, the thermal radiation emitted by an object cannot be directly observed with the eyes because it is composed of frequencies which lie in the infrared region of the spectrum. Around 600-700 °C, a body holds enough thermal energy to emit radiation in the visible range and it turns pale red. As the temperature of an object increases, its color changes to bright red and eventually to "hot white".

To better understand the thermal radiation emitted by an object at a certain temperature, it is useful to introduce the concept of a black body. A black body is an ideal object which is a perfect absorber at all frequencies. An example of a black body would be a cavity with a small hole in its walls, as it is depicted in Fig. 1.1. In this system, the radiation which enters the cavity has a very low probability of exiting the system without being absorbed before by the walls of the cavity. In 1879, Josef Stefan derived from experimental data a relation between the power emitted by a blackbody per unit area and its temperature [1]:

$$I_{\mathrm{BB}} = \sigma T^4, \tag{1.1}$$

where I_{BB} is the total thermal power radiated per unit area, T is the temperature and $\sigma = 5.6703 \times 10^{-8}$ W/(m^2 K^4) is Stefan's constant. This relation was also derived 5

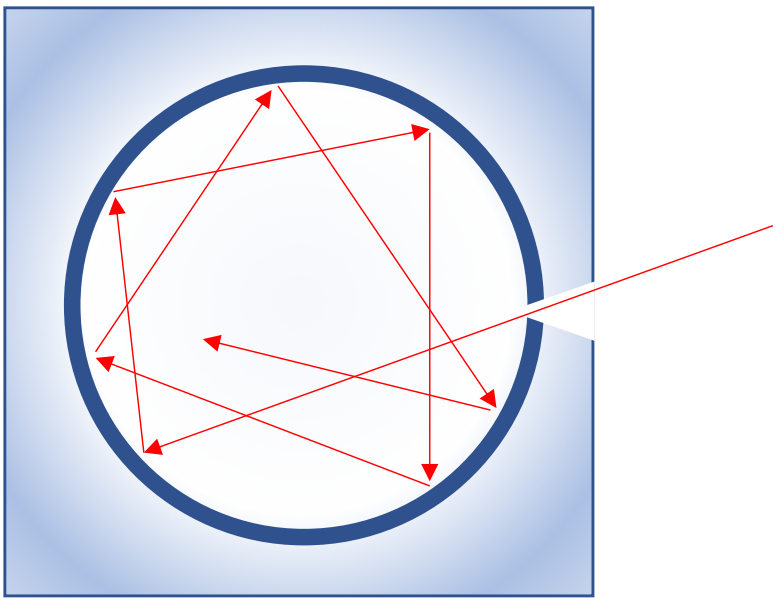

Figure 1.1: A black body can be realized using a cavity with a tiny hole in its walls. The EM radiation which enters the system will be reflected multiple times inside the cavity. Therefore, it will be eventually absorbed before it is able to exit the hollow sphere.

years later by Ludwig Boltzmann using thermodynamical arguments and that is the reason why Eq. (1.1) is called Stefan-Boltzmann law. It is worth mentioning that the power emitted by a black body per unit area does only depend on the temperature and it is independent of any other property of the object, such as its shape or chemical composition.

Real objects, however, are not black bodies and they emit less radiation at the same temperature. Their thermal emission does depend in this case on its color and composition. These effects can be considered by defining a factor called emissivity (ϵ), which multiplies the right hand side of Eq. (1.1). The values of ϵ range from 0 for perfect reflectors to 1 for black bodies.

As we have described above, the thermal radiation is not uniformly distributed among the different wavelengths λ. We can define the spectral distribution ($I_{\mathrm{BB}}(\lambda, T)$) as the power emitted by an object at temperature T per unit of area and wavelength. Wilhelm Wien discovered in 1893 that the wavelength at which $I_{\mathrm{BB}}(\lambda, T)$ is maximum (λ_{Th}) is inversely proportional to the temperature and it verifies the following relation [1]

$$\lambda_{\mathrm{Th}} T = 2.898 \times 10^{-3}\ \mathrm{m{\cdot}K}. \tag{1.2}$$

This result is known as Wien's displacement law and it was found experimentally. However, understanding theoretically the spectral distribution of thermal radiation was a huge challenge at the end of the 19$^{\text{th}}$ century. Following the laws of classical physics, it is possible to calculate the density of EM modes inside a blackbody and thus $I_{\text{BB}}(\lambda, T)$. However, for very short wavelengths, the classical theory predicts that $I_{\text{BB}}(\lambda, T) \to \infty$, while the experimental evidence shows that in the limit $\lambda \to 0$, $I_{\text{BB}}(\lambda, T) \to 0$. This discrepancy between theory and experiment was referred to as the *ultraviolet catastrophe*. Indeed, the predictions from the classical theory imply that every object would emit an infinite amount of energy.

This issue was not overcome until 1900, when the physicist Max Planck solved the problem by considering a rather awkward assumption. He proposed that the energy of every EM mode is quantized, *i.e.*, it can only take values which are multiples of a certain number. More precisely, he established that the energy E_n of the n^{th}-mode can only adopt the following form:

$$E_n = nhf \quad (n = 0, 1, 2, \ldots), \tag{1.3}$$

where h is Planck's constant and f is the frequency of the mode. Using this hypothesis, it is possible to derive the following expression for $I_{\text{BB}}(\lambda, T)$ [2]:

$$I_{\text{BB}}(\lambda, T) = \frac{2\pi hc^2\lambda^{-5}}{e^{hc/\lambda k_{\text{B}}T} - 1}. \tag{1.4}$$

Here, c is the speed of light and $k_{\text{B}} = 1.381 \times 10^{-23}$ J/K $= 8.617 \times 10^{-5}$ eV/K is Boltzmann's constant. This last expression is known as Planck's law and it was the first step in the development of quantum mechanics. From Eq. (1.4), it is possible to derive both Eq. (1.1) and Eq. (1.2). The value of Planck's constant can be obtained by fitting Eq. (1.4) to experimental data and its value is $h = 6.626 \times 10^{-34}$ J·s$= 4.136 \times 10^{-15}$ eV·s. The function $I_{\text{BB}}(\lambda, T)$ is plotted in Fig. 1.2 for different values of T.

So far, we have focused on the thermal radiation emitted by one body. When two bodies are placed close by at different temperatures T_1 and T_2, they exchange energy via radiation. The heat power transferred (P) between two black bodies can be found by applying Stefan-Boltzmann law (Eq. (1.1)) and it is expressed as

$$P = A_1 F_{12} \sigma (T_1^4 - T_2^4), \tag{1.5}$$

where A_1 corresponds to the geometric cross section of body 1 and F_{12} is the view

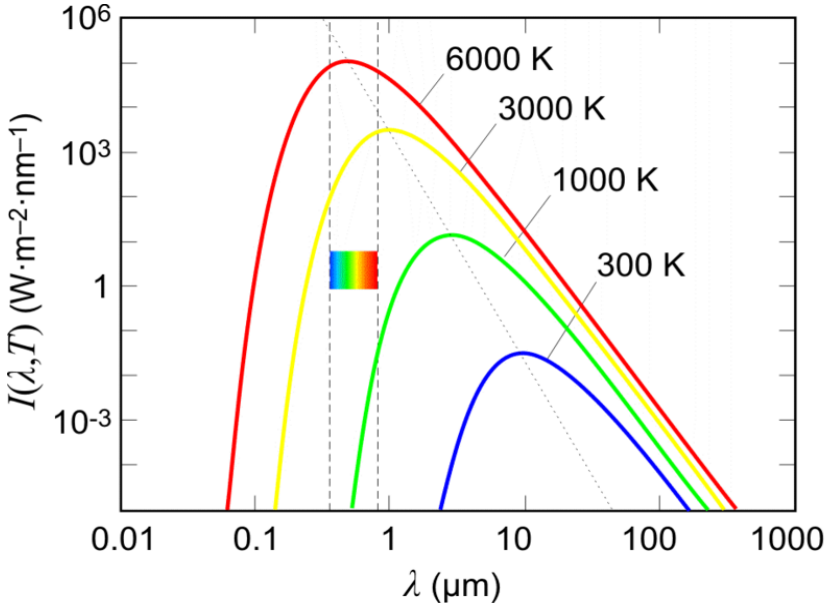

Figure 1.2: Spectral distribution $I_{\mathrm{BB}}(\lambda, T)$ of the blackbody radiation. The different lines correspond to distinct temperatures. The dotted line represents Wien's law and shows how the peak of $I_{\mathrm{BB}}(\lambda, T)$ is blueshifted with increasing temperature. The dashed vertical lines delimit the visible region of the spectrum and manifest that this frequency range is only thermally occupied at high temperatures.

factor, which is defined as the fraction of the radiation leaving the surface of body 1 that is intercepted by body 2 [3]. The view factor can be calculated by integrating over the appropiate solid angle, and for infinite plates it is therefore equal to 1. Equation 1.5 can be also rewritten in terms of the geometric cross section of body 2 (A_2) and its corresponding view factor F_{21}. If the objects considered are not black bodies, the expression for the radiative power transfer is more complicated and it is given by [3]:

$$P = \frac{\sigma(T_1^4 - T_2^4)}{\frac{1-\epsilon_1}{\epsilon_1 A_1} + \frac{1}{A_1 F_{12}} + \frac{1-\epsilon_2}{\epsilon_2 A_2}}, \tag{1.6}$$

where ϵ_i represents the emissivity of body i.

Let us emphasize that both Eq. (1.5) and Eq. (1.6) assume that Planck's law is correct irrespective of the objects, temperatures and distances considered. Indeed, Planck's law describes with great precision the experimental results in very different scenarios, from the thermal emission of incandescent objects to the cosmic microwave background. However, Planck himself recognized in his seminal work [2] (see Fig. 1.3) that his law is only strictly valid when all relevant spatial length scales are much larger than the thermal wavelength λ_{Th}, which at room temperature is approximately $\lambda_{\mathrm{Th}} \approx 10\ \mu$m. In

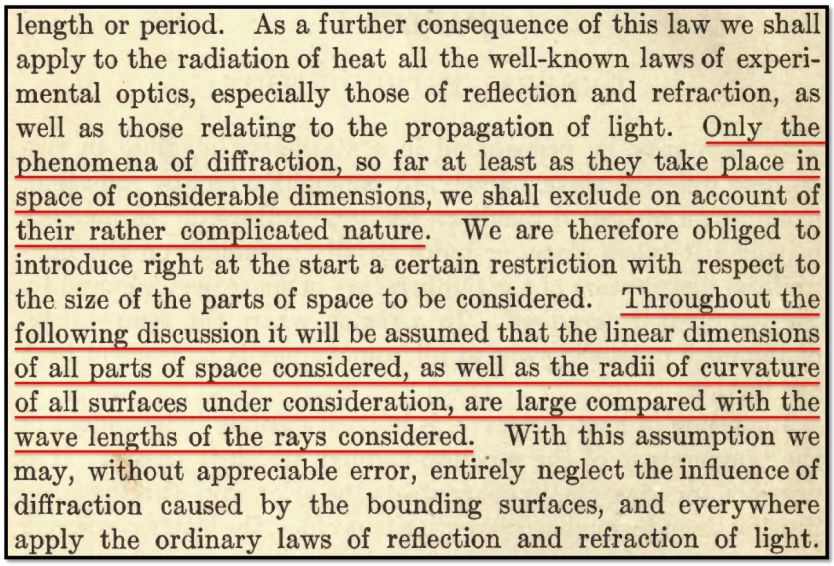
length or period. As a further consequence of this law we shall apply to the radiation of heat all the well-known laws of experimental optics, especially those of reflection and refraction, as well as those relating to the propagation of light. Only the phenomena of diffraction, so far at least as they take place in space of considerable dimensions, we shall exclude on account of their rather complicated nature. We are therefore obliged to introduce right at the start a certain restriction with respect to the size of the parts of space to be considered. Throughout the following discussion it will be assumed that the linear dimensions of all parts of space considered, as well as the radii of curvature of all surfaces under consideration, are large compared with the wave lengths of the rays considered. With this assumption we may, without appreciable error, entirely neglect the influence of diffraction caused by the bounding surfaces, and everywhere apply the ordinary laws of reflection and refraction of light.

Figure 1.3: Extract from Planck's original book [2] where he explains the limitations of his law.

the next section we study how the radiative heat flow between two objects can exhibit very different features in the near field, *i.e.*, when the separation distance between them is smaller than λ_{Th}. We analyze this phenomenon by reviewing the pioneering theoretical and experimental studies on this topic.

1.2. Thermal radiation exchange beyond Planck's law in the near-field: a brief historical review

The predictions of Planck's law for the thermal radiation were not questioned until the decade of 1950s. Bijl [4] was the first to realize that the approach considered by Planck could yield incorrect results for the thermal emission from a small cavity at very low temperatures. More precisely, he indicated that Planck's law (Eq. 1.4) would be inappropriate to calculate the thermal radiation from a cavity of volume 1 cm^3 placed at a temperature $T = 1$ K, as the size of the thermal wavelength λ_{Th} would be of the order of the cavity dimensions (Eq. 1.2). Therefore, in this regime, "*...Wien's and Stefan's law are no longer significant.*". He was the first in suggesting that a more complicated theoretical framework was needed to describe the thermal radiation when the dimensions

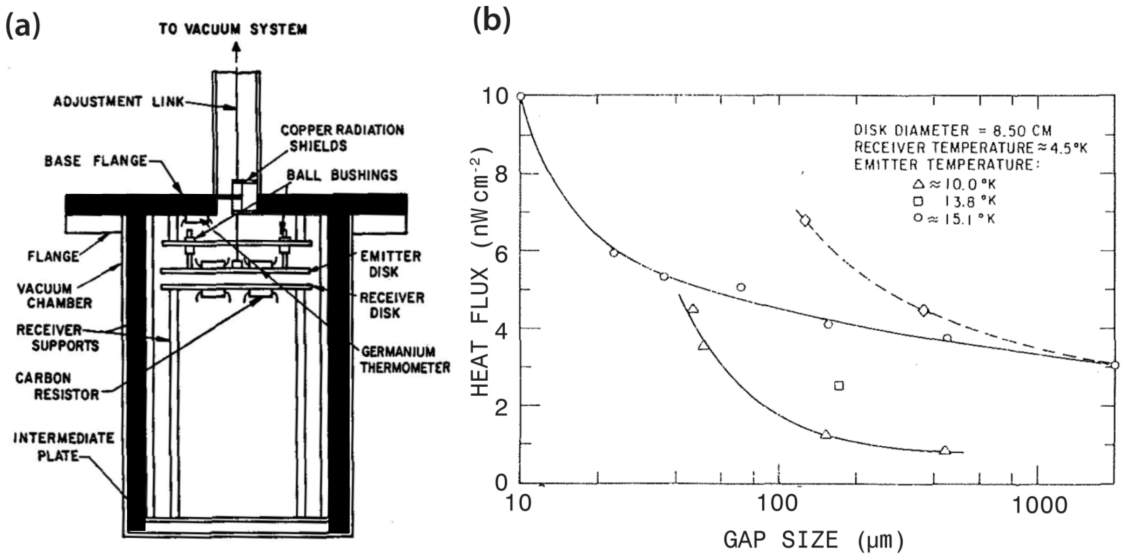

Figure 1.4: (a) Scheme of the setup employed by Cravalho *et al* [7] to measure the RHT between two parallel copper plates. (b) Results [8] for the heat flux as a function of the gap size between the two objects. The different lines correspond to distinct temperatures of the emitter plane (see legend).

of the heat transfer problem are of the order of λ_{Th}.

In 1953, Rytov developed the theoretical framework of fluctuational electrodynamics (FE) [5, 6], which is the basis of the theoretical description of the Casimir effect and near-field thermal radiation nowadays. This formalism makes use of the fluctuation-dissipation theorem to find the fluctuating EM fields. The fluctuation-dissipation theorem is a general result in quantum mechanics that relates the expected value of the product of two operators with the imaginary part of their response function. Moreover, he calculated the radiative heat transfer (RHT) between two semi-infinite parallel plates: one of them was made by an arbitrary material while the other was a nearly-perfect reflector. Rytov explained that, when the gap between two objects is decreased, the heat flow could be greatly enhanced with respect to the predictions of Planck's law.

The first experiment that explored the RHT when the gap size between two objects is smaller than λ_{Th} appeared in 1968 and was performed by Cravalho, Domoto, Tien and Boehm [7, 8]. They measured the radiative heat flux between two parallel copper disks which where immersed in liquid helium (see Fig. 1.4). Indeed, at liquid helium temperature (≈ 4.2 K), $\lambda_{\mathrm{Th}} = 690$ μm, so the gap size that must be established between the two plates in order to observe deviations from Planck's law is larger than at room temperature and, therefore, easier to achieve experimentally. They found an enhancement

in the RHT of a factor of 5 at the smallest gap consider ($\sim$ 10 μm), and they showed for the first time that the radiative heat flow can depend on the gap size, in contrast to the predictions of Planck's law. One year later, Hargreaves measured the RHT in the near-field regime at room temperature for the first time [9, 10]. He also considered two parallel plates coated with chromium (100 nm thick), and he employed piezoelectric ceramic pillars to tune both the gap and the parallelism between the two systems. He reported a enhancement of a factor of 4 in the heat flow at the smallest gaps considered (1 μm).

Motivated by Hargreave's experiments on the radiative heat flow between closely-spaced metals, Polder and Van Hove derived in 1971 an expression to calculate the RHT between two arbitrary identical semi-infinite parallel plates [11]. In contrast to Rytov's approach, who considered fluctuating fields as the random thermal source [5], Polder and Van Hove considered in their seminal work fluctuational electrical currents. Both formalisms are equivalent, but the second one is more convenient to find compact expressions for the RHT between two parallel plates. We shall analyze in the next section the approach followed by them and use their result to understand the new physics that arises in the near-field.

1.3. RHT between closely-spaced parallel plates

Following Polder and Van Hove [11], we now consider the near-field radiative heat transfer (NFRHT) between two identical semi-infinite parallel plates that are separated by a gap d, see Fig. 1.5. Thanks to the symmetry of this geometry, the RHT between the two plates can be expressed by an analytical expression. Following Fig. 1.5, we refer to the left plate as medium 1, the vacuum gap as medium 2, and the right plate as medium 3.

In any object there are multiple processes than can generate radiation emission, such as the motion of charged particles or the oscillation of electric dipoles. However, it is impossible to study all of them individually in order to find the total RHT, being necessary to consider statistical arguments to solve the problem. The theoretical analysis of the RHT in our system is carried out in the framework of FE [5, 6]. Briefly, within this theory, thermal radiation is assumed to be generated by random fluctuating currents $\mathbf{J}$ inside the different materials. While the statistical average of these currents vanishes, *i.e.*, $\langle \mathbf{J} \rangle = 0$, their correlations are given by the fluctuation-dissipation theorem [12, 13]

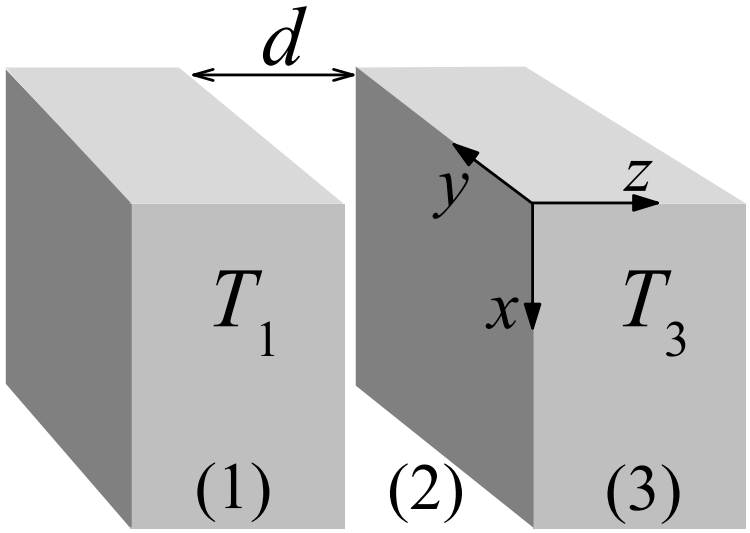

Figure 1.5: Schematic representation of the system under study: two parallel plates at temperatures T_1 and T_3 separated by a vacuum gap of width d.

$$\langle J_k(\mathbf{R},\omega)J_l^*(\mathbf{R}',\omega)\rangle = \frac{4\epsilon_0\epsilon''\omega}{i\pi}\Theta(\omega,T)\delta(\mathbf{R}-\mathbf{R}')\delta_{kl}, \tag{1.7}$$

where $\mathbf{R}$ and $\mathbf{R}'$ are the positions of the currents in real space, ω and ω' their frequencies, ϵ'' represents the imaginary part of ϵ, the dielectric constant of the material, which is considered to be local in space, and ϵ_0 is the dielectric constant in vacuum. The Kronecker delta δ_{kl} is a consequence of isotropy and the Dirac delta $\delta(\mathbf{R}-\mathbf{R}')$ is implied by locality. Finally, $\Theta(\omega,T) = \hbar\omega/[\exp(\hbar\omega/k_\mathrm{B}T)-1]$ is the mean energy of Planck oscillators at temperature T. Notice that in the expression of $\Theta(\omega,T)$ a term equal to $\hbar\omega/2$ that accounts for vacuum fluctuations has been omitted since it does not affect the net radiation heat flux. This term, however, needs to be included to study other fluctuation-induced phenomena such as Casimir forces. These forces arise when the expected value of the EM energy in vacuum is modified by the presence of dielectric o metallic media [14].

Once we have quantified the sources of thermal radiation, we need to solve Maxwell equations considering the fluctuating currents defined in Eq. (1.7). This problem can be solved with a variety of methods, depending mostly on the geometry of the objects considered. In all cases, the physical magnitude that has to be calculated to find the radiative heat flow between two bodies is the expected value of the Poyinting vector. In Chapter 3 we show explicitly how to solve for the RHT between two semi-infinite parallel

plates, finding the following expression for the net power per unit of area exchanged by two isotropic parallel plates:

$$Q(d,T_1,T_3)=\int_0^\infty \frac{d\omega}{2\pi}\left[\Theta(\omega,T_1)-\Theta(\omega,T_3)\right]\int\frac{d\mathbf{k}}{(2\pi)^2}\left[\tau_s(\omega,\mathbf{k},d)+\tau_p(\omega,\mathbf{k},d)\right], \quad (1.8)$$

where $\mathbf{k}$ represents the parallel wave vector $\mathbf{k}=(k_x,k_y)$ along the x and y directions, and $\tau_{\alpha=s,p}$ is the transmission coefficient for s or transverse electric (TE) and p or transverse magnetic (TM) polarized EM waves. These transmissions can be expressed as [11]:

$$\tau_{\alpha=s,p}(\omega,\mathbf{k},d)=\begin{cases}(1-|r_{21}^\alpha|^2)(1-|r_{23}^\alpha|^2)/|D_\alpha|^2, & k<\omega/c,\\ 4\mathrm{Im}\{r_{21}^\alpha\}\mathrm{Im}\{r_{23}^\alpha\}e^{-2|q_2|d}/|D_\alpha|^2, & k>\omega/c,\end{cases} \quad (1.9)$$

where $q_i=\sqrt{\epsilon_i\omega^2/c^2-k^2}$ is the transverse or z-component of the wave vector in layer i, k represents the magnitude of $\mathbf{k}$ and $\epsilon_i(\omega)$ is the corresponding dielectric constant and $D_\alpha=1-r_{21}^\alpha r_{23}^\alpha e^{2iq_2d}$. r_{ij}^α represent the different Fresnel coefficients, which are given by

$$r_{ij}^s = \frac{q_i-q_j}{q_i+q_j}, \quad (1.10)$$

$$r_{ij}^p = \frac{\epsilon_j q_i-\epsilon_i q_j}{\epsilon_j q_i+\epsilon_i q_j}. \quad (1.11)$$

Notice that the second integral in Eq. (1.8) is carried out over all possible directions of $\mathbf{k}$ and it includes the contribution of both propagating waves with $k<\omega/c$ and evanescent waves with $k>\omega/c$. Although Eq. (1.8) seems a bit complex at first sight, it can be understood in very simple terms. In order to find the total radiative power exchanged per unit of area, we need to integrate the transmission across our specific setup (in this case, two parallel plates) of all the existing EM modes. Finally, we need to evaluate if these modes are more thermally occupied at the hotter body than and the colder multiplying by $[\Theta(\omega,T_1)-\Theta(\omega,T_3)]$. This calculation thus tells us the net radiative heat flow between the two objects.

Throughout this thesis we mainly focus on the analysis of the radiative linear heat conductance per unit of area, h, which is referred to as the heat transfer coefficient (HTC) when the systems under study are infinite. This coefficient is given by

$$h(d,T)=\lim_{\Delta T\to 0^+}\frac{Q(d,T_1=T+\Delta T,T_3=T)}{\Delta T}, \quad (1.12)$$

where T is the absolute temperature that will be around 300 K in most of the cases discussed in this thesis. Additionally, we define the spectral heat flux (or spectral HTC

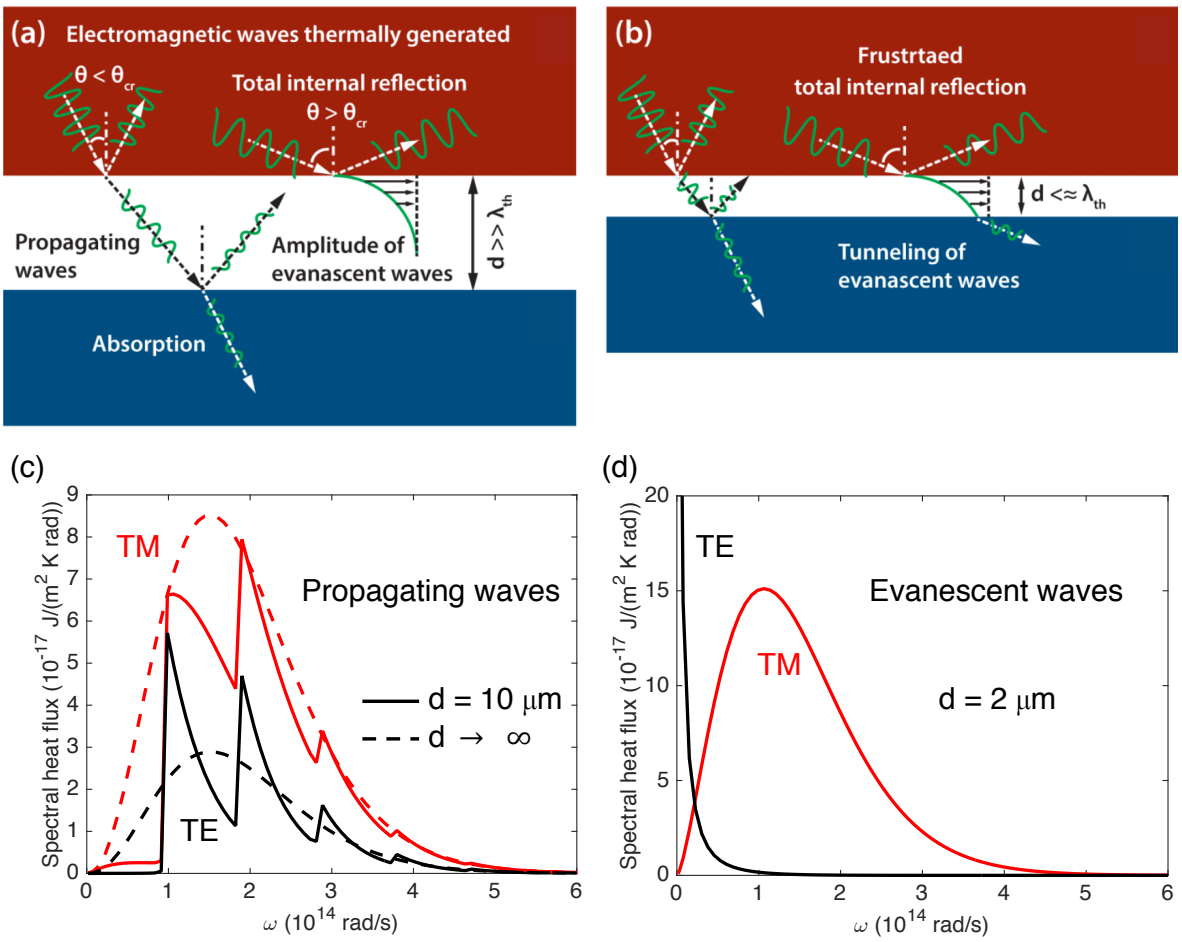

Figure 1.6: (a) Scheme of the RHT between a hot (1) and a cold body (2) [15]. Some of the EM waves thermally generated in body 1 are propagated to body 2, but others suffer total internal reflection, generating an evanescent wave in the vacuum gap. As long as this vacuum gap is much longer than λ_{Th}, these waves will not contribute to the total heat transfer. However, if both objects are sufficiently close (b), these evanescent waves can effectively tunnel to the second body, contributing to the total RHT. (c-d) Spectral heat flux due to propagating (c) and evanescent (d) waves for two semi-infinite Au plates at room temperature.

for infinite systems) h_ω as the radiative heat conductance per unit of frequency:

$$h(d,T) \equiv \int_0^\infty h_\omega(d,T,\omega)d\omega. \tag{1.13}$$

The total heat conductance between two objects ($G(d,T)$) can be found by integrating $h(d,T)$ over a certain area or calculating directly the radiative heat flow per unit Kelvin of two finite-size objects.

1.3.1. Interference effects in the near-field

Let us now use the theoretical expression for the NFRHT between two parallel plates (Eq. (1.8)) to discuss the new physics arising from reducing the gap between the bodies (see Fig. 1.6(a)-(b)). In the near-field regime, there are two new effects that modify the predictions of Plank's law. First, the interference of propagating waves inside the vacuum gap can modify substantially the spectral heat flux. This effect can be clearly observed in Fig. 1.6(c), where the propagating waves contribution ($k < \omega/c$) to the spectral heat flux (h_ω) between two semi-infinite Au parallel plates at room temperature is plotted for two different gaps and for both s (TM) and p (TE) polarization. The effect of constructive and destructive interference can be clearly observed when comparing the results between $d = 10$ μm and $d \to \infty$. Indeed, the frequency spacing between two consecutive peaks can be easily calculated using the resonance condition for a Fabry-Perot interferometer, which is in this case $\omega_s = \pi c/d = 9.42 \times 10^{13}$ rad/s and it nicely coincides with the results in Fig. 1.6(c). Furthermore, the term from the analytical expression Eq. (1.9) that considers interference effects is $|D_\alpha|^2$, which has the expected form of a Fabry-Perot denominator.

1.3.2. Contribution of photon tunneling to the energy transfer

The second effect that modifies the RHT between closely spaced bodies in vacuum is the contribution of evanescent waves. This effect can be understood by taking a look to Fig. 1.6(a-b). Inside a dielectric object, the speed of light is reduced by a factor n, which corresponds to the refractive index of the material. As the speed of the propagating EM modes is reduced, the density of states must be higher. These extra modes have larger wave vectors in the direction parallel to the surface (x-y plane, see Fig. 1.5). When these modes try to escape the material, they cannot propagate in vacuum, so they experience total internal reflection. If the second object is far enough, these waves will decay before reaching the new body and will not have any effect in the thermal interchange (Fig. 1.6(a)) However, if the two bodies are separated by a distance smaller than λ_{Th}, these totally internally reflected modes can tunnel into the second medium (Fig. 1.6(b)) and effectively contribute to the RHT [16]. This effect is the photonic analogy to electron tunneling in, for example, a scanning tunneling microscope (STM).

Therefore, in order to achieve a remarkable contribution of phonon tunneling to the total radiative transfer, we must consider materials that can host a large density of

states of propagating modes. Moreover, these modes must exist in a frequency range that can be excited at around room temperature. Metals such as gold or platinum are great candidates because they behave as perfect mirrors at infrared frequencies, which can be thermally excited easily.

Figure 1.6(d) shows the contribution of TE and TM evanescent waves to the RHT between two Au parallel plates separated by 2 μm. As one can see, the magnitude of the spectral heat flux is larger than the results shown in Fig. 1.6(c) for propagating waves. The contribution of evanescent waves gets higher as the distance between the two bodies is reduced, as it can be observed in Fig. 1.7, where the HTC is plotted for parallel plates made by different materials. The closest the two objects are, the more EM modes can tunnel and more efficiently. The contribution of these waves can be truly remarkable: the enhancement of the RHT at distances smaller than 10 nm can be of more than 3 orders of magnitude compared to the heat flow in the far-field. NFRHT thus offers thermal interchanges that are orders of magnitude higher than the blackbody predictions. Besides, NFRHT depends dramatically on the gap, in contrast with the predictions from the classical laws of thermal radiation.

1.3.3. Enhancing NFRHT with surface EM modes

Totally internally reflected waves are not the only EM modes that can be evanescent in the gap. Surface EM waves can also exist at the surface of the different bodies and thus contribute to the NFRHT. The main difference between these modes and the previous ones is that they decay exponentially both in the vacuum gap and inside the objects. One example of surface EM waves are surface phonon polaritons (SPhPs), which arise from a strong coupling between light and optical phonons. They exist in polar dielectrics such as silicon dioxide (SiO_2) and silicon nitride (SiN), and they are generated by the vibration of their atomic dipoles. Fortunately, these modes appear at energies comparable to $k_B T$ (25 meV at room temperature), so they can also be used to enhanced the NFRHT. It can be observed in Fig. 1.7 that SPhPs can boost the NFRHT [17, 18] and can even beat the result between two Au plates at nanometer-distances. Moreover, the NFRHT between polar dielectrics does not saturate at very small gaps, as it happens in the metallic case. The reason for this is that the hybridization of the SPhPs at the interfaces of the two bodies is higher when the separation between the two planes is decreased. Therefore, the density of photonic states will also be larger and thus the NFRHT increases monotonically for smaller gaps. More precisely, the HTC between polar dielectrics scales as d^{-2} in the near-field down to gap sizes of $\sim$ 1 nm [18]. For smaller gaps, the local approximation

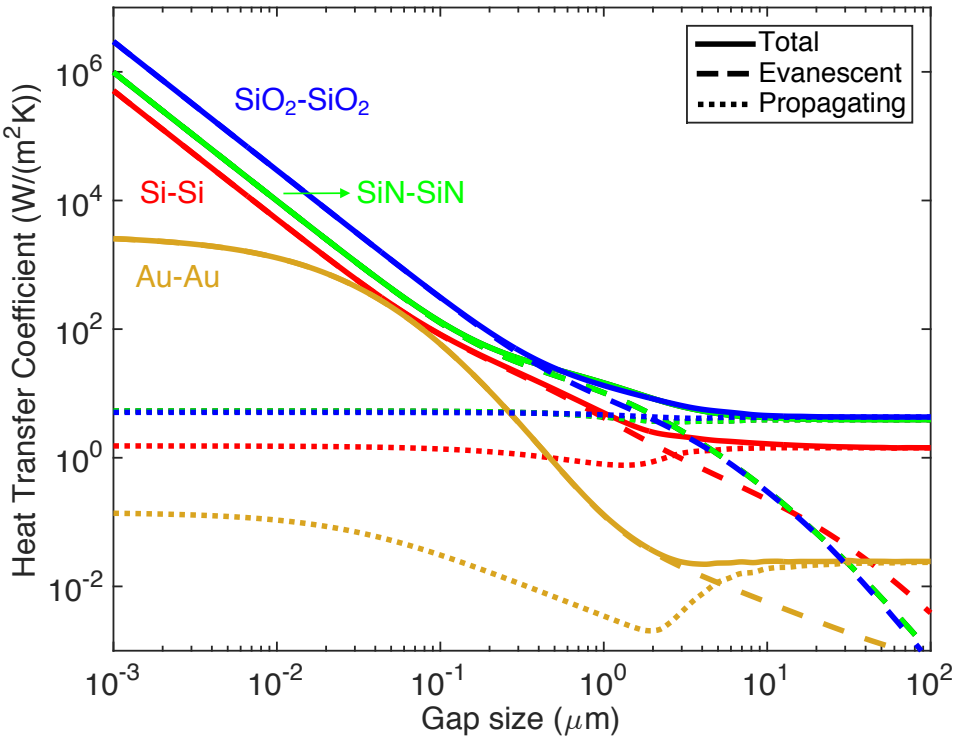

Figure 1.7: Heat transfer coefficient as a function of the gap size between two semi-infinite plates made by different materials: metals (Au), polar dielectrics (SiO_2 and SiN) and doped semiconductors (doped Si). All of them experience a enhancement of RHT in the near-field, but its physical origin is completely different for every system. These four materials will be further studied throughout the thesis. It can be observed that for small gap sizes, the evanescent contribution is the dominant one for the HTC.

for the dielectric constant breaks down and it is necessary to consider new processes such as phonon tunneling to calculate accurately the total heat flow [19].

Metals also host surface modes known as surface plasmon polaritons (SPPs) that could potentially be used to enhance the NFRHT. The physical origin of these modes is the coupling between photons and the oscillations of free electrons in the metal (plasmons). However, the energies necessary to excite them are much higher than 25 meV and thus they do not contribute to the RHT at room temperature. On the other hand, doped semiconductors such as Si do also support SPPs, but they can be excited at much lower energies. These modes behave very similarly to SPhPs with respect to the NFRHT, as it can be observed in Fig. 1.7.

In this section, we have used the parallel plate calculation to illustrate the new physics that arises when two objects interchange energy via radiation in the near-field. However, this is only one of all the possible geometries of an object and thus further theoretical

tools are needed to analyze the radiative heat flow between bodies with different shapes. We will see in the next section which are the available theoretical techniques to calculate the NFRHT between arbitrary objects.

1.4. Theoretical approaches to calculate the radiative heat flow in the near-field

After Polder and Van Hove published their seminal work on the thermal energy exchange between two parallel plates in 1971 [11], there did not appear many theoretical studies on NFRHT during the next years. One of the reasons was the lack of experiments that could measure the heat flow enhancement in new regimes. Moreover, extending the plate-plate calculation to other geometries was very complex and computationally demanding. Fortunately, the development of novel experimental techniques in the new century has motivated the theoretical study of NFRHT and in the next section we will briefly review the existing approaches to find the radiative heat flow in different scenarios.

1.4.1. Analytical results

In the last 10 years, several research groups have found exact semi-analytical expressions for the NFRHT between highly-symmetric objects. These results have been found using the scattering approach to EM phenomena. The scattering formalism encodes the scattering properties of an object through a matrix called the T-matrix, which components relates the amplitudes of incoming and outgoing waves from the body [20]. For these symmetric objects, is is possible to find analytical expressions for the T-matrix, usually in terms of special functions such as spherical harmonics. Once this matrix is known, it is possible to calculate the radiative heat flow between two objects in the near-field. Several works have derived compact matrix-trace formulas which relate the scattering properties of a single body with the NFRHT between two or more objects [21–23].

Within this approach, an analytical result for the NFRHT between two arbitrary plates has been derived. Bimonte found a expression for the total radiative power that depends only on the reflection coefficients at the different surfaces [24]. This result can be used to find the heat transfer between multilayered and periodic systems. Therefore, it is a very powerful approach to calculate the NFRHT between photonic crystals, nanostructured materials (see Fig. 1.8(a)) and metasurfaces, and it has been widely used in the literature [25–32].

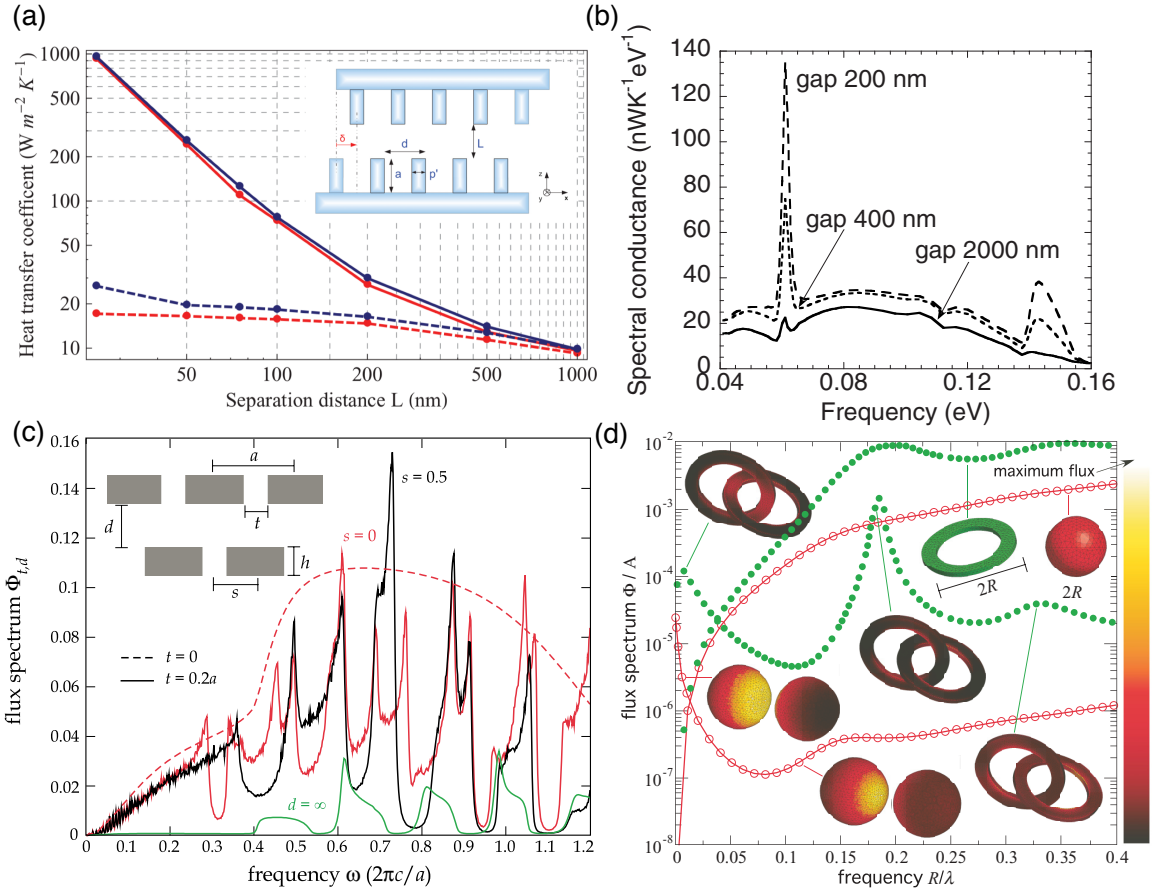

Figure 1.8: (a) HTC as a function of the separation distance (L) between two identical gratings (d=1500 nm, $a = 500$ nm and $p' = 300$ nm, see inset), both when the gratings are not laterally separated (blue solid line) and when they are by half a period (blue dashed line) [26]. The red lines show an approximated calculation. (b) Spectral heat flux between two silica spheres of radius $R = 20$ μm and three different gaps [34]. The results were obtained using a semi-analytical approach. (c) Flux spectrum between two photonics crystals for different geometrical parameters, calculated with a FDTD method [35]. (d) Flux spectra of isolated and interacting spheres and rings of radius $R = 1$ μm, normalized to their surfaces areas and calculated with a FSC formulation of the heat transfer problem [38]. The insets show the spatial distribution of the surface flux pattern.

Similar derivations have been performed to find the near-field heat flow between a sphere and a semi-infinite plate [33] and between two spheres [34], as it is shown in Fig. 1.8(b). However, for lossy objects, it is only possible to obtain closed-form T-matrix when the considered body is a sphere, a semi-infinite cylinder or a semi-infinite slab [20]. Therefore, it is necessary to use numerical methods to study and understand the NFRHT between any other geometries.

1.4.2. Numerical methods

One of the numerical methods that has been employed to calculate the heat flow in the near field has been the finite-difference time-domain (FDTD) method. In this technique, both space and time are discretized in a finite grid and the electric and magnetic fields are sequentially solved. It is widely employed in electromagnetism and it is useful to obtain quantities such as the absorption or the reflection spectrum of a certain scatterer. Moreover, as it is a time-domain method, it can yield a broadband frequency response with just a single simulation run. In the context of NFRHT, it has been used to calculate the heat flow between two photonic crystal slabs [35]. The results obtained for the spectral heat flux are shown in Fig. 1.8(c). In this case, the thermal emission is considered by incorporating a Langevin approach to the Brownian motion [36]. The main advantages of the FDTD method are its simplicity, its low memory requirements and its possibility to implement arbitrary geometries and materials. However, as it is a method of statistical nature, its results are usually very noisy and it is necessary to perform several simulations and average over them to obtain accurate results.

Another numerical method which has been used in the heat transfer context is the boundary element method (BEM) [37]. Rodriguez an coworkers [38, 39] have recently put forward a fluctuating-surface-current (FSC) formulation of the heat transfer problem. This formulation can be combined with the BEM to describe the heat transfer between bodies of arbitrary shape. An example of the results obtained via this formulation can be observed in Fig. 1.8(d), where the RHT between objects with different geometries is shown. This method can be applied to systems composed by several bodies and it is also able to calculate the heat flow when an object is embedded in another one. Moreover, it can compute the spatially resolved pattern of the Poynting flux on the surface of the bodies (Fig. 1.8(d)). It is worth stressing that this approach provides numerically exact results for the heat transfer within the framework of FE. In general, BEM method is computationally faster than the FTDT as it only discretizes the surface of the bodies and not all its volume. On the other hand, it employs dense matrices which can require too much computer memory in complex situations.

1.5. Experimental setups for measuring NFRHT

Measuring the radiation exchanged by two bodies separated by a very small gap is extremely challenging. It requires being able to control the distance between two objects at the micrometer and sub-micrometer scale while measuring the change in temperature in them due to the contribution of evanescent waves. Moreover, the experiment must be realized in vacuum to avoid the conductive contribution to the heat transfer. Due to these difficulties, while there are plenty of theoretical works on NFRHT, the number of experiments is rather limited. In this section, we will briefly recall the different experimental techniques that has been used to demonstrate and further understand this phenomenon [15].

As we have seen in Sec. 1.2, the first measurements of NFRHT were done in a setup where two parallel-plates are brought into close proximity. This geometry is one of the hardest to realize from a experimental point of view, as it is very challenging to obtain and maintain good parallelism between macroscopic plates at nanometer separations. However, as the whole macroscopic surface is brought to a subwavelength gap, the effects of NFRHT are more dramatic and the thermal signal can be more easily measured. After Hargreaves' experiment in 1969 there was not any further progress in the measurement of NFRHT until 2008, when Hu *et al* [40] measured the NFRHT between parallel glass optical plates, which support SPhPs in the infrared regime. They established a micrometer gap between the plates by placing polystyrene spacers between the two objects. These spacers had a very low thermal conductivity to assure that the dominant contribution to the heat transfer was the radiative one. Their results show that the NFRHT is twice as large as the far-field heat transfer and it is 1.5 times larger than the blackbody predictions. However, this approach did not allow to realize a systematically study of the gap-size dependence. In the following years, two new studies [41, 42] reported a gap-varying measurement of NFRHT between two parallel plates. The results obtained by these works not only agree rather well with the theoretical calculations, but they also reported a huge enhancement over the blackbody limit. More precisely, Ref. [42] demonstrated a heat flow 100 times larger than the predictions of the classical theory at a gap size of 2 μm. But still none of these experiments could measure the RHT in the submicron-regime.

Only in the last years it has been possible to measure the heat flow at distances smaller than a micron using the plate-plate approach. On the one hand, experiments using high-

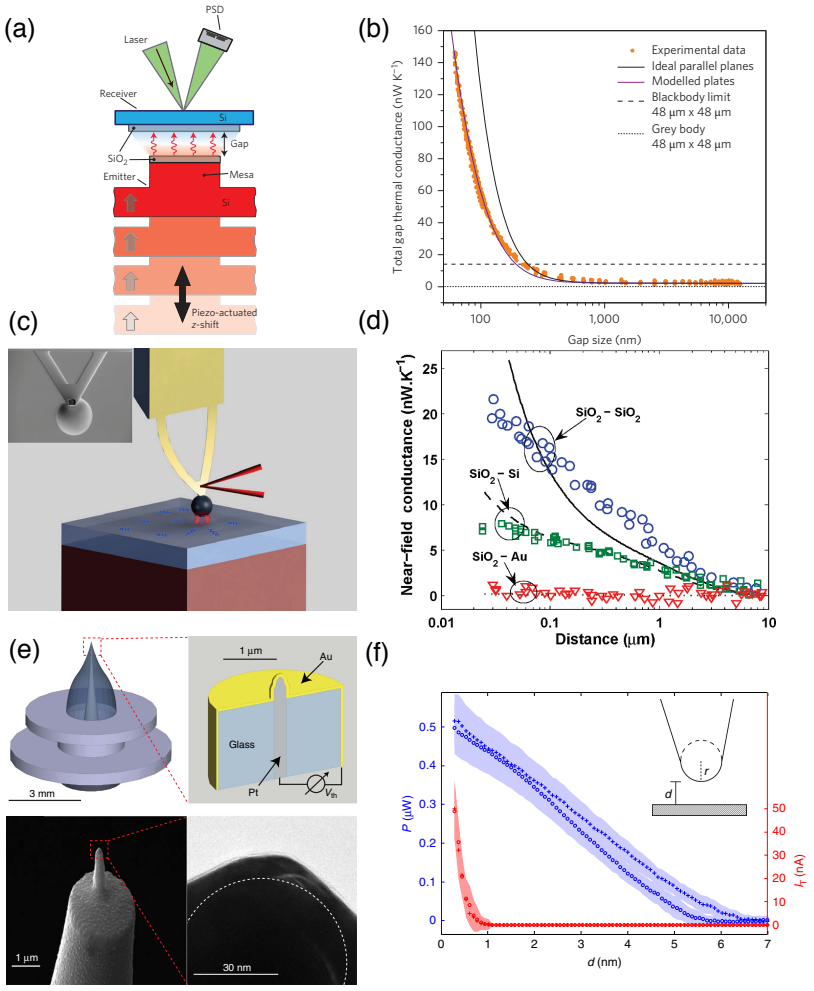

Figure 1.9: (a-b) Left: Scheme of the custom-built nanopositioning platform employed to measure the NFRHT between two parallel plates separated by gaps of $\sim$ 100 nm [44]. The contact between both plates can be detected using the laser beam together with the position sensitive detector. Right: Thermal conductance between two parallel Au plates of dimensions 48×48 μm^2 as a function of the gap size. (c-d) Left: Bimaterial cantilever employed to measure the radiative heat flow between a sphere and a plate [49]. The device consists on a silicon nitride AFM cantilever which is coated with a 70 nm-thick gold film and has attached a silica microsphere. The inset shows a scanning electron microscope (SEM) image of the apparatus. Right: Near-field thermal conductance between a SiO_2 sphere and plates of different materials. The different points represent the experimental data while the black solid lines correspond to theoretical computations. (e-f) Left: Near-field scanning thermal microscope [52]. The upper panels show a a scheme of the device. At the region where the gold is in contact with the platinum, a thermocouple is formed. The lower panels show a SEM and a transmission electron microscope images of the probe. Right: Total measured radiative power between a tip coated with gold and a sample of the same material as a function between the distance between them. The tunnelling current as a function of the gap is also plotted.

precision microscopic electromechanical systems have been able to measure the NFRHT between nanostructures separated down to 42 nm [43]. On the other, using a custom-built nanopositioning platform (see Fig. 1.9(a-b)), it has been possible to measure the heat flow between two parallel plates, obtaining a enhancement over blackbody larger than 3 orders of magnitude [44] . In both cases, the measurements show a very good agreement with the predictions from FE theory.

Another possible configuration to study experimentally the NFRHT is the sphere-plate approach. The main advantage of this configuration respect to the previous one is that there is no need to align and parallelize the two objects, so it is much easier to achieve smaller gaps ($\approx$ 10 nm). Conversely, as all the sphere surface is not separated from the plate by the smaller gap, the near-field enhancement is less dramatic. The basis element used to measure the heat flow in this scenario is a bimaterial cantilever. This witty device consists on a cantilever made by two different materials with distinct thermal expansion coefficients. When the temperature of this system changes, the cantilever is deflected and thus it can be used to measure the RHT in the near-field, as it can be observed in Fig. 1.9(c-d). The deflection of the cantilever can be measured using a laser beam, either interferometrically [45–47] or by detecting its reflection onto a position sensitive detector [48, 49]. The distance between the sphere and the plate can be tuned by a piezoelectric control of the sample position. These experiments are able to measure the NFRHT down to 30 nm, and their results show again a good agreement with the theoretical predictions.

Although the cantilever-based approach was one of the main advances in NFRHT experiments, it has some drawbacks. First, the contact distance between the sphere and the plate is done with the cantilever, which is also used to monitor the heat flux. Therefore, these two measurements are correlated, which might induce in some error. Secondly, the cantilever can be bended not only by the heat flux but also due to electrostatic or Casimir forces, questioning the values obtained for the heat flow.

The two previous techniques (plate-plate and sphere-plate) has been successfully applied to evaluate the heat flow down to a gap of $\approx$ 10 nm. However, for smaller gaps, it is necessary to employ a technique able to measure the NFRHT more locally. The configuration of a sharp scanning tip and a plate bridges the gap and enables a spacing of $\sim$ 1 nm without the need of performing technically challenging alignment and parallelizing procedures. However, as the area of the tips is much smaller than in the previous cases, the heat flow between the two bodies is extremely low, so new calorimetric techniques with a very high resolution are required to perform this kind of experiments.

Until recently, only the research group of Professor Achim Kittel in the University of Oldenburg could measure the NFRHT in this regime, using a near-field scanning thermal

microscope [50–52]. Their tips are based on a commercial scanning tunneling microscope who has been modified to include a nano-thermocouple at its apex. Therefore, this device is able to measure both the tip-sample distance and the local heat flux. The radius of curvature of this tip is much smaller than the dimensions of the previous setups ($\sim$ 30 nm), so it allows for a much more local evaluation of the NFRHT.

The results of these experiments show an extraordinary large heat flux when the tip-plate distance is in the range $1-6$ nm and both objects are made by gold [52]. A scheme of the experimental device together with the results obtained by this technique can be found in Fig. 1.9(e-f). The values found are not only more than five orders of magnitude larger than the blackbody predictions, but they are also 4 orders of magnitude larger than the values predicted by the FE theory, which has described accurately all the previous experiments. It is thus necessary to perform additional studies to better understand the heat flow in this regime. Actually, this will be one of the topics covered by the present thesis.

1.6. Technological applications of RHT at the nanoscale

The huge enhancement of RHT in the nanoscale is not only interesting from a fundamental point of view but it can also be key for the development of different thermal technologies. For example, it has been proposed [53] that near-field radiation could be used to improve the performance of thermophotovoltaic (TPV) devices [54]. These systems try to overcome the intrinsic Shockley-Queisser limit, which states that the efficiency of a solar cell made by a single $p-n$ junction cannot be higher than 33% [55]. The solar spectrum is broad but the semiconductor layer of a solar cell cannot absorb efficiently all these photons: those whose energy is lower than the bandgap cannot be converted into electricity and photons with higher energy do contribute to the energy conversion process, but they lose part of their energy when they relax to the band edge [56]. TPV systems include an intermediate element between the sun and the photovoltaic cell, which is used to tailor the solar light to the bandgap of the semiconductor (see Fig. 1.10). It has been shown that the efficiency of a solar cell could be ideally increased up to 85% by using a perfect intermediate material [57]. Near-field thermal emitters have been proposed as intermediate systems because of two main reasons. First, NFRHT can be very narrow-banded when it is mediated by surface modes, so it could be ideally adjusted to the bandgap of

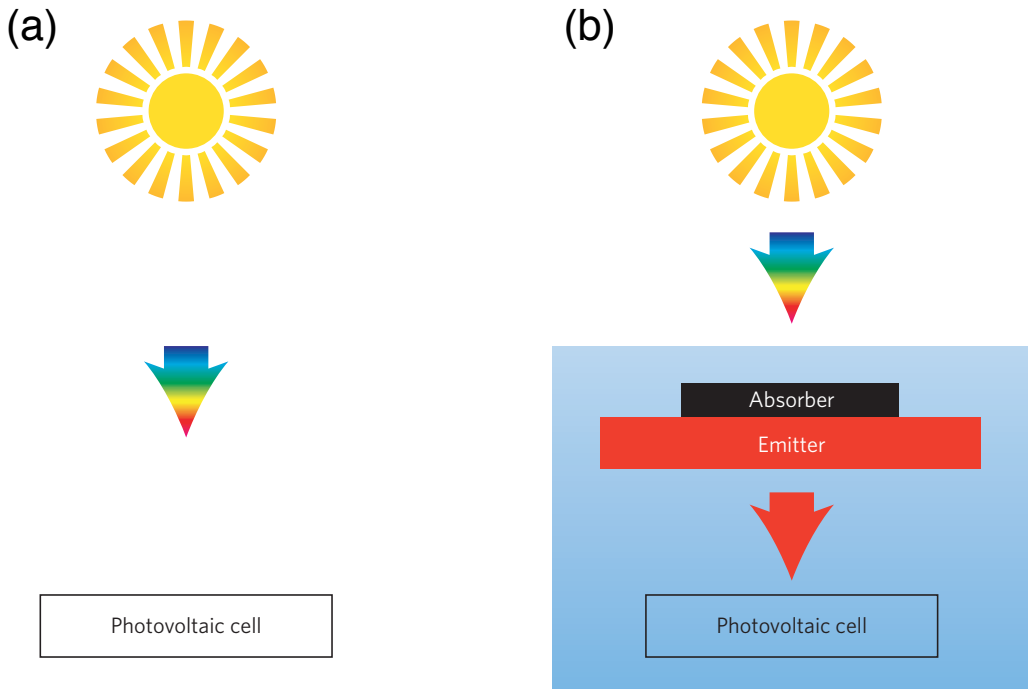

Figure 1.10: (a) A solar cell is normally exposed to direct solar light. However, due to the broadband nature of sunlight, a photovoltaic cell cannot convert all the photons into a electric current. (b) Scheme of a TPV device [56]. In this case, an intermediate system is placed between the Sun and the solar cell. This auxiliary mechanism is composed of a good absorber of radiation, which is able to trap most of the sunlight, and a tailored emitter. This last part radiates photons whose energy is ideally right above the photovoltaic's cell bandgap.

the solar cell. Secondly, the heat flow is dramatically increased in the near-field, so the operating power of the device could be also improved. Despite the multiple appealing proposals of near-field thermophotovoltaic devices [58–60] to date there has not been any experimental realization of this idea.

It has also been proposed that near-field radiation could be potentially use to achieve high resolution thermal litography [16] . To implement this idea, a hot mask could be patterned with two different materials. One of them is a very good near-field emitter whereas the other one is not. At a submicron distance from the mask, a wafer can be placed and be selectively heated below the good near-field emitter. This system could accomplish a thermal litography method with a higher resolution than state-of-the-art procedures. Finally, let us mention that NFRHT could be used to optimize the performance of heat-assisted magnetic recording [61, 62]. This technology employs a plasmonic antenna to heat up a magnetic recording medium. It is expected that the

heat flow in the nanoscale could have an important role in the steady-state temperature achieved in the magnetic medium.

1.7. RHT in the far-field between subwavelength objects

So far, in this General Introduction we have focused on the properties of the RHT between objects separated by distances smaller than λ_{Th}. We have seen that in this regime, Plank's law for black bodies is no longer valid and the Planckian limit can be surpassed by orders of magnitude. As already acknowledged by Planck in his seminal work [2], another limitation of his law is related to the description of RHT between objects with dimensions smaller than λ_{Th} (see Fig. 1.3). In this case, Planck's law, which is based on ray optics, is expected to fail even in the far-field regime, where separations are larger than λ_{Th}. Thus, one may wonder whether the Planckian limit can also be overcome in the far-field regime, something that is not possible with extended (infinite) objects [63]. It is known that the emissivity of a finite object can be greater than 1 at certain frequencies [64, 65], but that is not enough to emit more than a black body. In fact, only a modest super-Planckian thermal emission has been predicted in rather academic situations [66, 67], and it has never been observed. For instance, Ref. [68] reports one of the few experiments exploring the thermal radiation of an object smaller than λ_{Th}. In that work, the thermalization of an optical fiber was investigated and Planck's law was shown to incorrectly describe the thermal emission, but the fiber was actually found to emit much less than a corresponding blackbody, *i.e.*, no super-Planckian thermal emission was observed. In the context of RHT between two objects, there are neither theoretical proposals nor observations of super-Planckian far-field RHT. This fact is mainly due to the lack, until recently, of numerical techniques able to describe the RHT between objects of arbitrary size and shape that can, in turn, guide the design of appropriate experiments.

1.8. Open problems in the field of RHT

During the last 10 years, the field of RHT has flourished and many theoretical and experimental studies have been performed. The 1970's early theoretical predictions for the radiative heat flow enhancement in the near-field have been confirmed in a variety

of experimental setups, as it has been explained in Sec. 1.5. However, there were still multiple open questions at the beginning of this thesis work and that is the reason why we have performed new research efforts to shed light in this exciting field of research.

From a fundamental point of view, it was still unknown if FE is able to describe the RHT when the distance between two objects is smaller than 10 nm. So far, NFRHT experiments had verified that this theoretical framework can explain quantitatively the radiative heat flow between two bodies when they are separated by a gap down to some tens of nanometers ($\sim$ 30 nm). Moreover, recent experiments [50, 51] that had measured the heat flow at gap distances smaller than 10 nm had reported a thermal conductance which is four orders of magnitude larger than the values predicted from FE. Therefore, new experimental and theoretical analysis were needed to better understand the heat transfer in this regime and elucidate which are the physical mechanisms that dominate the energy transfer process in this regime.

In order to solve this discrepancy, it was necessary to compare the novel experimental results with the best available numerical techniques. Until recently, the comparisons between theory and experimental results had only considered the simplest plate-plate calculation together with the so-called Derjaguin or proximity approximation (See Sec. 2.3.2). However, experimental systems have in general more complicated shapes, specially the scanning tips employed to evaluate the heat flow at nanometer distances [51]. It was therefore necessary to use numerical approaches to exactly simulate the geometries that are exchanging radiative heat. Moreover, the surface of the tips and samples considered are not flat but normally contain a nanoscale roughness profile. Considering this fact in the theoretical computations could be crucial to perform a faithful comparison between the experiments and the simulations, especially when the gap distance between the objects can be of the same order than the roughness profile.

Another remaining challenge in the field was the study of the limits of near-field radiative enhancement. It had been already proved that the heat flow can be enhanced by orders of magnitude in the nanoscale, but it was still unknown if this process can be further boosted. The highest radiative heat flow predicted so far was the one between polar dielectric materials, which can host SPhPs in the infrared region of the spectrum. However, there was no reason to believe that it was impossible to overcome their near-field performance. New strategies such as considering periodic nanostructures could tune the EM density of states of the objects and therefore increase even more the heat flow in the near-field.

The enhancement of thermal energy interchanged in the near-field could potentially contribute to the development and improvement of several technological applications, as

we have discussed in Sec. 1.6. However, in order to realize these interesting proposals, several issues must be overcome. One of them was to check if the enhancements found between bulk materials could also be obtained with thin films. This advance was essential to leverage NFRHT and export it in a variety of nanoscale devices. Another aspect that should be improved was the tuning of heat flow in the nanoscale. So far, the existing proposals were either very complicated to be implemented or did not provide a large degree of tunability. Therefore, it was necessary to analyze new systems and materials which exhibit a high active tuning of near-field heat flow.

As we have seen in Sec. 1.7, Planck's law is also not strictly applicable when the size of the objects is much smaller than λ_{Th}. One could thus wonder whether a enhancement of the RHT could also arise between subwavelength objects even in the far-field, where only propagating waves do contribute to the thermal radiation. There were neither theoretical predictions nor experimental observations of this phenomenon, so understanding the RHT between subwavelength objects would be of great interest from both a fundamental and an applied point of view, as Planck's law is the main tool for calculating the far-field radiative heat transfer (FFRHT) between nano and micro-devices.

1.9. Structure of this manuscript

This thesis deepens the subject of RHT from a theoretical point of view and tries to answer some of the open questions in the field. The different chapters can be grouped into two distinct blocks. Chapters 2-5 analyze NFRHT in a variety of scenarios. On the other hand, Chapters 6-7 investigate whether the predictions of Planck's law can be overcome in the far-field. Finally, Appendix A-C include additional details on the calculations performed. Here we explain in more detail the structure of the thesis.

Chapters 2-5 explore several aspects of NFRHT. More precisely, Chapter 2 is devoted to analyze the near-field heat flow between a silica (SiO_2) sphere and a SiO_2 thin film deposited on a gold substrate. This study has been performed in collaboration with the experimental group of Pramod Reddy and Edgar Meyhofer from the University of Michigan. The gap size between the SiO_2 thin film and the sphere ranges from 20 nm to 10 μm, and the thickness of the film varies from 50 nm to bulk silica. The experiments were performed using a micro-fabricated calorimetric platform that enables quantitative studies of gap-size-dependent heat currents from a spherical hot surface to a planar colder surface. Chapter 3 analyzes theoretically the magnetic field dependence of NFRHT within the framework of FE between two parallel plates made of a variety of materials.

More precisely, we consider magneto-optical materials, as their dielectric function can be modified by an external magnetic field. N-doped semiconductors, such as InSb and Si, are perfect candidates to carry out our analysis. Afterwards, Chapter 4 investigates the NFRHT between two Si-based metasurfaces featuring two-dimensional periodic arrays of holes. We use a rigorous coupled wave analysis to study how is the radiative heat flow modified when doped-Si is nanostructured. The periodic structure modifies the density of EM states in the gap between the two metasurfaces and the NFRHT can thus exhibit novel features. Later, in Chapter 5, we study the NFRHT between a scanning probe and a sample when their separation gap is between 2 and 50 nanometers. Again, in a collaboration with our experimental colleagues of the University of Michigan, we analyze the NFRHT between both metals and dielectrics. The experiments are performed with custom-fabricated scanning probes with embedded thermocouples, in conjuntion with new microdevices capable of periodic temperature modulation. We have performed numerical simulations that take into account the exact shape of the experimental devices, including the existing roughness. We also investigate the role of surface contamination effects in the heat transfer by analyzing the apparent tunneling barrier heights measured by a scanning thermal microcopy probe.

The last block of the thesis (Chapters 6-7) is devoted to study the FFRHT between objects with dimensions smaller than the thermal wavelength. In Chapter 6 we derive a relation between the FFRHT and the directional absorption efficiency of the objects involved. This result is used to calculate the FFRHT in a variety of geometries, such as spheres, cubes and parallelepipeds. We finally compute the radiative heat flow between suspended-pad microdevices that are widely employed in calorimetric experiments. Chapter 7 explores the RHT between coplanar two-dimensional materials, such as graphene and single-layer black phosphorus (SLBP). We find the absorption efficiency of these materials both numerically and analytically and afterwards this result is used to calculate the total radiative heat flow between one-atom-thick systems. Finally, the physical mechanisms that dominate the RHT in this regime are analyzed.

2 | Enhancement of near-field radiative heat transfer using polar dielectric thin films.

2.1. Introduction

In the previous chapter, we have explained how the radiative heat flux between two bodies can be increased by orders of magnitude in the near-field. However, so far we have only focused on bulk materials and we have not discussed whether this remarkable enhancement can be observed in thin films. Moreover, in order to leverage near-field radiation in emerging technologies such as the ones described in Sec. 1.6, is key to determine if the dramatic transport enhancements observed for bulk materials are also characteristic of thin slabs.

In this chapter, we analyze in collaboration with an experimental group the NFRHT between media coated by nanometric dielectric films [69]. We find dramatic increases in RHT -comparable to those obtained between bulk materials- even for very thin dielectric films (50-100 nm) as long as the spatial separation between the materials is comparable to the film thickness. This phenomenon can be explained by analyzing the spectral characteristics and the mode shapes of cavity surface phonon polaritons (CSPhPs), which dominate near-field radiative heat transport in polar dielectric thin films. We also compare our theoretical calculations with a novel experimental platform that leverages pi-

cowatt resolution heat-flow calorimetry [70]. This experiment is able to measure for the first time directly the NFRHT from devices with such coatings.

The chapter is organized as follows. First, we give a brief explanation of the experimental setup that is modeled theoretically in this thesis. Afterwards, we explain our theoretical framework for studying NFRHT in multi-layered structures. More precisely, we employ the expressions presented in Sec. 1.3 to calculate the RHT in our specific system. Then, we compare our results with experimental data and explain the enhancement of heat transfer by the existence of CSPhPs, a confined EM wave, the existence of which is related to the polar nature of the materials considered. Finally, we characterize the dispersion relation and properties of these bound modes.

2.2. Experimental setup.

In this part of the chapter we will describe briefly the setup which is able to measure NFRHT in thin films for the first time. These experiments have been performed at the University of Michigan, in the groups of Professors Pramod Reddy and Edgar Meyhofer.

The experimental setup is sketched in Fig. 2.1(a). To experimentally study the dependence of NFRHT on film thickness they have developed an ultra-sensitive, microfabricated calorimetric platform that enables quantitative studies of gap-size-dependent heat currents from a spherical hot surface (called emitter) to a planar, colder surface (called receiver) for a broad range of film thicknesses, see Fig. 2.1(b). The emitter device consists of a suspended region onto which a 53 μm diameter silica (SiO_2) is attached. It is glued to the heating calorimeter by a water-soluble adhesive that provides excellent thermal contact. Therefore, the temperature of the silica sphere matches exactly the one of the heating calorimeter.

Afterwards, the emitter is stepped towards the receiver with a piezoelectric actuator. The receiver (Fig. 2.1(a,c-d)) is made from silicon nitride (SiN) and is suspended via thin, long beams to achieve a thermal conductance of $G_{\text{beams}} \sim 2$ μW/K. It is partly coated with SiO_2 layers of varying thickness (50 nm - 3 μm) deposited on a 100 nm thick gold film (Fig. 2.1(b,d)). Both the emitter and the receiver feature an integrated platinum resistance thermometer which can resolve small temperature changes ($\sim$ 50 μK) enabling detection of small heat currents of $\sim$ 100 pW (2 $\mu W/K$ $\times$ 50 μK). The beams and suspended regions of the receiver incorporates ribs leading to stiff devices ($\sim$ 50 N/m) with extremely flat suspended regions. Given the excellent sensitivity of the receiver, they are able to resolve heat currents at distances as large as 10 μm. The

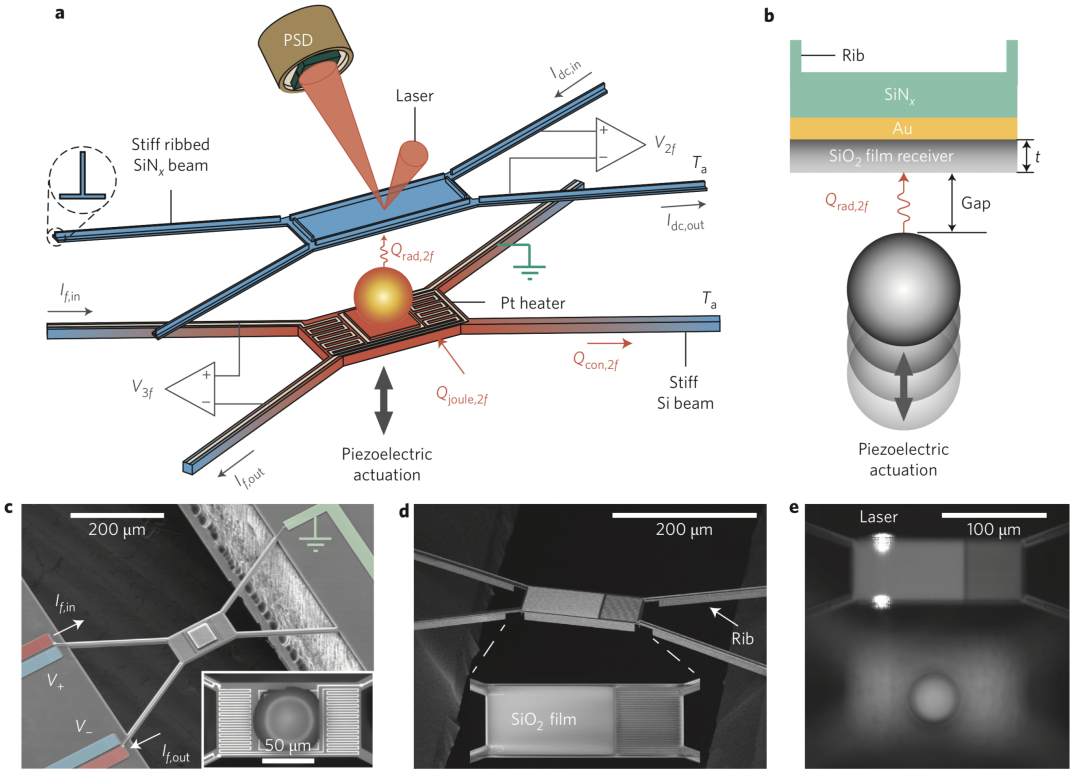

Figure 2.1: (a) Schematic of the experimental setup. The emitter consists of a suspended silicon platform, with an attached silica sphere, and integrated electrical heater-thermometer. The receiver is a stiff silicon nitride platform coated with gold and silica films of various thickness. (b) Schematic cross section of the planar receiver region and the spherical silica emitter. (c) SEM of the suspended platform and optical image (inset) of the spherical emitter. (d) SEM images of the receiver with ribbed, stiff beams. (e) An optical image of the emitter and receiver during alignment. For this image, they were laterally displaced to enable visualization of both devices.

smallest gap that can be achieved in such a platform is ~ 20 nm. A laser, together with a position sensitive detector (PSD) enable nanometer-resolution emitter-receiver contact detection (See Fig. 2.1(a) and (e) to observe how it is reflected off the receiver).

The described setup is placed into a vacuum chamber ($< 10^{-6}$ torr, room temperature) and a ~ 10 K gradient is established between the emitter and the receiver by the lower heating calorimeter. Near-field thermal conductance (heat transfer per unit Kelvin) at different gaps can now be calculated as: $G_{\text{gap}} = G_{\text{beams}} \times \Delta T_{\text{rec}}/[\Delta T_{\text{emit}} - \Delta T_{\text{rec}}]$, where $\Delta T_{\text{rec,emit}}$ stands for the temperature change at the receiver and at the emitter, respectively. This experimental technique contributes several improvements for NFRHT measurements over previously used bimaterial cantilever-based approaches [45, 49], where the deflection of the bimaterial cantilever is potentially affected by both temperature changes and forces (such as electrostatic or Casimir), posing challenges to the interpre-

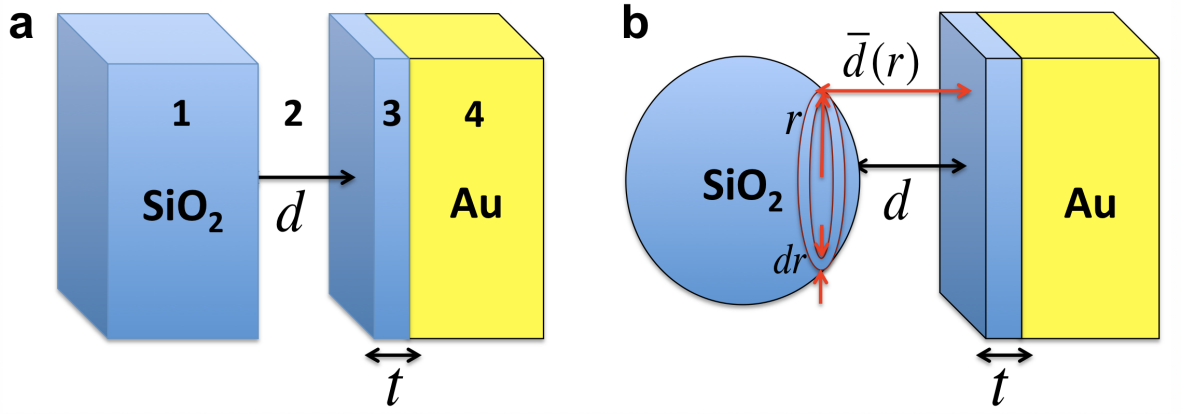

Figure 2.2: (a) Multi-layered system used as an intermediate step to compute the RHT in our experimental system. Here, a semi-infinite silica surface (medium 1) is separated by an air gap (medium 2) of size d from a silica film of thickness t (medium 3) coating a semi-infinite Au surface (medium 4). (b) The sphere-coated layer system investigated to compare with our experimental results. Here, we also illustrate the Derjaguin approximation [76] used to compute the heat transfer with the help of the results obtained for the multi-layered system in (a), as described in Eq. (2.3). In this approximation the sphere is sliced into infinitesimal rings of width dr and radius r. The heat transfer between a ring and the coated layer, which is a distance of the disk $\bar{d} = d + R - \sqrt{R^2 - r^2}$, is equal to the heat transfer per unit of area calculated for the multi-layered system, see Eq. (2.1), times the area of the disk, $2\pi r dr$.

tation of experiments [71]. In contrast, in the present technique, mechanical contact (detected optically) does not affect temperature measurements that are performed independently with a resistance thermometer. Moreover, this setup allows to modulate the temperature of the emitter and thus employ lock-in based techniques that enhance [70] the heat flow resolution to about 100 pW.

In the next section we will see how to properly model this experiment and then we will compare the experimental results with the theoretical simulations.

2.3. Theoretical modelling

In this section we will analyze the RHT measured by the previous experimental setup from a theoretical point of view. Our calculation of the RHT in the sphere-coating layer system proceeds in two steps. We first consider the heat transfer between a semi-infinite SiO_2 surface and a SiO_2 thin film coated on a semi-infinite Au surface, see Fig. 2.2(a). Afterwards, by using the Derjaguin approximation (see Sec. 2.3.2), we will calculate the heat transfer between the sphere and the layered system (Fig. 2.2(b)).

2.3.1. Multi-layered heat transfer calculation

Let us start by defining the multi-layered system under study. A semi-infinite silica surface (medium 1) is separated by an air gap of size d from a silica film of thickness t (medium 3) coating a semi-infinite Au surface (medium 4), as it is shown in Fig. 2.2(a). Moreover, we consider that the silica surface is set at a temperature T_1, while the silica coating and the Au surface are at a temperature T_3. In this case, the RHT between the two plates can be calculated using again Eq. (1.8) [72, 73].

$$Q(d, T_1, T_3) = \int_0^\infty \frac{d\omega}{2\pi} \left[\Theta(\omega, T_1) - \Theta(\omega, T_3)\right] \int \frac{d\mathbf{k}}{(2\pi)^2} \left[\tau_s(\omega, \mathbf{k}, d) + \tau_p(\omega, \mathbf{k}, d)\right]. \quad (2.1)$$

The expressions for the transmission probabilities τ_s (TE modes) and τ_p (TM modes) are modified in this case due to the SiO_2 coating of the gold plate [72, 73]:

$$\tau_{\alpha=s,p}(\omega, \mathbf{k}, d) = \begin{cases} (1 - |r_{21}^\alpha|^2)(1 - |R^\alpha|^2)/|D_{ML}^\alpha|^2, & k < \omega/c, \\ 4\mathrm{Im}\{r_{21}^\alpha\}\mathrm{Im}\{R^\alpha\}e^{-2|q_2|d}/|D_{ML}^\alpha|^2, & k > \omega/c, \end{cases} \quad (2.2)$$

where $R^\alpha = \dfrac{r_{23}^\alpha + r_{34}^\alpha e^{2iq_3t}}{1 - r_{34}^\alpha r_{32}^\alpha e^{2iq_3t}}$ and $D_{ML}^\alpha = 1 - r_{21}^\alpha R^\alpha e^{2iq_2d}$. r_{ij}^α represent the different Fresnel coefficients (Eqs. (1.10) and (1.11)) and the indexes i and j run from 1 to 4 following the labelling defined in Fig. 2.2(a). The dielectric constant of SiO_2 was taken from Ref. [74], while the corresponding one for Au was obtained from Ref. [75]. These constants are shown in Fig. 2.3 in the energy range of interest for the heat transfer at room temperature. Since in our experiments the temperature difference between the silica sphere and the coated film was only 10 K, we restrict ourselves to the linear response regime and compute the heat transfer coefficient $h(d, T)$, as defined in Eq. (1.12). In all the calculations shown in this Chapter we consider an absolute temperature of $T = 300$ K. In the next section we will see how to move from our semi-infinite multi-layered structure (Fig. 2.2(a)) to the sphere plane case (Fig. 2.2(b)).

2.3.2. Derjaguin approximation

In a second step, and in order to establish a direct comparison with our experimental results, we use the results obtained for the multi-layered system above to compute the radiative linear thermal conductance, $G(d, T)$, between a 53-micron-diameter silica sphere and a thin film coated surface by making use of the so-called Derjaguin approximation

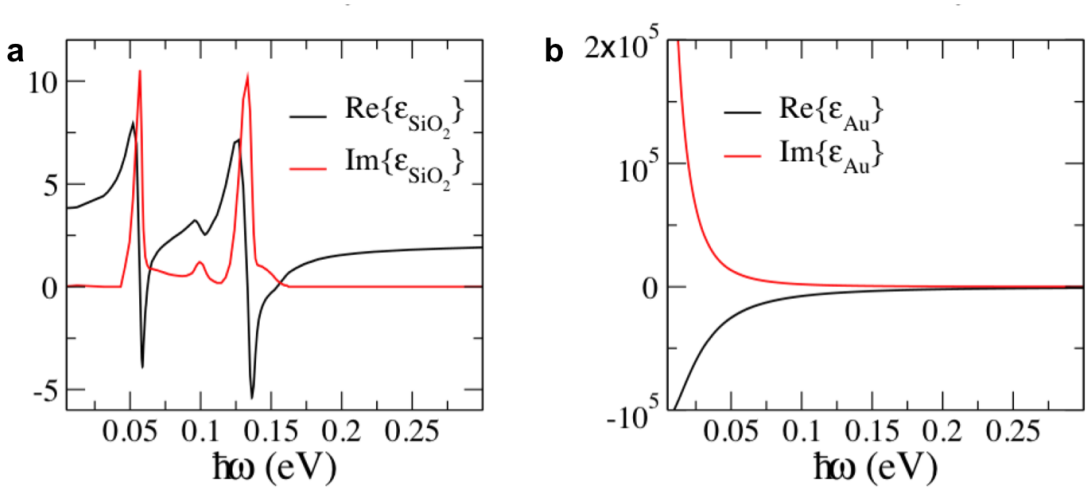

Figure 2.3: (a) Real and imaginary parts of complex dielectric constant of silica as a function of energy. Notice that the real part becomes negative in two narrow regions due to the existence of phonon polaritons in this dielectric material. This is the origin of the appearance of SPhPs in our multi-layered structure, which in turn dominate the NFRHT. (b) The same as in panel (a) for gold.

[76]. As illustrated in Fig. 2.2(b), in this approximation the sphere is thought to be sliced into a series of infinitesimal rings of different radii and the heat transfer between every ring and the coated film is computed using the result of Eq. 2.1. This means in practice that the heat conductance is computed as follows

$$G(T,d) = \int_0^R 2\pi r h(\bar{d}(r),T)dr, \tag{2.3}$$

where R is the radius of the sphere and $\bar{d} = d+R-\sqrt{R^2-r^2}$ is the local distance between the silica film and the rings defined in the sphere, see Fig. 2.2(b). This approximation has been successfully used in the literature [45, 48, 49] and it is expected to give a good result in our case in the most interesting regime where the gap size is much smaller than the radius of the silica sphere. Moreover, we have performed additional numerical calculations in Sec. 2.4.3 to verify the validity of this approximation in our specific problem. Notice that this approach does not consider Mie resonances of the sphere. Luckily, in the frequency domain where the heat conductance is large, silica is very lossy (Im$\{\epsilon\}$ is high) so the coherence length along the surface and the decay length inside the sphere are much smaller than the sphere radius [45].

2.4. Results

In this section we will show our theoretical results and compare them with experimental measurements. Then, we will study in detail the physics underneath in order to understand the special features of NFRHT in thin polar dielectric coatings.

2.4.1. Computed radiative heat conductance and comparison with experimental results

The computed gap dependence of the radiative linear thermal conductance per unit area (h) for the multi-layered structure is shown in Fig. 2.4. The different curves correspond to different thicknesses of the silica coating. For large values of the gap, the thermal conductance holds constant for each coating. At those distances, only propagating waves can transfer heat from one object to the other. Besides, effects related with resonant reflection are negligible as the gap distance is much larger than the thermal wavelengths involved ($\lambda_T << d$). This is the far-field heat transfer regime. We can understand the decrease of the thermal conductance with the coating thickness at large distances due to the mismatch of dielectric constants between silica and gold.

For gaps smaller than a micron, we observe that the heat conductance increases dramatically and becomes orders of magnitude higher than the far-field result. Besides, for gaps smaller than 100 nm the heat conductance value no longer depends on the coating thickness. What is the physical origin of both phenomena? We will answer this question later on, but let's first analyze which is the role of the SiN membrane placed below the Au layer.

In our experimental system, the receiver consists of a silica coating film deposited on a 100 nm thick gold film, which in turn lies on top of a silicon nitride (SiN) membrane (see Fig. 2.1). However, in the multi-layered system used to compute the heat transfer (Fig. 2.5(b)) we assumed that the Au layer is semi-infinite, which requires some justification. The reason is that for all purposes a 100 nm thick Au layer is optically thick and the SiN membrane underneath plays no role in the heat transfer. To demonstrate this fact, we extended the theory described above to take into account the finite thickness of the Au layer (100 nm) and the presence of a semi-infinite layer of SiN underneath. This extension only requires generalizing the expression of the coefficients in Eq. (2.2) to take into account the additional SiN layer. In Fig. 2.4 we show a comparison of the results for the radiative linear heat conductance per unit of area in the multi-layered system with

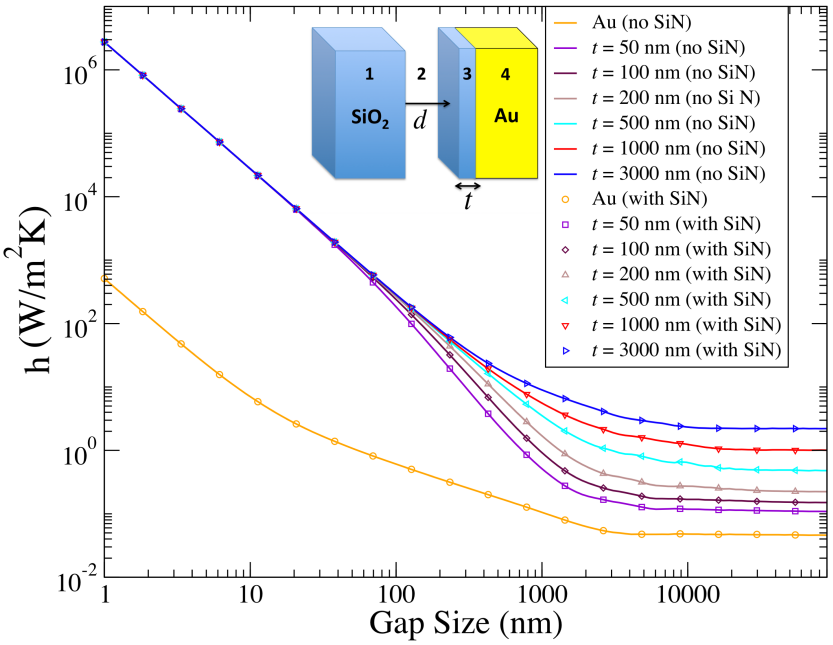

Figure 2.4: Computed linear thermal conductance per unit of area as a function of the gap size for the multilayer shown in the inset. This structure comprises a semi-infinite silica separated by an air gap of size d from a silica thin dilelectric coating a semi-infinite Au surface (see inset). The different curves correspond to different thicknesses of the silica coating. The solid lines correspond to the results where the Au layer is assumed to be semi-infinite, while the open symbols correspond to the structure where the Au layer is 100 nm-thick and there is a semi-infinite SiN layer underneath. Notice that the results are identical, even when there is no coating (orange curve and symbols).

and without the SiN membrane. In these calculations, we used the dielectric constant of SiN reported in Ref. [77]. As one can see, irrespective of the gap size or the coating thickness, the SiN plays no role in the heat transfer in our system. For this reason, we assume throughout this work that the Au layer is in practice semi-infinite.

Once we have verified that the SiN membrane plays no role in the NFRHT problem, let us compare the experimental results with the theoretical simulations. The results for the theoretical calculations of the near-field thermal conductance for the sphere-coated layer system (G_{NF}) can be observed in Fig. 2.5(a). Again, the different curves correspond to different values of the coating thickness. As we have seen in Sec. 2.3.2, they are computed from the semi-infinite multi-layered system by applying Derjaguin approximation to the results displayed at Fig. 2.4(a). In order to get only the near-field contribution, the thermal conductance in the far-field regime ($d = 70$ μm) has been subtracted. The experimental data for the NFRHT is shown in Fig. 2.5(b). Far-field heat transfer has been also subtracted in order to make a fair comparison. Both experimental

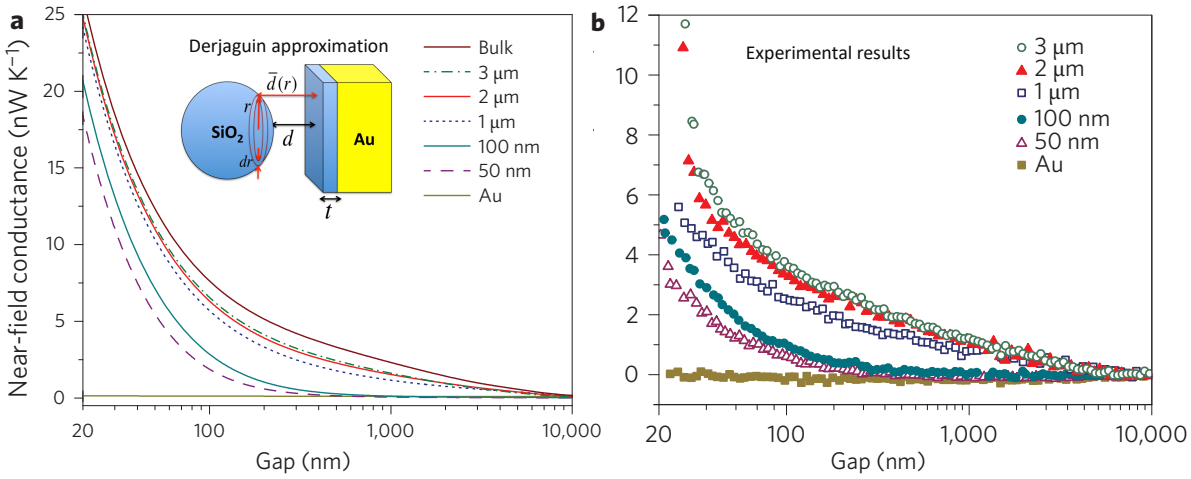

Figure 2.5: (a) Calculated near-field conductance as a function of the gap size for the sphere-coated layer system shown in the inset. The sphere has a diameter of 53 microns and SiO_2-Au structure is assumed to be infinite in the transversal direction. The different curves correspond to distinct values of the coating thickness. These results were obtained using the results of Fig. 2.4(a) within the Derjaguin approximation. Moreover, we subtracted the far-field contribution to make a closer comparison with our experiments. (b) Experimental near-field thermal conductance as a function of the film thicknesses. Far-field results have been subtracted from the total conductance. Data for each film thickness represent an average of ~ 10 different data sets. Standard deviations are small and not shown for visual clarity.

and theoretical results demonstrate that at small gaps, heat transfer is strongly enhanced. Besides, for each coating, G_{NF} remains almost unchanged until the gap is of the same order as the coating thickness. At that point, it starts to increase rapidly and almost converges to the bulk result!

The computed conductances (Fig. 2.5(a)) are in good overall agreement with the measurements (Fig. 2.5(b)) although the calculated conductances consistently overestimate the measured thermal conductance. We attribute this discrepancy to the inevitable uncertainties associated with the structural and optical properties of the microfabricated devices. The observed agreement between measurements and theoretical predictions suggests that FE successfully captures the key aspects of the gap-dependent NFRHT in these thin film structures. But we still do not understand neither the sudden increase of G_{NF} at small gaps nor the film thickness dependence of the conductance. We will try to answer both questions in the next section.

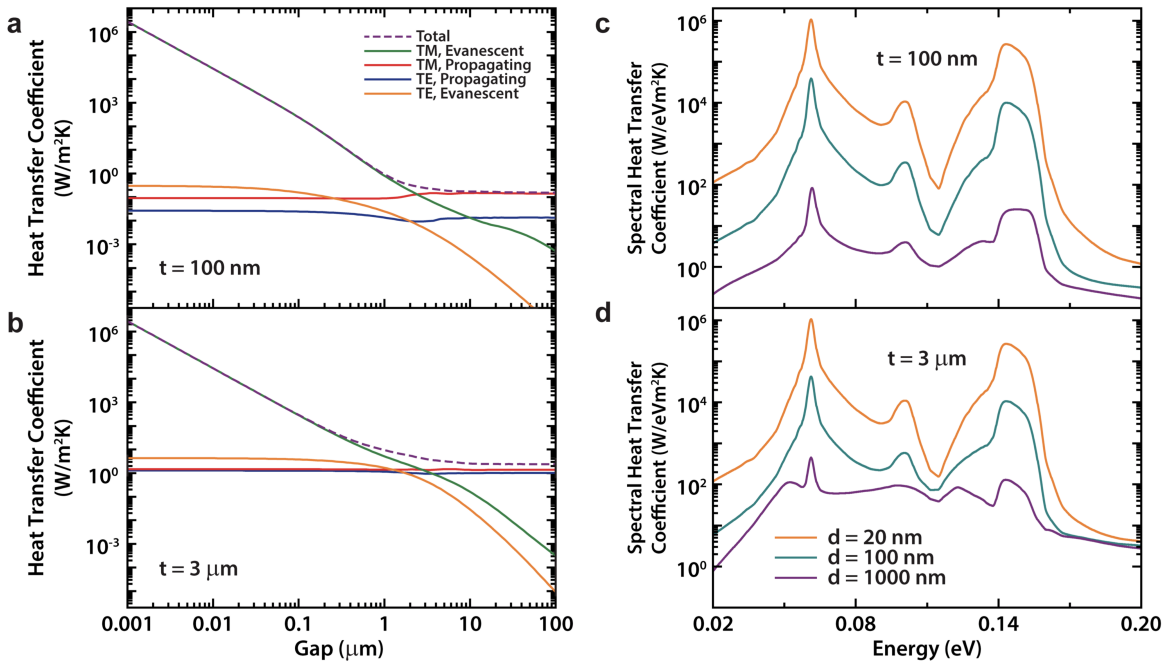

Figure 2.6: (a-b) Heat transfer coefficient (h) for the multi-layered system of Fig. 2.2(a) as a function of the gap size and for two different thicknesses of the silica coating, t. The solid lines correspond to the different contributions coming from the TM and TE modes, both evanescent and propagating, while the dashed line shows the total conductance. Notice that below 1 micron the contribution to the RHT is dominated by evanescent TM modes that correspond to SPhPs, as we show below. (c-d) The corresponding spectral heat transfer coefficient as a function of the radiation energy for several gap sizes and two different coating thicknesses, as indicated in the panels. Notice that the main contribution to the conductance comes from the regions where the real part of the dielectric constant of silica becomes negative, see Fig. 2.3, which is precisely where SPhPs exist.

2.4.2. Role of cavity surface phonon polaritons in NFRHT

The goal of this section is to show that NFRHT can be explained in terms of the basic properties of the CSPhPs, which are supported by the cavity formed by the narrow air gap between the SiO_2 layers. These modes will dominate heat transfer in our system. For this purpose, we focus on the analysis of the heat transfer in the multilayer shown in Fig. 2.2(a). The conclusion of this analysis can be trivially extrapolated to the sphere-coated film system in the spirit of the Derjaguin approximation.

Let us start by analyzing the different contributions to the RHT in the multi-layered system. In Fig. 2.6(a-b) we show the linear heat conductance per unit of area (h) as a function of the gap size for two different coating thicknesses (100 and 3000 nm). We show the individual contributions of the TM and TE modes, see Eq. 2.1, for both propagating waves ($k \leq \omega/c$) and evanescent waves ($k > \omega/c$). As one can see, for both thicknesses

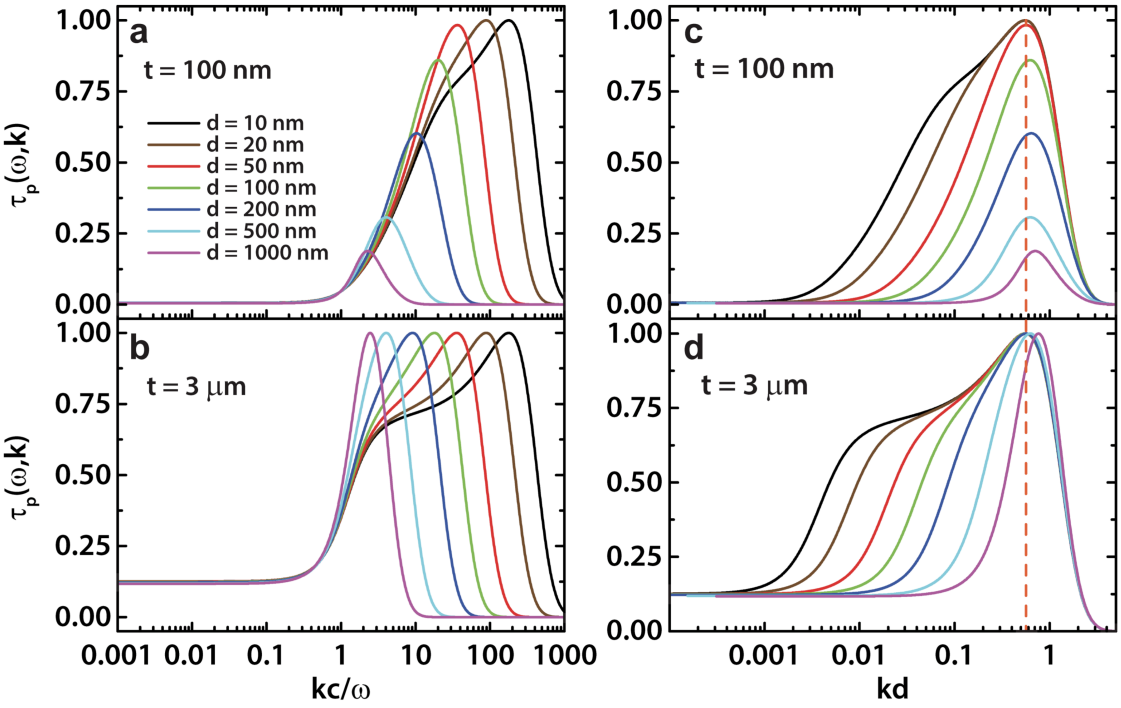

Figure 2.7: (a-b) Transmission coefficient of TM modes ($\tau_p(\omega, \mathbf{k})$) as a function of the magnitude of the parallel component of the wave vector normalized by ω/c for different values of the gap and two different coating thicknesses. The radiation energy has been fixed here to the value $\hbar\omega = 61.28$ meV, which is the energy at which the spectral conductance reaches its maximum, see Fig. 2.6(c-d). Notice that for small gaps the transmission reaches its maximum equal to 1 for values $k >> \omega/c$, i.e. for very evanescent waves. (c-d) The same as in panels (a-b), but shown as a function of the parallel wave vector multiplied by the gap, d. Notice that all the curves show a maximum roughly at the same value, a value that approximately corresponds to the wave vector of the CSPhP at this frequency as given by Eq. (2.5) and indicated by means of vertical dashed lines.

the heat transfer is dramatically enhanced for gaps below 1 μm, and in this near-field regime the heat transfer is completely dominated by evanescent p-waves (or TM-waves). This is a first indication that the NFHRT in our system with a polar material (SiO_2) is governed by the excitation of CSPhPs [18]. Further evidence of this fact can be obtained with the analysis of the spectral heat transfer coefficient (h_ω), which simply gives the contribution to the conductance per unit of frequency (see Eq. (1.13)). We show this quantity in Fig. 2.6(c-d) for several gaps in the near-field regime and two different coating thicknesses. Notice that the frequency regions that dominate the heat transfer correspond to those in which the dielectric constant of SiO_2 has a negative real part, see Fig. 2.3(a), which is a necessary condition of for the existence of SPhPs.

Having established that the evanescent p-waves dominate the NFRHT, it is interesting

to analyze the transmission of these modes ($\tau_p(\omega, \mathbf{k})$). In Fig. 2.7(a-b) we show this transmission as a function of the parallel wave vector for a radiation energy of $\hbar\omega = 61.28$ meV , which corresponds to the maximum of the spectral conductance, see Fig. 2.6(c-d). To be precise, we show the transmission for two different coating thicknesses (again, 100 and 3000 nm) and different values of the gap size. As one can see, the transmission reaches a maximum equal to one for a parallel wave vector that increases as gap decreases, reaching huge values ($k > 100\ \omega/c$) for the smallest gaps. This is the reason for the huge enhancement of NFRHT at small gaps, as it can be deduced from Eq. (2.1). It is also worth mentioning that for the coating film of thickness 100 nm, the transmission maximum does not reach the value of one when the gap size is of the order of the thickness (100 nm) and it tends to decrease progressively as the gap size increase above this value. On the other hand, in Fig. 2.7(c-d) we present the same information, but this time the parallel wave vector is multiplied by the gap size. With this normalization we want to illustrate the fact that the transmission maximum appears at a wave vector that scales with the inverse of the gap size. Again, this dependence of the transmission of the p-polarized radiation clearly suggests that CSPhSs are responsible for these maxima.

In order to demonstrate unambiguously that CSPhSs are responsible for the behaviour of the NFRHT in our system, we have computed the dispersion relation of these surface EM modes. One can show that this dispersion relation is given by the solution of the following secular equation

$$D^p_{ML}(\omega, k) = 1 - r^p_{21}(\omega, k) R^p(\omega, k) e^{2iq_2 d} = 0. \tag{2.4}$$

Notice that D^p_{ML} is the denominator that appears in the expression of $\tau_p(\omega, \mathbf{k})$ in Eq. (2.2). In Fig. 2.8 we show the dispersion relations of the CSPhPs obtained from the numerical solution of Eq. (2.4) for two different coating thickness (3000 and 100 nm) and different gap sizes ranging from 20 nm to 200 nm. As one can see, the parallel wave vector of the CSPhPs increases as the gap decreases and therefore, they progressively become more localized to the silica-air interfaces as the gap diminishes. In the limit of small gaps (smaller than the coating thickness), the dispersion relation can be obtained analytically. In this limit, $R^p \approx r^p_{23}$, which allows us write the solution of Eq. (2.4) in the electrostatic limit ($|k| >> \omega/c$) as

$$k_{\mathrm{m}} d = \ln\left(\pm\frac{\epsilon(\omega) - 1}{\epsilon(\omega) + 1}\right), \tag{2.5}$$

where $\epsilon(\omega)$ is the complex dielectric constant of SiO_2 and the subindex m emphasizes

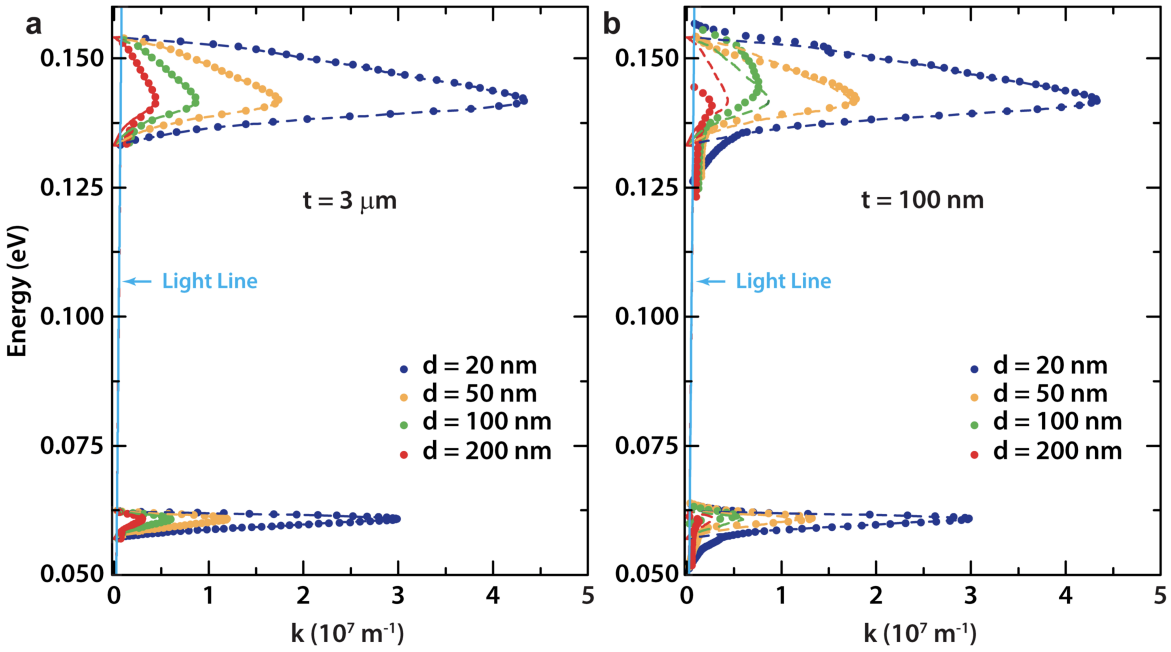

Figure 2.8: (a) Dispersion relation for $t = 3000$ nm and different gaps. The open symbols correspond to the results of the exact numerical solution of equation (2.4), while the dashed lines correspond to the analytical result of equation (2.5). Notice that the analytical result describes very accurately the numerical ones. (b)The same as in panel (a) but for a thickness $t = 100$ nm. Notice that the analytical result ceases to reproduce the exact results when the gap becomes comparable to the coating thickness.

that the wave vector corresponds to our bound mode. Notice that there are two branches corresponding to an antisymmetric (+) and a symmetric mode (-) , but they are degenerate in the sense that both of them have the same real part of the wave vector. The symmetry of the modes is given by the shape of the parallel component of the electric field. In Fig. 2.8 we show that this analytical result nicely reproduces the numerical solution of Eq. (2.4) in its range of validity ($d < t$). More importantly, as we show in Fig. 2.7(c-d) (see vertical dashed line), Eq. (2.5) reproduces the position of the transmission maxima. This is further illustrated in Fig. 2.9 where we show that this dispersion relation describes very accurately the transmission maxima for the whole range of frequencies. Thus, there is no doubt that the CSPhSs are responsible for the NFRHT in our system. The enhancement in heat transfer for small gaps is therefore due to the excitation of these surfaces modes.

Now, it is easy to understand the thickness dependence of the NFRHT in terms of the penetration depth [78] of the CSPhPs. This penetration depth is given, in the electrostatic limit, by $\delta_{\mathrm{m}}(\omega) = 1/[2\mathrm{Re}\{k_{\mathrm{m}}(\omega)\}]$, which in the limit of small gaps reduces to

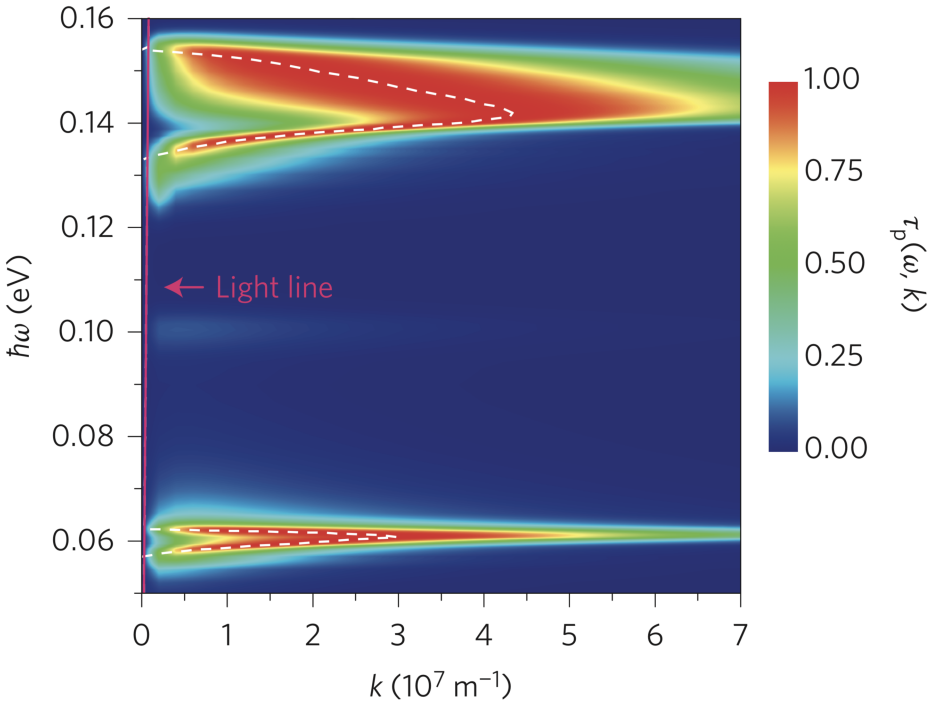

Figure 2.9: Transmission probability for TM modes, $\tau_p(\omega, \mathbf{k})$, as a function of the radiation energy and the magnitude of the parallel wave vector. The white dashed line corresponds to the analytical dispersion relation of the CSPhPs (see text), while the pink solid line next to the y-axis corresponds to the light line, i.e. $\omega = kc$. The maxima of the transmission appear largely to the right of the light line and therefore they correspond to evanescent waves.

$$\delta_{\mathrm{m}} = \frac{d}{2\mathrm{Re}\left\{\ln\left(\frac{\epsilon(\omega)-1}{\epsilon(\omega)+1}\right)\right\}}. \tag{2.6}$$

The denominator in this expression is of the order of 1 for frequencies close to that of the maximum of the spectral conductance. Thus, Eq. (2.6) tells us that the penetration depth of the CSPhPs for small gaps is of the order of the gap size and it is independent of the thickness of the coating. Therefore, CSPhPs are not just simply superpositions of the SPhPs at the two air-SiO_2 interfaces, but have distinct properties. This implies that for small gaps, only a small portion of the coating thickness contributes to the NFRHT and therefore, the heat transfer is independent of the coating thickness, as we can see in Fig. 2.4(a). On the other hand, if the gap size becomes of the order of the coating thickness, the CSPhSs penetrate completely inside the SiO_2 coating film and these surface modes start to feel the Au surface underneath. This is reflected in a decrease of the transmission of these modes, see Fig. 2.7(a), and the subsequent reduction of the heat transfer. This naturally explains the difference between thin coating films

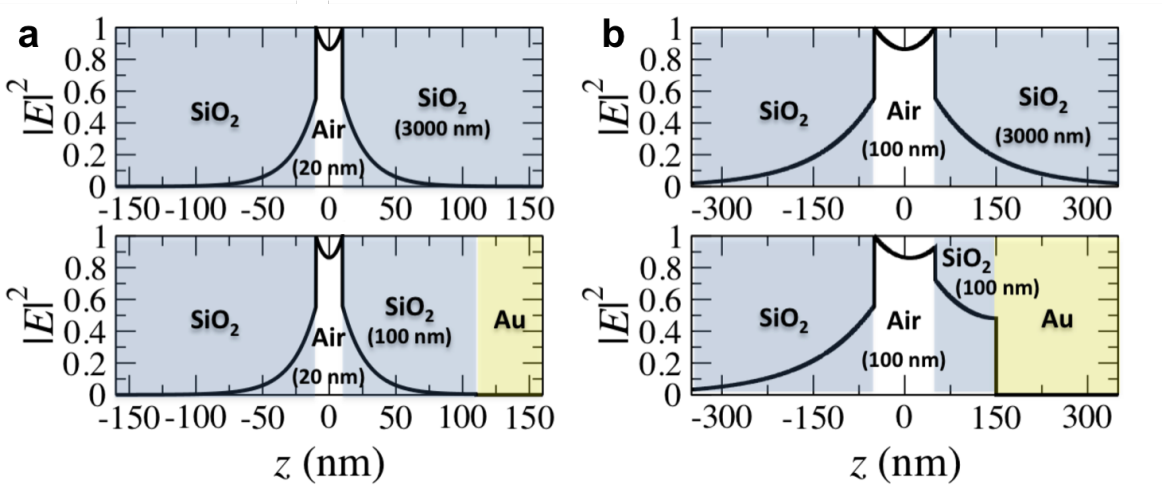

Figure 2.10: (a) Normalized electric field intensity of a representative CSPhP mode ($\hbar\omega$ = 61.28 meV) for a gap of 20 nm and thickness of $t = 3$ μm (upper panel) and thickness of $t = 100$ nm (lower panel), normalized to peak intensity. The blue regions correspond to SiO2 and the yellow region represents Au. (b) Same as in (a) but for a gap of 100 nm.

and thicker ones for intermediate gaps.

It is worth mentioning that in the context of metal-insulator-metal plasmonic waveguides, it is well-known that the penetration depth of the surface EM modes increases with increasing gap size [79]. In that case, the cavity modes are plasmon polaritons, rather than phonon polaritons like in our case, and their relevant frequencies are in the visible range, while in our system they lay in the infrared. The lower energies of our modes allows them to contribute significantly to the heat transfer at room temperature.

Finally, let us say that a convenient way to illustrate the evolution of the CSPhPs penetration depth with the gap size is to represent the electric field spatial profile of these surface modes across the multi-layered structure. We have computed these profiles in a standard manner using the scattering matrix formalism [80]. We show some representative examples in Fig. 2.10, where one can see the normalized electric field intensity profiles as a function of the coordinate z that measures the position along the direction perpendicular to the layer planes (its origin is taken in the middle of the air layer, while the Au layer is on the right hand side). The energy of these modes was chosen again to be $\hbar\omega = 61.28$ meV, which corresponds to the maximum of the spectral heat conductance, while the corresponding wave vectors were computed from the solution of Eq. (2.4). In order to illustrate the typical behaviour of both thin and thick films, we have included the results for two coating thicknesses (100 nm and 3000 nm). The left panel shows the results for a small gap of 20 nm, while in the right one we display the result for a 100 nm

gap, where the gap is equal to the thickness of the thinner film. Notice that in the case of $d = 20$ nm the profiles for the two thicknesses are identical and the penetration depth of the SPhPs remains smaller than both coating thicknesses. This illustrates the fact that for small gaps (smaller than the coating thickness) the NFRHT is independent of the coating thickness simply because only a small portion of the silica layers contribute to the heat transfer. On the other hand, as one can see in Fig. 2.10(b), when the gap becomes comparable to the coating thickness, the SPhPs penetrate completely in the silica coating (see curve for $t = 100$ nm) and then, the field drops abruptly at the interface with the Au layer simply because of the mismatch of dielectric constants between silica and gold. Thus, for these intermediate gaps the profiles for thin films differ markedly from those of thick films or bulk samples. This is reflected in a reduction of the transmission of these modes for thin films and the corresponding lowering of the NFRHT as compared to thick films. The above analysis shows that insights from plasmonics, which enables intricate control of mode shapes, can be employed to tune NFRHT in a variety of nanoscale systems.

2.4.3. Validity of the Derjaguin Approximation and Role of the Film Roughness.

The validity of the Derjaguin approximation has been investigated in the past. For instance, Sasihithlu and Narayanaswamy studied this issue [81] in the context of the heat transfer between two silica microspheres. These authors concluded that the Derjaguin approximation does provide excellent results when the far-field contribution is systematically accounted for using classical RHT theories. Further analysis on the validity of the Derjaguin approximation was performed by Otey and Fan for the case of a silica sphere and a silica infinite plate [33], which is a closer approximation to our system than the work by Sasihitulu *et al.* These authors showed that the Derjaguin approximation provides a very accurate description of the NFRHT when the sphere radius is much larger than the gap size (with relative errors within 1%). This is precisely the scenario in our work as the diameter of our sphere is 53 μm and the gap-size of interest for near-field effects is in the 20 nm - few μm range. Therefore, the use of Derjaguin approximation in our work is well justified.

In order to further bolster these conclusions and directly test the validity of the Derjaguin approximation, we have performed our own numerical calculations of heat transfer between a silica sphere and a silica plate. For this purpose, we have employed the open-

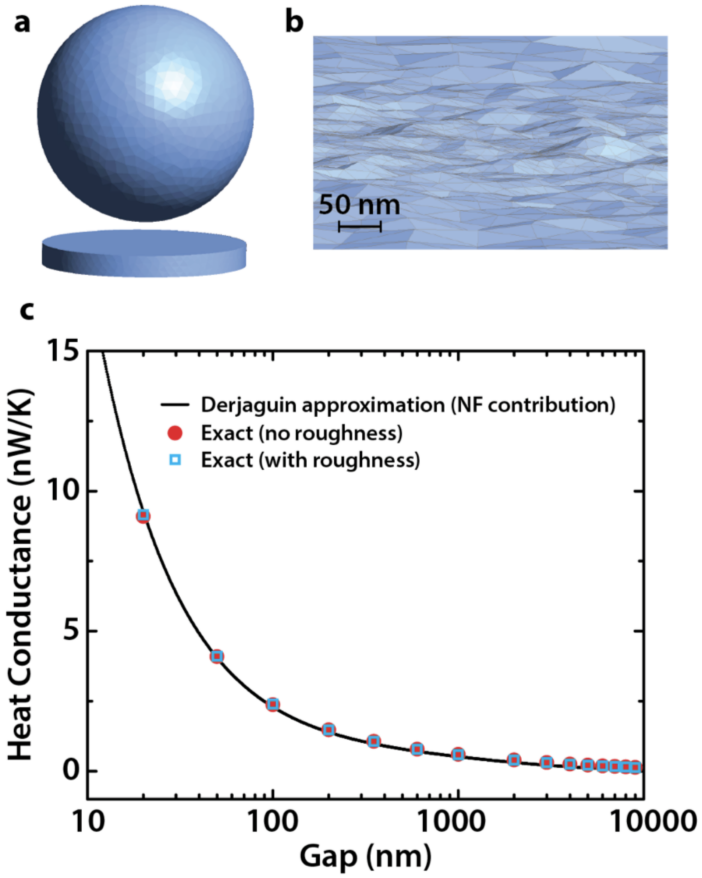

Figure 2.11: (a) The sphere-finite plate used to study the validity of the Derjaguin approximation and the role of the film thickness. The silica sphere has a diameter of 20 μm, while the silica disk has a diameter of 18.9 μm and a thickness of 2 μm. (b) Blow up of the receiver rough surface used to investigate the role of the film roughness. (c) Calculated room temperature radiative heat conductance as a function of the distance between the sphere and the disk. The black solid curve corresponds to the Derjaguin approximation where only the near-field contribution has been taken into account. The red filled circles correspond to the exact numerical results for the total heat conductance for the system shown in a as obtained with the FSC method, while the blue open squares correspond to the exact numerical results for the case where the disk has a rough surface, as shown in panel (b).

source SCUFF-EM software package [82, 83]. This software implements the FSC formulation of the heat transfer problem that has been recently put forward by Rodriguez and coworkers [39].

In our calculation we analyzed a scenario with a silica sphere (diameter 20 μm) and a silica disk (diameter 18.9 μm) as shown in Fig. 2.11a (the diameter of the disk was chosen to be smaller than that of the sphere to reflect the ratio of the emitter and receiver dimensions used in our experiment). Further, the choice of the slightly smaller size of the sphere and disk in the calculations keeps the problem computationally tractable

(computational resources scale polynomially with size of the system) and enables validation of the Derjaguin approximation for systems with sphere- and gap-sizes comparable to those employed in our experiments. We have chosen a disk instead of a rectangle to avoid the singularities in the EM fields associated with the sharp corners of a rectangle. This choice facilitates computational convergence and is reasonable because the near-field heat flow is dominated by a small region at the centre of the disk. In Fig. 2.11(c) we present a comparison of the exact results (red filled circles) of the total thermal conductance (which exactly capture the near-field and far-field contributions) to that obtained using the Derjaguin approximation (see Sec. 2.3.2) which includes only the near-field contribution (black solid line). As one can see, the Derjaguin approximation is able to reproduce the exact results for a wide range of gap sizes, which nicely demonstrates the validity of this approximation in the context of our work. Moreover, this agreement also suggests that the finite size of our receiver (the disk) does not play any role. Notice that the only deviations between these two results occur at large gaps (of the order of 5-10 μm), which are simply due to the fact that the exact result contains a small far-field contribution that has not been subtracted here to avoid any post-processing of the exact data. In any case, notice that at large gaps the heat conductance is quite low and therefore, these small deviations are completely irrelevant for the conclusions of our work. Thus the analysis provided above in conjunction with past work unambiguously supports the use of the Derjaguin approximation for analyzing the experimental results of our work.

The use of the FSC formulation in combination the SCUFF-EM package also allows us to address another important issue. The experimental SiO_2 films exhibit a surface roughness of 10 nm. We performed analysis to evaluate if this roughness affects NFRHT and if the Derjaguin approximation is still applicable to devices with rough films. Specifically, we investigated heat transfer in the sphere-disk system discussed above, where the disk is assumed to have a rough surface. To faithfully describe the experimental situation, we introduced random Gaussian noise in the profile of the disk surface with a maximum protrusion height of 18 nm and a correlation length between protrusions of 30 nm. We show in Fig. 2.11(b) a blow up of the surface of the disk for this example. The results for the total heat conductance as a function of the gap size are shown in Fig. 2.11(c) as blue open squares. The obtained conductances are identical to those obtained for those with a smooth disk, which clearly shows that the presence of the roughness in our coating films does not play any significant role for the range of gaps explored in our experiments ($>$ 20 nm). The reason for this insensitivity to surface roughness is that the sphere radius is much larger than the scale of the roughness and thus, the sphere

averages over a large portion of the rough surface. The net result is that the total heat transfer is only very slightly (<1 %) higher than in the ideal smooth case. In summary, our results unambiguously validate the use of the Derjaguin approximation to analyze NFRHT in our experiments.

2.5. Conclusions

In this work we have studied the NFRHT in thin polar dielectric films. We have shown that the enhancement of NFRHT at small gaps can be achieved with nanometric dielectric coatings. First, we have explained the theoretical tools used for the project, based on the fluctuation-dissipation theorem and the scattering matrix formalism. Afterwards, we have compared our numerical simulations with experimental results, obtaining a good agreement and capturing the key aspects of the experiment. Finally, we have explain the enhancement and thick dependence of NFRHT in terms of CSPhPs: EM waves confined at the cavity and originated by the coupling between phonons and photons in polar materials. The results reported here are of great importance to future nanotechnologies [16, 54, 84] that seek to take advantage of near-field effects for thermal management, lithography and thermo-photovoltaic applications.

3 | Magnetic-field control of NFRHT and the realization of highly-tunable hyperbolic thermal emitters

3.1. Introduction

Presently, one of the central research lines in the field of RHT is the search for materials where the NFRHT exhibits novel features. Recently, it has been predicted that hyperbolic metamaterials could behave as broadband super-Planckian thermal emitters [85–87]. Hyperbolic metamaterials are a special class of highly anisotropic media that have hyperbolic dispersion. In particular, they are uniaxial materials for which one of the principal components of either the permittivity or the permeability tensors is opposite in sign to the other two principal components [88]. Hyperbolic media have been mainly realized by means of hybrid metal-dielectric superlattices and metallic nanowires embedded in a dielectric host [89, 90]. It has been demonstrated that these metamaterials exhibit exotic optical properties such as negative refraction, subwavelength imaging and focusing, and they can be used to do density of states engineering [89, 90]. In the context of RHT, what makes these metamaterials so special is the fact that they can

support EM modes that are evanescent in a vacuum gap, but they are propagating inside the material. This leads to a broadband enhancement of transmission efficiency of the evanescent modes [86]. This special property has motivated a lot of theoretical work on the use of hyperbolic metamaterials for NFRHT [91–100]. However, no experimental investigation of this issue has been reported so far, which is mainly due to the difficulties in handling these metamaterials. In this sense, it would be highly desirable to find much simpler realizations of hyperbolic thermal emitters and, ideally, with tunable properties.

So far, we have seen how the RHT between two objects can be dramatically enhanced in the near field due to the contribution of evanescent waves, both in bulk materials and in thin films. However, in order to make use of this phenomenon in technological applications, it would be desirable to achieve an active control and modulation of NFRHT. In this respect, several proposals have been put forward recently. One of the them is based on the use of phase-change materials [101, 102], where the change of phase leads to a significant change in the material dielectric function. These materials include an alloy called AIST, where the phase change can be induced by applying an electric field [102], and VO_2, which undergoes a metal-insulator transition as a function of temperature [101]. It has also been suggested that the NFRHT between chiral materials with magnetoelectric coupling can be tuned by ultrafast optical pulses [103]. Another proposal to tune the NFRHT is to use ferroelectric materials under an external electric field [104], although the predicted changes are rather modest ($< 17\%$). Let us also mention that very recently it has been proposed that the heat flux between two semiconductors can be controlled by regulating the chemical potential of photons by means of an external bias [105]. So in short, although these proposals are certainly interesting, some of them are not easy to implement and others are either not very efficient or they are restricted to very specific materials. In this sense, the challenge remains to introduce strategies to actively control NFRHT in an easy and relatively universal way.

In this Chapter [106] we tackle and resolve some of the open problems described above by presenting an extensive theoretical analysis of the influence of an external dc magnetic field in the RHT between two parallel plates made of a variety of materials. We show that an applied magnetic field can indeed largely affect the NFRHT in a broad class of materials, namely doped (polar and non-polar) semiconductors. We find that, irrespective of its orientation, the magnetic field reduces the NFRHT with respect to the zero-field case and we show that the reduction can be as large as a factor of 7 for fields of about 6 T at room temperature. This effect originates from the fact that the magnetic field not only strongly modifies the surface waves that dominate the NFRHT in doped semiconductors (both SPhPs and SPPs), but it also generates broadband hyperbolic

modes (HMs) that tend to govern the heat transfer as the field is increased. In particular, when the applied field is perpendicular to the plates surfaces, the semiconductors behave as hyperbolic thermal emitters with highly tunable properties. By changing the field magnitude one can continuously tune the system and realize situations where (i) surface waves dominate the NFRHT, (ii) both surface waves and HMs contribute significantly to the near-field thermal radiation, and (iii) only HMs contribute to the NFRHT and surface waves cease to exist. On the other hand, when the field is parallel to the surfaces the NFRHT is nonmonotonic as a function of the magnetic field. For moderate fields, surface waves and hyperbolic modes coexisting, while for high fields the NFRHT is largely dominated by HMs. We emphasize that all these striking predictions are amenable to measurements and do not require the use of any complicated metamaterial. Thus, our work offers a simple strategy to actively control NFRHT in a broad variety of materials and it also provides a very appealing recipe to realize hyperbolic materials and, in particular, hyperbolic thermal emitters with highly tunable properties.

The remainder of this Chapter is structured as follows. Section 3.2 describes the system under study and the general formalism for the description of NFRHT in the presence of a magnetic field. We then turn in Sec. 3.3 to the application of the general results to the case of n-doped InSb as an example of a polar semiconductor. We discuss in this section both the results for different magnetic field orientations and the realization of highly tunable hyperbolic thermal emitters. Section 3.4 is devoted to the case of Si as an example of non-polar semiconductor. Finally, Section 3.5 summarizes our main results and discusses future directions. Technical details of the general formalism and additional calculations that support the claims of this Chapter can be found in Appendices A, B and C.

3.2. RHT in the presence of a magnetic field: General formalism

Our main goal is to compute the RHT in the presence of an external dc magnetic field within the framework of FE [5, 6]. For simplicity, we shall concentrate here in the heat exchanged between two infinite parallel plates made of arbitrary non-magnetic materials and that are separated by a vacuum gap of width d, see Fig. 3.1(a). The magnetic field can point in any direction and following Fig. 3.1(a), we shall refer to the left plate as medium 1, the vacuum gap as medium 2, and the right plate as medium 3.

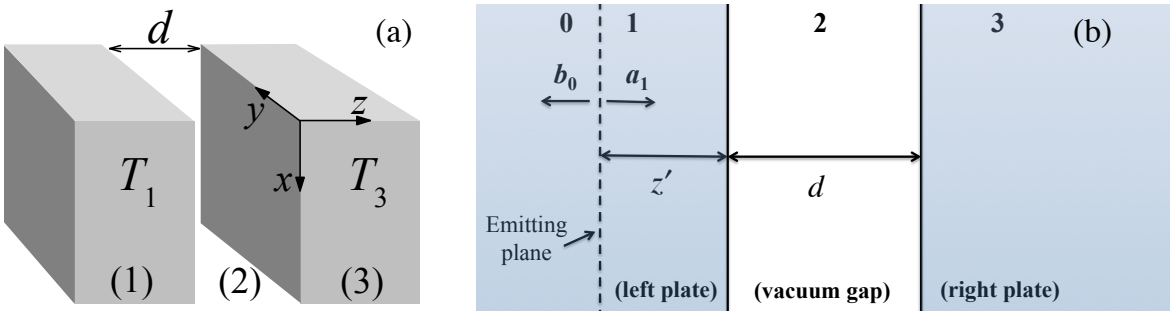

Figure 3.1: (a) Two parallel anisotropic plates at temperatures T_1 and T_3 and separated by a vacuum gap of width d interchange thermal radiation. (b) Same system as in (a). The vertical dashed line inside the left plate indicates the position of an emitting plane that contains the radiation sources that generate the field amplitudes $\mathbf{b_0}$ and $\mathbf{a_1}$.

When a magnetic field is applied to any object, it results in an optical anisotropy that can be described by the following general permittivity tensor [107]

$$\hat{\epsilon} = \begin{pmatrix} \epsilon_{xx} & \epsilon_{xy} & \epsilon_{xz} \\ \epsilon_{yx} & \epsilon_{yy} & \epsilon_{yz} \\ \epsilon_{zx} & \epsilon_{zy} & \epsilon_{zz} \end{pmatrix}, \tag{3.1}$$

where according to Fig. 3.1(a), x and y lie in the interface planes and z corresponds to the surface normal. The components of the permittivity tensor depend on the applied magnetic field, as we shall specify below, and on the frequency (local approximation). Let us recall that the off-diagonal elements in Eq. (3.1) are responsible for all the well-known magneto-optical (MO) effects (Faraday effect, Kerr effects, etc.) [107].

We will derive now an analytical expression for the RHT problem between two anisotropic infinite plates. We will again make use of the fluctuation-dissipation theorem to calculate the correlations of the random fluctuating currents $\mathbf{J}$ inside the different materials. The expression shown in Eq. 1.7 can be generalizes to anisotropic bodies and it can be written as [12, 13]:

$$\langle J_k(\mathbf{R},\omega) J_l^*(\mathbf{R}',\omega)\rangle = \frac{2\epsilon_0\omega}{i\pi}\Theta(\omega,T)\delta(\mathbf{R}-\mathbf{R}')\left[\epsilon_{kl}(\mathbf{R},\omega) - \epsilon_{lk}^*(\mathbf{R},\omega)\right], \tag{3.2}$$

Our strategy to compute the net RHT between the two plates follows closely that of the seminal work by Polder and Van Hove [11]. First, we compute the radiation power per unit of area transferred from the left plate to the right one, $Q_{1\to3}$. For this purpose, we first compute the statistical average of the z-component of the Poynting vector $\langle S_z(\omega,\mathbf{k},z')\rangle$ describing the power emitted from a plane located at $z=z'$ inside

the left plate (see Fig. 3.1(b)) for a given frequency and parallel wave vector and then, we integrate the result over all possible values of z', ω, and parallel wave vector $\mathbf{k}$ ($\mathbf{k} = (k_x, k_y)$), *i.e.*,

$$Q_{1\to3}(d, T_1) = \int_0^\infty d\omega \int d\mathbf{k} \int_0^\infty dz' \langle S_z(\omega, \mathbf{k}, z') \rangle. \tag{3.3}$$

A similar calculation for the power $Q_{3\to1}$ transferred from the right plate to the left one completes the computation of the net transferred power per unit of area. $\langle S_z(\omega, \mathbf{k}, z') \rangle$ shall be evaluated at $z = 0$, but it does not need to be propagated to the right plate (layer 3), as it will carry the same energy at both sides of the interface. Thus the z component of the Poyinting vector evaluated at $z = 0$ (see Fig. 3.1(a)) in the vacuum can be written in its more general form as:

$$S_z(\omega, \mathbf{k}, z') = \frac{c}{4\omega}\sqrt{\frac{\mu_0}{\epsilon_0}} \left\{ \boldsymbol{h}_\parallel^\dagger(z=0)\boldsymbol{e}_\parallel(z=0) + \boldsymbol{e}_\parallel^\dagger(z=0)\boldsymbol{h}_\parallel(z=0) \right\}_2, \tag{3.4}$$

where μ_0 is the vacuum permeability while $\boldsymbol{h}_\parallel$ and $\boldsymbol{e}_\parallel$ represent the vectors $\boldsymbol{h}_\parallel(z) = (h_x(z), h_y(z))^T$ and $\boldsymbol{e}_\parallel(z) = (-e_y(z), e_x(z))^T$, respectively. $e_{x,y}(z)$ and $h_{x,y}(z)$ are the amplitudes of the electric and magnetic fields along the different axes (see Appendix A).

Let us focus now on the analysis of the power emitted by a plane inside the left plate, see Fig. 3.1(b). This emitting plane defines a fictitious interface between layers 0 and 1, which are both inside the left plate. To determine the power emitted to the right plate we first compute the field amplitudes $\boldsymbol{a}_1$ on the right hand side of the plane. In order to calculate these amplitudes, we have made use of the scattering matrix (S-matrix) method applied to the description of thermal radiation. By definition, the S-matrix relates the vectors of the amplitudes of forward and backward going waves, $\boldsymbol{a}_l$ and $\boldsymbol{b}_l$, where l now denotes the layer, in the different layers of the structure as follows

$$\begin{pmatrix} \boldsymbol{a}_l \\ \boldsymbol{b}_{l'} \end{pmatrix} = \hat{S}(l', l) \begin{pmatrix} \boldsymbol{a}_{l'} \\ \boldsymbol{b}_l \end{pmatrix} = \begin{pmatrix} \hat{S}_{11} & \hat{S}_{12} \\ \hat{S}_{21} & \hat{S}_{22} \end{pmatrix} \begin{pmatrix} \boldsymbol{a}_{l'} \\ \boldsymbol{b}_l \end{pmatrix}. \tag{3.5}$$

Appendix A describes in detail how to apply the scattering matrix approach for anisotropic multilayer systems [108]. Later, in Appendix B, we show how this formalism can be used to describe the thermal radiation between two anisotropic parallel plates. Using this method, it is possible to find a expression for the z-component of the Poyinting

vector as a function of the field amplitudes in the vacuum region $\boldsymbol{a}_2$ and $\boldsymbol{b}_2$:

$$S_z(\omega,\mathbf{k},z') = \frac{c}{2q_2\omega}\sqrt{\frac{\mu_0}{\epsilon_0}}\begin{cases} \boldsymbol{a}_2^\dagger\hat{A}\boldsymbol{a}_2 - \boldsymbol{b}_2^\dagger\hat{A}\boldsymbol{b}_2, & k<\omega/c, \\ e^{-iq_2^* d}\boldsymbol{b}_2^\dagger\hat{A}\boldsymbol{a}_2 - e^{iq_2 d}\boldsymbol{a}_2^\dagger\hat{A}\boldsymbol{b}_2, & k>\omega/c, \end{cases} \tag{3.6}$$

where k is the magnitude of $\mathbf{k}$, $q_2 = \sqrt{\omega^2/c^2 - k^2}$ is the transverse or z-component of the wave vector in vacuum and the matrix $\hat{A}$ can be expressed as:

$$\hat{A} = \begin{pmatrix} \omega^2/c^2 - k_y^2 & k_x k_y \\ k_x k_y & \omega^2/c^2 - k_x^2 \end{pmatrix}. \tag{3.7}$$

Now we can substitute the expressions obtained for $\boldsymbol{a}_2$ and $\boldsymbol{b}_2$ using the S-matrix approach (See Appendix A) in Eq. (3.6). Then, the expected value can be applied to $S_z(\omega,\mathbf{k},z')$ and the amplitude of the fluctuating currents can be substituted from Eq. (3.2). Finally, after integrating over all the emitting planes located at different z' (see Appendix B for more details), one arrives at the following result for the power per unit of area transferred from the left plate to the right one

$$Q_{1\to3}(d,T_1) = \int_0^\infty \frac{d\omega}{2\pi}\Theta(\omega,T_1)\int\frac{d\mathbf{k}}{(2\pi)^2}\tau(\omega,\mathbf{k},d). \tag{3.8}$$

Let us recall that $\Theta_i(\omega) = \hbar\omega/[\exp(\hbar\omega/k_\mathrm{B}T_i) - 1]$, T_i is the absolute temperature of the layer i, ω is the radiation frequency, $\mathbf{k} = (k_x, k_y)$ is the wave vector parallel to the surface planes, and $\tau(\omega,\mathbf{k},d)$ is the total transmission probability of the EM waves and it is given by

$$\tau(\omega,\mathbf{k},d) = \begin{cases} \mathrm{Tr}\left\{[\hat{1} - \hat{\mathcal{R}}_{21}\hat{\mathcal{R}}_{21}^\dagger]\hat{\mathcal{D}}^\dagger[\hat{1} - \hat{\mathcal{R}}_{23}^\dagger\hat{\mathcal{R}}_{23}]\hat{\mathcal{D}}\right\}, & k<\omega/c, \\ \mathrm{Tr}\left\{[\hat{\mathcal{R}}_{21} - \hat{\mathcal{R}}_{21}^\dagger]\hat{\mathcal{D}}^\dagger[\hat{\mathcal{R}}_{23}^\dagger - \hat{\mathcal{R}}_{23}]\hat{\mathcal{D}}\right\}e^{-2|q_2|d}, & k>\omega/c. \end{cases} \tag{3.9}$$

Again, $q_2 = \sqrt{\omega^2/c^2 - k^2}$ is the z-component of the wave vector in the vacuum gap and the 2×2 matrices $\hat{\mathcal{R}}_{ij}$ are the reflections matrices characterizing the two interfaces. These matrices have the following generic structure

$$\hat{\mathcal{R}}_{ij} = \begin{pmatrix} r_{ij}^{s,s} & r_{ij}^{s,p} \\ r_{ij}^{p,s} & r_{ij}^{p,p} \end{pmatrix}, \tag{3.10}$$

where $r_{ij}^{\alpha,\beta}$ with $\alpha,\beta = s,p$ is the reflection amplitude for the scattering of an incoming α-polarized plane wave into an outgoing β-polarized wave. Finally, the 2×2 matrix $\hat{\mathcal{D}}$

appearing in Eq. (3.9) is defined as

$$\hat{\mathcal{D}} = [\hat{1} - \hat{\mathcal{R}}_{21}\hat{\mathcal{R}}_{23}e^{2iq_2d}]^{-1}. \tag{3.11}$$

Notice that this matrix describes the usual Fabry-Pérot-like denominator resulting from the multiple scattering between the two interfaces.

Following a similar reasoning, one can compute the power transferred per unit of area from the right plate to the left one, and the expression obtained is very similar to Eq. (3.8) but substituting T_1 by T_3. Thus the net power per unit of area exchanged by the plates is given by the Landauer-like expression [109] obtained from the subtraction of both equations :

$$Q(d, T_1, T_3) = \int_0^\infty \frac{d\omega}{2\pi} [\Theta(\omega, T_1) - \Theta(\omega, T_3)] \int \frac{d\mathbf{k}}{(2\pi)^2} \tau(\omega, \mathbf{k}, d). \tag{3.12}$$

.

In Appendixes A and B, we show explicitly how the different reflection matrices appearing in Eq. (3.9) can be computed within a scattering-matrix approach for anisotropic multilayer systems [108]. This approach provides, in turn, a natural framework to analyze different issues that will be crucial later on such as the nature of the EM modes responsible for the heat transfer. In the following sections, we apply the general results presented here to different materials and magnetic field configurations.

3.3. Polar semiconductors: InSb

The first obvious question to be answered is: In which materials can a magnetic field modify the NFRHT? Since the thermal radiation of an object is primarily determined by its dielectric function, we need materials in which this function can be modified by an external magnetic field, that is we need MO materials. Focusing on room temperature experiments, the MO activity must be exhibited in the mid-infrared. Thus, doped semiconductors, where the MO activity is due to conduction electrons, are ideal candidates [110]. In these materials, one can play with the doping level to tune the plasma frequency to values comparable to the cyclotron frequency at experimentally achievable magnetic fields, which is an important requirement to have sizable magnetic-induced effects in the NFRHT (see discussion below). Moreover, in semiconductors the NFRHT in the absence of field is typically dominated by surface EM waves (both SPhPs and SPPs), which in turn are known to be strongly influenced by an external magnetic field [110, 111]. Thus,

it seems natural to expect a magnetic-field modulation of NFRHT in semiconductors.

There is a variety of semiconductors that we could choose to illustrate our predictions. In this section we focus on InSb for several reasons. First, it is a polar semiconductor where the NFRHT in the absence of field is dominated by two different types of surface waves (SPhPs and SPPs), which allows us to study a very rich phenomenology. Second, InSb has a small effective mass, which enables to tune the cyclotron frequency to values comparable to those of the plasma frequency with moderate fields. Finally, InSb has been the most widely studied material in the context of magnetoplasmons and coupled magnetoplasmons-SPhPs. Thus, the magnetic field effect in the surface waves has been very well characterized experimentally [112–115].

3.3.1. Perpendicular magnetic field: The realization of hyperbolic near-field thermal emitters

Let us first discuss the RHT between two identical plates made of n-doped InSb when the magnetic field is perpendicular to the plate surfaces, *i.e.* $\mathbf{H} = H_z\hat{\mathbf{z}}$, see Fig. 3.1(a). In this case, the permittivity tensor of InSb adopts the following form [114]

$$\hat{\epsilon}(H) = \begin{pmatrix} \epsilon_1(H) & -i\epsilon_2(H) & 0 \\ i\epsilon_2(H) & \epsilon_1(H) & 0 \\ 0 & 0 & \epsilon_3 \end{pmatrix}, \tag{3.13}$$

where

$$\begin{aligned} \epsilon_1(H) &= \epsilon_\infty \left(1 + \frac{\omega_L^2 - \omega_T^2}{\omega_T^2 - \omega^2 - i\Gamma\omega} + \frac{\omega_p^2(\omega + i\gamma)}{\omega[\omega_c^2 - (\omega + i\gamma)^2]}\right), \\ \epsilon_2(H) &= \frac{\epsilon_\infty \omega_p^2 \omega_c}{\omega[(\omega + i\gamma)^2 - \omega_c^2]}, \\ \epsilon_3 &= \epsilon_\infty \left(1 + \frac{\omega_L^2 - \omega_T^2}{\omega_T^2 - \omega^2 - i\Gamma\omega} - \frac{\omega_p^2}{\omega(\omega + i\gamma)}\right). \end{aligned} \tag{3.14}$$

Here, ϵ_∞ is the high-frequency dielectric constant, ω_L is the longitudinal optical phonon frequency, ω_T is the transverse optical phonon frequency, $\omega_p^2 = ne^2/(m^*\epsilon_0\epsilon_\infty)$ defines the plasma frequency of free carriers of density n and effective mass m^*, Γ is the phonon damping constant, and γ is the free-carrier damping constant. Finally, the magnetic field enters in these expressions via the cyclotron frequency $\omega_c = eH/m^*$. The important features of the previous expressions are: (i) the magnetic field induces an optical anisotropy

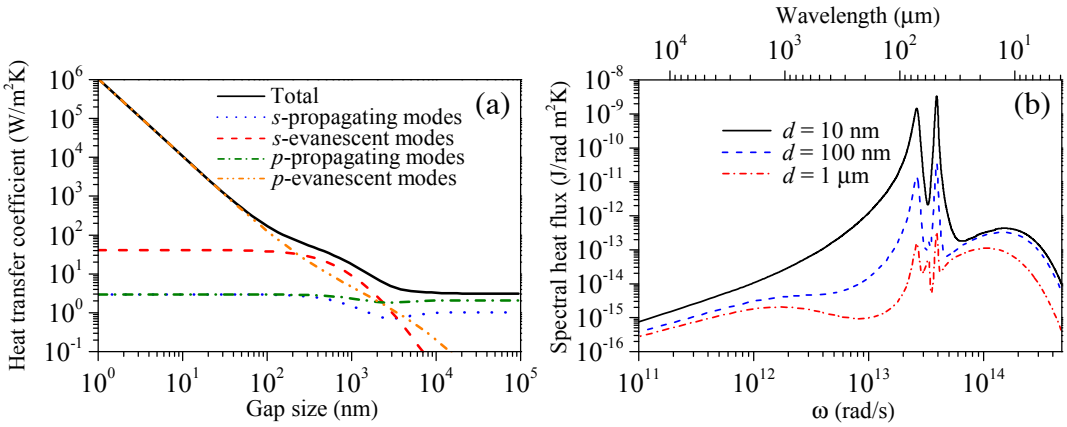

Figure 3.2: (a) HTC of n-doped InSb as a function of the gap at zero magnetic field. We show the total result and the individual contributions of s- and p-polarized waves (both propagating and evanescent). (b) The corresponding zero-field spectral heat flux as a function of frequency (and wavelength) for three different gaps.

(via the modification of the diagonal elements and the introduction of off-diagonal ones), (ii) there are two major contributions to the diagonal components of the dielectric tensor: optical phonons and free carriers, and (iii) the MO activity is introduced via the free carriers, which illustrates the need to deal with doped semiconductors. In what follows we shall concentrate in a particular case taken from Ref. [114], where $\epsilon_\infty = 15.7$, $\omega_L = 3.62 \times 10^{13}$ rad/s, $\omega_T = 3.39 \times 10^{13}$ rad/s, $\Gamma = 5.65 \times 10^{11}$ rad/s, $\gamma = 3.39 \times 10^{12}$ rad/s, $n = 1.07 \times 10^{17}$ cm^{-3}, $m^*/m = 0.022$, and $\omega_p = 3.14 \times 10^{13}$ rad/s. As a reference, let us say that with these parameters $\omega_c = 8.02 \times 10^{12}$ rad/s for a field of 1 T. Let us point out that in this configuration, and due to the structure of the permittivity tensor, the transmission coefficient appearing in Eq. (3.12) only depends on the magnitude of the parallel wave vector, which considerably simplifies the calculation of the RHT.

Let us now briefly review the expectations for the heat transfer in the absence of magnetic field. As we show in Fig. 3.2(b), the HTC features a large near-field enhancement for gaps below 1 μm. For $d < 100$ nm this enhancement is largely dominated by p-polarized evanescent waves and the HTC increases as $1/d^2$ as the gap decreases, which are two clear signatures of a situation where the heat transfer is dominated by surface EM waves. This can be further confirmed with the analysis of the spectral heat flux, see Fig. 3.2(c), which in the near-field regime is dominated by two narrow peaks that can be associated to SPPs (low-frequency peak) and SPhPs (high-frequency peak), as it will become evident below. Thus, the case of InSb constitutes an interesting example where two types of surface waves contribute significantly to the NFRHT. Let us now see how

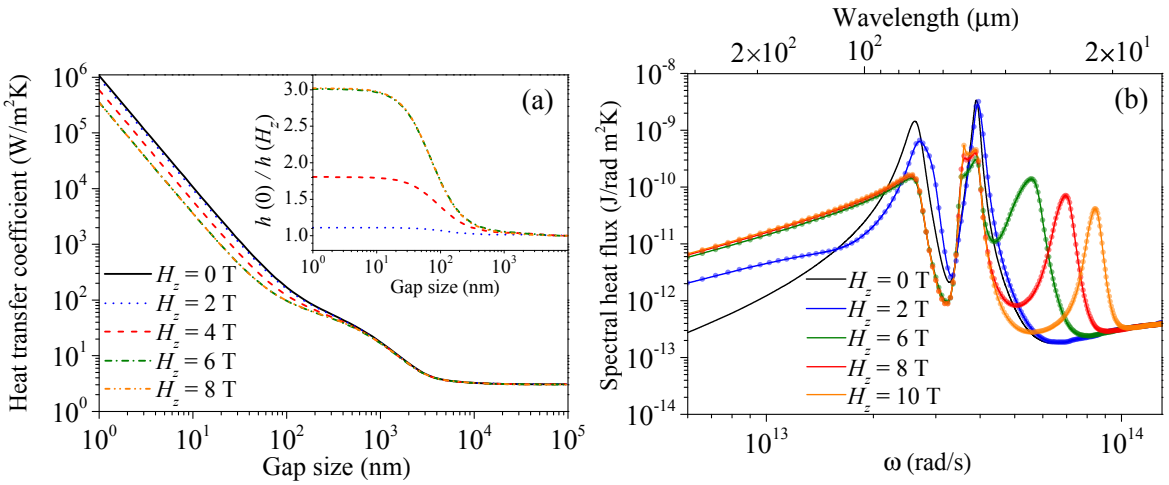

Figure 3.3: (a) HTC for n-doped InSb as a function of the gap for different values of the magnetic field perpendicular to the plate surfaces. The inset shows the ratio between the zero-field coefficient and the coefficient for different values of the field in the near-field region. (b) The corresponding spectral heat flux as a function of the frequency (and wavelength) for a gap of $d = 10$ nm and different values of the perpendicular field. The solid lines correspond to the exact calculation and the circles to the uniaxial approximation where the off-diagonal terms of the permittivity tensor are assumed to be zero.

these results are modified in the presence of a magnetic field.

In Fig. 3.3(a) we show the HTC as a function of the gap size for different values of the perpendicular magnetic field. There are three salient features: (i) the far-field heat transfer is fairly independent of the magnetic field, (ii) in the near-field regime (below 300 nm) the magnetic field suppresses the heat transfer by up to a factor of 3 (see inset), and (iii) by increasing the field, the HTC tends to saturate at around 6 T, although it is slightly reduced upon further increasing the field above 10 T (not shown here). The strong modification of heat transfer due to the magnetic field is even more apparent in the spectral heat flux. As one can see in Fig. 3.3(b), the magnetic field not only distorts and reduces the height of the peaks related to the surface waves, but it also generates a new peak that shifts to higher frequencies as the field increases. This additional peak appears at the cyclotron frequency and its presence illustrates the high tunability that can be achieved. Notice, for instance, that for a field of 6 T the thermal emission at the cyclotron frequency is increased by almost 3 orders of magnitude with respect to the zero-field case.

To shed more light on these results it is convenient to examine the transmission of the p-polarized waves, which can be shown to dominate the heat transfer for any field. We present in Fig. 3.4 this transmission as a function of the magnitude of the parallel wave

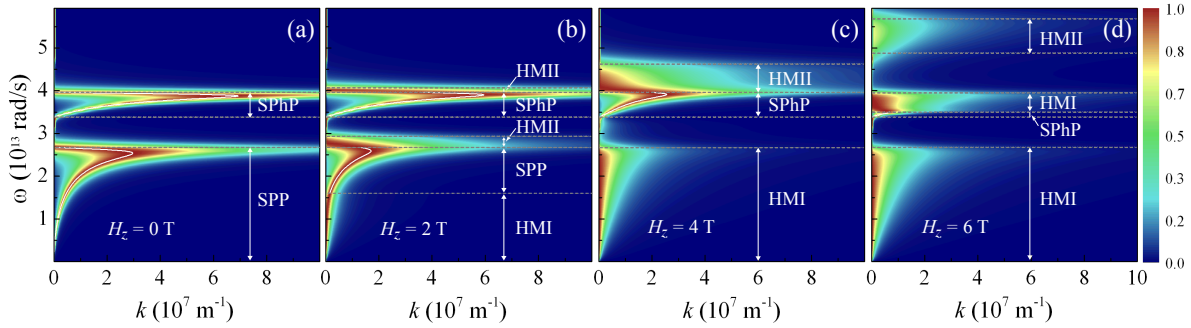

Figure 3.4: The transmission coefficient for p-polarized waves as a function of the magnitude of the parallel wave vector and frequency for InSb and a gap of $d = 10$ nm. The different panels correspond to different values of the magnetic field that is perpendicular to the surfaces. The horizontal dashed lines separate the regions where transmission is dominated by surface waves (SPPs and SPhPs) or HMs of type I and II (HMI and HMII). The white solid lines correspond to the analytical dispersion relation of the surface waves of Eq. (3.15).

vector, k, and the frequency for a gap $d = 10$ nm and different values of the magnetic field. As one can see, at low fields the transmission maxima are located around a restricted area of k and ω, clearly indicating that surface waves dominate the NFRHT. Notice also that their dispersion relation is modified by the field, see Fig. 3.4(b). By increasing the field, those areas are progressively replaced by areas where the maximum transmission is reached for a broad range of k-values and finally, the surface waves are restricted to the reststrahlen band $\omega_T < \omega < \omega_L$ for the highest fields, see Fig. 3.4(d). What is the nature of these magnetic-field-induced modes?

To answer this question and explain all the results just described, it is important to realize that the off-diagonal elements of the permittivity tensor do not play a major role in this configuration. This is illustrated in Fig. 3.3(b) where we show that the approximation consisting in setting $\epsilon_2 = 0$ in Eq. (3.13) reproduces very accurately the exact results for the spectral heat flux for arbitrary magnetic fields. This means that the polarization conversion is irrelevant and the plates effectively behave as uniaxial media where their permittivity tensors are diagonal: $\hat{\epsilon} = diag[\epsilon_{xx}, \epsilon_{xx}, \epsilon_{zz}]$, where $\epsilon_{xx} = \epsilon_1$ and $\epsilon_{zz} = \epsilon_3$. Within this approximation, which hereafter we refer to as uniaxial approximation, it is easy to compute the dispersion relation of the surface EM modes in our geometry (see Appendix C). In the electrostatic limit $k \gg \omega/c$, the dispersion relation of these cavity modes is given by

$$k_{\mathrm{SW}} = \frac{1}{d} \ln \left(\pm \frac{\epsilon_{xx} - \sqrt{\epsilon_{xx}/\epsilon_{zz}}}{\epsilon_{xx} + \sqrt{\epsilon_{xx}/\epsilon_{zz}}} \right), \tag{3.15}$$

with the additional constraint that both ϵ_{xx} and ϵ_{zz} must be negative. In the zero-field limit, this expression reduces to the known result for cavity surface modes in isotropic materials [69]. As we show in Fig. 3.4, see white solid lines, the dispersion relation of Eq. (3.15) nicely reproduces the structure of the transmission maxima in those frequency regions in which surfaces waves are allowed ($\epsilon_{xx}, \epsilon_{zz} < 0$). It is worth stressing that this dispersion relation describes in a unified manner both the SPPs that appear below the reststrahlen band and the SPhPs due to the optical phonons. More importantly, this dispersion relation tells us that the magnetic field reduces the parallel wave vector of the surface waves and restricts the frequency region where they exist. Indeed, at high fields the SPPs disappear, while the SPhPs are restricted to the reststrahlen band, Fig. 3.4(d). These two effects are actually the cause of the reduction of the NFRHT in the presence of a magnetic field. But what about the other modes that appear by increasing the field? Their nature can also be understood within the uniaxial approximation. As we show in Appendix C, the allowed values for the transverse component of the wave vector inside these uniaxial materials are given by $q_{\mathrm{o}} = \sqrt{\epsilon_{xx}\omega^2/c^2 - k^2}$ for ordinary waves and $q_{\mathrm{e}} = \sqrt{\epsilon_{xx}\omega^2/c^2 - k^2\epsilon_{xx}/\epsilon_{zz}}$ for extraordinary waves. The dispersion of the extraordinary waves can be rewritten as

$$\frac{k_x^2 + k_y^2}{\epsilon_{zz}} + \frac{q_{\mathrm{e}}^2}{\epsilon_{xx}} = \frac{\omega^2}{c^2}, \tag{3.16}$$

a dispersion that becomes hyperbolic when ϵ_{xx} and ϵ_{zz} have opposite signs [88]. This is exactly what happens in our case in certain frequency regions at finite field. This illustrated in Fig. 3.4(b-d), where we have indicated the hyperbolic regions defined by the condition $\epsilon_{xx}\epsilon_{zz} < 0$. Notice that those regions correspond exactly to the areas where the transmission reaches its maximum for a broad range of k-values. This fact shows unambiguously that our InSb plates effectively behave as hyperbolic materials. More importantly, and as it is evident from Fig. 3.4, we can easily modify the hyperbolic regions by changing the field. Thus, we can change from situations where the HMs coexist with both types of surface waves to situations where the HMs dominate the NFRHT, which is what occurs at high fields, see Fig. 3.4(d). Moreover, contrary to what happens in most hybrid hyperbolic metamaterials, we can have in a single material HMs of type I (HMI), where $\epsilon_{xx} > 0$ and $\epsilon_{zz} < 0$, and HMs of type II (HMII), where $\epsilon_{xx} < 0$ and $\epsilon_{zz} > 0$, see Fig. 3.4(b-d).

Let us recall that what makes HMs so special in the context of NFRHT is the fact that, as it is evident from their dispersion relation, they are evanescent in the vacuum gap and propagating inside the hyperbolic material for $k > \omega/c$ (HMI) or $k > \sqrt{|\epsilon_{zz}|}\omega/c$

(HMII). Thus, they are a special kind of frustrated internal reflection modes that exhibit a very high transmission over a broad range of k-values that correspond to evanescent waves in the vacuum gap [86]. As shown in Ref. [86], the number of HMs that contributes to the NFRHT is solely determined by the intrinsic cutoff in the transmission, which has the form $\tau(\omega, k) \propto \exp(-2kd)$ for $k \gg \omega/c$. From this condition it follows that the heat flux due to HMs scales as $1/d^2$ for small gaps, as the contribution of surface waves. This explains why the appearance of HMs as the field increases does not modify the parametric dependence of the NFRHT with the gap size. Notice, however, that in spite of the high transmission of these HMs, their appearance does not enhance the NFRHT because they replace surface waves that possess even larger k-values (notice that the conditions of HMs and surface waves are mutually excluding). Thus, we can conclude that the NFRHT reduction induced by the magnetic field is due to both the modification of the surface waves and their replacement by HMs that, in spite of their propagating nature inside the material, turn out to be less efficient transferring the radiative heat in the near-field region than the surface waves.

Let us point out that within the uniaxial approximation, the heat transfer can be obtained in a semi-analytical form. In this case, the transmission coefficient is given by the isotropic result of Eq. (1.9), where the reflections coefficients adopt now the form

$$r_{21}^{s,s} = r_{23}^{s,s} = \frac{q_2 - q_\mathrm{o}}{q_2 + q_\mathrm{o}} \tag{3.17}$$

$$r_{21}^{p,p} = r_{23}^{p,p} = \frac{\epsilon_{xx} q_2 - q_\mathrm{e}}{\epsilon_{xx} q_2 + q_\mathrm{e}}. \tag{3.18}$$

The uniaxial approximation is also useful to understand the high field behavior of the NFRHT. The tendency to saturate the thermal radiation as the field increases is due to the to the fact that the cyclotron frequency becomes larger than the plasma frequency and the last term in the expression of $\epsilon_{xx} = \epsilon_1$, see Eq. (3.14), progressively becomes more irrelevant. Thus, the permittivity tensor becomes field-independent and the heat transfer is simply given by the result for uniaxial media, where $\epsilon_{zz} = \epsilon_3$ has the form in Eq. (3.14), but $\epsilon_{xx} = \epsilon_1$ does not contain the last term in the first expression of Eq. (3.14). We find that the strict saturation of the NFRHT occurs at around 20 T and there is an intermediate regime, between 6 and 20 T, in which the near-field thermal radiation slightly increases upon increasing the field (not shown here), leading to a nonmonotonic behavior. This behavior is due to an increase in the efficiency of the HMs that dominate the NFRHT in this high-field regime.

To conclude this subsection, let us explain why the far-field heat transfer is rather

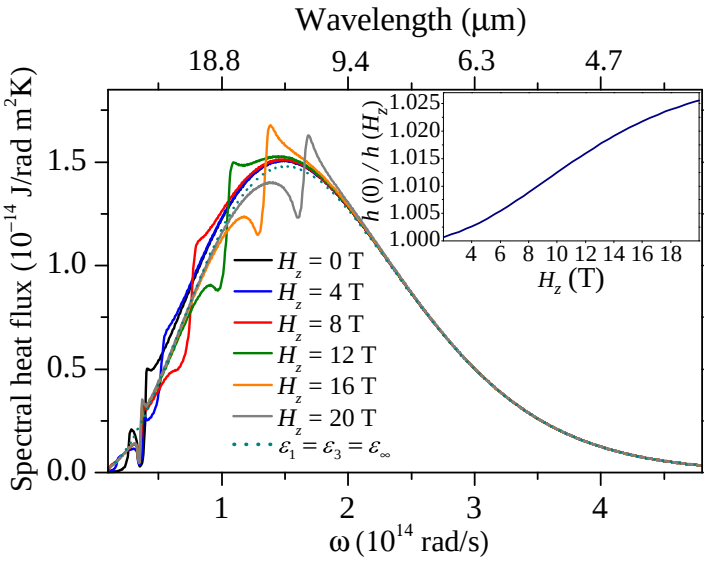

Figure 3.5: Far-field spectral heat flux for InSb as a function of the frequency (and wavelength) for different values of the perpendicular field. These spectra have been computed for a gap $d = 1$ m. The dotted line corresponds to the result for plates made of a dielectric with a frequency-independent dielectric constant equal to ϵ_∞. The inset shows the corresponding ratio between the zero-field heat transfer coefficient and the coefficient for different values of the field.

insensitive to the magnetic field. For gaps much larger than the thermal wavelength (9.6 μm), the heat transfer is dominated by propagating waves and, as we show in Fig. 3.5, the spectral heat flux in the absence of field exhibits a broad spectrum with a peak at around 1.5×10^{14} rad/s. Indeed, the spectrum is very similar to that of a dielectric with a frequency-independent dielectric constant $\hat{\epsilon} = \epsilon_\infty \hat{1}$, see dotted line in Fig. 3.5. As we illustrate in that figure, the presence of a magnetic field only modifies this spectrum in a significant way in a small region around the cyclotron frequency. This fact leads to a tiny modification of the heat transfer upon the application of an external field. As it can be seen in the inset of Fig. 3.5, the magnetic field reduces the far-field heat transfer coefficient as the magnetic field increases, but this reduction is quite modest and, for instance, it amounts to only 2.5% at a very high field of 20 T.

3.3.2. Parallel magnetic field

Let us now turn to the case in which the magnetic field is parallel to the plate surfaces. For concreteness, we consider that the field is applied along the x-axis, $\mathbf{H} = H_x \hat{\mathbf{x}}$, but obviously the result is independent of the field direction as long as it points along the surface plane, as we have explicitly checked. In this case, the permittivity tensor of InSb

adopts the form

$$\hat{\epsilon}(H) = \begin{pmatrix} \epsilon_3 & 0 & 0 \\ 0 & \epsilon_1(H) & -i\epsilon_2 \\ 0 & i\epsilon_2(H) & \epsilon_1(H) \end{pmatrix}, \tag{3.19}$$

where the ϵ's are given by Eq. (3.14). Let us emphasize that in this case the transmission coefficient appearing in Eq. (3.12) depends both on the magnitude of the parallel wave and on its direction, which makes the calculations more demanding. Let us also say that we consider here the same parameter values for the n-doped InSb as in the example analyzed above.

The results for the magnetic field dependence of the HTC for the parallel configuration are summarized in Fig. 3.6(a). As in the perpendicular case, the far-field is barely affected by the magnetic field, the near-field thermal radiation is suppressed by the field, and at high fields the NFRHT tends to saturates. Interestingly, it saturates to the same value as in the perpendicular configuration. In spite of the similarities, there are also important differences. In this case, the NFRHT is much more sensitive to the field and a significant reduction is already achieved at 1 T. Notice also that in this case the HTC is clearly nonmonotonic and the maximum reduction is reached at around 6 T. Finally, notice also that the reduction is more pronounced than in the perpendicular case and the NFRHT can be diminished by up to a factor of 7 with respect to the zero-field case, see inset of Fig. 3.6(a). This more pronounced reduction in the parallel configuration is also apparent in the spectral heat flux, as one can see in Fig. 3.6(b). Notice that also in this case there appears a high-frequency peak that is blue-shifted as the field increases. This peak appears at the cyclotron frequency and it has the same origin as in the perpendicular case.

Again, to understand this complex phenomenology, it is convenient to examine the transmission of the p-polarized waves, which dominate the NFRHT for any field. Since in this case the transmission also depends on the direction of $\mathbf{k}$, we choose to analyze the two most representative directions. In the first one, the in-plane wave vector $\mathbf{k}$ is parallel to the field, *i.e.* $\mathbf{k} = (k_x, 0)$, and in the second one, $\mathbf{k}$ is perpendicular to the field, *i.e.* $\mathbf{k} = (0, k_y)$. The transmission of p-polarized waves for these two directions is shown in Fig. 3.7 as a function of the magnitude of the wave vector and as a function of the frequency for different values of the field. As one can see, the transmission exhibits very different behaviors for these two directions. While for $\mathbf{k} \parallel \mathbf{H}$ the situation resembles that of a perpendicular field (see discussion above), for $\mathbf{k} \perp \mathbf{H}$ it seems like the transmission

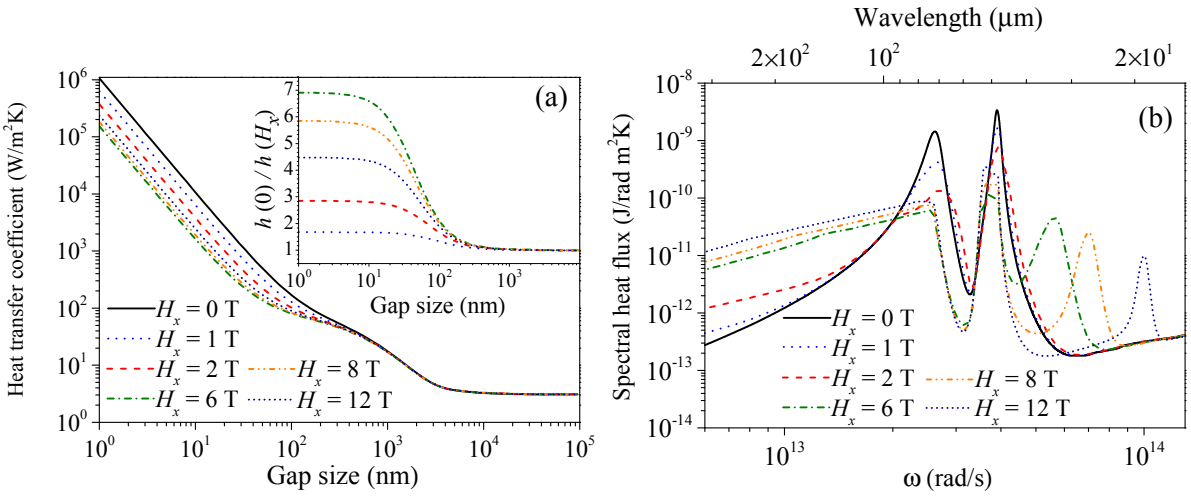

Figure 3.6: (a) HTC for n-doped InSb as a function of the gap for different values of the magnetic field applied along the surfaces of the plates. The inset shows the ratio between the zero-field coefficient and the coefficient for different values of the field in the near-field region. (b) The corresponding spectral heat flux as a function of the frequency (and wavelength) for a gap of $d = 10$ nm and different values of the parallel field.

is dominated by surface waves that are severely affected by the magnetic field (with the appearance of gaps in their dispersion relations). These very different behaviors can be understood with an analysis of both the surface waves and the propagating waves inside the material in these two situations. In the case $\mathbf{k} \parallel \mathbf{H}$, one can show that a uniaxial approximation, similar to that discussed above, accurately reproduces the results for the transmission found in the exact calculation. In this case, the permittivity tensor can be approximated by $\hat{\epsilon} = diag[\epsilon_{xx}, \epsilon_{zz}, \epsilon_{zz}]$, where $\epsilon_{xx} = \epsilon_3$ and $\epsilon_{zz} = \epsilon_1$. Within this approximation, the dispersion relation of surface waves in the electrostatic limit $k \gg \omega/c$ is also given by Eq. (3.15) (see Appendix C). As we show in Fig. 3.7(a-c), this dispersion relation nicely describes the structure of the transmission maxima in the regions where the surface waves can exist ($\epsilon_{xx}, \epsilon_{zz} < 0$). On the other hand, as we show in Appendix C, the allowed values for the transverse component of the wave vector inside these uniaxial-like materials are given by $q_o = \sqrt{\epsilon_{zz}\omega^2/c^2 - k^2}$ for ordinary waves and $q_e = \sqrt{\epsilon_{xx}\omega^2/c^2 - k^2\epsilon_{xx}/\epsilon_{zz}}$ for extraordinary waves. Again, the dispersion of these extraordinary waves is of hyperbolic type when ϵ_{xx} and ϵ_{zz} have opposite signs. In Fig. 3.7(a-c) we identify the frequency regions where the HMs exist with the condition $\epsilon_{xx}\epsilon_{zz} < 0$, regions that progressively dominate the transmission as the field increases. Thus, we see that for $\mathbf{k} \parallel \mathbf{H}$ the situation is very similar to that extensively discussed in the case in which the field is perpendicular to the materials' surfaces.

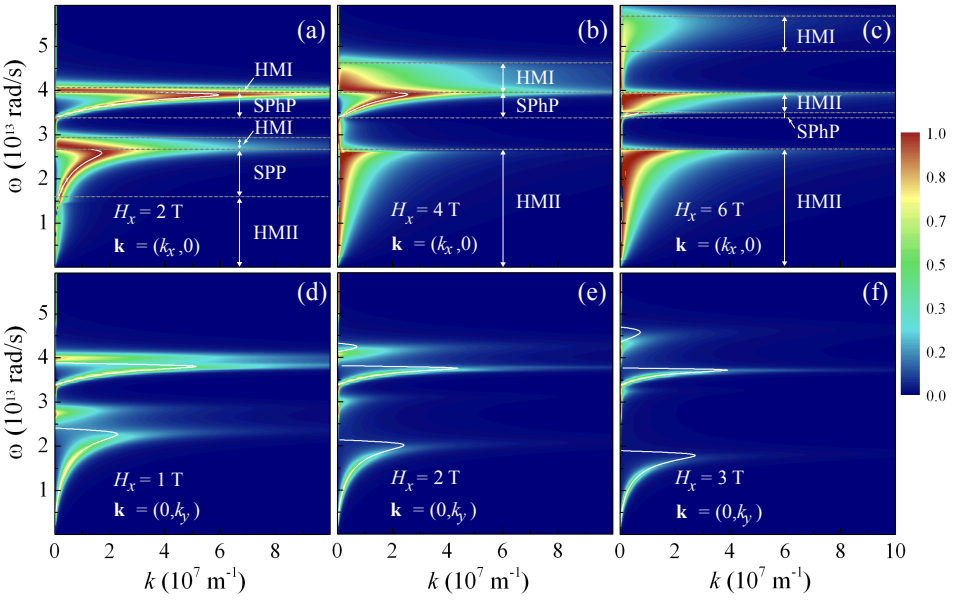

Figure 3.7: The transmission coefficient for p-polarized waves as a function of the magnitude of the parallel wave vector and frequency for InSb and a gap of $d = 10$ nm. In all cases the field is parallel to the plate surfaces, $\mathbf{H} = H_x\hat{\mathbf{x}}$. The panels (a-c) correspond to different values of the magnetic field for wave vectors parallel to field, $\mathbf{k} = (k_x, 0)$, while panels (d-f) correspond to wave vectors perpendicular to the field, $\mathbf{k} = (0, k_y)$. The horizontal dashed lines separate the regions where transmission is dominated by surface waves (SPPs and SPhPs) or HMs of type I and II (HMI and HMII). The white solid lines correspond to the analytical dispersion relation of the surface waves of Eq. (3.15) in panels (a-c) and of Eq. (3.20) in panels (d-f).

On the contrary, the situation is very different for $\mathbf{k} \perp \mathbf{H}$. In this case, there are no HMs and no uniaxial approximation can describe the situation. As we show in Appendix C, the allowed q-values are given by $q_{\mathrm{o},1} = \sqrt{\epsilon_{xx}\omega^2/c^2 - k^2}$ and $q_{\mathrm{o},2} = \sqrt{(\epsilon_{yy}^2 + \epsilon_{yz}^2)\omega^2/(c^2\epsilon_{yy}) - k^2}$, which both describe waves with no hyperbolic dispersion. On the other hand, the dispersion relation of the surface waves in the electrostatic limit is given by

$$k_{SW} = \frac{1}{2d} \ln\left(\frac{(\eta_{yy} - 1 + i\eta_{yz})(\eta_{yy} - 1 - i\eta_{yz})}{(\eta_{yy} + 1 + i\eta_{yz})(\eta_{yy} + 1 - i\eta_{yz})}\right), \tag{3.20}$$

where $\eta_{yy} = \epsilon_{yy}/(\epsilon_{yy}^2 + \epsilon_{yz}^2)$ and $\eta_{yz} = -\epsilon_{yz}/(\epsilon_{yy}^2 + \epsilon_{yz}^2)$. As we show in Fig. 3.7(d-f), this dispersion relation explains the complex structure of the transmission maxima in this case. We emphasize that this dispersion relation is reciprocal in our symmetric geometry and for this reason we only show results for $k_y > 0$. Notice that this dispersion is very sensitive to the magnetic field and already fields of the order of 1 T strongly affect the surface waves. Notice also the appearance of gaps in the dispersion relations, a subject

that has been extensively discussed in the case of a single interface [110, 111]. Overall, the field rapidly reduces the k-values of the surface waves and restricts the regions where they can exist. This strong sensitivity of the surface waves with $\mathbf{k} \perp \mathbf{H}$ is the reason for the more pronounced reduction of the NFRHT for this field configuration.

In general, for an arbitrary direction $\mathbf{k} = (k_x, k_y)$ the situation is somehow a combination of the two types of behaviors just described. The complex interplay of these behaviors for different $\mathbf{k}$-directions is responsible for the nonmonotonic dependence with magnetic field, along with the change in efficiency of the HMs upon varying the field. On the other hand, at very high fields the cyclotron frequency becomes much larger than the plasma frequency and the off-diagonal elements of the permittivity tensor become negligible. At the same time, the field-dependent terms in the diagonal elements also become very small. Thus, the systems effectively become uniaxial and field-independent and the heat transfer is identical to the case in which the field is perpendicular. Finally, in the far-field regime, the heat transfer is not sensitive to the magnetic field for the same reason as in the perpendicular configuration.

Let us conclude this section with two brief comments. First, as it is obvious from the discussions above, another way to modulate the NFRHT is by rotating the magnetic field, while keeping fixed its magnitude. Actually, we find that for any field magnitude, the NFRHT is always smaller in the parallel configuration. Thus, one can increase or decrease the near-field thermal radiation by rotating appropriately the magnetic field. Second, we have focused here in the case of doped InSb, but similar results can in principle be obtained for other doped polar semiconductors such as GaAs, InAs, InP, PbTe, SiC, etc.

3.4. Non-polar semiconductors: Si

In the previous section we have seen that when the field is parallel to the surfaces, one can have hyperbolic emitters, but the HMs always coexist to some degree with surface waves (even at the highest field). We show in this section that in the case of non-polar semiconductors, where phonons do not play any role, it is possible to tune the system with a magnetic field to a situation where only HMs contribute to the NFRHT. For this purpose, we choose Si as the material for the two plates. It has been predicted [116, 117], and experimentally tested [118, 119], that in doped Si the NFRHT in the absence of field can be dominated by SPPs even at room temperature. Let us see now how this is modified upon applying a magnetic field.

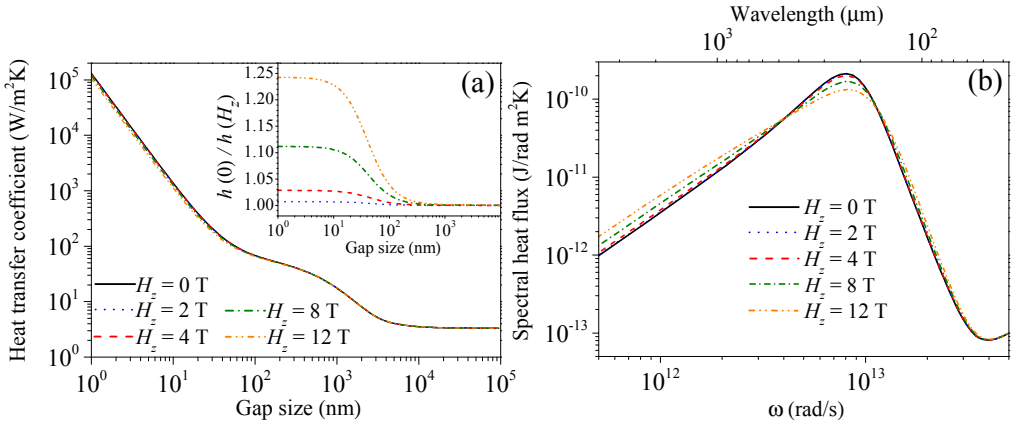

Figure 3.8: (a) HTC for n-doped Si as a function of the gap for different values of the magnetic field perpendicular to the plate surfaces. The inset shows the ratio between the zero-field coefficient and the coefficient for different values of the field in the near-field region. (b) The corresponding spectral heat flux as a function of the frequency (and wavelength) for a gap of $d = 10$ nm.

The dielectric properties of doped Si are similar to those of InSb, the only difference being the absence of a phonon contribution. Thus, the dielectric functions of Eq. (3.14) now read

$$\begin{aligned} \epsilon_1(H) &= \epsilon_\infty \left(1 + \frac{\omega_p^2(\omega + i\gamma)}{\omega[\omega_c^2 - (\omega + i\gamma)^2]}\right), \\ \epsilon_3 &= \epsilon_\infty \left(1 - \frac{\omega_p^2}{\omega(\omega + i\gamma)}\right), \end{aligned} \tag{3.21}$$

while $\epsilon_2(H)$ remains unchanged. Using the results of Ref. [116] for the dielectric constant of doped Si, we focus on a room temperature case where the electron concentration is $n = 9.3\times10^{16}$ cm^{-3}, $\epsilon_\infty = 11.7$, $\gamma = 8.04\times10^{12}$ rad/s, $m^*/m = 0.27$, and $\omega_p = 9.66\times10^{12}$ rad/s. We have chosen this doping level to have a situation in which the plasma frequency is not too high so that we can affect the NFRHT with a magnetic field, and not too low so that the NFRHT in the absence of field is still dominated by SPPs.

The results for the HTC and spectral heat flux for a perpendicular magnetic field are displayed in Fig. 3.8. Although there are several features that are similar to those of the InSb case, there are also some notable differences. To begin with, notice that now higher fields are needed to see a significant reduction of the NFRHT (the required fields are around an order of magnitude higher than for InSb) and the reduction factors are clearly more modest, see inset of Fig. 3.8(a). This is mainly a consequence of the smaller cyclotron frequency in the Si case for a given field due to its larger effective mass.

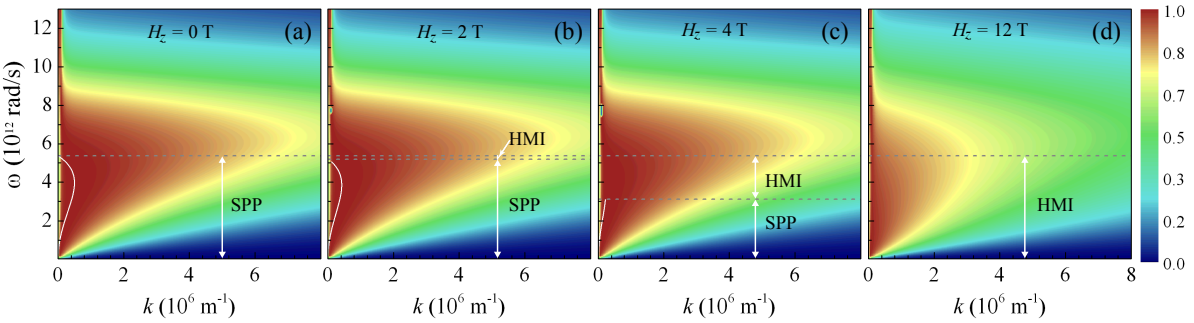

Figure 3.9: The transmission coefficient for p-polarized waves as a function of the magnitude of the parallel wave vector and frequency for Si and a gap of $d = 10$ nm. The different panels correspond to different values of the magnetic field that is perpendicular to the surfaces. The horizontal dashed lines separate the regions where transmission is dominated by SPPs or HMs of type I (HMI). The white solid lines correspond to the analytical SPP dispersion relation of Eq. (3.15).

Another consequence of the small cyclotron frequency is the fact that there is no sign of saturation of the NFRHT for reasonable magnetic fields. On the other hand, the spectral heat flux at low fields is dominated this time by a single broad peak that originates from SPPs (see discussion below). As the field increases, the peak height is reduced and the peak itself is broadened and deformed. As we show in what follows, this behavior is due to the appearance of HMs that at high fields completely replace the surface waves.

Again, we can gain a further insight into these results by analyzing the transmission of the p-polarized waves for different fields, which is illustrated in Fig. 3.9. As one can see, the transmission is dominated by evanescent waves (in the vacuum gap) in a frequency region right below the plasma frequency. The origin of the structure of the transmission maxima can be understood with the uniaxial approximation discussed above in the context of InSb. Again, this approximation reproduces very accurately all the results for arbitrary perpendicular fields (not shown here). Within this approximation, one can see that at low fields the transmission is dominated by SPPs, as we illustrate in Fig. 3.9(a-b) in which we have introduced the dispersion relation of the SPPs given by Eq. (3.15). As soon as the magnetic magnetic field becomes finite, the system starts to develop HMs of type I in a tiny frequency region right above the region of existence of the SPPs, see Fig. 3.9(b). The origin of these HMs is identical to that of the InSb case, but the main difference in this case is that upon increasing the field, one reaches a critical field value (of 4.36 T for this example) for which the surface waves cease to exist and the transmission is completely dominated by HMs turning the Si plates into “pure" hyperbolic thermal emitters, see Fig. 3.9(c-d).

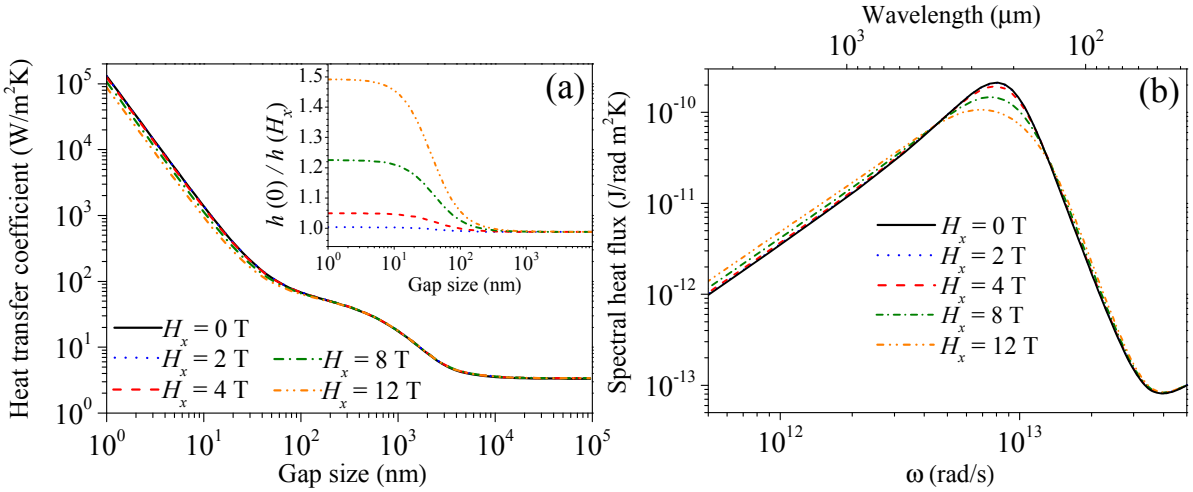

Figure 3.10: (a) HTC for n-doped Si as a function of the gap for different values of the magnetic field applied along the surfaces of the plates. The inset shows the ratio between the zero-field coefficient and the coefficient for different values of the field in the near-field region. (b) The corresponding spectral heat flux as a function of the frequency (and wavelength) for a gap of $d = 10$ nm.

For completeness, we have also studied the heat transfer in the parallel configuration and the results for the HTC and spectral heat flux are shown in Fig. 3.10. In this case the results are rather similar to those of the perpendicular configuration. In particular, contrary to the InSb case we do not find a nonmonotonic behavior. Moreover, the NFRHT reduction is not much more pronounced than in the perpendicular case, although one can reach reduction factors of 50% for 12 T. Finally, saturation is not reached for these high fields for the same reason as in the perpendicular configuration. As in the case of InSb, all these results can be understood in terms of the modes that govern the near-field thermal radiation. In this sense, for a direction where $\mathbf{k} \parallel \mathbf{H}$, the SPPs that dominate the NFRHT at low fields are progressively replaced by HMIs upon increasing the field and above 4.36 T they “eat out" all surface waves. On the contrary, for $\mathbf{k} \perp \mathbf{H}$ there are no HMs and the only magnetic field effect is the modification of the SPP dispersion relation. Again, the interplay between these two characteristic behaviors among the different $\mathbf{k}$-directions explains the evolution of the NFRHT with the field.

Let us conclude this section by saying that the behavior reported here for Si could also be observed for other non-polar semiconductors such as Ge.

3.5. Outlook and conclusions

The results reported in this work raise numerous interesting questions. Thus for instance, in all cases analyzed so far, we have found that the magnetic field reduces the NFRHT as compared to the zero-field result. Is there any fundamental argument that forbids a magnetic-field-induced enhancement? In principle, there is no such an argument. The reduction that we have found in doped semiconductors is due to the fact that the we have explored cases where surface waves, which are extremely efficient, dominate the NFRHT in the absence of field. In this sense, one may wonder if a field-induced enhancement could take place in a situation where the NFRHT in the absence of field is dominated by standard frustrated internal reflection modes, as it happens in metals [120]. Obviously, metals are out of the question due to their huge plasma frequency, but one can investigate non-polar semiconductors with a low doping level. Indeed, we have done it for the case of Si and again, we find that the magnetic field reduces the NFRHT and moreover, exceedingly high fields are required to see any significant effect. Of course, we have by no means exhausted all possibilities and, for instance, we have not explored asymmetric situations with different materials. Thus, the question remains of whether the application of a magnetic field can under certain circumstances enhance the near-field thermal radiation.

The discovery in this work of the induction of HMs upon the application of a magnetic field may also have important consequences for layered structures involving thin films. Recently, it has been demonstrated that thin films made of polar dielectrics may support NFRHT enhancements comparable to those of bulk samples due to the excitation of SPhPs [69]. Since HMs have a propagating character inside the material, they may be severely affected in a thin film geometry by the presence of a substrate. Thus, one could expect much more dramatic magnetic-field effects in systems coated with semiconductor thin films.

Obviously, the question remains of whether one can modulate the NFRHT with a magnetic field in other classes of materials. For instance, since a MO activity is required, what about ferromagnetic materials? Ideally, one could imagine to tune the NFRHT by playing around with the relative orientation of the magnetization, following the spin-valve experiments in the context of spintronics.

Another question of general interest for the field of metamaterials is if a doped semiconductor under a magnetic field could exhibit the plethora of exotic optical properties reported in hybrid hyperbolic metamaterials [89, 90]. We have shown here that it can

behave as a hyperbolic thermal emitter, but can it also exhibit negative refraction or be used do to subwavelength imaging and focusing in the infrared? These are very important questions that we are currently pursuing.

So in summary, we have presented in this work a very detailed theoretical analysis of the influence of a magnetic field in the NFRHT. By considering the simple case of two parallel plates, we have demonstrated that for doped semiconductors the near-field thermal radiation can be strongly modified by the application of an external magnetic field. In particular, we have shown that the magnetic field may significantly reduce the NFRHT and the reduction in polar semiconductors can be as large as 700% at room temperature. Moreover, we have shown that when the field is perpendicular to the parallel plates, doped semiconductors become ideal hyperbolic thermal emitters with highly tunable properties. This provides a unique opportunity to explore the physics of thermal radiation in this class of metamaterials without the need to resort to complex hybrid structures. Finally, all the predictions of this work are amenable to measurements with the present experimental techniques, and we are convinced that the multiple open questions that this work raises will motivate many new theoretical and experimental studies of this subject.

4 | Enhancing near-field radiative heat transfer with Si-based metasurfaces.

4.1. Introduction

In previous Chapters, we have shown that the heat flow between two bodies can be enhanced by orders of magnitude in the near-field due to the contribution of evanescent waves. So far, the largest enhancements have been reported in polar dielectrics [18, 121], where the near-field thermal radiation is dominated, as we have analyzed in Chapter 1, by the excitation of SPhPs. Up to date, the polar material that exhibits the highest near-field thermal conductance is silica (SiO_2).

In this context, the question on the fundamental limits of NFRHT is attracting a lot of attention. Very recently, an upper bound for the RHT between two objects has been obtained [122, 123]. By applying energy conservation and the reciprocity theorem of optics, the authors derived an upper limit for the RHT between two closely-spaced bodies which is much higher than the current enhancements observed in the near-field. The limit found is independent of the exact shape of the objects and only depends on the distance between the objects and on their material susceptibilities [122, 123]. However, there has not been still any proposal of an extended structure that has a HTC exceeding that between two planar polar dielectric surfaces.

Hyperbolic materials were introduced as a promising strategy to enhance the NFRHT of extended structures [86, 97]. However, they do not show in practice a larger thermal conductance than the best polar dielectrics. In an attempt to tune NFRHT, several calculations of NFRHT between periodic metallic nanostructures in both 1D [27, 28, 31, 124] and 2D [32] have been reported. These calculations have shown some degree of tunability and a NFRHT enhancement over the corresponding material without nanostructuration. However, the reported NFRHT in these structures is still smaller than in the case of parallel plates made of polar dielectrics. There have also been theoretical studies of the NFRHT between photonic crystals and periodic metamaterials made of dielectrics [29, 30, 35] that show how the radiative properties can be enhanced with respect to the bulk counterpart. However, the resulting NFRHTs are again much smaller than in planar polar dielectrics.

In this Chapter we show that metasurfaces of doped Si (see Fig. 4.1) can be used to boost NFRHT. Making use of a rigorous coupled wave analysis, we demonstrate that one can design Si metasurfaces that not only exhibit a room-temperature NFRHT much larger than that of bulk Si or other proposed periodic structures [29, 30, 32], but they also outperform the best unstructured polar dielectric (SiO_2). By appropriately choosing the geometrical parameters of the metasurfaces, the enhancement over polar dielectrics occurs over a broad range of separations (from 13 nm to 2 μm). The underlying physical mechanisms responsible of this striking behavior are the existence of broad-band SPPs in doped Si, and the ability to tune via nanostructuration the dispersion relation of these SPPs that dominate NFRHT in our structure. The predictions of this work show the great potential of metasurfaces for the field of NFRHT and can be tested with recent advances to measure NFRHT in parallel extended structures [44].

4.2. Modelling the NFRHT between two metasurfaces

The system that we consider consists of two identical metasurfaces formed by 2D periodic arrays of square holes drilled in a doped Si layer, see Fig. 4.1. The metasurfaces are deposited on semi-infinite planar substrates. The geometrical parameters of the metasurfaces are the lattice constant a, the distance between holes p, the gap size d, and the thickness of the metasurfaces τ, which is equal to the depth of the holes in the structure. We define the filling factor of this structure as $f = (a-p)^2/a^2$, which describes

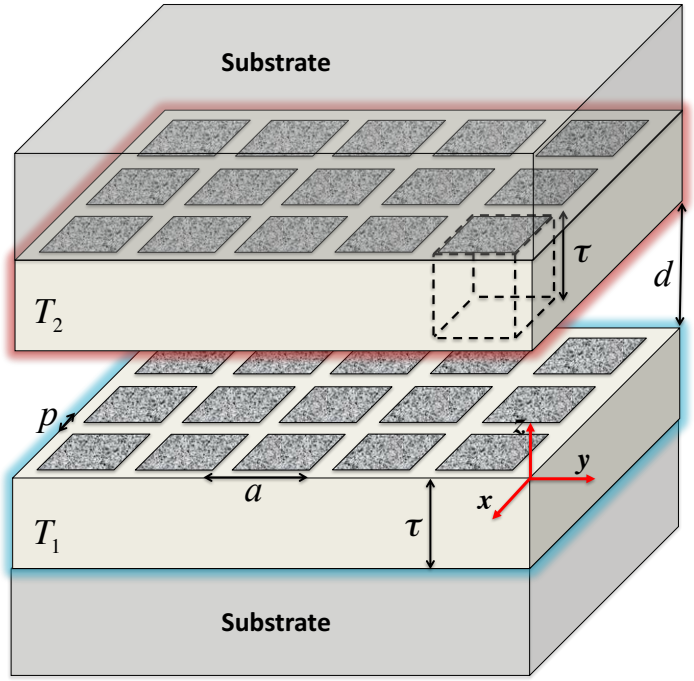

Figure 4.1: Schematics of two doped-Si metasurfaces made of 2D periodic arrays of square holes placed on semi-infinite planar substrates and held at temperatures T_1 and T_2. The key parameters are shown: lattice parameter (a), distance between holes (p), gap size (d), and metasurface thickness (τ).

the fraction of vacuum in the structure ($f = 0$ means no holes, while $f = 1$ means no Si). The dielectric function of doped Si is described within a Drude model [125]: $\epsilon_{Si}(\omega) = \epsilon_\infty - \omega_p^2/(\omega^2 + i\gamma\omega)$, where $\epsilon_\infty = 11.7$, $\omega_p = 711$ meV is the plasma frequency, and $\gamma = 61.5$ meV is the damping. These values correspond to a doping level of 10^{20} cm^{-3}. The choice of this material and the doping level were motivated by the possibility to sustain SPPs at frequencies that can be thermally excited at room temperature. This is not possible for very high doping levels, while for very low ones the SPPs are not very confined and give a modest contribution to the NFRHT. Our main idea is that by introducing holes in the Si layers, one can reduce the losses and the effective plasma frequency that, in turn, should redshift the surface modes. This way, these modes could be more easily occupied at room temperature leading to an enhancement of the NFRHT.

To test this idea we need a formalism which is able to calculate the NFRHT between two periodic systems (See Fig. 4.1). As we are dealing with periodic structures, it is convenient to use the rigorous coupled wave analysis (RCWA) and express the fields in our system as a sum of plane waves using Bloch theorem. The expression derived in

4. Enhancing near-field radiative heat transfer with Si-based metasurfaces.

Section 3.2 (Eq. 3.12) can be used again to calculate the RHT between the two parallel periodic plates. Therefore, we can express in this case the HTC, which corresponds to the radiative linear heat conductance per unit area (see Eq. 1.12) as:

$$h(d,T) = \int_0^\infty \frac{d\omega}{2\pi}\frac{\partial\Theta(\omega,T)}{\partial T}\int_{-\pi/a}^{\pi/a}\int_{-\pi/a}^{\pi/a}\frac{d\mathbf{k}}{(2\pi)^2}\mathcal{T}(\omega,\mathbf{k}), \tag{4.1}$$

where again $\Theta(\omega,T) = \hbar\omega/[\exp(\hbar\omega/k_{\rm B}T)-1]$, T is the absolute temperature of the system, ω is the radiation frequency, $\mathbf{k}=(k_x,k_y)$ is the wave vector parallel to the surface planes, and $\mathcal{T}(\omega,\mathbf{k})$ is the sum over polarizations of the transmission probability of the EM waves. This transmission function above can be obtained by combining scattering matrices of the different interfaces in reciprocal space. In particular, if we place the coordinates origin at metasurface 1, the transmission coefficient can be expressed as [24]

$$\mathcal{T}(\omega,\mathbf{k}) = \mathrm{Tr}\left\{\hat{D}\hat{W}_1\hat{D}^\dagger\hat{W}_2\right\}, \tag{4.2}$$

where

$$\hat{D} = (\hat{1}-\hat{S}_1\hat{S}_2)^{-1}, \tag{4.3}$$

$$\hat{W}_1 = \hat{\Sigma}^{pw}_{-1} - \hat{S}_1\hat{\Sigma}^{pw}_{-1}\hat{S}_1^\dagger + \hat{S}_1\hat{\Sigma}^{ew}_{-1} - \hat{\Sigma}^{ew}_{-1}\hat{S}_1^\dagger, \tag{4.4}$$

$$\hat{W}_2 = \hat{\Sigma}^{pw}_{+1} - \hat{S}_2^\dagger\hat{\Sigma}^{pw}_{+1}\hat{S}_2 + \hat{S}_2^\dagger\hat{\Sigma}^{ew}_{+1} - \hat{\Sigma}^{ew}_{+1}\hat{S}_2. \tag{4.5}$$

Here, $\hat{S}_1 = \hat{R}_1$ and $\hat{S}_2 = e^{iq_{\rm air}d}\hat{R}_2e^{iq_{\rm air}d}$, where $\hat{R}_1$ and $\hat{R}_2$ are the reflection matrices of the two vacuum-metasurface interfaces and $q^2_{\rm air} = \omega^2/c^2 - k^2$. These matrices were computed with the scattering-matrix approach of Ref. [108]. This formalism extends the scattering-matrix method employed in Chapter 3 and explained in Appendix A to the case of periodic systems. The matrix $\hat{\Sigma}^{pw(ew)}_{-1(+1)}$ is a projector into the propagating (evanescent) sector. All these matrices are $2N_g \times 2N_g$ matrices, where N_g is the number of reciprocal lattice vectors included in the plane-wave expansions. On the other hand, the $\mathbf{k}$-integral in Eq. (4.1) must be calculated in the interval $(-\pi/a,\pi/a)$ for both k_x and k_y. A key point in our method is the use of the so-called fast Fourier factorization when dealing with the Fourier transform of two discontinuous functions in the Maxwell equations [108, 126]. This factorization solves the known convergence problems of the RCWA approach. Let us explain in more detail the fast Fourier factorization in two dimensional photonic crystals, as it has been crucial to perform all the calculations shown in this chapter.

4.2.1. Fast Fourier factorization to calculate the reflection matrix of a 2D square lattice

The scattering approach does have important convergence problems, specially when the analyzed periodic structure is metallic [108]. These problems are well-known in the field of photonic gratings [127] and they originate due to the incorrect Fourier factorization of the product of two discontinuous functions. One example of this is the constitutive relation $\mathbf{D} = \epsilon\mathbf{E}$, which is equal to the product of two discontinuous functions at some regions of the grating.

Let us know explain in more detail how to carry out the Fourier factorization in this case. The Fourier transform h of the product of two arbitrary functions f and g is given by Laurent's rule:

$$h_n = \sum_{m=-\infty}^{\infty} f_{n-m} g_m, \tag{4.6}$$

where h_n is the n^{th} Fourier component of h. We can write the last expression in matrix notation:

$$[h] = [\![f]\!]\,[g]\,. \tag{4.7}$$

Here, $[g]$ is a column vector constructed with the N_g Fourier components g_n and $[\![f]\!]$ denotes the $N_g \times N_g$ Toeplitz matrix whose (n, m) entry is f_{n-m}. However, if f and g are piecewise smooth periodic functions, which are discontinuous at the same points, but their product fg remains continuous everywhere, the appropriate way to Fourier transform the product $h = fg$ is [126, 127]:

$$[h] = [\![1/f]\!]^{-1}\,[g]\,. \tag{4.8}$$

When the number of Fourier terms is infinite, Eq. (4.7) and Eq. (4.8) are equivalent. However, when we consider truncated series, as we do numerically, Eq. (4.8) is the only expression that warrants convergence of the Fourier transform of function h.

We consider now a 2D square grating as the one depicted in Fig. 4.1, where both the dielectric constant ϵ and the electric field in the x-direction E_x are discontinuous at the boundaries parallel to the y-axis. Besides, the product ϵE_x is continuous with respect to x, so when performing a Fourier transform along the x-direction, the so-called inverse rule (Eq. (4.8)) should be followed. On the other hand, as E_x is continuous with respect

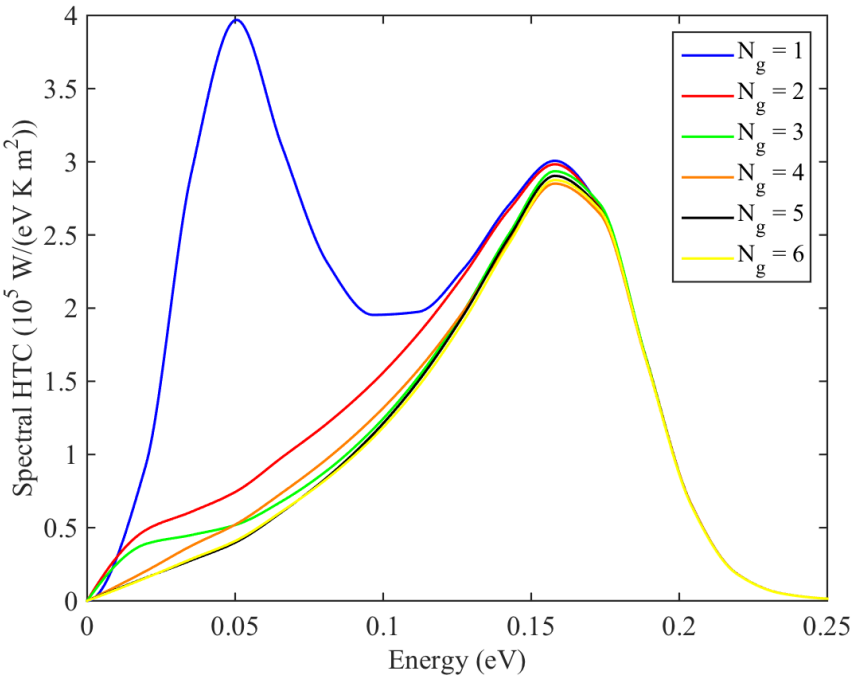

Figure 4.2: Spectral HTC as a function of the photon energy for a gap of $d = 20$ nm, lattice constant $a = 50$ nm and filling factor $f = 0.4$. The different lines correspond to different values of the number of reciprocal lattice vectors N_g used in the calculations.

to y, the Laurent's rule must be applied for a Fourier transform along y. Eventually, the matrix which corresponds to the Fourier transform of the dielectric constant component ϵ_{xx} is given by [127]:

$$(\epsilon_{xx})_{mn,m'n'} = \frac{1}{a}\int (\mathbf{A}^{-1})_{m,m'} e^{-2i\pi(n-n')y/a} dy, \tag{4.9}$$

where $\mathbf{A}$ is a Toeplitz matrix whose components are the Fourier coefficients of the permittivity respect to the x-direction:

$$\mathbf{A}_{m,m'} = \frac{1}{a}\int \frac{1}{\epsilon} e^{-2i\pi(m-m')x/a} dx, \tag{4.10}$$

where m, m' (n, n') represent the Fourier indices along the $x(y)$-direction. In summary, the inverse of ϵ is Fourier transform along x following the inverse rule. Afterwards, it is inversed and Fourier transformed along the y-axis, applying Laurent's rule. The same procedure has to be followed to calculate $(\epsilon_{yy})_{mn,m'n'}$. As we are considering an isotropic material and a square grating, $(\epsilon_{xx})_{mn,m'n'} = (\epsilon_{yy})_{mn,m'n'}$. Besides, $\epsilon_{xy} = \epsilon_{yx} = 0$.

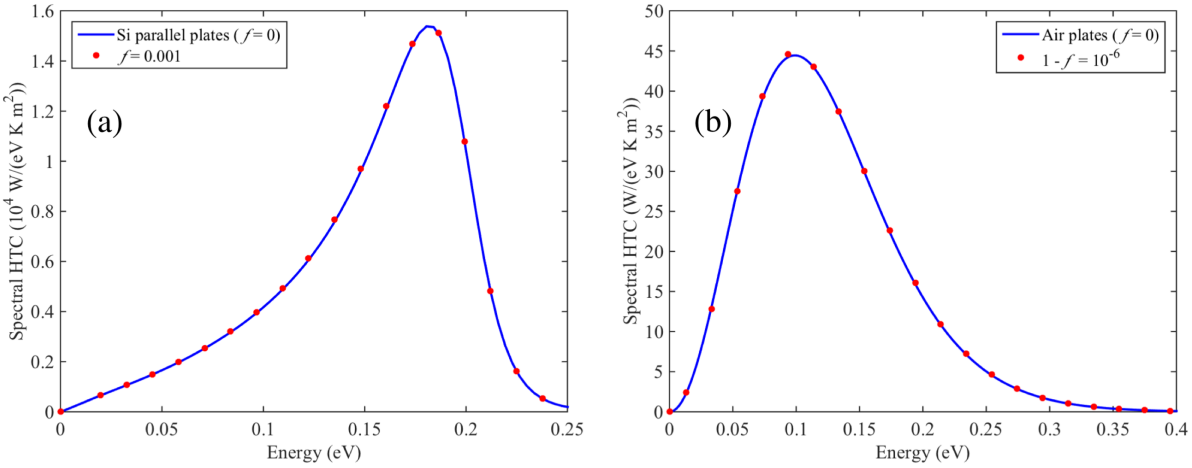

Figure 4.3: (a) Spectral HTC as a function of the photon energy for a gap of $d = 20$ nm and a lattice constant $a = 50$ nm. The blue line corresponds to the case of bulk doped silicon, while the red dots are the numerical results obtained with our RCWA method for $f = 0.001$. (b) Spectral HTC as a function of the photon energy for a gap of $d = 20$ nm and a lattice constant $a = 50$ nm. The blue line corresponds to the case of two air plates, while the red dots correspond to the results obtained with our method for $1 - f = 10^{-6}$.

4.2.2. Testing the validity of our formalism.

Before analyzing the results obtained for the NFRHT between our two doped-Si metasurfaces, we have tested the validity and the accuracy of our method based on the rigorous coupled wave analysis (RCWA). First of all, it is important to emphasize that we have carefully checked the convergence of all our results with the number of reciprocal lattice vectors (N_g) used in our RCWA-based calculations. This convergence is illustrated in Fig. 4.2 where we show the spectral HTC (see Eq. 1.13) as a function of energy between our Si metasurfaces for a filling factor $f = 0.4$, a lattice constant $a = 50$ nm and a gap size $d = 20$ nm. The different curves in Fig. 4.2 correspond to different values of N_g and, as one can see, the results nicely converge as the number of plane waves in the calculations is increased. Moreover, it is worth stressing that the use of the so-called fast Fourier factorization employed in this chapter ensures that the calculations converge to the correct result. We have made sure that all the results presented in this work are converged with a relative accuracy of better than 1%.

A second test that we have done is to verify that our approach is able to reproduce known results in two different limits, namely in the limits of small and large filling factors. In the first one, when the filling factor tends to zero, one has to recover the results of the heat transfer between two planar doped-Si surfaces. As we show in Fig. 4.3(a) for

the case of $f = 0.001$, our results for the spectral HTC do reproduce the known results for two Si parallel plates. In the opposite limit of filling factors close to 1, one should recover the results for two parallel plates made of air, i.e., one should recover the results for two black-body plates. As we show in Fig. 4.3(b) below for the case of $1 - f = 10^{-6}$, our RCWA-based results accurately reproduce this limit as well.

4.3. Results: overcoming the NFRHT between polar dielectrics.

After demonstrating the validity of our formalism, we start the discussion of the results by illustrating the main finding of our work. For simplicity, we first assume that the Si layer thickness is infinite (no substrate). In Fig. 4.4(a) we show the room-temperature HTC as a function of the gap size for two metasurfaces with $a = 50$ nm and $f = 0.9$. This result is compared with the HTC for two doped-Si and two SiO_2 parallel plates. Notice that the NFRHT between the Si metasurfaces is more than an order of magnitude larger than the corresponding result for Si plates for a broad range of separations. More importantly, the Si metasurfaces also exhibit a higher HTC than the silica plates in a broad distance range (from 13 nm to 2 microns), an enhancement that reaches a factor 3 for gap sizes of about 100 nm. Let us emphasize that our structure exhibits a super-Planckian radiative heat transfer in that range of gaps (see arrow on the right). We also show in Fig. 4.4(a) the contribution of evanescent TM-polarized waves to the HTC of the doped-Si metasurfaces. Notice that this contribution dominates the NFRHT for separations below 1 μm, which is a first hint that surface modes are responsible for the enhancement in this regime.

To get further insight into the role of nanostructuration, we show in Fig. 4.4(b) the spectral HTC of the metasurfaces for a gap $d = 20$ nm, a lattice constant $a = 50$ nm, and for different filling factors. This spectral HTC is defined as the HTC per unit of frequency or photon energy. As one can see, the maximum of the spectral HTC is redshifted upon increasing the size of the holes from 0.2 eV for $f = 0$ up to around 0.05 eV for $f = 0.98$. Notice also that the HTC (the integral of these spectral functions) also increases drastically with the filling factor reaching a maximum at $f \approx 0.98$. These results illustrate the high tunabilibity of NFRHT in metasurfaces.

The origin of the redshift in the spectral HTC can be understood with an analysis of the frequency and parallel wave vector dependence of the transmission $\mathcal{T}(\omega, \mathbf{k})$. Such a

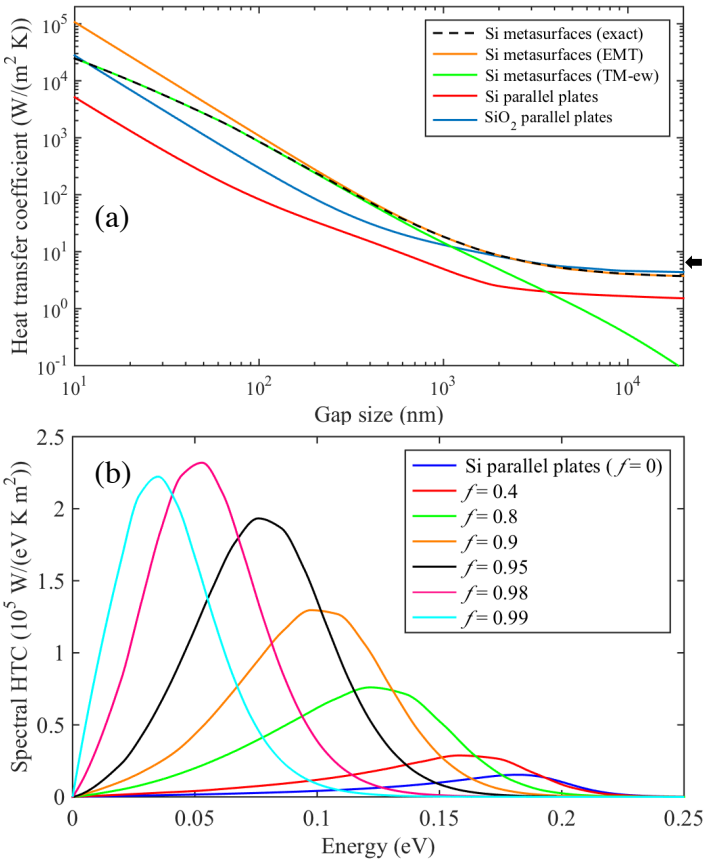

Figure 4.4: (a) Room-temperature HTC as a function of the gap size for doped-Si metasurfaces with $a = 50$ nm and $f = 0.9$ (black dashed line). For comparison, we show the results for the Si metasurfaces computed with effective medium theory (orange line), SiO_2 parallel plates (blue line), and doped-Si parallel plates (red line). The green line shows the contribution of evanescent TM-polarized waves to the HTC of the Si metasurfaces and the arrow on the right indicates the blackbody limit, 6.1 W/(m^{2}K). (b) Spectral HTC as a function of the photon energy for a gap of $d = 20$ nm and a lattice constant $a = 50$ nm. The different lines correspond to different filling factors.

dependence is displayed in Fig. 4.5 for p-polarized waves, which dominate the NFRHT. In particular, we show the transmission along the x-direction [$\mathbf{k} = (k_x, 0)$], see Fig. 4.1, for $d = 20$ nm, $a = 50$ nm, and different filling factors. As shown in Fig. 4.5(a) for the case of two Si parallel plates ($f = 0$), the transmission maxima resemble the dispersion relation of a surface mode. As shown below, it corresponds to a cavity SPP mode that emerges from the hybridization of the SPP modes of the two vacuum-Si interfaces. Notice that the transmission maxima lie to the right of the light line (or dispersion relation of light in vacuum), which indicates that these modes correspond to evanescent waves (both in vacuum and inside Si). As the filling factor increases, we find that the transmission

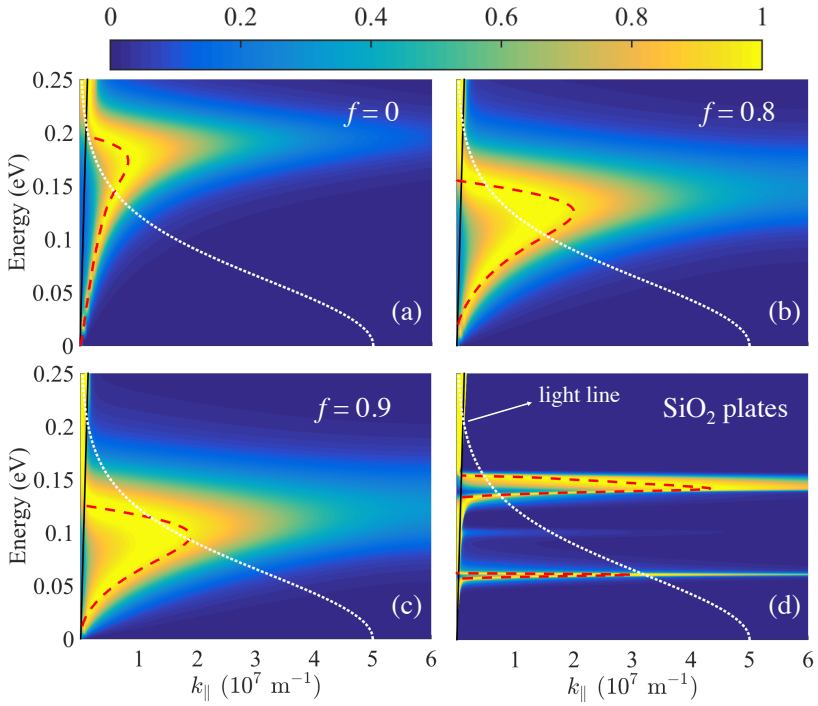

Figure 4.5: Transmission of p-polarized waves along the x-direction for $d = 20$ nm. (a-c) Si metasurfaces with lattice parameter $a = 50$ nm. The different panels correspond to various filling factors. The red dashed lines correspond to the dispersion relation of the SPPs, see Eq. (4.12), and the black lines shows the dispersion relation of light in vacuum. (d) The same as in the other panels but for two SiO_2 parallel plates. In this case, the red dashed line corresponds to the dispersion relation of the SPhPs in this structure. The white dotted lines in all panels correspond the occupation factor $\partial\Theta(\omega, T)/\partial T$, see Eq. (4.1), in arbitrary units.

maxima redshift, see Fig. 4.5(b-c), which is consistent with our observation above about the spectral HTC. Indeed, the frequency at which the maxima of the spectral HTC occur, see Fig. 4.4(b), corresponds exactly to the position at which the transmission maxima fold back towards the light line. The reason is that in that frequency region the transmission is not only maximum, but also k takes the largest value, maximizing thus the density of photonic modes.

4.4. Effective medium theory analysis

To confirm that cavity SPPs are indeed responsible for the NFRHT in our structure, we have analyzed their dispersion relation. For this purpose, we have made used of an effective medium theory (EMT) [128]. Within this theory our metasurfaces can be modeled as uniaxial materials with a diagonal permittivity tensor: $\hat{\epsilon} = \mathrm{diag}(\epsilon_o, \epsilon_o, \epsilon_e)$, where the

subindex o and e denote the ordinary and extraordinary optical axis, respectively. The components of the dielectric tensor are given by [128]

$$\epsilon_{\mathrm{o}} = \epsilon_{\mathrm{Si}} \frac{\epsilon_{\mathrm{Si}}(1-f)+1+f}{\epsilon_{\mathrm{Si}}(1+f)+1-f}, \;\; \epsilon_{\mathrm{e}} = f + (1-f)\epsilon_{\mathrm{Si}}. \tag{4.11}$$

In such an system, light propagates along the optical axes with perpendicular components of the wave vector given by $q_{\mathrm{o}}^2 = \epsilon_{\mathrm{o}}\omega^2/c^2 - k^2$ and $q_{\mathrm{e}}^2 = \epsilon_{\mathrm{o}}\omega^2/c^2 - k^2\epsilon_{\mathrm{o}}/\epsilon_{\mathrm{e}}$. Within this approximation, the SPP dispersion relation is given by the solution of the following equation [106]

$$e^{iq_{\mathrm{air}}d} = \pm\left(\frac{q_{\mathrm{e}} - \epsilon_{\mathrm{o}} q_{\mathrm{air}}}{q_{\mathrm{e}} + \epsilon_{\mathrm{o}} q_{\mathrm{air}}}\right). \tag{4.12}$$

In the electrostatic limit ($k \gg \omega/c$), this equation leads to the following dispersion relation for the cavity SPPs

$$k_{\mathrm{SPP}}(\omega) = \frac{1}{d}\ln\left(\pm\frac{\epsilon_{\mathrm{o}}(\omega) - \sqrt{\epsilon_{\mathrm{o}}(\omega)/\epsilon_{\mathrm{e}}(\omega)}}{\epsilon_{\mathrm{o}}(\omega) + \sqrt{\epsilon_{\mathrm{o}}(\omega)/\epsilon_{\mathrm{e}}(\omega)}}\right). \tag{4.13}$$

The exact dispersion relations obtained from Eq. (4.12) are shown in Fig. 4.5 as red dashed lines. These dispersion relations nicely coincide with the transmission maxima for the whole range of filling factors, which unambiguously demonstrates that cavity SPPs dominate the NFRHT in our system. Moreover, this shows that NFRHT is drastically enhanced upon increasing the filling factor because the surfaces modes shift to lower frequencies, which increases their thermal occupation at room temperature. This is illustrated in Fig. 4.5 where we show the frequency dependence of the factor $\partial\Theta(\omega,T)/\partial T$ that determines the occupation of these surface modes.

The enhancement of NFRHT in our metasurfaces over polar dielectrics like SiO_2 can be understood as follows. As we show in Fig. 4.5(d), the transmission between two silica plates is dominated by SPhPs [18], whose dispersion relation is given by Eq. (4.13) with $\epsilon_{\mathrm{o}} = \epsilon_{\mathrm{e}} = \epsilon_{\mathrm{SiO_2}}$ [69]. Although theses modes exhibit larger k-values than the SPPs in our Si metasurfaces and therefore larger photonic density of states, they are restricted to rather narrow frequency regions corresponding to the two Reststrahlen bands in this material. Thus, the larger extension in frequency of the SPPs in the Si structures is one of the key factors that leads to a higher NFRHT.

The fact that the EMT nicely describes the position of the transmission maxima raises the question of whether this theory can also accurately describe the NFRHT. This is

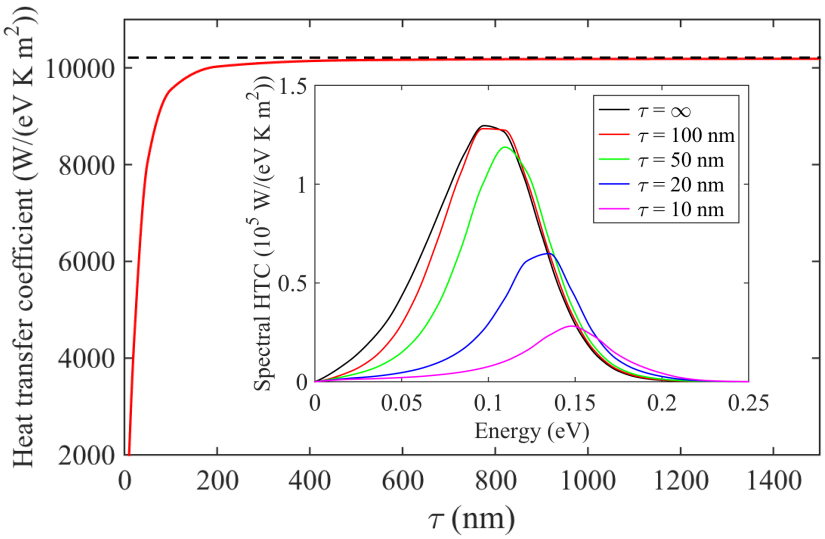

Figure 4.6: HTC as a function of the thickness of the periodically patterned Si layers for $d = 20$ nm, $a = 50$ nm, and $f = 0.9$. The dashed line corresponds to $\tau = \infty$. The inset shows the spectral HTC as a function of energy for several metasurface thicknesses.

actually not the case because EMT assumes that the geometrical features are much smaller than the relevant physical length scales of the problem. In our case, where there is a considerable damping, the natural lateral scale is set by the propagation length of the cavity SPP wavelengths, $1/(2\mathrm{Im}\{k_{\mathrm{SPP}}\})$. For frequencies close to the folding back of the dispersion relation, which are the ones that dominate the spectral HTC, this propagation length can obtained from Eq. (4.13). Thus for instance, for the structure analyzed in Fig. 4.4(a), Eq. (4.13) predicts that the SPP propagation length for the frequency of the spectral HTC maximum becomes of the order of the lattice parameter for $d \approx 100$ nm. Thus, the EMT is expected to fail below this gap size. To confirm this idea, we have computed the HTC in this structure within the EMT using the formalism for anisotropic planar systems of Ref. [106] and the result is shown in Fig. 4.4(a). As one can see, the EMT fails for gaps below the SPP propagation length. This analysis illustrates the need of an exact approach to accurately predict the NFRHT in these metasurfaces. Besides, the agreement between EMT results and the exact calculations for large gaps is an additional evidence of the validity of our approach.

4.5. Metasurface behaviour

Let us stress that our periodic structures truly behave as metasurfaces, which can be understood as follows. From Eq. (4.13) we can estimate the penetration depth of the cavity SPPs, which in the electrostatic limit is given by $1/(2\mathrm{Re}\{k_{\mathrm{SPP}}\})$. Thus, we see that this penetration depth diminishes as the gap is reduced, which implies that the NFRHT is dominated by the surface of the periodic structures. Thus for instance, for $d = 20$ nm, $a = 50$ nm, and $f = 0.9$ the penetration depth estimated from Eq. (4.13) is about 27 nm for the frequency of the spectral HTC maximum. Thus, one expects that all periodic structures with Si layers thicker than this penetration depth behave in the same way. To test this idea we have computed the HTC as a function of the thickness of the periodic Si layers, τ, assuming that the substrate underneath is also made of (unstructured) doped Si. In Fig. 4.6 we show the results for this thickness dependence for the case mentioned above. Notice that when the layer thickness becomes larger than the gap, which is comparable to the SPP penetration depth, the HTC quickly tends to the result for a semi-infinite structure. This behavior is illustrated in the inset of Fig. 4.6 with the corresponding spectral HTCs. Thus, we can conclude that our periodic structures effectively behave as true metasurfaces as long as their thickness is larger than the gap size.

4.6. Conclusions

In summary, we have proposed a novel mechanism to further enhance NFRHT with the use of Si-metasurfaces, which is based on the broad spectral bandwidth and high tunability of the SPPs that dominate NFRHT in these structures. We have shown that these metamaterials can exhibit room-temperature near-field radiative heat conductances higher than any existent or proposed structure. The fabrication of these metasurfaces is feasible with the state-of-the-art nanolithography [129] and our predictions could be tested with the recent developments in the measurement of NFRHT in parallel extended structures [44].

5 | Radiative heat transfer in the extreme near-field.

5.1. Introduction

As we have discussed in Section 1.5, a number of experimental studies [40, 43–45, 49, 69, 130, 131] have demonstrated super-Planckian thermal transport for gap sizes ranging from hundreds of nanometers to as small as 20 nm. Generally, the results from these measurements were found to be in good agreement with the predictions based on FE for a broad range of materials and geometries.

In spite of the important progress described above, there remains significant disagreement in the literature about RHT in the extreme near-field (gap size < 10 nm). Specifically, measurements [50–52] for two gold (Au)-coated surfaces with gap size in the range of $\sim$ 0.2-10 nm have suggested and extraordinarily large near-field enhancement—over 4 orders of magnitude larger than the predictions from conventional FE [6, 39]. These surprising results question the validity of current theories of heat transfer for these small gaps. Some studies have explored the possibility of reconciling the experimental data with computations, by relaxing the local approximation for the dielectric constant [132]. This approximation is often employed in calculations of NFRHT and is assumed in all the calculations shown in this thesis (see Sec. 1.3). However, such investigations [120, 133] suggest that the inclusion of nonlocal effects leads to relatively modest changes of heat fluxes in the extreme near-field (down to gap sizes fo a few Å). The contribution of phonons to thermal transport across vacuum gaps has also been investigated [134–138].

For example, a recent computational analysis [19] of RHT between plane-parallel surfaces of NaCl, based on microscopic Maxwell's equations, has shown that deviations from the predictions of FE (for example, via acoustic phonon tunneling), occur only for gap sizes <0.5 nm. In particular, at a gap size of $\sim$ 3 Å the phononic contribution to the total thermal conductance was found to be approximately three times higher than its photonic counterpart. This disagreement between experimental results and theoretical predictions is of great concern both from a fundamental point of view, as the physical mechanisms that govern the heat transfer in the extreme near-field are still unclear, and from an applied perspective, because understanding RHT in the extreme near-field (eNFRHT) is critical for the development of a range of novel technologies [16, 61, 139].

In this Chapter [140, 141] we study the eNFRHT from both theoretical and experimental points of view. The experimental group of professors Pramod Reddy and Edgar Meyhofer (University of Michigan) has measured the radiative heat flow down to gap sizes of $\sim$ 2 nm for polar dielectrics (SiO_2 and SiN) and $\sim$ 3 nm for metallic materials (Au). These experiments have been performed using custom-fabricated scanning probes with embedded thermocouples [142, 143] in conjunction with new microdevices capable of periodic temperature modulation. We have carried out state-of-the-art calculations of RHT, performed within the theoretical framework of FE. As we show below, our computations are in excellent agreement with the experimental results, providing unambiguous evidence that confirms the validity of this theory for modelling RHT in gaps as small as a few nanometers [140]. Furthermore, in order to confirm our conclusions, we also explore the RHT in Ångtrom- and nanometer-sized gaps between a Au-coated scanning thermal microscopy probe and a heated planar Au substrate. The experimental results obtained by our colleagues, together with our numerical simulations, suggest that past reports [50–52] of large deviations from the predictions of FE are probably due to surface contamination effects [141].

5.2. Experimental measurement of eNFRHT

Let us now explain the experimental strategy followed by our colleagues in the University of Michigan to measure the radiative heat flow in this regime. Experimental elucidation of RHT across few-nanometer-sized gaps is exceedingly difficult, owing to numerous technical challenges in creating and stably maintaining such gaps while simultaneously

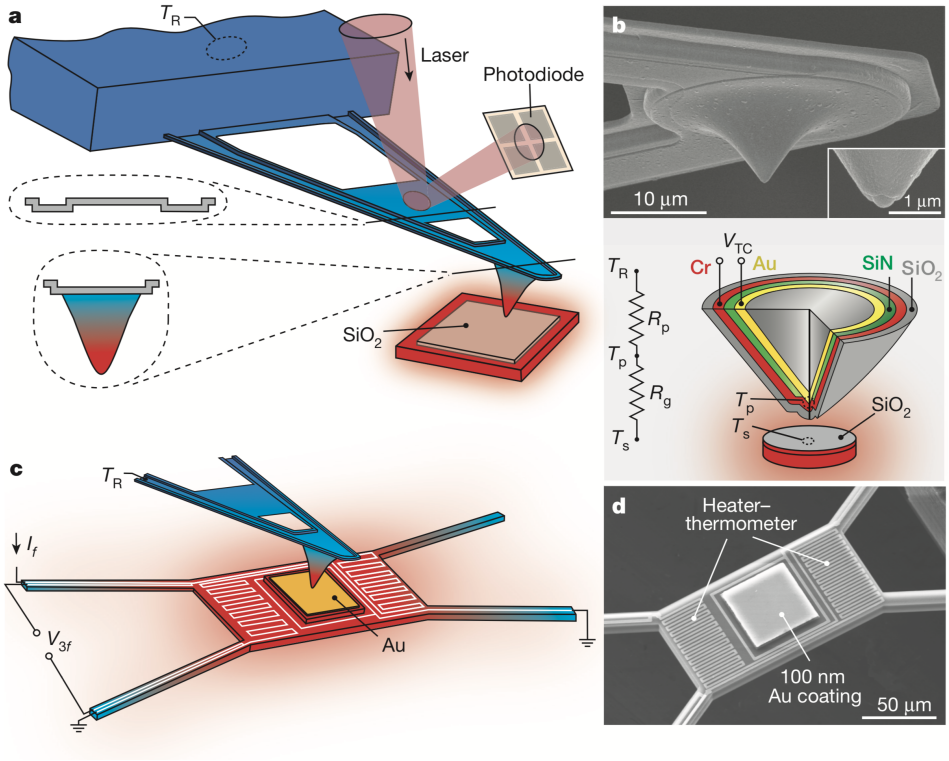

Figure 5.1: (a) Schematic of the experimental setup, in which an SThM probe is in close proximity to a heated substrate (insets show cross-sections of the SThM probe). The scenario for SiO_2 measurements is shown (the coating on the substrate is replaced with SiN and Au in other experiments) (b) SEM image (top) of a SThM probe. The inset shows an SEM image of the hemispherical probe tip, which features an embedded Au-Cr thermocouple from which the thermoelectric voltage is measured. The bottom panel illustrates a schematic cross-section for a SiO_2-coated probe used in SiO_2 measurements. For SiN and Au measurements, the outer SiO_2 coating is appropriately substituted. A resistance network that describes the thermal resistance of the probe (R_P) and the vacuum gap ($R_g = (G_{eNFRHT})^{-1}$), as well as the temperatures of the substrate (T_S), tip (T_P) and reservoir (T_R) is also shown. (c) Schematic showing the measurement scheme used for high-resolution eNFRHT measurements of Au-Au. The amplitude of the supplied sinusoidal electric current is I_f, the sinusoidal temperature oscillations at $2f$ are related to the voltage output V_{3f} (d) SEM image of the suspended microdevice featuring the central region coated with Au and a serpentine Pt heater-thermometer.

measuring minute (pW) heat currents across them. One key innovation used in this work to overcome the technical challenges was to leverage highly sensitive, custom-fabricated probes with embedded Au-Cr thermocouples (Fig. 5.1(a-c)), called scanning thermal microscopy (SThM) probes [142]. The SThM probes were fabricated by deposition of multiple metal and dielectric layers to create a nanoscopically small Au-Cr thermocouple at the very end of the tip. The probes were optimized to have both a high thermal resistance [144] ($R_P \approx 10^6$ KW^{-1}) and stiffness [142] (> 4 Nm^{-1}), and were coated

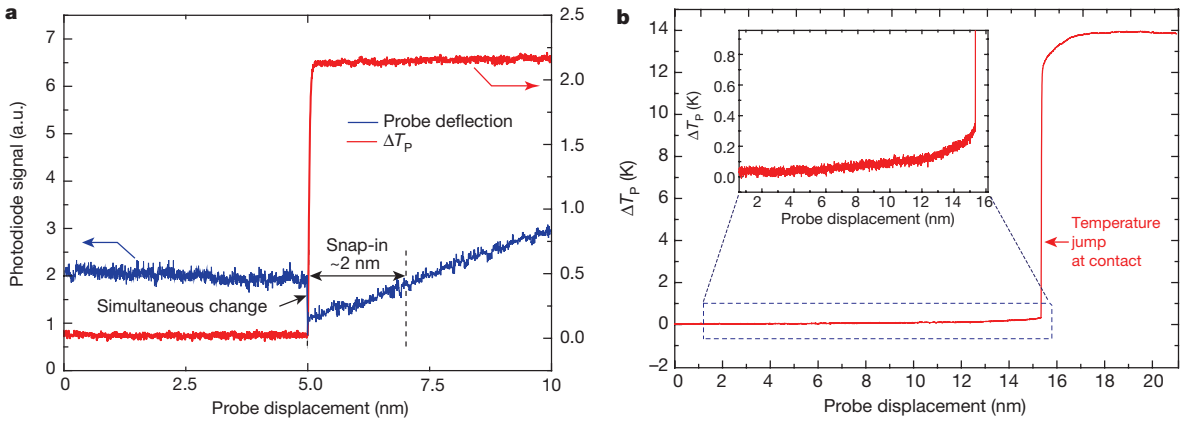

Figure 5.2: (a) Data from an experiment in which a SiO_2-coated probe at about 400 K (heated by the incident laser) is displaced towards a heated SiO_2 substrate at 425 K. The deflection of the scanning probe (blue), reported in arbitrary units (a.u.), and rise in temperature of probe, ΔT_P (red), are shown. The sudden decrease in the deflection signal due to snap-in coincides with a simultaneous increase in the tip temperature due to conduction of heat from the hot substrate to the cold tip, clearly showing that contact can be readily detected by the large temperature jump. The snap-in distance is seen to be $\sim$ 2 nm (b) Measured ΔT_P when an unheated probe (310 K, laser turned off) is displaced towards the substrate. A sudden increase in the tip temperature is seen when the cold tip contacts the substrate. Inset shows the increase in the tip temperature due to eNFRHT.

with a desired dielectric (silica (SiO_2) or silicon nitride (SiN)) or metal (Au) layer. The resulting probes have tip diameters ranging from 350 nm to 900 nm (see Fig. 5.1(b)).

The basic strategy for quantifying NFRHT is to record the tip temperature, via the embedded nanoscale thermocouple, which rises in proportion to the radiative heat flow when the tip is displaced towards a heated substrate. To eliminate conductive and convective heat transfer and to remove any water adsorbed to the surfaces, all measurements were performed in an ultra-high vacuum (UHV) using a modified scanning probe microscope (RHK UHV 7500) housed in an ultra-low-noise facility. In performing the measurements, the substrate is heated to an elevated temperature (T_S = 425 K) while the SThM probe, mounted in the scanner of the scanning probe microscope, is connected to a thermal reservoir maintained at a temperature T_R = 310 K. The spatial separation between the probe and the substrate is reduced at a constant rate of 0.5 nm s^{-1} from a gap size of 50 nm until probe-substrate contact. During this process, the temperature difference between the tip (T_P) and the reservoir (T_R), $\Delta T_P = T_P - T_R$, is monitored via the embedded thermocouple, while the deflection of the cantilever is concurrently measured optically via an incident laser (Fig. 5.1(a)).

A typical deflection trace for a SiO_2-coated tip approaching a SiO_2-coated surface is

shown in Fig. 5.2(a). From the deflection trace it is apparent that the gap size can be controllably reduced to values as small as $\sim$ 2 nm, below which the tip rapidly "snaps" towards the substrate and makes contact. This instability is created by attractive forces between the tip and the substrate that arise owing to Casimir and/or electrostatic forces. Figure 5.2(a) shows the simultaneously measured ΔT_{P}, which represents the sudden increase in temperature that occurs when the tip snaps into the substrate. This rapid increase in tip temperature ($\sim$ 2 K) upon mechanical contact is due to heat conduction, via the solid-solid contact, from the hot substrate (425 K) to the tip of the SThM probe, the temperature of which is $\sim$ 400 K (heating by the incident laser results in an elevated temperature).

The tight temporal correlation between the mechanical snap-in and the temperature jump of the probe makes it possible to identify tip-substrate contact solely on the basis of temperature signals. In Fig. 5.2(b), the recorded tip temperature is shown as a probe approaches a heated substrate with the laser beam turned off. The recorded temperature signals with and without laser tracking are basically identical (Fig. 5.2(a-b)), except that the magnitude of the jump reflects the tip-substrate temperature difference with and without laser excitation. Thus, mechanical contact can be readily detected from the robust temperature jump without laser excitation, thereby avoiding probe heating and laser interference effects. Therefore, all experiments were performed by first estimating the snap-in distance using the optical scheme and subsequently turning the laser off to perform eNFRHT measurements.

To determine the gap (d)-dependent near-field radiative conductance (G_{eNFRHT}), ΔT_{P} was measured and G_{eNFRHT} was directly estimated from $G_{\mathrm{eNFRHT}}(d) = \Delta T_{\mathrm{P}}/[R_{\mathrm{P}}(T_{\mathrm{S}} - T_{\mathrm{R}} - \Delta T_{\mathrm{P}})]$, where R_{P} is the thermal resistance of the probe, which was experimentally independently determined. This technique provides a noise floor of $\sim$ 220 pWK^{-1} in the measurement of the thermal conductance in the eNFRHT. This sensitivity is sufficient to measure the heat flow between polar materials, but it is not good enough to resolve quantitatively the heat flow between Au-coated probes and samples. In order to improve the resolution of the conductance measurements, a new microdevice was employed (see Fig. 5.1(c-d)). This system features a suspended island whose temperature can be readily modulated at f = 18 Hz. Sinusoidal electric currents (9 Hz) supplied to the embedded electrical heater resulted in sinusoidal temperature oscillations at the second harmonic with amplitude ($\Delta T_{\mathrm{S},f=18\,\mathrm{Hz}}$) that was accurately measured using a lock-in technique [69, 70]. To characterize eNFRHT, a Au-coated SThM probe (30 nm Au thickness) was positioned in close proximity to the surface of the microfabricated device, which features a suspended region that is 50 μm $\times$ 50 μm large and was coated with 100 nm of Au.

The amplitude of temperature modulation of the probe ($\Delta T_{\mathrm{P},f=18\,\mathrm{Hz}}$), due to eNFRHT, was measured at various gap sizes in a bandwidth of 0.78 mHz. Given the low noise in this bandwidth it was possible to resolve temperature changes as small as $\sim 20\ \mu$K, which corresponds to a conductance noise floor of $\sim$6 pW K^{-1}, when $\Delta T_{\mathrm{S},f=18\,\mathrm{Hz}}$ is 5 K . The measured $\Delta T_{\mathrm{P},f=18\,\mathrm{Hz}}$ values were used to estimate G_{eNFRHT} via: $G_{\mathrm{eNFRHT}}(d) = \Delta T_{\mathrm{P},f=18\,\mathrm{Hz}}/[R_{\mathrm{P,Au}}(\Delta T_{\mathrm{S},f=18\,\mathrm{Hz}} - \Delta T_{\mathrm{P},f=18\,\mathrm{Hz}})]$, where $R_{\mathrm{P,Au}} = 0.7 \times 10^6$ K W^{-1} is the thermal resistance of the Au-coated probe. The smallest gap size at which measurements could be accomplished is $\sim$ 3 nm and is limited by both snap-in and deflections of the microdevice due to periodic thermal expansion resulting from bimaterial effects.

5.3. Theoretical modelling of eNFRHT

Let us explain in this section how we have analyzed theoretically the radiative heat flow between the SThM probes and the substrates. As explained in previous chapters, modeling of NFRHT requires the frequency-dependent complex dielectric function of materials as a key input. It is well-known that even for nominally identical materials, the dielectric functions may differ due to variations in actual material compositions and microstructures as a function of preparation methods and conditions. The use of different dielectric functions for the same nominal material could lead to significant discrepancies in the calculated near-field heat fluxes, analogous to what has been reported in the case of Casimir force [149] calculations.

While there is relatively little uncertainty in the composition of SiO_2 and Au films, the stoichiometry of SiN films is sensitive to deposition conditions. Hence the frequency-dependent complex dielectric function of the SiN films deposited on the substrates used in our measurements was characterized by the external company Woollam$^{\mathrm{TM}}$. These measurements were performed to accurately account for the fact that the properties (porosity, chemical composition, dielectric function, etc.) of SiN films could vary significantly with different deposition methods and parameters. The dielectric function obtained from these measurements is shown in Fig. 5.3. For Au and SiO_2, the dielectric constants were taken from previous works and they are the ones employed in Chapter 2 (See Fig. 2.3).

5.3.1. Formalism employed for computing RHT

In order to model theoretically the RHT between a thermal scanning tip and a sample, we need a numerical method which can described the RHT between arbitrary geometries

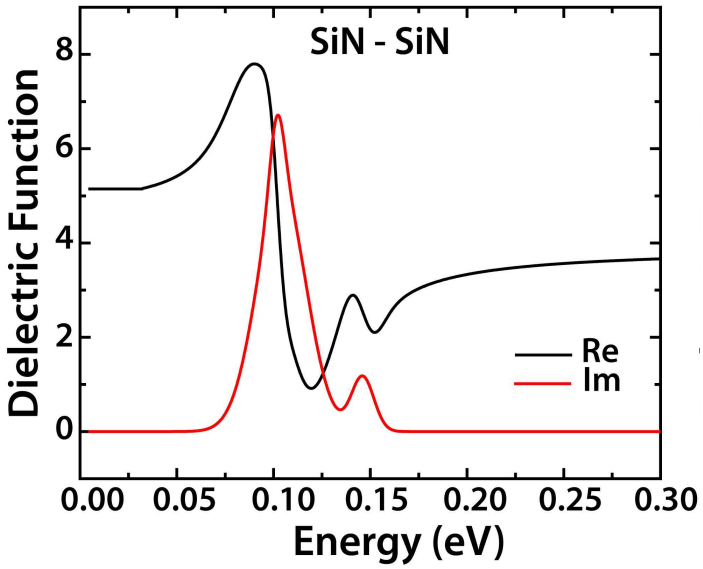

Figure 5.3: Real and imaginary parts of the dielectric function of SiN employed in our simulations as a function of energy.

in the near-field. One option would be to use the scattering matrix approach, which relates the RHT between two arbitrary objects with the scattering properties of each individual object [21–23]. These scattering matrices are generally expressed in terms of spectral basis which are adapted to the geometry of the object. The main advantage of an appropriate basis choice is that it speeds up the convergence of the method, for instance if spherical harmonics are chosen to describe the RHT between two spheres. However, in order to describe the RHT between arbitrary objects these bases do not offer a exponential convergence anymore.

Another option would be to use a direct method such as the FTDT to calculate numerically the heat flow between the SThM and the samples. This method can be applied to arbitrary geometries and requires a very low use of memory. However, due to its statistical nature [35], as we have explained in Sec. 1.4, this method is very noisy and it exhibits convergence issues. We have finally opted to use a BEM implementation of the FSC formulation of RHT which was recently derived by Rodriguez *et al* [39]. We have chosen this method due to several reasons. First of all, it offers numerically exact results within the framework of local FE. Moreover, this method discretizes only the surface of the bodies involved in the RHT problem in order to find the unknown surface currents. This simplifies in principle the complexity of the problem from a computational point of view. We briefly explain this formalism in the next section.

5.3.2. FSC formulation of RHT

In this section we outline the FSC formulation of RHT introduced by Rodriguez *et al* [39]. In general, the total radiative power (P_{rad}) exchanged between two objects a different temperatures can be expressed as:

$$P_{\text{rad}} = \int_0^\infty d\omega \left[\Theta(\omega, T_1) - \Theta(\omega, T_3)\right] \Phi(\omega), \tag{5.1}$$

where $\Theta(\omega, T) = \hbar\omega/[\exp(\hbar\omega/k_{\text{B}}T) - 1]$ and $\Phi(\omega)$ is the heat flux per unit frequency emitted from one body to the other. The problem is how to solve for $\Phi(\omega)$ to find the total power exchanged between two objects. In this method, one of the main ideas is to employ the principle of equivalence of electromagnetism [145–147], which states that the EM fields inside body i due to interactions with other bodies (this includes both the fields generated by sources in other bodies and the fields scattered off the interface of body i) can be said to be generated by some fictitious electric and magnetic currents ξ^i which exist on the boundary of body i. Using this principle, it is possible to express the spectral heat flux $\Phi(\omega)$ as:

$$\Phi(\omega) = \frac{1}{2\pi}\text{Tr}\left[\left(\text{sym}G^1\right) W^{21,*} \left(\text{sym}G^2\right) W^{21}\right], \tag{5.2}$$

where G^i is the self-interaction Green's function for surface currents within body i, $\text{sym}O = (O + O^*)/2$ corresponds to the Hermitian component of an operator and W^{ij} represents the interaction between body i and j and relates the incident fields at the surface of body j to the surface currents at body i. More precisely, W^{ij} is the off-diagonal block of the inverse of the total Green's function of the system. The components of the Green's function connecting surface currents within object i are given by the following inner product:

$$G^i_{\alpha\beta} = \left\langle f_\alpha, \Gamma^i \star f_\beta \right\rangle, \tag{5.3}$$

where $\langle g, h\rangle = \int g^* h$ and Γ^i is the well-known dyadic Green's tensor for a homogeneous medium with the dielectric properties of body i. The functions f_α and f_β are two components of the basis chosen in which the surface currents $\xi^i(x)$ can be expressed. More explicitly, $\xi^i(x) = \sum_\alpha \xi_\alpha f_\alpha(x)$. The basis function f_α is normally, in BEM, a piecewise-polynomial "element" function which is defined in meshed pieces at the surface of every object.

The compact expression for the RHT found using this formalism (Eq. 5.2) is very

convenient computationally as it does not need to consider any fields or sources in the volumes or separate between incoming and outgoing EM waves. This formulation of the heat transfer problem has been implemented in the open-source SCUFF-EM software package [82, 83], which we have used to perform all the simulations shown in this chapter. This code makes use of the BEM to discretize the surfaces of the bodies into triangular elements or panels and the surface currents in each element are described by piecewise low-degree polynomials. In particular, SCUFF-EM employs the so-called RWG [148] basis of vector-valued polynomial functions defined on a mesh of triangular panels. This basis is suitable to deal with arbitrary geometries and yields results that converge with increasing resolution (smaller triangles). Further technical details can be found in Refs. [38, 39, 82].

5.3.3. Tip-substrate geometries and convergence of simulations

In order to provide a quantitative description of our experiments, we consider tip-substrate geometries like the one shown in Fig. 5.4. The tip has a conical shape and ends in a spherical cap. The angle of the cone and the radius of the spherical cap have been obtained in every case from the SEM images of the experimental probes. The experimental tip radii were 450 nm for Au, 225 nm for SiO_2, and 175 nm for SiN. The height of the tip was chosen to be 3 μm for Au and 1.3 μm for SiO_2 and SiN. The substrate was modeled by a finite disk of radius 4 μm for Au and 2 μm for SiO_2 and SiN, and thickness 2 μm for Au and 1 μm for SiO_2 and SiN. The dimensions of both the tip and the substrate were carefully chosen so that there are no finite-size effects. To maintain high fidelity to the experimental conditions, we also accounted for the small roughness of our probes by including random Gaussian-correlated noise in the tip profile (Fig. 5.6(c-d)). More precisely, the maximum protrusion height on the tip and the correlation length between protrusions were chosen to be 10 nm and 17 nm, respectively, on the basis of the surface characteristics observed in the SEM images. We investigated the effect of surface roughness by computing G_{eNFRHT} for every material from 15 different tip-substrate ensembles with roughness profiles generated as described earlier Let us remark that in our theoretical approach we assume that the RHT can be well described in terms of dielectric functions that only depend on frequency or energy (local approximation).

A key issue in our numerical simulations is the choice of the mesh of triangular panels for the RWG-BEM approach. To obtain accurate results, the size of the triangular

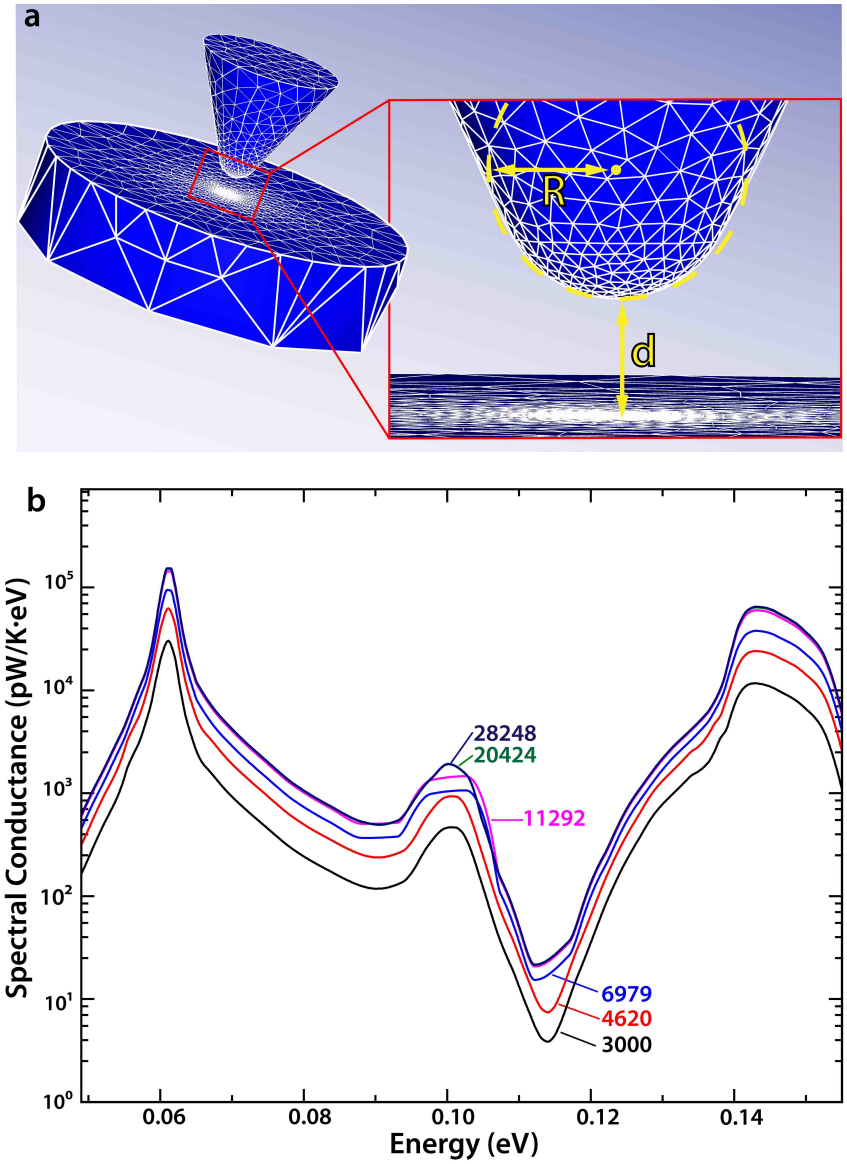

Figure 5.4: (a) Example of the tip-substrate geometries employed in our numerical simulations. The tip has a conical shape and ends in a spherical cap, while the substrate is modelled as a thick disk. The solid white lines correspond to the mesh of triangular panels used in the BEM calculations. The right inset shows a blow-up of the tip apex region. Here, R is the tip radius, and d is the gap size (or distance between the tip and the substrate). (b) Example of a convergence test of the numerical results upon refinement of the mesh of triangular panels for a SiO_2 tip-substrate geometry with a tip radius of 200 nm and a gap size of 4 nm. In this case, the tip was assumed to not have any roughness. The different curves correspond to different numbers of basis functions employed in the BEM calculations as indicated in the figure. Notice that the two curves for the largest numbers of basis functions lie on top of each other illustrating the excellent convergence of our results. The reservoir temperatures in this calculation were assumed to be 310 K for the tip and 425 K for the substrate.

panels must be comparable to the (local) gap size or smaller. This was accomplished by employing a non-uniform grid that was finer at both the tip apex and in the centre of the plate (Fig. 5.4). The convergence of our results was checked, for every combination of materials and every tip-substrate distance, by progressively refining the mesh, *i.e.*, by reducing the size of the triangles and increasing the number of basis functions in the BEM calculations. In Fig. 5.4 (b) we show an example of our convergence tests for the case of a SiO_2 tip-substrate geometry. It can be seen that the results progressively converge to a single solution (or spectral conductance) as the number of basis functions is increased. For calculations that included the presence of tip roughness, we have defined a smaller spherical cap around the tip apex where the triangular panels were chosen to have an equal size. The same was done in the substrate for a circular region around its centre. Again, the size of these triangles was checked to be sufficiently small to obtain converged results. We note that the convergence of the results with the size and the number of triangles critically depends on the material of choice. For metals (Au) the convergence is faster than for polar dielectrics (SiN, SiO_2) due to the different physical mechanism that dominates the NFRHT. In metals, NFRHT is governed by total internally reflected waves and does not depend critically on the distance between the tip and the plate. In contrast, NFRHT in polar dielectrics is dominated by SPhPs, EM waves whose dispersion relation is very sensitive to the distance between the two objects. Thus, the simulations for polar dielectrics require much more refined grids with considerably higher number of basis functions, *i.e.*, with much smaller triangular panels.

5.4. Results

5.4.1. Comparison of the numerical simulations with the experimental measurements

Once we have described the modeling of the eNFRHT in the tip-plate system, let us compare the experimental results with the numerical computations. Fig. 5.5 shows the measured extreme near-field conductances for both dielectric and metal surfaces. The red solid lines correspond to the average experimental conductance from 15 independent measurements, while the light red band represents the standard deviation. The blue solid line shows the average of the computed radiative conductance for 15 different tips with stochastically chosen roughness profiles, as we have explained before. Fig. 5.5(a-b) show the radiative conductance for SiO_2 and SiN surfaces, respectively. It can be seen

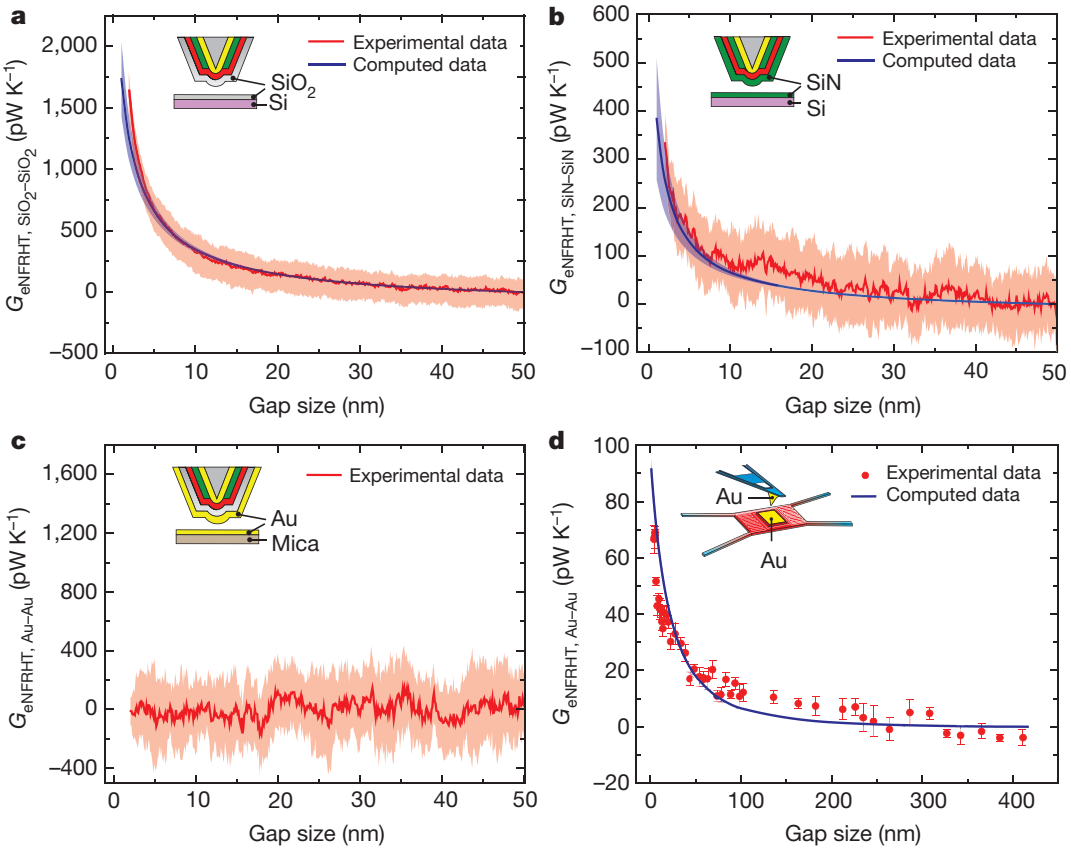

Figure 5.5: (a) Measured and computed near-field radiative conductance between a SiO_2-coated probe (310 K) and a SiO_2 substrate at 425 K. The red solid line represents experimental data while blue line corresponds to the numerical simulations. (b-c) Same as (a), but for SiN-SiN and Au-Au, respectively. The tip diameter is 350 nm for the SiN-coated tip. Computed results are not included for Au-Au. (d) Near-field conductance from experiments with a Au-coated probe and a suspended microdevice (see inset) The red dots represents the measurements while the blue line corresponds to the computed conductance (tip diameter is 900 nm).

that G_{eNFRHT} increases monotonically until the probe snaps into contact (gap size at snap-in is 2 nm for both SiO_2 and SiN measurements). Furthermore, it can be seen that the eNFRHT is larger between the SiO_2-coated tip and sample. The agreement between the experimental results and the computed values is very good for both SiO_2 and SiN devices.

This remarkable agreement between eNFRHT measurements and computational predictions raises important questions with regards to recent experiments [50] investigating eNFRHT between Au surfaces, which suggested strong disagreements ($\sim$ 4 orders of magnitude) between predictions of FE and the results of experiments. One may wonder if the good agreement reported above is unique to eNFRHT between polar dielectric

materials. To answer this question unambiguously, we show the measured conductance between Au-coated probes and substrates in Fig. 5.5(c). It can be seen that the measured G_{eNFRHT} with decreasing gap size remains comparable to the noise floor of $\sim$ 220 pW K^{-1} for Au-coated probes at an applied temperature differential of $\sim$ 115 K and is much smaller than that observed for polar dielectrics. These measurements set an upper bound of $\sim$ 250 pW K^{-1} for G_{eNFRHT} in our Au-Au experiments. This result is particularly surprising because previous studies that used probes with smaller diameters [50] reported conductances >40 nW K^{-1}, which are at least two orders of magnitude larger than conductances measured by us and predicted by theory. Figure 5.5(d) shows the near-field conductance between a Au-coated tip and a suspended microdevice whose temperature can be modulated. The red dots correspond to the average from 10 different experiments (temperature periodically modulated at 18 Hz) and the error bars represent the standard deviation. Again, the blue solid line represents the computed conductance. The Au-Au G_{eNFRHT} (Fig. 5.5(d)) is indeed much smaller than that obtained in the SiO_2-SiO_2 (Fig. 5.5(a)) and SiN-SiN (Fig. 5.5(b)) case. In contrast to previous experiments [50], our measured G_{eNFRHT} for Au-Au surfaces is in excellent agreement with the predictions of FE.

5.4.2. Physical mechanisms of RHT enhancement

To elucidate the underlying physical mechanism and explain the differences in eNFRHT between different material combinations, we compute the spectral conductance (heat conductance per unit of energy) for several gap sizes as shown in Fig. 5.6(a-c) for SiO_2, SiN and Au, respectively. In Fig. 5.6(a), one can see that the dominant contributions to the spectral conductance of SiO_2 come from two narrow energy ranges centered around $\sim$ 0.06 eV and $\sim$ 0.14 eV, which correspond to the energies of the transverse optical phonons of SiO_2. This strongly suggests that for SiO_2, eNFRHT is dominated by SPhPs, as we previously found in Chapter 2 when we studied the NFRHT between a sphere and a thin film at larger gaps. In turn, this explains the marked decrease in heat transfer as the gap size increases, which is a consequence of the rapid decrease in the number of available surface EM modes for radiation to tunnel across the vacuum gap.

We show in Figure. 5.6(b) the spectral heat conductance for a SiN tip-substrate geometry for three different gap sizes. As one can see, the major contribution to heat transfer comes from an energy region around 0.12 eV, which corresponds to the energy of the transverse optical phonons in this material. As in the case of SiO_2, the coupling of optical phonons to EM waves gives rise to SPhPs that dominate the NFRHT. For this

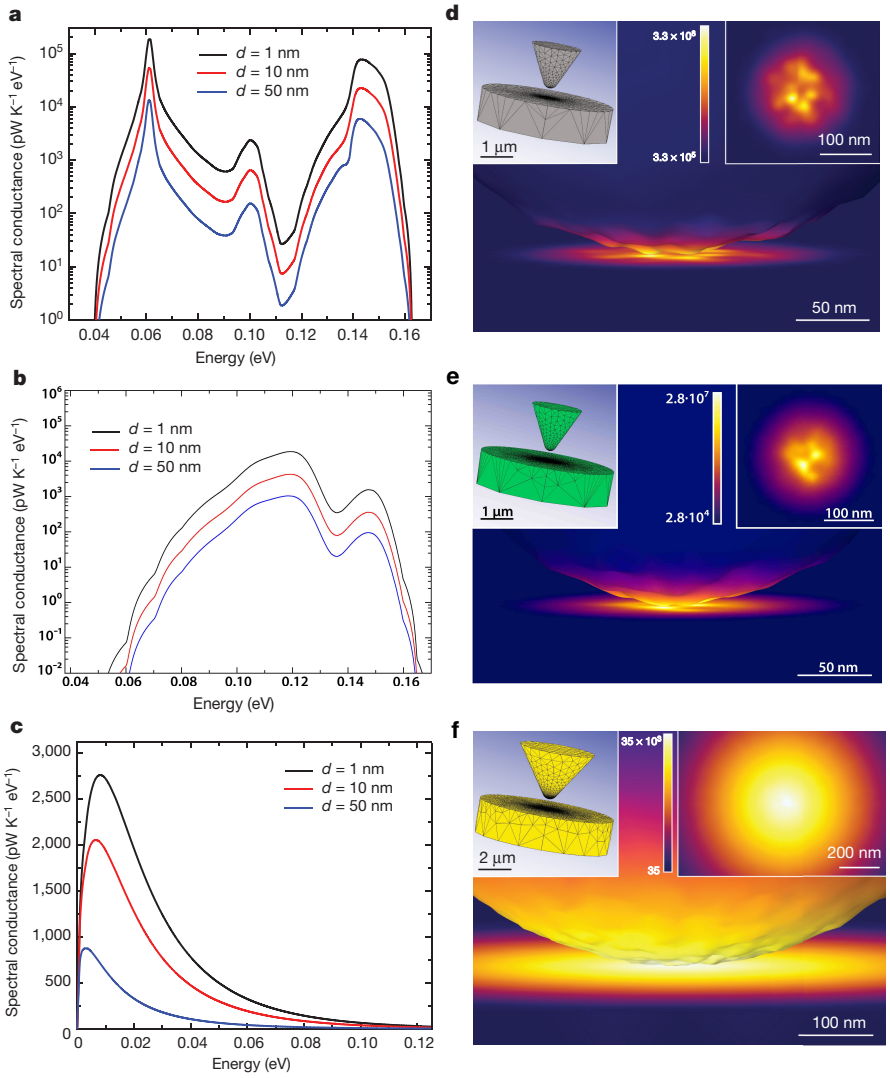

Figure 5.6: (a) Spectral conductance as a function of energy for a SiO_2 tip-substrate geometry for three different gap sizes. The tip diameter is 450 nm, and the reservoir temperatures are 310 K for the tip and 425 K for the substrate. Notice the logarithmic scale in the vertical axis. (b) Same as (a), but for SiN. In this case, the tip radius is 175 nm. (c) Same as (a,b), but for Au. Now the tip radius is 450 nm, and the tip and substrate temperatures are 300 K and 301 K, respectively. (d) Surface-contour plot showing the spatial distribution of the Poynting-flux pattern on the surface of the bodies for the SiO_2 tip-substrate geometry corresponding to that in a with a gap of 1 nm. The color scale is in units of W (K eV m^2)$^{-1}$ and the plot was computed at an energy of 61 meV, which corresponds to the maximum of the spectral conductance. The right inset shows the corresponding surface heat flux on the substrate; the left inset displays the whole tip-substrate geometry simulated, including the mesh used in the calculations. (e-f) Same as d, but for SiN and Au respectively. The surface-contour plots have been computed at an energy of 0.12 eV (SiN) and 9 meV (Au), which correspond to the maximum of the spectral conductance in every case.

reason, the NFRHT rapidly decays with the gap size, very much like in the SiO_2 case. An important conceptual difference between SiO_2 and SiN is that for SiN the real part of the dielectric constant never becomes negative, see Fig. 5.3. This means in practice that, even in the energy region where the optical phonons exist, SiN behaves as a lossy dielectric material. However, one can show that it is still possible to have surface EM waves in this material with properties that are similar to those of SPhPs. The surface waves in the interface between a dielectric like vacuum and a lossy dielectric like SiN are often referred to in the literature as Zenneck waves [150].

In contrast with the previous materials, eNFRHT for Au exhibits a rather broad spectral conductance that decays more slowly with gap size (Fig. 5.6(c)). This slow decay is reminiscent of the situation encountered for metals in the plate-plate geometry which was analyzed in Sec 1.3.2. As we have explained in that section, NFRHT is dominated in the Au-Au case by frustrated internal reflection modes, that is, by modes that are evanescent in the vacuum gap but are propagating inside the Au tip and substrate whose contribution saturates for gaps below the skin depth [120], which for Au is around 25 nm. This naturally explains the weaker dependence of eNFRHT on gap size observed in our Au-Au measurements. The fundamental difference in eNFRHT between dielectrics and metals is also apparent from the computed Poynting-flux patterns on the surfaces (Fig. 5.6(d-f)), which show that eNFRHT in the SiO_2 and in the SiN case is much more concentrated in the tip apex than it is in the Au case. This difference reflects the fact that in a polar dielectric, such as SiO_2 and SiN, eNFRHT has a very strong distance dependence due to the excitation of SPhPs with a penetration depth comparable to the gap size, as we derived in Sec. 2.4.2 of Chapter 2 (see Eq. 2.6). Given these differences between metals and dielectrics, it is not surprising that Au-Au eNFRHT is relatively insensitive to small surface roughness (see Sec. 5.4.3). For this reason, the large differences between our results for Au and those of previous work [50, 51], which disagree with the predictions of FE, cannot be attributed to differences in the surface roughness. Our computational results, when compared with our experimental data, provide unambiguous evidence that FE accurately describes eNFRHT.

5.4.3. Role of the tip roughness in the calculations of eNFRHT

As explained in the previous sections, in our simulations we have taken into account the roughness present in our experimental probes. For completeness, we illustrate here

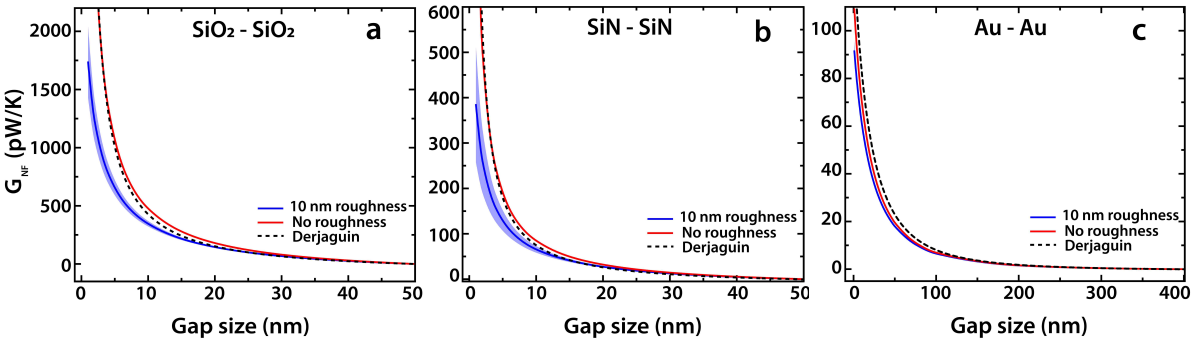

Figure 5.7: (a) Computed near-field radiative conductance as a function of the gap size for a SiO_2 tip-sample geometry. The tip radius is 225 nm, and the reservoir temperatures are 310 K for the tip and 425 K for the substrate. The solid blue line corresponds to the average result obtained for 15 different tips featuring a roughness of 10 nm, while the blue shaded region represents the corresponding standard deviation. The red solid line corresponds to the result for an ideal tip without any roughness. The black dashed line corresponds to the result obtained using the proximity approximation, see text. (b) The same as in panel (a), but for a SiN tip-sample geometry. In this case the tip radius is 175 nm, and the reservoir temperatures are 310 K for the tip and 425 K for the substrate. (c) The same as in panel (a), but for a Au tip-sample geometry. In this case the tip radius is 450 nm, and the reservoir temperatures are 300 K for the tip and 301 K for the substrate.

the impact of the tip roughness. Towards this goal, in Fig. 5.7 we compare the results with and without roughness for the three materials investigated in this work (SiO_2, SiN and Au).From this comparison, one can draw two main conclusions: (i) the presence of roughness tends to reduce the radiative heat conductance and (ii) the roughness has a larger impact on the conductance of polar dielectrics. The first property is a simple consequence of the fact that the gap size is defined as the shortest tip-sample distance (following our AFM experiments). Thus, the presence of roughness effectively leads to an increase in the average tip-sample distance, as compared with the ideal tip with no roughness. This fact leads naturally to a reduction of the RHT at a given gap size. Notice also that the impact of the roughness is obviously larger for the smallest gaps, where it can lead to a reduction of the conductance on the order of a factor of two, while it is negligible when the gap size becomes larger than the natural scale of the roughness (10 nm in our case). Furthermore, the larger impact of the roughness in the case of SiO_2 and SiN, as compared with Au, is again due to the fact that in polar dielectrics the RHT is much more localized in the tip apex due to the excitation of SPhPs with very short penetration depths.

To conclude, it is interesting to compare the results for the ideal tips (with no roughness) with those obtained using the so-called proximity or Derjaguin approximation (see

Sec. 2.3.2), which is frequently used to estimate the RHT in complex geometries. For this purpose, we assume that the tips can be modelled by spheres of the same radius and compute the NFRHT between a sphere and an infinite plate. The results obtained with this approximation for the three materials considered in this work are shown in Fig. 5.7 (black dashed lines). It can be seen that this simple approximation provides a very good estimate of the gap-size dependent NFRHT in the case of the ideal tips. Therefore, it is clear that for ideal tips the proximity approximation can be used as a good first approximation to estimate the RHT.

5.5. Role of contaminants in eNFRHT measurements

In this Chapter, we have shown so far that the RHT between two objets separated by single-nanometer distances can be described using the formalism of FE [140]. However, as we have explained in the Introduction, other measurements [50–52] have suggested an extraordinary large heat flux in this regime that is more than four orders of magnitude larger than the values predicted by conventional theory of FE. In these works, the gap size is quantified by measuring the tuneling current between the tip and the sample. Conversely, in the experiments performed by our colleagues from University of Michigan, the gap size was measured using compliant cantilevers that enabled direct detection of mechanical contact ensuring that the measurements were performed only under conditions where a vacuum gap was present between the surfaces that were being studied. In order to resolve this controversy, the experimental group of Professor Pramod Reddy and Edgar Meyhofer has performed further experiments [141] on eNFRHT between an Au-coated tip and a sample measuring the gap size from the tunneling current, as in previous works [50–52]. Further details on the experimental details can be found in Ref. [141].

5.5.1. Experimental results

In a first set of experiments, a probe, thoroughly cleaned in acetone to remove potential contaminants and residue from fabrication and handling, was loaded into a UHV scanning probe microscope along with a Au surface to study NFRHT. In this experiment the sample temperature was chosen to be 343 K, while the probe was held at a lower temperature of 303 K, thus establishing a temperature differential (ΔT) of 40 K. The

measurements were performed at various locations on the Au sample to evaluate any possible surface inhomogeneity effects. Figure 5.8 shows the measured radiative thermal conductance (pink) and tunneling current (blue) from 15 independent measurements as the gap size between the probe and the sample is reduced at a constant speed (~ 0.1 nm s^{-1}). The solid lines represent the mean value of the data, whereas the transparent color represents the standard deviation (s.d.). It can be seen from the data that the observed thermal conductance begins to increase monotonically as the gap size is reduced below ~ 2.5 nm and reaches a value as large as ~ 30 nWK^{-1} at the smallest gap size. This behavior is similar to what was reported in recent papers [51, 52]. As a comparison, in Ref. [51], the measured heat flux begins to monotonically increase below gaps of ~ 4.5 nm, whereas in Ref. [52] for a probe similar to that used in Ref. [51], the monotonic increase with declining gap size starts at ~ 6 nm, and the thermal conductance at the smallest gap is reported to be ~ 3 nWK^{-1}—a value smaller than that observed by us, possibly because of the smaller tip size of the probes employed in Ref. [52] (our probe's diameter is approximately five times larger). This experimentally observed conductance (~ 30 nWK^{-1}) for our solvent-cleaned probes is almost three orders of magnitude larger than that predicted by calculations performed using FE (see Fig. 5.9, calculation details explained later).

A possible explanation for the large thermal conductance observed in our first experiments with solvent-cleaned probes is the presence of contaminants that may bridge the tip and the sample before the Au on the tip contacts the Au atoms on the sample, thus providing a pathway for heat transfer via conduction. One may hypothesize that such contamination arises from imperfect removal of any molecules bound to the SThM probe during fabrication, contamination during storage and handling, or due to recontamination of the tip due to diffusion of molecules present elsewhere on the sample or the tip. Given the small size of the SThM tip (diameter of $\sim$ 300nm), a direct characterization of its surface is challenging. Therefore, as a first test of our hypothesis that the sample is contaminated we analyzed the tunneling current curves following a procedure reported elsewhere [151, 152]. Specifically, we fitted the tunneling current data to a tunneling barrier model to obtain the apparent barrier height (ϕ_{ap}, in eV) from

$$\phi_{ap} = \left(\frac{1}{1.025} \frac{\mathrm{d}(\ln(I_t))}{\mathrm{d}z} \right)^2 \tag{5.4}$$

where z is the gap size in Å and I_t is the tunneling current. From the slope of the tunneling current shown in Fig. 5.8(a) we obtained a value for ϕ_{ap} of 1.1 eV. This low barrier height is in contrast to the large ($\sim 4.7 \pm 1$ eV) barrier heights [151] expected

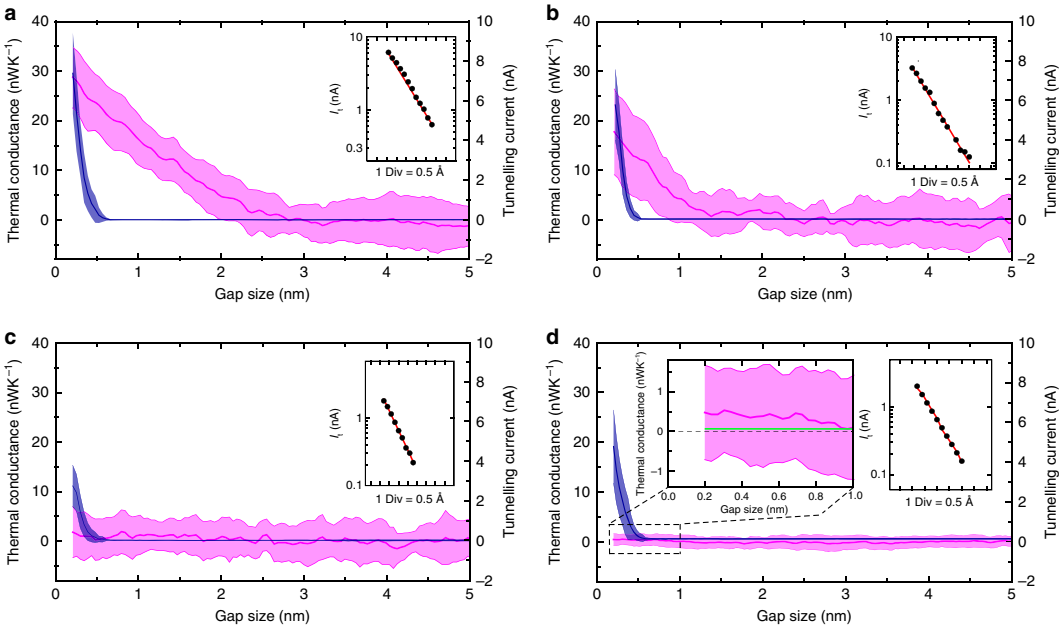

Figure 5.8: Measured gap size-dependent thermal conductance and tunneling current. Each thermal conductance (pink) and tunneling current (blue) curve is averaged over 15 repeated measurements. The shaded region represents the s.d. The first three panels show representative experimental results from (a) organic solvent-cleaned, (b) oxygen plasma-cleaned and (c) repeated oxygen plasma-cleaned probes. The gold sample is heated while the probe is maintained at a lower temperature to create a temperature difference $\Delta T = 40$ K. (d) The measurement results obtained in experiments where a large temperature differential (ΔT) of 130 K was applied. The thermal conductance data in the subnanometer region is shown on an expanded scale in the inset to facilitate visualization. The green line in the inset panel corresponds to the near-field radiative thermal conductance calculated from FE. Further, the measured tunneling currents versus displacement are shown in insets for each of the plots and were used in the analysis of the apparent tunnelling barrier height ϕ_{ap}. The estimated values of ϕ_{ap} are 1.1, 1.6, 1.7 and 1.9 eV for (a-d), respectively.

for ultraclean Au surfaces and is indeed consistent with the presence of surface contamination [151, 152]. We note that careful analysis of tunneling current curves presented in previous studies [50–52] also suggested low barrier heights (<1 eV), indicating the possibility of contamination.

In order to explore the feasibility of reducing or eliminating surface contamination effects, oxygen plasma-based techniques were employed [153] for cleaning the probe. Subsequently, the conductance measurements were repeated following an approach identical to that used in obtaining the data in Fig. 5.8(a). The data obtained from this experiment are shown in Fig. 5.8(b), in which we can clearly see that the thermal conductance is reduced by a factor of 2 and the thermal conductance starts to monotonically increase

from a smaller gap size of $\sim$ 1 nm. Since this measurement employed the same probe, sample and experimental procedures as that in Fig. 5.8(a), we conclude that surface contaminants are the most probable reason for the observed spurious thermal conductances. This conclusion is further supported by our analysis of the tunneling current data (obtained from the cleaned sample and tip), which yielded a ϕ_{ap} of 1.6 eV, a value significantly larger than that obtained for the data in Fig. 5.8(a). Upon reducing the effect of potential surface contaminants, the oxygen plasma-cleaning process was repeated (three times for both the probe and the sample) to evaluate whether the cleanliness can be further improved. Data obtained from experiments performed after these additional cleaning steps are shown in Fig. 5.8(c). It can be seen that there is no discernible increase in thermal conductance until the probe contacts the sample. Further, the apparent barrier height was further increased to $\sim$ 1.7 eV, reflecting the increased cleanliness of the surfaces. The data in Fig. 5.8(c) (corresponding to the solid line) show that the thermal conductance is less than 2.5 nWK^{-1} for subnanometer gaps. To get a more refined estimate of this conductance, the temperature differential was increased to 130 K by increasing the sample temperature to 445 K (the probe temperature increases to 315 K). Such increased temperature differentials resulted in an enhanced signal-to-noise ratio as the noise remains (largely) unchanged, whereas the signal increases, to first order, proportionally to the applied temperature differential. This larger temperature differential leads to deviations from the linear response regime; however, the expected deviations in the thermal conductance are small (see inset of Fig. 5.9(b)). Further, application of this larger temperature differential enables a more direct comparison with past experiments [50–52] where similarly large temperature differentials were applied. Data obtained from these experiments (Fig. 5.8(d)) show a significantly reduced noise floor ($\sim$ 900 pWK^{-1}) and the mean from 15 different experiments (solid pink line in the inset) shows that the maximum possible thermal conductance at the smallest gaps ($\sim$ 2 Å) is $\sim$ 0.5 nWK^{-1} –a value much smaller than that reported in previous works [50–52].

5.5.2. Numerical simulations

In order to simulate the experiments as accurately as possible, we considered tip-substrate geometries very similar to the ones considered for the previous experiments, as it can be observed Fig. 5.9(a). Again, we followed the SEM images of the thermal probes and modelled the gold tip with an irregular conical shape that ends in a hemispherical cap of radius 150 nm, while the substrate was modeled by a thick disk whose dimensions have been carefully chosen to avoid any finite-size effects. The roughness from the tips,

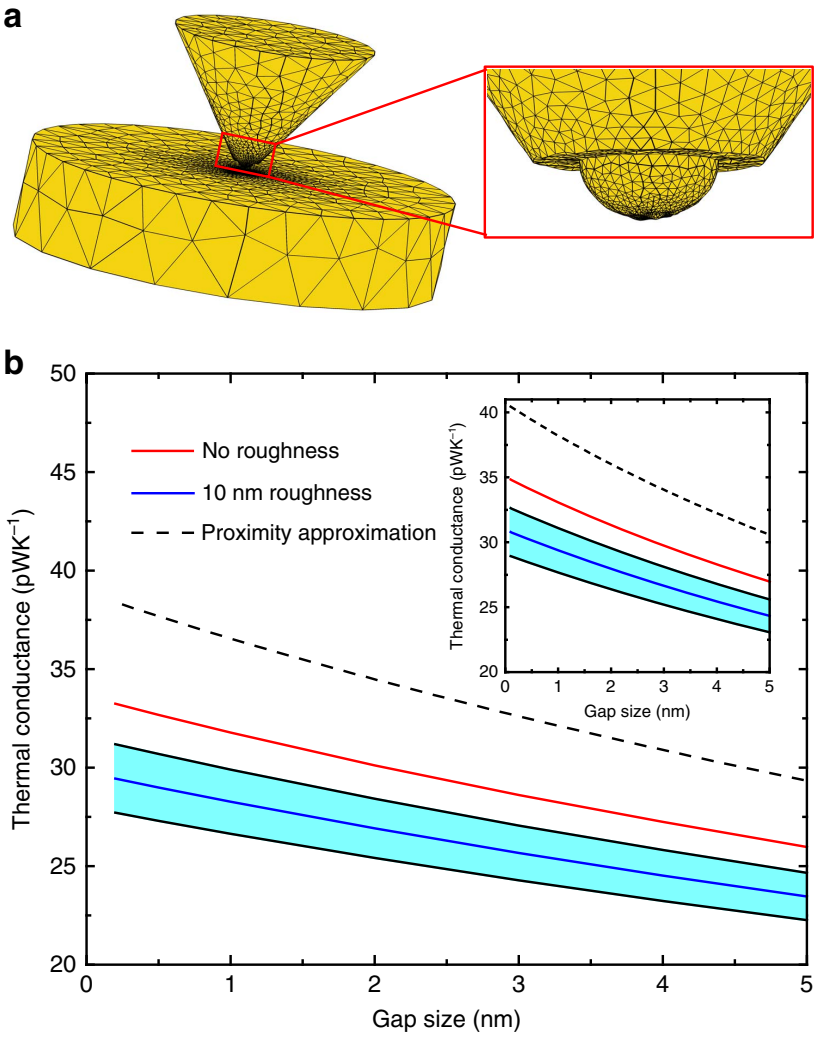

Figure 5.9: (a) Tip-substrate geometry employed in our numerical simulations. Following the SEM images of our thermal probes, the tip was modeled as an irregular cone that ends in a hemisphere, while the substrate was modeled as a thick disk. The height of the cone was chosen to be 3 μm and the radius of its base was 1.9 μm. The radius of the disk was 4 μm and its thickness was 2 μm. The solid black lines depict the triangular mesh employed in the BEM calculations. The right inset shows a blow-up of the tip apex region. (b) The computed total radiative thermal conductance as a function of the gap size between the Au tip and substrate. The red solid line corresponds to the ideal tip (no roughness) and the blue line to the average obtained for 15 different tips with stochastically chosen roughness profiles, while the shaded region indicate the s.d. The black dashed line is the computed thermal conductance from the proximity approximation for the case of no roughness. The tip diameter in these calculations is 300 nm, while the temperature of the probe and substrate were chosen to be 303 and 343 K, respectively. Inset, similar to the main panel except that the probe and substrate temperatures are 315 and 445 K, respectively.

which has a similar profile than in the previous case (see Fig. 5.6), has also been taken into account by simulating an ensemble of 15 tips with different roughness profiles. We emphasize that the only input information in our simulations, apart from the geometry, is the frequency-dependent dielectric function of gold that we obtained from published work [75].

The results of the simulations for the total radiative thermal conductance between the gold tip and the gold substrate are shown in Fig. 5.9(b) for gap sizes from 0.1 to 5 nm. This figure displays the results for an ideal tip (no roughness) and for 15 tips featuring roughness (both mean value and s.d.). It can be seen that the tip roughness has no major impact on the thermal conductance. More importantly, the thermal conductance for the smallest gap size is of the order of 30 pWK^{-1}, which is $\sim$ 30 times smaller than the noise floor ($\sim$ 900 pWK^{-1}) in our large bias measurements (see Fig. 5.8(d)). The results obtained by using the proximity approximation (see Sec. 2.3.2) are also shown in Fig. 5.9(b) and are found to show similar trends (that is, increase in conductance with reducing gap size) as our exact simulations but fail to accurately reproduce the simulation results. These calculations support our conclusion that the large signals observed in our experiments before the cleaning procedure cannot be explained in terms of RHT. For completeness, we note that the slow decay of the thermal conductance with gap size (Fig. 5.9(b)) is the characteristic of metals. This is due to the fact that RHT is dominated by evanescent (in the vacuum gap) TE modes resulting from total internal reflection, the contribution of which saturates at single-nanometre gaps [120]. In addition, the role of nonlocal effects in the dielectric function of gold has been studied [120] in the context of RHT and has been shown to be very small for the gap sizes explored in our work.

5.6. Conclusions

In this chapter [140, 141] we have analyzed the RHT between a scanning tip and a substrate from both a experimental and a theoretical point of view. The measurements presented here provide the first experimental evidence for extremely large enhancements of RHT in the extreme near-field between both dielectric and metal surfaces surfaces. Our theoretical modeling of the experimental setups, which takes into account the exact shape of the objects together with their nanometric roughness, shows an excellent agreement (deviations $< 15\%$) with the experimental results. Let us remark that our numerical simulations do not consider any free parameter and their only input is the local dielectric constant of the different materials. The results presented in this chapter establish the

funtamental validity of FE in modelling NFRHT down to gaps as small as 2-3 nanometers, for both metals and dielectrics.

An interesting question pertains to the gap size at which FE fails to describe RHT. First, we note that, while some deviations from computational predictions can be seen in the inset of Fig. 5.8(d) for subnanometer-sized gaps, these deviations are within the noise floor of our measurement technique, making it hard to draw any robust conclusions about the failure of current theories. We note that for small gap sizes electrons can also make significant contributions to heat transfer. For Au electrodes, the electronic contribution to thermal conductance ($G_{\text{th,electronic}}$) can be readily computed using the Wiedemann-Franz law that relates $G_{\text{th,electronic}}$ to the electrical conductance G_{e}, by $G_{\text{th,electronic}} = L_0 T G_{\text{e}}$, where $L_0 = 2.44 \times 10^{-8}$ WΩK^{-2} is the Lorentz number and T is the absolute temperature. Since the measured electrical conductance, corresponding to the smallest gap sizes in the experiments, is $\sim 0.1\ G_0$ we estimate $G_{\text{th,electronic}}$ to be ~ 60 pWK^{-1}, which is also below our noise floor.

Finally, our results suggest that past reports [50–52] of large deviations from the predictions of FE are probably because of surface contamination effects. We also demonstrate, from measurements of apparent tunneling barrier heights, that such deviations can be systematically attenuated by carefully cleaning the surfaces as indicated by an increase in the apparent barrier height. In contrast to previous studies [50–52], which observed both conductances as large as 3 nWK^{-1} (three to four orders larger than the predictions of FE) and conductance enhancements beginning at gap sizes as large as 4-5 nm, our results (Fig. 5.8(d)) suggest that deviations, if any, are in the subnanometer regime and are much smaller in magnitude (~ 0.5 nWK^{-1}, based on the observed mean value). These deviations in subnanometer-sized gaps could potentially result from monolayer-level contaminations that may still be present on our surfaces and cannot be detected from our probes. Further, this work highlights the need for the development of probes, that can accurately resolve the small heat fluxes expected for Au surfaces at subnanometer gaps while independently quantifying the gap size, surface roughness and interaction forces with the substrate. Such approaches are crucial for drawing careful conclusions about extreme near-field radiation.

6 | Super-Planckian far-field radiative heat transfer

6.1. Introduction

In the previous Chapters, we have analyzed RHT in different situations when two objects are separated by distances smaller than λ_{Th}. In this regime, Plank's law is no longer valid and the Planckian limit for blackbodies can be surpassed by orders of magnitude due to the contribution of evanescent waves. Another limitation of Planck's law is related to the description of RHT between objects with dimensions smaller than λ_{Th}. In this case, this law is expected to fail even in the far-field regime, where separations are larger than λ_{Th}.

The goal of this Chapter [159] is to demonstrate that Planck's law can fail dramatically when describing the far-field RHT (FFRHT) between finite objects and, more importantly, that the Planckian limit can be greatly overcome in the far-field regime. For this purpose, we have combined state-of-the-art numerical simulations within FE with analytical insight provided by a general relation derived here between the FFRHT between finite objects and their directional absorption efficiencies. Guided by this relation, we show that the FFRHT between highly anisotropic systems can greatly overcome the Planckian limit when some of their dimensions are smaller than λ_{Th}. This exploits that due to its inherent directionality, super-Planckian RHT can occur even if the involved objects are not super-Planckian emitters. In particular, we illustrate this phenomenon with the analysis of the RHT between micron-sized suspended pads made of polar dielectrics (SiN and SiO_2). To be precise, we show that when the thickness of these pads is

much smaller than λ_{Th}, the far-field radiative thermal conductance at room temperature can be several orders of magnitude higher than that between blackbodies of the same dimensions. Let us stress that this type of dielectric pads are widely used in the context of thermal transport measurements of nanowires and low-dimensional systems [70, 154–158], and they thus constitute an available technology with which our predictions can be quantitatively tested.

The rest of the Chapter is organized as follows. In Section 6.2 we derive several analytical formulas relating the FFRHT between finite objects and the directional absorption efficiencies. Section 6.3 is devoted to illustrate why it is so difficult to overcome the Planckian limit in the far-field regime. For this purpose, we present in this section results for the FFRHT between optically isotropic systems like spheres and cubes. In Section 6.4, we demonstrate the possibility to greatly overcome the Planckian limit in the far field by exploring the RHT between parallelepipeds made of polar dielectrics (SiN and SiO_2). Then, in Section 6.5 we illustrate the super-Planckian FFRHT in suspended pads made of dielectric materials, where we show in particular that our predictions can be quantitatively tested with existent technology. We conclude the Chapter in Section 6.6 with a brief summary of the main conclusions of our work.

6.2. Relation between FFRHT and absorption efficiencies

In principle, the theory of FE provides a general framework to describe the RHT between arbitrary objects both in the near-field and in the far-field regime [6]. So, in this sense, one may be tempted to think that the search for super-Planckian FFRHT should be straightforward. However, in practice, one encounters several problems. First of all, there is an infinite number of possibilities in terms of materials, shapes, and sizes of the bodies. More importantly, until very recently there were no numerical methods capable of describing the RHT between objects of arbitrary size and shape, and this actually continues to be a very important practical problem that is often insurmountable. For this reason, it would be highly desirable to have, for instance, a relation between the FFRHT of objects of arbitrary size and shape and their radiation absorption properties, something that has been widely studied over the years [64]. The goal of this section is to present such a relation, which will turn out to be extremely useful in our quest for super-Planckian FFRHT.

In what follows, we derive a relation between the FFRHT between two objects and their directional absorption efficiencies. This result was obtained with the help of the thermal discrete dipole approximation (TDDA) put forward in Ref. [160], see also Refs. [161, 162]. This approach allows us to compute the RHT between finite objects of arbitrary size and shape within the framework of FE. The full derivation is actually quite cumbersome. For this reason, we shall show in some detail how this result can be obtained in the limit of very small objects and then, we shall indicate how it can be extended to objects of arbitrary size. So, let us first consider the RHT between two small objects that can be approximated by (electrical) dipolar particles. In this case, the power exchanged by them in the form of thermal radiation is given by Eq. (35) in Ref. [160]. That equation tells us that the net power exchanged by two identical dipoles at temperatures T_1 and T_2 and located at positions $\mathbf{r}_1$ and $\mathbf{r}_2$ such that their separation $d = |\mathbf{r}_2 - \mathbf{r}_1|$ is much larger than the thermal wavelength is given by

$$P = 8\pi^2 \int_0^\infty k_0^2 \,\mathrm{Tr}\left\{\hat{G}\hat{\chi}\hat{G}^\dagger\hat{\chi}\right\}\left[I_{\mathrm{BB}}(\omega, T_1) - I_{\mathrm{BB}}(\omega, T_2)\right] d\omega. \tag{6.1}$$

Here, ω is the radiation frequency, $k_0 = \omega/c$, c being the speed of light in vacuum, and $I_{\mathrm{BB}}(\omega, T)$ is the Planck distribution function given by

$$I_{\mathrm{BB}}(\omega, T) = \frac{\omega^2}{4\pi^3 c^2} \frac{\hbar\omega}{\exp(\hbar\omega/k_{\mathrm{B}}T) - 1}, \tag{6.2}$$

where $\hbar$ is Planck's constant, k_{B} is Boltzmann's constant and T is the temperature. On the other hand, the (3×3) matrix $\hat{\chi}$ is given by [160]

$$\hat{\chi} = \frac{1}{2i}\left(\hat{\alpha} - \hat{\alpha}^\dagger\right) - \frac{k_0^3}{6\pi}\hat{\alpha}^\dagger\hat{\alpha}, \tag{6.3}$$

where $\hat{\alpha}$ is the polarizability tensor of the particles. Finally, $\hat{G}$ is the dyadic Green tensor connecting the two dipoles that in the far-field limit is given by $\hat{G} = e^{ik_0 d}[1 - \hat{\mathbf{r}} \otimes \hat{\mathbf{r}}/(4\pi d)]$, where $\hat{\mathbf{r}} = (\mathbf{r_2} - \mathbf{r_1})/d$ and $\otimes$ denotes the exterior product. The result of Eq. (6.1) is valid for dipolar particles of arbitrary shape and made of materials with an arbitrary dielectric tensor. Let us focus now on the case of optically isotropic materials and particles with a scalar polarizability tensor, like spheres or cubes, such that $\hat{\chi} = \chi\hat{1}$. In this case, one can show that the absorption cross section, which in this case is independent of the direction and of the light polarization, is given by $\sigma_{\mathrm{abs}}(\omega) = k_0\chi(\omega)$ [160]. Thus, it is easy to show

that Eq. (6.1) reduces to

$$P = \pi A F_{12} \int_0^\infty Q^2(\omega) \left[I_{\mathrm{BB}}(\omega, T_1) - I_{\mathrm{BB}}(\omega, T_2) \right] d\omega, \tag{6.4}$$

where A is the area of the bodies, F_{12} is a geometrical view factor, and $Q(\omega)$ is the absorption efficiency defined as $Q(\omega) = \sigma_{\mathrm{abs}}(\omega)/\sigma_{\mathrm{geo}}$, where σ_{geo} is the geometrical or physical cross section. For isotropic particles, the absorption cross section is given by [160]

$$\sigma_{\mathrm{abs}}(\omega) = \frac{k_0 \mathrm{Im}\{\alpha_0(\omega)\}}{\left| 1 - i k_0^3 \alpha_0(\omega)/(6\pi) \right|^2}, \tag{6.5}$$

where $\alpha_0(\omega) = 3V[\epsilon(\omega) - 1]/[\epsilon(\omega) + 2]$ is the quasistatic polarizability, $\epsilon(\omega)$ being the frequency-dependent dielectric function of the material, and V is the volume of the particle. In the case of spherical particles we have that

$$A = 4\pi R^2, \; F_{12} = \frac{R^2}{4d^2}, \; \sigma_{\mathrm{geo}} = \pi R^2, \; V = \frac{4}{3}\pi R^3, \tag{6.6}$$

where R is the particle radius. In the case of cubic particles, we have

$$A = L^2, \; F_{12} = \frac{L^2}{\pi d^2}, \; \sigma_{\mathrm{geo}} = L^2, \; V = L^3, \tag{6.7}$$

where L is the cube side. Let us recall that for black bodies $Q(\omega) = 1$ for all frequencies and Eq. (6.4) reduces to the Stefan-Boltzmann law [1]: $P_{\mathrm{BB}} = \sigma A F_{12}(T_1^4 - T_2^4)$, where $\sigma = 5.67 \times 10^{-8}$ W/(m^{2}K^4).

As we shall show later in Section 6.4, we need a certain degree of anisotropy in the shape of the bodies to achieve the super-Planckian FFRHT. For this reason, we now consider the simplest case of anisotropic dipolar particles, namely rectangular parallelepipeds of sides L_x, L_y and L_z. Here, we assume that the z-axis is oriented along the line joining the two dipolar particles. In this case, the polarizability tensor adopts the diagonal form $\hat{\alpha} = \mathrm{diag}(\alpha_x, \alpha_y, \alpha_z)$, which from Eq. (6.3) implies that $\hat{\chi} = \mathrm{diag}(\chi_x, \chi_y, \chi_z)$ with $\chi_j = \mathrm{Im}\{\alpha_j\} - (k_0^3/6\pi)|\alpha_j|^2$ and $j = x, y, z$. Thus, using Eq. (6.1), it is straightforward to show that the net power exchanged by these two dipolar particles is given by

$$P = \pi A F_{12} \int_0^\infty \frac{1}{2}(Q_x^2(\omega) + Q_y^2(\omega)) \left[I_{\mathrm{BB}}(\omega, T_1) - I_{\mathrm{BB}}(\omega, T_2) \right] d\omega, \tag{6.8}$$

where $A = L_x L_y$, $F_{12} = L_x L_y/(\pi d^2)$, and $Q_{x,y}(\omega)$ are the absorption efficiencies for a plane wave impinging in the parallelepiped along the z-direction and with linear po-

larization along the x and y directions, respectively. These efficiencies are defined as $Q_j(\omega) = \sigma_{\mathrm{abs},j}(\omega)/\sigma_{\mathrm{geo}}$ $(j = x, y)$, where $\sigma_{\mathrm{geo}} = L_x L_y$ and $\sigma_{\mathrm{abs},j} = k_0 \chi_j$. Finally, the different components of the polarizability tensor are given by [160]

$$\alpha_j(\omega) = \frac{V}{\frac{1}{\epsilon(\omega)-1} + \Lambda_j - iV\frac{k_0^3}{6\pi}}, \tag{6.9}$$

with $V = L_x L_y L_z$ and

$$\Lambda_j = \frac{2}{\pi} \arctan\left(\frac{V}{L_j^2\sqrt{L_x^2 + L_y^2 + L_z^2}}\right). \tag{6.10}$$

Again, the black-body limit is obtained by assuming that $Q_{x,y}(\omega) = 1$ for all frequencies.

Equations (6.4) and (6.8) can be generalized to the case of objects of arbitrary size employing the full TDDA formulation detailed in section IV of [160]. In particular, the starting point is Eq. (56) in that reference, together with the far-field approximation of Eq. (58). The results of Eqs. (6.4), for isotropic objects and (6.8), for parallelepipeds, are recovered when the gap is much larger than both the thermal wavelength and the characteristic dimensions of the objects. In the generalized formulas, the absorption efficiencies correspond to plane waves with normal incidence (along the line joining the two objects) and with a given polarization. It is important to stress that the corresponding absorption cross sections are no longer given by the analytical formulas above for dipolar particles, but they have to be calculated numerically, something that we have done with either the discrete dipole approximation (DDA) method [160] or with COMSOL MULTIPHYSICS. The corresponding view factors for finite objects are taken from Ref. [1], except for spheres, which are taken from Ref. [163] (see Sec. 6.2.1). In the following sections we shall test those formulas for bodies of arbitrary size against numerically exact calculations carried out with the TDDA method [160] and SCUFF-EM [39, 82]. In all cases, our numerical results confirm the validity of these formulas relating the FFRHT with the absorption efficiencies.

To conclude this section, let us say that Eq. (6.4) has the expected form from the expression of thermal emission of a sphere [6, 64, 66], where $Q(\omega)$ is independent of the direction and the polarization. However, to our knowledge, this result has not been reported in the literature for bodies of arbitrary size and its generalization to anisotropic bodies, for instance Eq. (6.8), is by no means trivial. As we shall see in the following section, these expressions provide very useful guidelines for the search of super-Planckian FFRHT.

6.2.1. View factors

In most of the cases discussed in this Chapter, we have presented the results of the far-field radiative thermal conductance normalized by the corresponding black-body results. Those results are given by the Stefan-Boltzmann law: $G_{\mathrm{BB}} = 4\sigma A F_{12} T^3$, where σ is the Stefan-Boltzmann constant, A is the area of the bodies (assumed to be identical), T is the absolute temperature and F_{12} is the so-called view factor [1]. For completeness, we present in this section the expressions for the different view factors used in this work. Moreover, let us recall that these view factors also appear in the formulas for the FFRHT, see e.g. Eqs. (6.4) and (6.8).

The view factor between two aligned parallel rectangles of sides L_x and L_y and separated by a gap d is given by [1]

$$F_{12}^{\mathrm{rectangles}} = \frac{2}{\pi \tilde{L}_x \tilde{L}_y}\left\{ \ln\left[\frac{(1+\tilde{L}_x^2)(1+\tilde{L}_y^2)}{1+\tilde{L}_x^2+\tilde{L}_y^2}\right]^{1/2} + \tilde{L}_x(1+\tilde{L}_y^2)^{1/2}\arctan\left[\frac{\tilde{L}_x}{(1+\tilde{L}_y^2)^{1/2}}\right] + \tilde{L}_y(1+\tilde{L}_x^2)^{1/2}\arctan\left[\frac{\tilde{L}_y}{(1+\tilde{L}_x^2)^{1/2}}\right] - \tilde{L}_x\arctan(\tilde{L}_x) - \tilde{L}_y\arctan(\tilde{L}_y)\right\}, \quad (6.11)$$

where $\tilde{L}_x = L_x/d$ and $\tilde{L}_y = L_y/d$. This is the view factor that has been used for the calculation of the RHT between parallelepipeds, including the pads and cubes. In the two-spheres case, there is no analytical expression for the view factor. However, when the gap d is larger than the sphere radius R, it can be approximated by [163]

$$F_{12}^{\mathrm{spheres}} = \frac{1}{2}\left\{1 - \left[1 - \left(\frac{R}{d+2R}\right)^2\right]^{1/2}\right\}. \quad (6.12)$$

This expression yields a value that differs less than 1% from the exact numerical result in most of the cases explored in this work. For all other cases, we have considered the exact numeric view factor. To be precise, the value of the view factor in those cases is: $F_{12}^{\mathrm{spheres}}(d = 100\ \mu\mathrm{m},\ R = 50\ \mu\mathrm{m}) = F_{12}^{\mathrm{spheres}}(d = 20\ \mu\mathrm{m},\ R = 10\ \mu\mathrm{m}) = 0.0161$, $F_{12}^{\mathrm{spheres}}(d = 20\ \mu\mathrm{m},\ R = 20\ \mu\mathrm{m}) = 0.0294$, and $F_{12}^{\mathrm{spheres}}(d = 20\ \mu\mathrm{m},\ R = 50\ \mu\mathrm{m}) = 0.0485$.

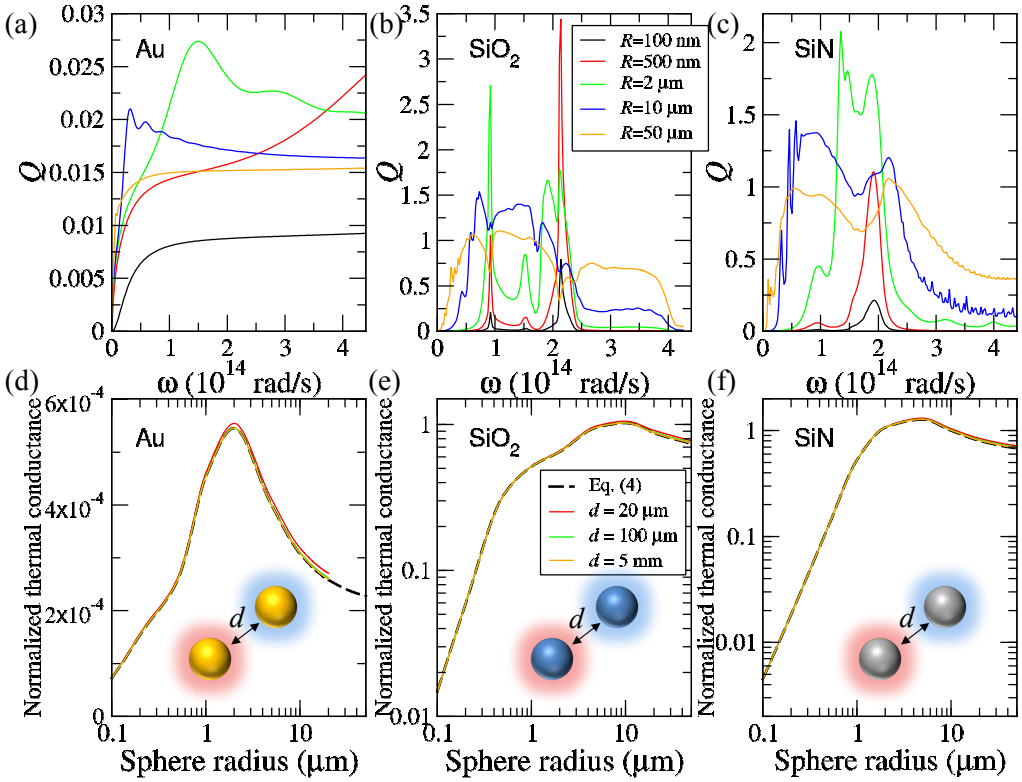

Figure 6.1: (a-c) Absorption efficiency of a sphere of Au (a), SiO_2 (b), and SiN (c) as a function of frequency for different values of the sphere radius R, see legend in panel (b). (d-f) Room-temperature radiative heat conductance, normalized by the blackbody results, for two identical spheres separated by a distance d as a function of the sphere radius. The spheres are made of Au (d), SiO_2 (e), and SiN (f). The solid lines are the exact calculations for different gaps, see legend in panel (e), while the black dashed line is the result obtained with Eq. (6.4) and the results of panels (a-c).

6.3. Why is it so difficult to overcome the Planckian limit in the far field?

As explained in the introduction, super-Planckian FFRHT has never been reported. Thus, we find instructive to devote this section to explain why this is a non-trivial phenomenon. Equations (6.4) and (6.8) derived in the previous section seem to provide a straightforward recipe to overcome the Planckian limit in the far-field regime. Since the absorption efficiency of a finite object can be larger than unity [64], those equations suggest that super-Planckian FFRHT might be possible if we find the right combination of material and object shape that leads to resonant absorption close to the maximum of

Planck's distribution at a given temperature. This appealing idea is, however, not easy to realize in practice, as we proceed to illustrate. For simplicity, let us first study the FFRHT between two identical spheres of arbitrary radius. In Fig. 6.1(a-c) we show the results for the absorption efficiency and the FFRHT for spheres made of a metal (Au) and two polar dielectrics (SiO_2 and SiN) with radii ranging from 100 nm to 50 μm. The absorption efficiencies, which in this case are independent of the angle of incidence and polarization, were obtained with analytical Mie theory [64], while the dielectric functions of these three materials were taken from tabulated values [74, 75, 77]. The RHT is characterized here in terms of the room-temperature linear heat conductance, which is normalized in Fig. 6.1(d-f) by the corresponding blackbody result: $G_{\mathrm{BB}} = 4\sigma A F_{12} T^3$. In this figure we present the results computed with Eq. (6.4) and the absorption efficiencies as well as numerical results for three gaps in the far-field regime (20 μm, 100 μm, and 5 mm) that were obtained with the code SCUFF-EM [39, 82].

The results of Fig. 6.1(d-f) show that the FFRHT between spheres does not overcome the Planckian limit and only becomes comparable to the blackbody result in the case of polar dielectrics with a sphere radius of the order of λ_{Th}. For small radii, smaller than the corresponding skin depth, the normalized conductance increases linearly with the radius, i.e., the conductance is proportional to the sphere volume because the whole particle contributes to the RHT. In the opposite limit, when the radius is much larger than λ_{Th} the conductance tends to the result for two parallel plates. It is worth stressing that the numerical results obtained for various gaps nicely confirm the validity of Eq. (6.4) for spheres of arbitrary size and material. In particular, this equation provides very accurate results even for a gap of 20 μm, which is on the edge of the far-field regime at room temperature.

To further illustrate the difficulty to beat the Planckian limit with optically isotropic objects, we now consider the case of cubes, focusing on polar dielectrics since metals have a very small emissivity (cf. Fig. 6.1). In Fig. 6.2 we present the results for the absorption efficiency and the FFRHT between cubes made of SiO_2 and SiN with sides L ranging from 100 nm to 20 μm. The absorption efficiencies, which again refer to a plane wave with normal incidence and the linear polarization indicated in the inset of Fig. 6.2(b), were obtained numerically with the DDA method [160]. Again, the RHT is characterized here in terms of the room-temperature linear thermal conductance normalized by the corresponding blackbody result. We present in this figure the results computed with Eq. (6.4), which in this case is equivalent to Eq. (6.8), and the absorption efficiencies as well as numerical results for two gaps in the far-field regime (20 μm and 500 μm) that were obtained with the TDDA approach [160]. As one can see, the results of Fig. 6.2

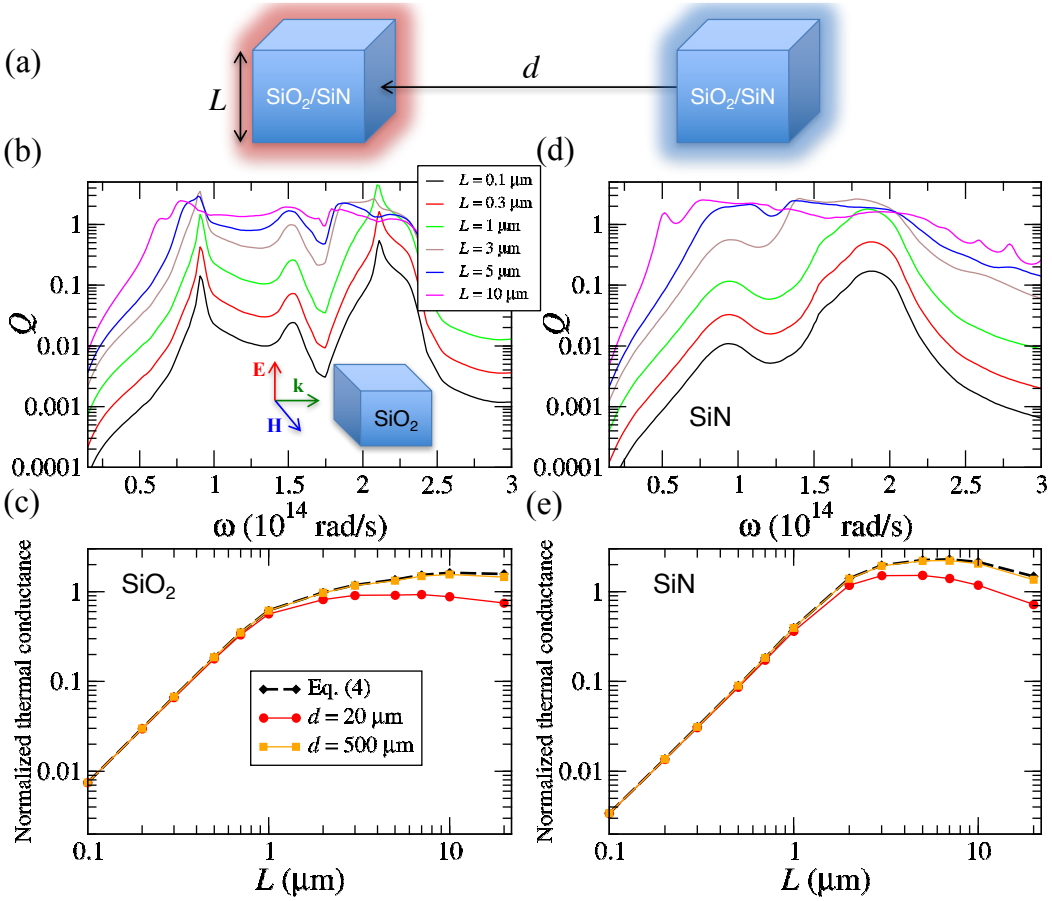

Figure 6.2: (a) Two identical cubes made of SiO_2 or SiN with side L and separated by a gap d. (b) Absorption efficiency as a function of the frequency for a linearly polarized plane wave impinging with normal incidence in a SiO_2 cube of side L, as indicated in the legend. The inset describes the polarization in terms of the direction of the electric field **E**, the magnetic field **H**, and the wave vector **k**. (c) Room-temperature radiative heat conductance, normalized by the blackbody results, for the system shown in panel (a) as a function of the cube side L. The solid lines correspond to the exact calculations for two gaps (see legend), while the black dashed line corresponds to the results obtained by combining Eq. (6.4) with the results of panel (b). (d-e) The same as in panels (b) and (c), but for SiN.

show that, in general, the FFRHT between cubes does not overcome the Planckian limit, similar to the case of spheres (Fig. 6.1). Only when the size of the cubes becomes of the order of $\lambda_{\rm Th}$ ($\approx$10 μm) the RHT becomes comparable to the blackbody result, and even a bit larger. Notice that the fact that in Fig. 6.2(c,e) the thermal conductance is lower for the smallest gap of 20 μm is simply due to the fact that the results are normalized by the blackbody ones. We emphasize that in the far-field regime, the thermal conductance decays monotonically with the distance between the objects. It is also worth stressing that once again the numerical results obtained for the largest gap (500 μm)

nicely coincide with those based on Eq. (6.4), confirming its validity.

The results presented in this section for spheres and cubes show that although the emissivity of an object can be larger than 1 for some frequencies, this does not imply super-Planckian FFRHT. From Eqs. (6.4) and (6.8) it is obvious that to overcome the Planckian limit one needs thermal emitters with directional emissivities larger than 1 over a broad range of frequencies around the maximum of Planck's distribution, something that is highly non-trivial to achieve. In the following section, we shall show how one can get around this problem.

6.4. Overcoming the Planckian limit

In the previous section we have seen the difficulty to overcome the Planckian limit in the far-field regime with optically isotropic bodies and we have also discussed with the help of Eq. (6.4) why this is so. Fortunately, the same equation also provides a possible strategy to overcome the Planckian limit, which consists in increasing as much as possible the corresponding directional absorption efficiency. This can be done by enhancing the absorption cross section, while maintaining the geometrical one. We shall illustrate this idea in this section by studying the RHT between two parallelepipeds.

Figure 6.3 shows the FFRHT between two parallelepipeds of SiO_2 and SiN as well as the relevant emissivities. It is worth stressing that the RHT in the extreme far-field regime is still given by Eq. (6.4) where the emissivity is given by the absorption efficiency related to the direction joining the parallelepipeds. In this case, we start with a cube of side 0.5 μm and we form an elongated rectangular parallelepiped by progressively changing one of the dimensions, L_z, while keeping constant the other two, L_x and L_y, see Fig. 6.3(a). Thus, we keep the geometrical cross section constant, while the normal-incidence absorption efficiency is expected to increase linearly with L_z as long as it is small compared to the propagation length of the radiation inside the structure, which is hundreds of microns (see next section). This can be understood as follows. The efficiency Q for normal incidence is roughly proportional to $[1-\exp(-2\alpha L_z)]$, where α is the attenuation constant of the parallelepiped guided modes, i.e., $1/2\alpha$ is the corresponding propagation length. Thus, in the limit $\alpha L_z \ll 1$, $Q \propto L_z$. Our calculations of these emissivities, which were performed with the TDDA approach [160], indeed confirm that they grow linearly with L_z in the regime explored here where $\alpha L_z \ll 1$, and that they can become much larger than 1 in a broad frequency range, see Fig. 6.3(b,d). As shown in Fig. 6.3(c,e), this fact leads to a far-field conductance that grows as L_z^2 and it reaches val-

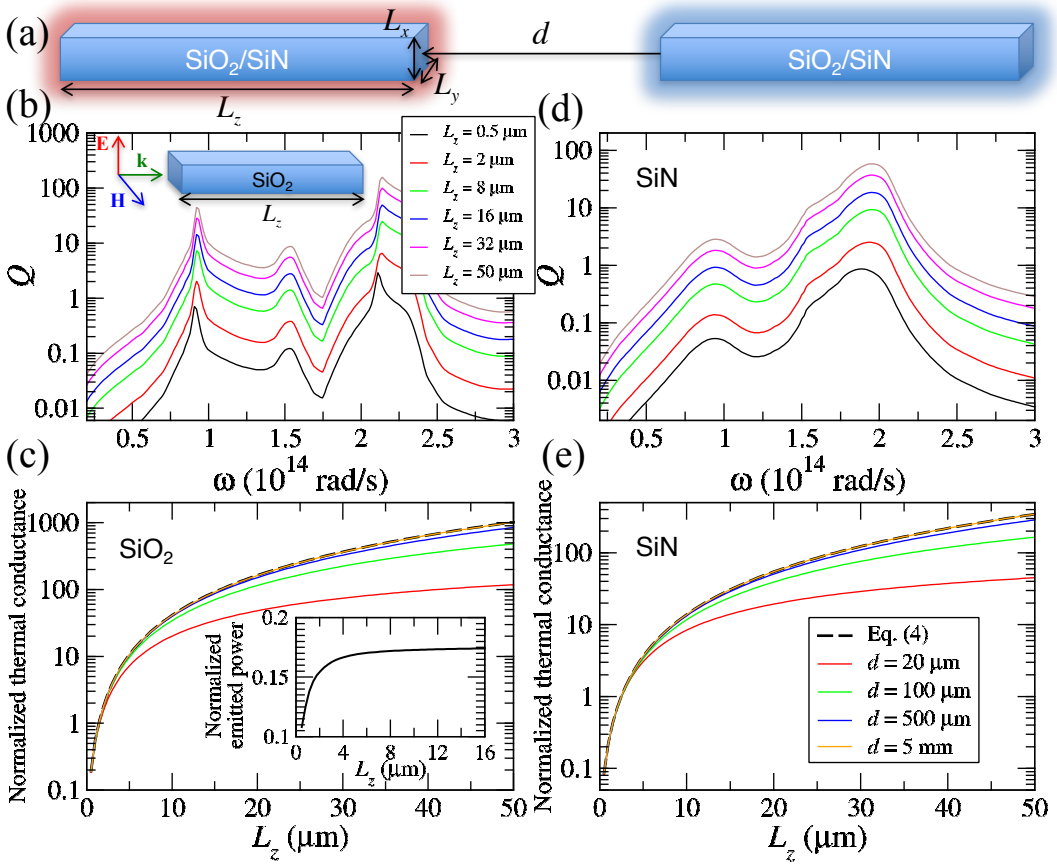

Figure 6.3: (a) Two identical parallelepipeds of SiO_2 or SiN with dimensions $L_x = L_y = 0.5$ μm and varying L_z and separated by a gap d. (b) Absorption efficiency as a function of frequency for a linearly polarized plane wave impinging with normal incidence, see inset, in a SiO_2 parallelepiped with $L_x = L_y = 0.5$ μm and various values of L_z, see legend. (c) Room-temperature radiative heat conductance, normalized by the blackbody results, for the system of panel (a) as a function of L_z. The solid lines are the exact calculations for different gaps, see legend in panel (e), while the black dashed line is the result obtained with Eq. (6.4). The inset shows the total power emitted, normalized by the blackbody result, by a single SiO_2 parallelepiped with $L_x = L_y = 0.5$ μm and varying L_z at 300 K. (d-e) The same as in panels (b) and (c), but for SiN.

ues that overcome the Planckian limit by several orders of magnitude when L_z becomes of the order of 50 μm. Notice that the numerical results for several gaps in the far-field regime coincide with those obtained via Eq. (6.4) in the limit of sufficiently large gaps. In any case, the Planckian limit is greatly overcome for all gaps in the far-field regime. Let us also stress that these parallelepipeds are not super-Planckian thermal emitters, i.e., they emit less thermal radiation than a corresponding blackbody. This is shown in the inset of Fig. 6.3(c) where we display the total power emitted, normalized by the

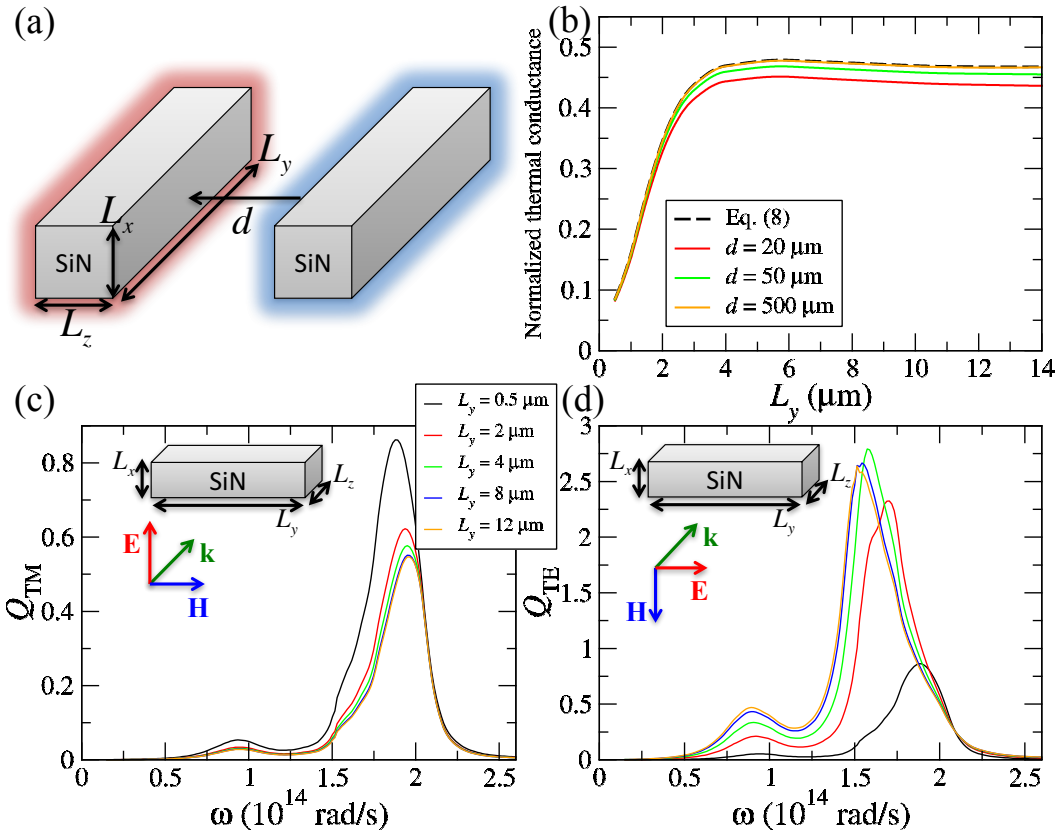

Figure 6.4: (a) SiN parallelepipeds with dimensions $L_x \times L_y \times L_z$ separated by a gap d. We keep constant the dimensions $L_x = L_z = 0.5$ μm, while we vary the transverse dimension L_y. (b) The room-temperature radiative thermal conductance normalized by the blackbody result for the system shown in panel (a) as a function of the dimension L_y. The solid lines correspond to the exact calculations for three gaps in the far-field (see legend), while the black dashed line corresponds to the results obtained by combining Eq. (6.8) with the results of panels (c) and (d). (c) Absorption efficiency as a function of the frequency for a plane wave impinging with normal incidence and TM polarization in a SiN parallelepiped with dimensions $L_x = L_z = 0.5$ μm and various values of L_y, as indicated in the legend. The meaning of this polarization is explained in the inset. (d) The same as in panel (c), but for a TE polarization.

blackbody result, by a single SiO_2 parallelepiped with $L_x = L_y = 0.5$ μm and varying L_z at room temperature. This emitted power was computed with the TDDA approach of Ref. [160]. This latter result shows that the super-Planckian RHT found here is possible due to the highly directional thermal emission of these systems.

To further illustrate the crucial role played by the directionality, we now investigate the same parallelepipeds, but oriented as shown in Fig. 6.4(a). In this case, the parallelepipeds have dimensions $L_x \times L_y \times L_z$, where z is the direction of the line joining the two objects and we keep constant the dimensions $L_x = L_z = 0.5$ μm, while we vary

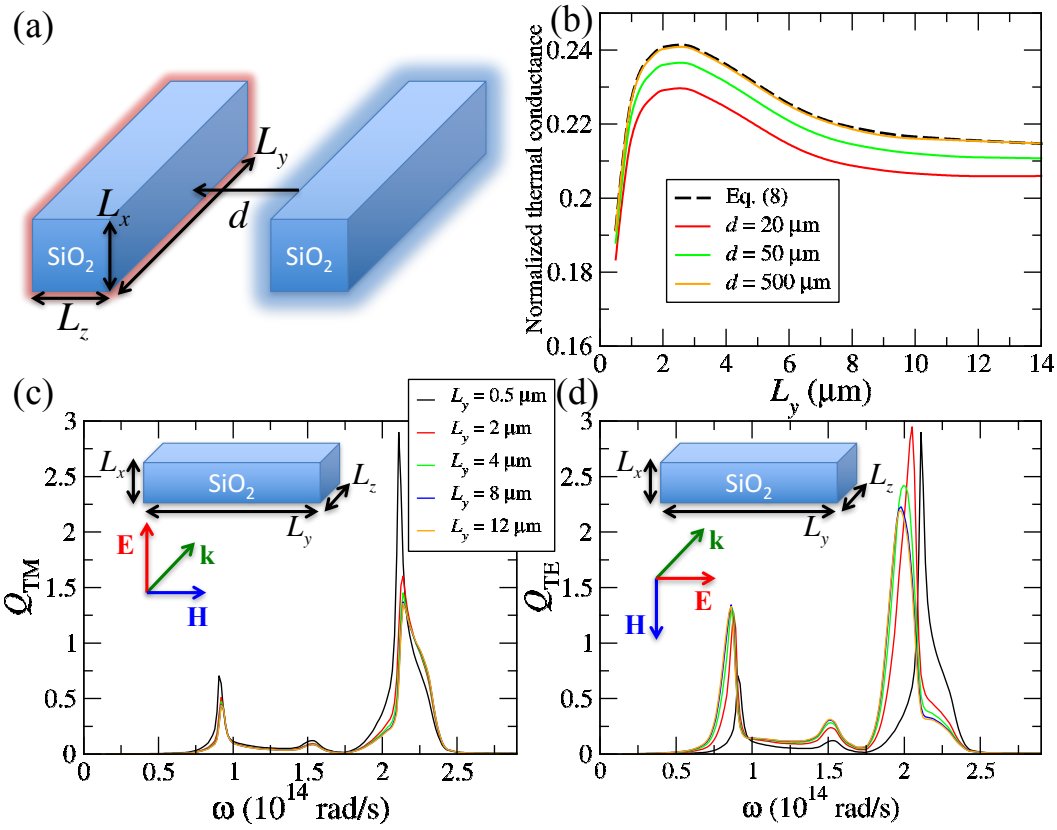

Figure 6.5: The same as in Fig. 6.4, but for SiO_2 parallelepipeds.

the transverse dimension L_y. Figure 6.4(b,d) show the results for the radiative thermal conductance at 300 K and the relevant absorption efficiencies for these parallelepipeds made of SiN. The corresponding results for SiO_2 parallelepipeds are shown in Sec. **??**. The results for the thermal conductance for various gaps, see Fig. 6.4(b), were computed with the TDDA approach [160] and the asymptotic result for very large gaps was obtained with the help of Eq. (6.8) and the absorption efficiencies shown in Fig. 6.4(c,d). These efficiencies were calculated with the DDA method [160] and they correspond to a plane wave impinging in a parallelepiped along normal incidence with polarizations x or TM, Fig. 6.4(c), and y or TE, Fig. 6.4(d).

The results for the thermal conductance of Fig. 6.4(b) show that as the transverse dimension L_y increases, the RHT remains below the blackbody result for all gaps in the far-field regime and the normalized conductance tends to saturate when this dimension becomes on the order of 10 μm. These results show once more the difficulty to achieve super-Planckian FFRHT and the crucial role played by the directionality of the thermal emission. On the other hand, it is worth stressing that the numerical results for a large

gap of 500 μm shown in Fig. 6.4(b) nicely coincide with the asymptotic result obtained via Eq. (6.8), which confirms the validity of this result for parallelepipeds. We present in Fig. 6.5 the RHT results for the parallelepipeds of Fig. 6.4, but in this case made of SiO_2. These results confirm the basic conclusions drawn from Fig. 6.4 for SiN, the main difference being that the normalized thermal conductance adopts lower values than in the SiN case as L_y increases.

6.5. Super-Planckian FFRHT in suspended pads

The results shown in Fig. 6.3 clearly demonstrate the possibility to largely overcome the Planckian limit in the far-field regime, but the conductance values for these structures make their measurement challenging. To illustrate super-Planckian heat transfer in a system that can be tested with existing technology, we focus in this section on the analysis of the RHT between two identical SiN pads with fixed lateral dimensions of 50×50 μm^2, see Fig. 6.6(a), which are larger than λ_{Th} at room temperature, and we vary their thickness, τ, from values much smaller than λ_{Th} to values larger than this wavelength. This challenging system for the theory is inspired by the suspended-pad micro-devices that are widely employed for measuring thermo-physical properties of low-dimensional nanostructures (nanotubes, nanowires or nanoribbons) [154–157]. These devices consist of two adjacent SiN membranes suspended by long beams. Each membrane features a platinum resistance heater/thermometer that is normally used to measure the heat conduction through a sample that bridges the gap between the membranes, but they can also be used to measure the RHT across the gap. In recent years, these micro-devices have reached sensitivities of $\sim$1 pW/K and below [70, 158].

The RHT between these suspended pads in the extreme far-field regime is described by Eq. (6.8). The directional absorption efficiencies entering this equation are now those for a plane wave with normal incidence and TM or TE polarization ($Q_{TM,TE}(\omega)$), see insets of Fig. 6.6(c,d). The results obtained with COMSOL MULTIPHYSICS for these efficiencies for thicknesses varying from 100 nm to 50 μm are displayed in Fig. 6.6(c,d) and they show that when $\tau \ll \lambda_{Th}$ they reach values of up to several hundreds, especially for TE polarization. Using these results together with Eq. (6.8), we have computed the radiative thermal conductance for different values of τ, see Fig. 6.6(b). The ratio with the blackbody result increases monotonically as τ decreases, becoming clearly larger than

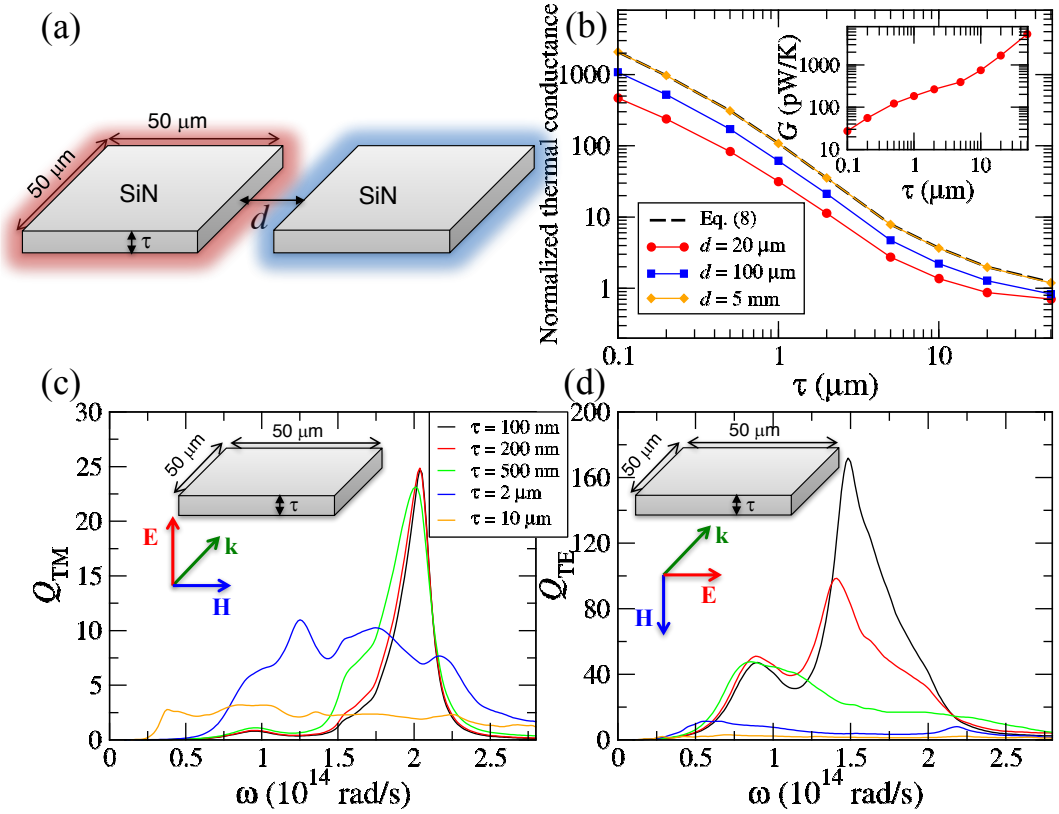

Figure 6.6: (a) SiN pads with lateral dimensions of 50×50 μm^2, a thickness τ, and separated by a gap d. (b) Room-temperature radiative heat conductance, normalized by the blackbody results, for the system of panel (a) as a function of τ. The solid lines are the exact calculations for three gaps (see legend) and the black dashed line is the result obtained with Eq. (6.8) and the results of panels (c) and (d). The inset shows the results for $d = 20$ μm without normalization. (c) Absorption efficiency as a function of frequency for a plane wave impinging with normal incidence and TM polarization in a SiN pad with lateral dimensions of 50×50 μm^2 and various thicknesses, see legend. The inset describes this polarization. (d) The same as in panel (c), but for TE polarization.

1 when $\tau < \lambda_{\rm Th}$, and reaching values as large as 2000 for a thickness of 100 nm. The occurrence of super-Planckian far-field RHT is confirmed by our SCUFF-EM results for several gap sizes, as shown in Fig. 6.6(b). These results show that, irrespective of the gap, the super-Planckian RHT takes place when $\tau < \lambda_{\rm Th}$ and that it should be readily observable in suspended-pad micro-devices, as we illustrate in the inset of Fig. 6.6(b) where we show the radiative thermal conductance without normalization. These results also prove once more that Eq. (6.8) provides the asymptotic result for gaps much larger than the dimensions of the objects, which is when the largest enhancements over the blackbody theory occur. Let us also say that we find similar results for the case of SiO_2 pads, as we show in Fig 6.7.

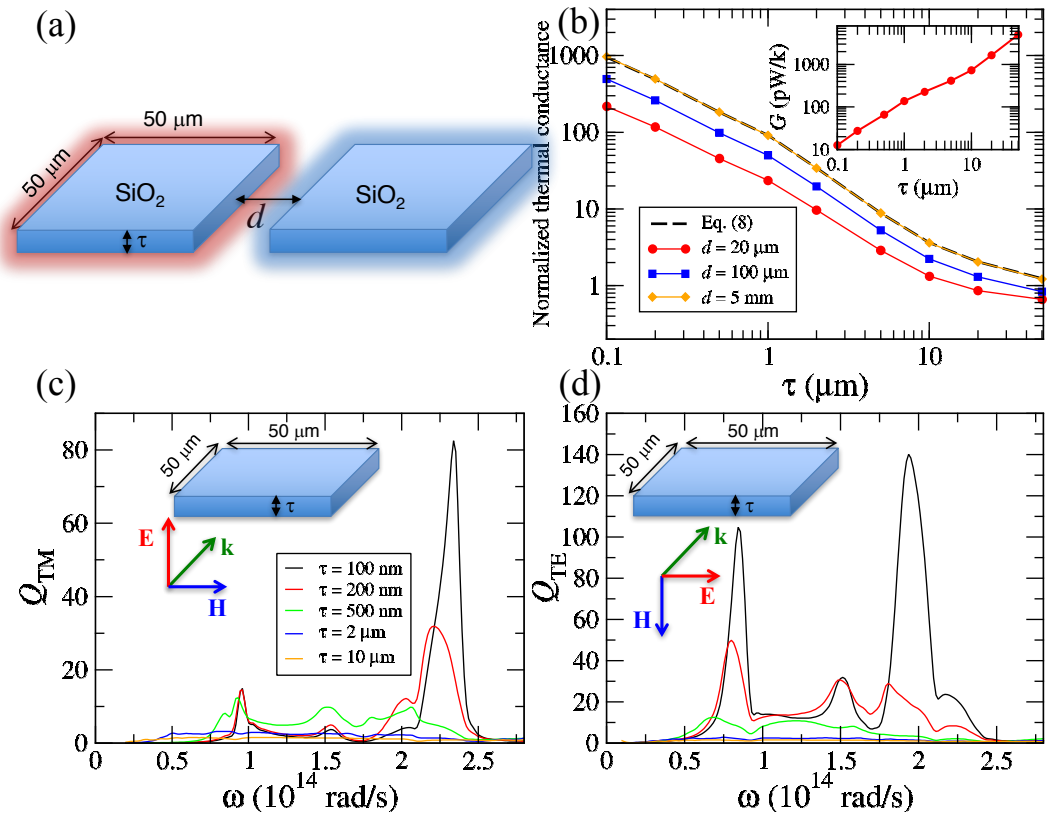

Figure 6.7: The same as in Fig. 6.6, but for SiO_2 pads.

The super-Planckian RHT found for the pads can be further enhanced by increasing their depth, in the very same way as we did for the parallelepipeds. We illustrate this fact in Fig. 6.8 where we investigate the RHT between two 100 nm-thick SiN pads that are assumed to be infinitely wide and have a depth L_z that can be varied, see Fig. 6.8(a). We have computed with COMSOL MULTIPHYSICS the relevant absorption efficiencies for different values of L_z ranging from 100 nm to 1 mm and the results are shown in Fig. 6.8(c,d). As one can see, the efficiencies grow linearly with L_z and reach enormous values in a broad range of frequencies. We have then used these results together with Eq. (6.8) to compute the FFRHT in the asymptotic limit of a gap much larger than the pad length. The corresponding results are displayed in Fig. 6.8(b) and, as one can see, the enhancement over the blackbody result now reaches impressive values of the order of 10^5 when L_z is of the order of 1 mm.

It is important to stress that none of the systems considered in this Chapter is a super-Planckian emitter, i.e., an object that emits more than a black body with the same dimensions. The existence of super-Planckian emitters, which is in principle pos-

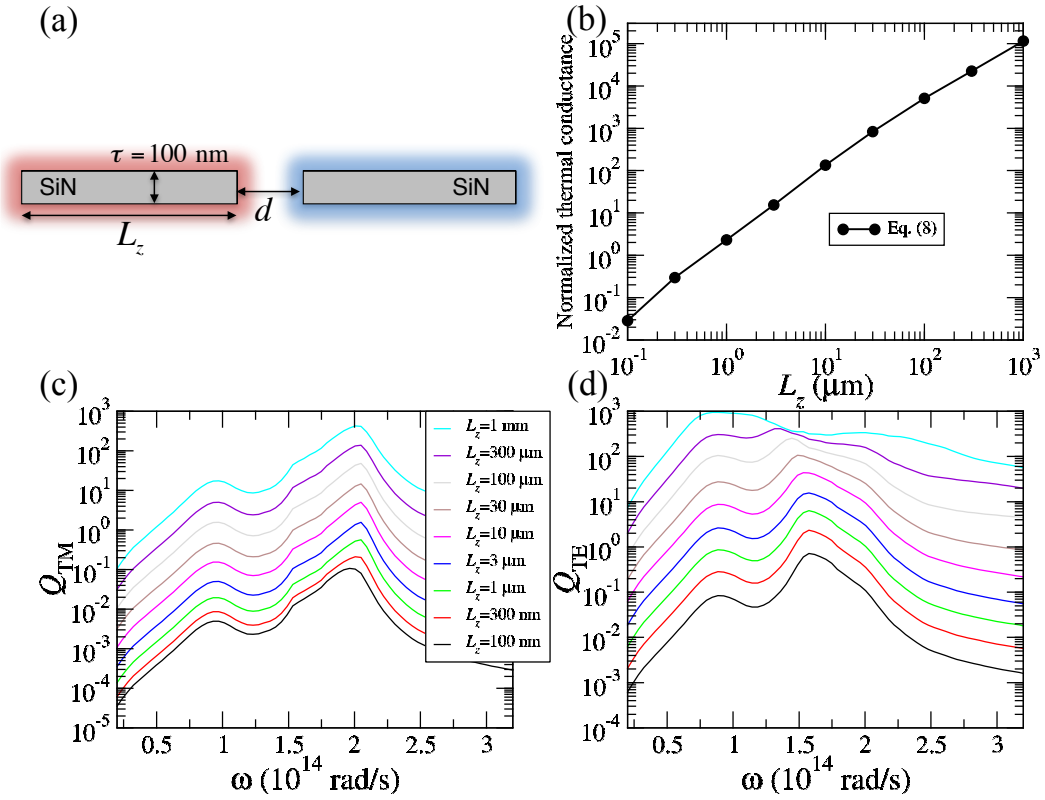

Figure 6.8: (a) SiN pads with a thickness of 100 nm, infinitely wide, a variable depth equal to L_z and separated by a gap d. (b) Room-temperature radiative heat conductance, normalized by the blackbody results, for the system shown in panel (a) as a function of the pad depth L_z. The result corresponds to a gap much larger than the pad depth and it was computed with Eq. (6.8) and the results of panels (c) and (d). (c) Absorption efficiency as a function of the frequency for a plane wave impinging with normal incidence and TM polarization in a SiN slab with dimensions described in panel (a). The different curves correspond to different values of L_z, as indicated in the legend. (d) The same as in panel (c), but for TE polarization.

sible, would make trivial the realization of super-Planckian RHT, but as explained in the introduction, the experimental realization of super-Planckian emitters is extremely challenging. We have already shown in section 6.4 that the parallelepipeds investigated in this work are not super-Planckian emitters, see inset in Fig. 6.3(c). For completeness, we show in Fig. 6.9 that the SiN pads studied above, see Fig. 6.6, are not super-Planckian emitters either. In particular, we show in this figure the total power emitted by the SiN pads considered before (Fig. 6.6), normalized by the black-body result. This quantity is the total emissivity of this object (integrated in frequencies, angles and polarizations). As one can see in Fig. 6.9, this emissivity is clearly smaller than 1, irrespective of the thickness, and it tends to its bulk value when the thickness becomes larger than the thermal wavelength.

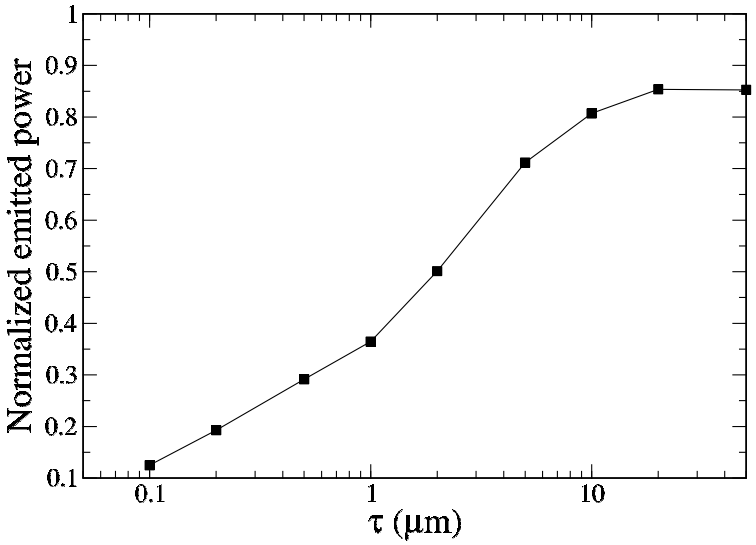

Figure 6.9: Total emitted power at room temperature, normalized by the black-body result, by a single SiN pad with lateral dimensions of 50×50 μm^2 as a function of its thickness τ. Notice that the result is clearly below 1, which shows that these pads are not super-Planckian emitters.

The last thing that remains to be understood in relation to the RHT between these suspended pads is the origin of their remarkable absorption efficiency. In what follows, we shall show that, in simple terms, these pads behave as (lossy) dielectric waveguides that efficiently absorb the radiation via the excitation of guided modes. This excitation is illustrated in the COMSOL MULTIPHYSICS simulation of Fig. 6.10(a). In that figure we display the Poynting vector obtained in a simulation of a TE-polarized plane wave impinging in a 100 nm-thick SiN pad for a frequency $\omega = 1.5 \times 10^{14}$ rad/s. In this case the pad length is 50 μm and it was assumed to be infinite in the transverse direction. As one can see, the pad is able to alter the incoming field over a region that is more than 100 times larger than its thickness. What happens is that, due to the low-impedance mismatch, the incident radiation couples efficiently into a guiding mode that has a large lateral extension outside the pad and the mode is then absorbed during their propagation, with the energy slowly flowing into the pad. The large spatial extent of the guided mode, and its large overlap with the incoming plane wave, is actually responsible for the corresponding cross section becoming so much larger than the physical size of the pad. To understand in more detail how the energy absorption in these pads takes place, we now proceed to study the nature of the guided modes in these dielectric structures.

In order to determine the electromagnetic modes sustained by the pads, we consider an infinite planar waveguide made of a SiN slab of thickness τ surrounded by air. Our goal

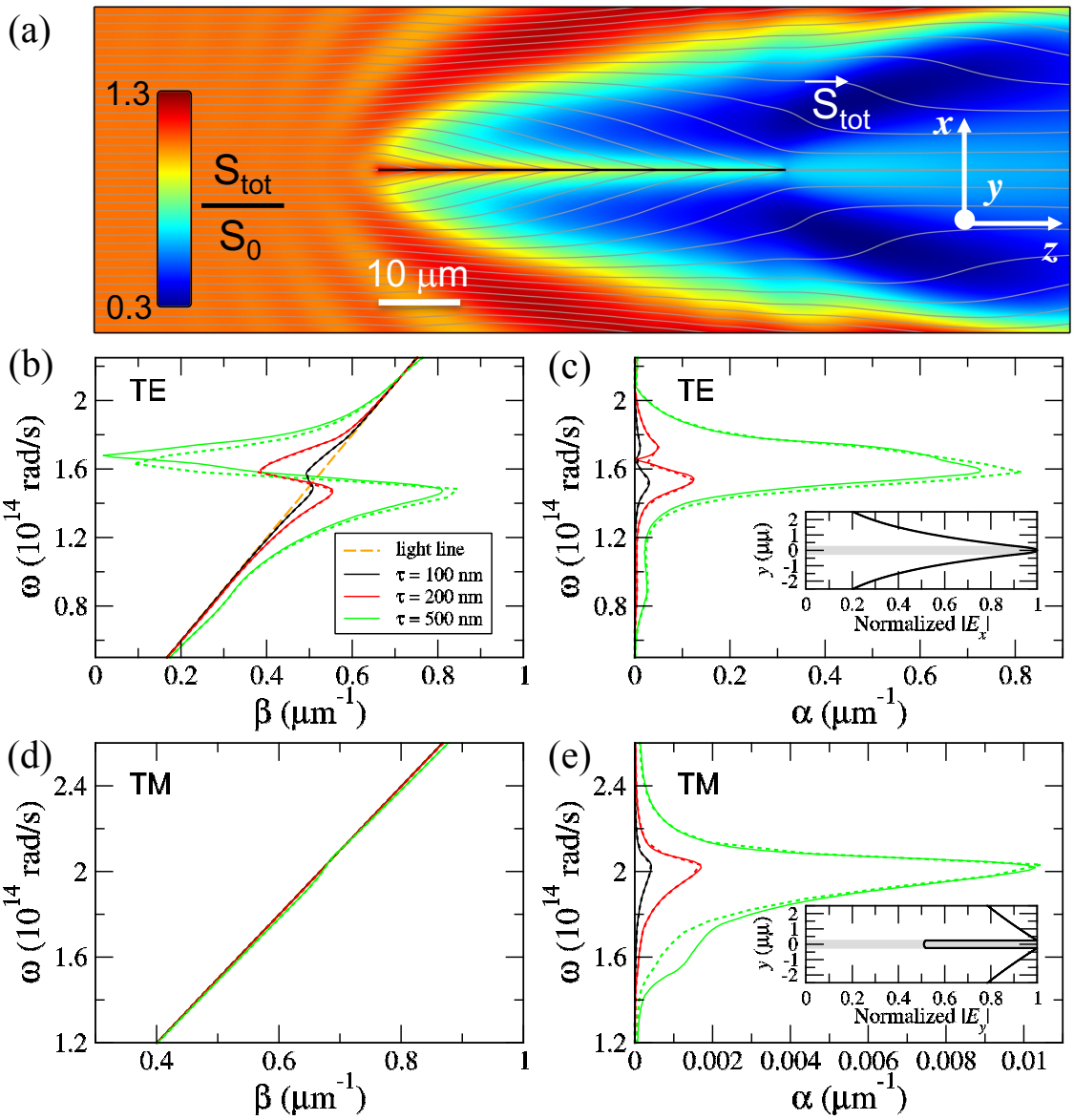

Figure 6.10: (a) Magnitude of the total Poynting vector S_{tot}, normalized by the incident value S_0, in a simulation of a TE-polarized plane wave impinging in a 100 nm-thick SiN pad (in black) for $\omega = 1.5 \times 10^{14}$ rad/s. The pad length is 50 μm and it is infinite in the transverse direction. A streamline representation of the Poynting vector is shown in grey solid lines. (b-c) Frequency versus propagation constant β (b) and attenuation constant α (c) for the TE modes of an infinite SiN slab for different values of its thickness τ. The solid lines correspond to the exact numerical solution of Eq. (6.13), while the dotted lines correspond to the analytical result of Eqs. (6.15) and (6.16). The dashed orange line in panel (b) is the light line in vacuum, $\omega = \beta c$, and it separates the modes into guided ones on the right hand side of this line and leaky ones on the left. (d-e) The same as in panels (b) and (c) for TM modes. The inset in panels (c) and (e) show the normalized electric field profile for the components E_x and E_y, respectively, for a 500 nm-thick slab. The shaded area represents the SiN slab.

is to obtain the dispersion relation of the guided modes in this structure. Using standard theory of dielectric waveguides [164], one can show that those dispersion relations are given by the solution of the following secular equations

$$1 - r_p^2 e^{2iq_{\mathrm{SiN}}\tau} = 0, \tag{6.13}$$

where the index p indicates the polarization of the mode (TE or TM). In this case, the modes with TE polarization have field components E_x, H_y and H_z according to the coordinate system shown in Fig. 6.10(a), while the TM modes have the following non-vanishing field components: H_x, E_y and E_z. On the other hand, the r_p's in Eq. (6.13) correspond to the Fresnel coefficients

$$r_{\mathrm{TE}} = \frac{q_{\mathrm{air}} - q_{\mathrm{SiN}}}{q_{\mathrm{air}} + q_{\mathrm{SiN}}} \quad and \quad r_{\mathrm{TM}} = \frac{\epsilon_{\mathrm{SiN}} q_{\mathrm{air}} - q_{\mathrm{SiN}}}{\epsilon_{\mathrm{SiN}} q_{\mathrm{air}} + q_{\mathrm{SiN}}}, \tag{6.14}$$

where $q_j = \sqrt{\epsilon_j \omega^2/c^2 - k^2}$ is the transverse component (y-component) of the wave vector in medium j (j = air, SiN), $\epsilon_j(\omega)$ is the corresponding dielectric function, and $k = \beta + i\alpha$ is the parallel component of the wave vector (z-component). Here, β is the propagation constant of the electromagnetic mode and α is the corresponding attenuation constant, which determines both the absorption and the propagation length of the mode.

In Fig. 6.10(b-e) we present the results for the frequency dependence of the propagation and attenuation constants of the modes sustained by a SiN slab of several thicknesses. In particular, we show with solid lines the exact results obtained with the numerical solution of Eq. (6.13) for both polarizations (TE or TM). The first thing to notice is that the attenuation constant, which determines the power absorption, strongly depends on the polarization and exhibits much larger values for the TE case, which explains the larger efficiency for this polarization, see Fig. 6.6(d). Moreover, the frequency dependence of the attenuation constant reproduces the corresponding dependence of the absorption efficiencies for both polarizations in the limit of thin pads. Interestingly, there is a frequency range in which the slab behaves as a hollow dielectric waveguide [164], with the real part of the core dielectric function being smaller than that of the cladding, and the propagation for TE polarization occurs via leaky modes [164], see Fig. 6.10(b,c).

It is worth recalling that these planar dielectric waveguides have no frequency cut-off, i.e., there exists at least one electromagnetic guiding mode for TE and TM polarizations for any value of the thickness τ. In order to have a second mode in our slab waveguide, q_{SiN} must fulfill the condition $\mathrm{Re}\{q_{\mathrm{SiN}}\}\tau = \pi$. In our case, the thinnest slab at which there is an additional mode for a certain ω is $\tau = 1.8$ μm, for both TE and TM polarization.

Thus, for the thickness range analyzed in Fig. 6.10, there is only one electromagnetic guided mode in the SiN slab.

In the limit of very thin slabs ($q_{\mathrm{SiN}}\tau \ll 1$), it is possible to find an analytical solution of Eq. (6.13). In this limit, the mode dispersion relations are given by

$$k_{\mathrm{TE}} = \frac{\omega}{c}\sqrt{1+\left(\frac{\omega\tau(\epsilon_{\mathrm{SiN}}-1)}{2c}\right)^2}, \tag{6.15}$$

$$k_{\mathrm{TM}} = \frac{\omega}{c}\sqrt{1+\left(\frac{\omega\tau(\epsilon_{\mathrm{SiN}}-1)}{2c\epsilon_{\mathrm{SiN}}}\right)^2}. \tag{6.16}$$

These expressions provide a very good approximation for the dispersion relation of the modes for the thickness range analyzed, as the dashed lines of Fig. 6.10(b-e) show. In the case of very thin slabs, it is possible to further simplify Eqs. (6.15) and (6.16) to obtain the following analytical expressions for the attenuation constant for both polarizations

$$\alpha_{\mathrm{TE}}(\omega) = \frac{\omega^3\tau^2}{4c^3}Im\left\{\epsilon_{\mathrm{SiN}}(\omega)\right\}\left[\mathrm{Re}\{\epsilon_{SiN}(\omega)\}-1\right], \tag{6.17}$$

$$\alpha_{\mathrm{TM}}(\omega) = \frac{\omega^3\tau^2}{4c^3}\frac{Im\left\{\epsilon_{\mathrm{SiN}}(\omega)\right\}\left[\left|\epsilon_{\mathrm{SiN}}(\omega)\right|^2-\mathrm{Re}\{\epsilon_{SiN}(\omega)\}\right]}{\left|\epsilon_{\mathrm{SiN}}(\omega)\right|^4}. \tag{6.18}$$

These expressions show that the attenuation constant that determines the power absorption in the slab scales with the thickness as τ^2, i.e., the propagation length of these modes increases upon reducing the waveguide thickness. It is important to emphasize that this propagation length of these modes, which is given by $1/2\alpha$, reaches values even larger than 1 mm for thicknesses below a few hundreds of nm for the relevant frequencies. This is especially true for the TM polarization. This fact explains why in all the cases considered in this section, see Figs. 6.6 and 6.8, the absorption efficiencies grow linearly with the dimension L_z. The idea is that, as we explained in section 6.4, the efficiencies Q for normal incidence are proportional to the factor $[1-\exp(-2\alpha L_z)]$, and since we have investigated here the limit $\alpha L_z \ll 1$, then $Q \propto L_z$.

Finally, and in order to get some further insight into the nature of the electromagnetic modes supported by these SiN slabs, we have plotted the electric field component that is perpendicular to the propagation direction of the mode (E_x for TE polarization and E_y for the TM case), see insets of Fig. 6.10(c,e). Both electric profiles are represented as a function of the y-coordinate for a slab of thickness $\tau = 500$ nm and frequencies $\omega = 1.47\times10^{14}$ rad/s and $\omega = 1.98\times10^{14}$ rad/s for the TE and TM mode, respectively. The E_y profile of the TM mode is discontinuous at the boundary and it extends longer in

the y-direction. Therefore, it has a smaller amplitude inside the slab as compared to the E_x profile of the TE mode. This explains why the attenuation constant is smaller in the TM case, and therefore the absorption along the SiN pads is larger for this polarization.

6.6. Conclusions

In summary, we have presented in this Chapter a theoretical study that demonstrates that the far-field RHT between objects with some of their dimensions smaller than the thermal wavelength can greatly overcome the Planckian limit. By finding a connection between the FFRHT and the directional absorption efficiencies of the objects involved, we have provided very intuitive guidelines on how to achieve super-Planckian far-field RHT. In particular, we have shown that a huge super-Planckian FFRHT can be achieved in micron-sized suspended devices of great importance for the field of thermal transport [70, 154–158], which in turn can be used to quantitatively test our predictions.

From a more general perspective, our work illustrates the need to revisit the far-field RHT between micro- and nano-systems in the light of FE theory. Our work is also important for the study of thermalization of small objects [68] with implications, e.g., in cavity optomechanics experiments [165] or in the study of interstellar dust in astrophysics [166]. Finally, our work also raises the question of the ultimate limit of the super-Planckian FFRHT in low-dimensional systems such as nanowires and 2D materials.

7 | Exploring the limits of super-Planckian far-field radiative heat transfer using 2D materials

7.1. Introduction

In the last chapter, it has been predicted that the Planckian limit can also be largely surpassed in the far-field regime [159], i.e., when the separation of the objects is larger than λ_{Th}. In particular, we have shown theoretically that the FFRHT between micron-size devices can overcome the black-body limit by several orders of magnitude if their thickness is much smaller than λ_{Th}. Moreover, we have shown that the enhancement over Planck's law increases monotonically as the device thickness is reduced, which leads us to the fundamental question on the limits of super-Planckian FFRHT. The goal of this chapter is to explore this issue with the help of two dimensional (2D) materials, i.e., with materials with a one-atom-thick geometrical cross section, which constitute the ultimate limit of thin systems.

2D materials have been extensively studied in recent years in the context of TM. In particular, several works have taken advantage of the near-field density of photonic states in these systems to modify the characteristics of emitters in a wide variety of scenarios. Most of the theoretical work in the case of graphene has focused on the possibility to tune and enhance the NFRHT mediated by the SPPs sustained by this material [167, 168]. For instance, it has been predicted that the NFRHT between polar dielectrics can be boosted by placing a graphene layer on top [169–171]. This prediction has been confirmed experimentally [47]. Other studies have proposed periodic graphene ribbon arrays to induce hyperbolic modes and thus further enhance the NFRHT between 2D

systems [172]. The NFRHT between graphene nanodisks has also been studied [173], and the analysis of the time scales of radiative heat transfer in this setup suggests that this process is ultrafast [174]. Let us also mention that the near field thermal conductance between Dirac 2D materials scales as the inverse of the distance between two flakes [175]. However, and despite all these recent advances, FFRHT between 2D materials remains unexplored. As explained above, 2D materials constitute ideal systems in which one can explore the ultimate limit of the violation of Planck's law in the far-field regime. Moreover, from an applied viewpoint, understanding the absorption and emission of radiation in 2D materials is key to properly characterize their thermal properties and harness their unique mechanical and electronic features [176].

For these reasons, we present in this chapter a theoretical study of the FFRHT between systems with a one-atom-thick geometrical cross section. In particular, we demonstrate that the FFRHT between sheets of 2D materials can be more than 7 orders of magnitude larger than the theoretical limit set by Planck's law for blackbodies and can be comparable to the heat transfer of two parallel sheets at the same distance. More precisely, we illustrate this phenomenon with different materials such as graphene, where the radiation can also be tuned by a external gate, and single-layer black phosphorus. In both cases the FFRHT is dominated by TE-polarized guiding modes and surface plasmons play no role. Our predictions provide a new insight into the thermal radiation exchange mechanisms between 2D materials.

7.2. FFRHT between coplanar graphene sheets

Let us start by analyzing the FFRHT between two coplanar graphene sheets. This system is schematically represented in Fig. 7.1(a). In this case, two identical graphene sheets at temperatures T_1 and T_2 ($T_1 < T_2$) are separated by a gap d. The length of the flakes is denoted by L_z and, for simplicity, we shall assume that they are infinitely wide in the x-direction ($L_x \to \infty$). Notice that, as shown in Fig. 7.1(a), both flakes are coplanar and thus, for the radiative problem they constitute systems with a one-atom-thick geometrical cross section. In order to compute the power exchanged in the form of thermal radiation between these 2D systems, we need the dielectric function of graphene, which can be determined from its electrical conductivity. The 2D conductivity of graphene, $\sigma_{2D}^{\text{graphene}}$, calculated within the random phase approximation can be expressed in terms

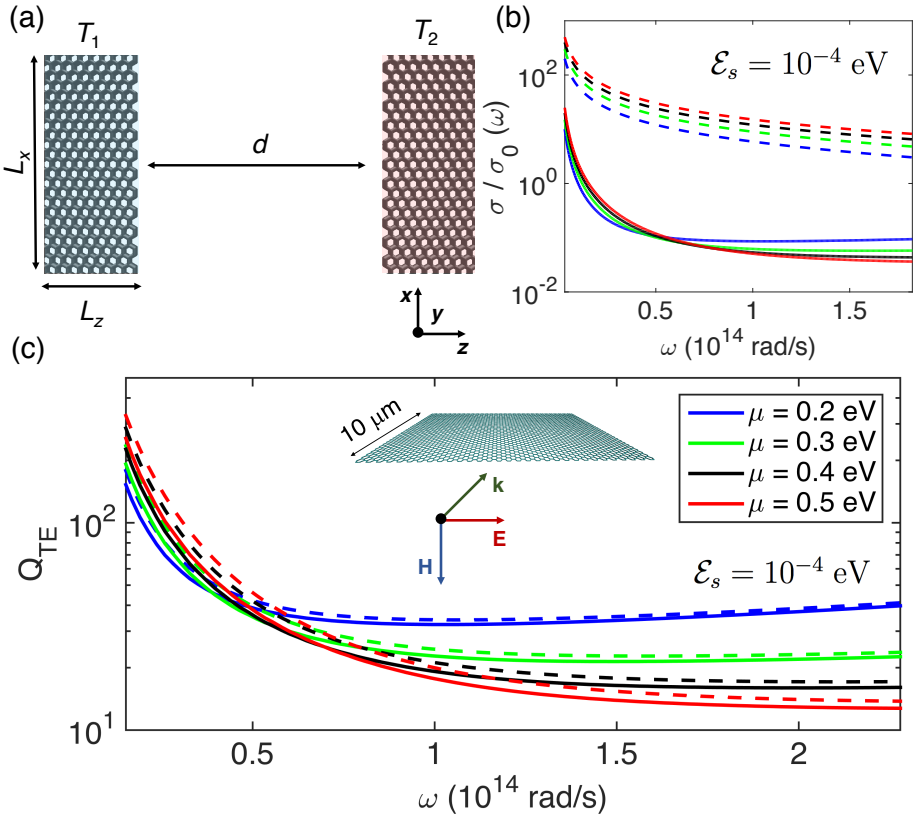

Figure 7.1: (a) Schematics of the FFRHT between two identical graphene flakes. The flakes have dimensions $L_x \times L_z$, are separated by a gap d, and are held at temperatures T_1 and T_2, respectively. (b) Real (solid lines) and imaginary (dashed lines) part of the normalized conductivity for $T = 300$ K, $\mathcal{E}_\mathrm{s} = 10^{-4}$ eV, and for different chemical potentials (μ), as indicated in the legend of panel (c). (c) Frequency-dependent absorption efficiency for a plane wave with TE polarization ($Q_\mathrm{TE}(\omega)$) and normal incidence into a graphene sheet with length $L_z = 10$ μm, infinite width (see inset), and for different values of μ (see legend). The solid lines correspond to the exact numerical results, while the dashed lines correspond to the results obtained with Eq. (7.8).

of the chemical potential (μ), temperature (T) and scattering energy ($\mathcal{E}_\mathrm{s}$) [177, 178]

$$\sigma_\mathrm{2D}^\mathrm{graphene} = \sigma_\mathrm{intra} + \sigma_\mathrm{inter}, \tag{7.1}$$

where the intraband and the interband contributions are given by

$$\begin{aligned} \sigma_\mathrm{intra} &= \frac{2ie^2 t}{\hbar\pi(\Omega + i\gamma)} \ln\left[2\cosh\left(\frac{1}{2t}\right)\right], \\ \sigma_\mathrm{inter} &= \frac{e^2}{4\hbar}\left[\frac{1}{2} + \frac{1}{\pi}\arctan\left(\frac{\Omega - 2}{2t}\right) - \frac{i}{2\pi}\ln\frac{(\Omega+2)^2}{(\Omega-2)^2 + (2t)^2}\right], \end{aligned} \tag{7.2}$$

with $\Omega = \hbar\omega/\mu$, $\gamma = \mathcal{E}_s/\mu$, and $t = k_B T/\mu$. In Fig. 7.1(b) we show the normalized 2D conductivity of graphene, in units of $\sigma_0 = e^2/2\pi\hbar$, for $T = 300$ K, $\mathcal{E}_s = 10^{-4}$ eV, and different values of the chemical potential. As one can see, graphene resembles a Drude metal in the infrared regime whose metallic character increases with the chemical potential. Let us remark that the value chosen in this case for $\mathcal{E}_s$ corresponds to a graphene sheet with a very large relaxation time, $\tau = \hbar/\mathcal{E}_s$, which is normally the desired scenario in the field of graphene plasmonics [179]. We will show below that the opposite limit is indeed more favorable for the absorption and emission of radiation between 2D materials.

In order to calculate the FFRHT, we make use of Eq. 6.8 derived in Chapter 6 [159] with the help of a TDDA [160]. This result establishes a connection between the FFRHT between two objects and their absorption efficiencies, *i.e.*, their absorption cross sections divided by their geometrical cross sections. Assuming that a sheet of a 2D material can be modeled as a parallelepiped (see below), this result indicates that the radiative power exchanged between two identical flakes at temperatures T_1 and T_2 and separated by a gap d much larger than both λ_{Th} and their characteristic dimensions is given by [159]

$$P = \frac{\pi}{2} A F_{12} \int_0^\infty \left[Q_{TE}^2(\omega) + Q_{TM}^2(\omega)\right] \left[I_{BB}(\omega, T_1) - I_{BB}(\omega, T_2)\right] d\omega, \tag{7.3}$$

where A is the geometrical cross section of the bodies and $F_{12} = \delta/2d$ is the geometrical view factor [3], where δ is the geometric thickness of the 2D material. On the other hand, $Q_{TM,TE}(\omega)$ is the frequency-dependent absorption efficiency for a plane wave with normal incidence and TM or TE polarization, and $I_{BB}(\omega, T)$ is the Planck distribution function, which is given by

$$I_{BB}(\omega, T) = \frac{\omega^2}{4\pi^3 c^2} \frac{\hbar\omega}{\exp(\hbar\omega/k_B T) - 1}, \tag{7.4}$$

where c is the speed of light. The black-body limit can be obtained by assuming that the absorption efficiencies $Q_{TM,TE}(\omega) = 1$ for all frequencies. In this case, Eq. (7.3) reduces to the Stefan-Boltzmann law [3]: $P_{BB} = \sigma A F_{12}(T_1^4 - T_2^4)$, where $\sigma = 5.67 \times 10^{-8}$ W/(m^{2}K^4).

According to Eq. (7.3), $Q_{TM,TE}(\omega)$ are required to calculate the FFRHT between two graphene sheets. Since our system is one-atom-thick in the y-direction (Fig. 7.1a), a wave impinging with the electric field pointing in the y-direction does not generate any current on that direction. Hence, the absorption cross section of TM plane waves vanishes ($Q_{TM}(\omega) = 0$) and only $Q_{TE}(\omega)$ contributes to the FFRHT. Note that free-space propagating waves cannot couple efficiently to surface plasmons in graphene, which lie

far outside the light line, due to the large mismatch in in-plane momentum. We have calculated this efficiency using COMSOL MULTIPHYSICS, where we have modeled our system as a 3D parallelepiped with an effective dielectric constant. Let us further explain how we have carried out this modeling.

A 2D flake can be modeled as a 3D parallelepiped of thickness h and conductivity $\sigma_{3D} = \sigma_{2D}/h$ [178] as long as h is much smaller than the wavelengths involved. As we study the FFRHT at room temperature ($\lambda_{Th} \approx 10$ μm), h must be, roughly speaking, smaller than 100 nm to obtain converged results. Therefore, we can write the dielectric function of a 2D material as $\epsilon_{3D} = 1 + i\sigma_{3D}/(\epsilon_0\omega)$, where ϵ_0 is the vacuum permittivity. We have verified that $Q_{TE}(\omega)$ does not depend on the parallelepiped thickness h, as long as this value is much smaller than the wavelengths involved.

In accordance with experimental evidence, we have taken $\delta_{graphene} = 0.37$ nm for the thickness of a graphene monolayer [180]. Fig. 7.1(c) shows $Q_{TE}(\omega)$ as a function of the radiation frequency ω (solid lines) for different chemical potentials and for a scattering energy $\mathcal{E}_s = 10^{-4}$ eV. Notice that the absorption cross section is much larger than the geometrical one in the infrared frequency range, which shows that graphene is a very efficient broadband infrared absorber, even when the incident vector of the plane wave is parallel to the graphene sheet (see inset in Fig. 7.1(c)). Notice also that $Q_{TE}(\omega)$ increases for decreasing frequency, which is due to the increase of losses in the system (see Fig. 7.1(b)).

In order to get further insight into the remarkable radiation absorption of a graphene flake, we have derived an analytical expression for Q_{TE}^{an} in Eq. (7.3). For this purpose, we consider the system shown in Fig. 7.2, where a TE-polarized plane wave impinges on a thin slab. This thin slab corresponds to the parallelepiped that models our 2D material. We assume that this parallelepiped is infinite along the x-direction, has a length L_z, and a thickness h. The electric field of the incoming plane wave is polarized along the x-direction. Taking advantage of the effectively vanishing thickness of the 2D material, we assume that the modes inside it are very similar to a plane wave, but having an evanescent tail in the y-direction in the air regions, as it is schematically shown in Fig. 7.2. Besides, this mode decays exponentially along the z-direction due to absorption losses in the 2D material. Therefore, we can express the amplitude of the x-component of the electric field of the TE waveguide mode of the slab as

$$E_{x,wm}(y,z) = E_{x,inc}(z=0)e^{-\mathrm{Im}\{k_{y,v}\}|y|}e^{-\mathrm{Im}\{k_z\}z}, \tag{7.5}$$

where $E_{x,inc}$ is x-component of the electric field amplitude of the incident plane wave

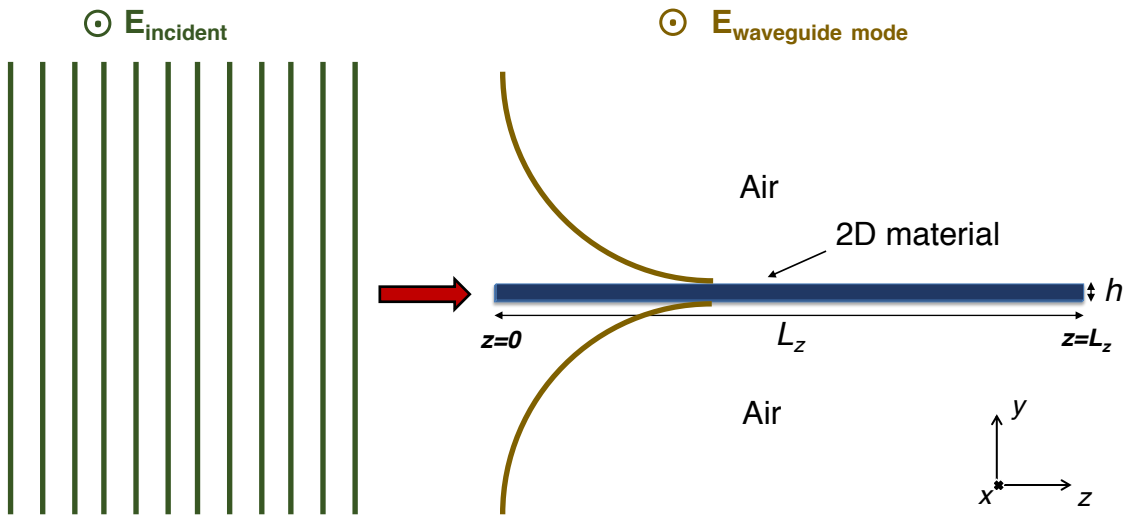

Figure 7.2: Scheme of the absorption of a plane wave by a slab of thickness h and depth L_z, which is assumed to be infinite in the x-direction. The green lines represent the plane wave, while the brown ones show schematically the waveguide electric mode profile. The origin of the coordinate axes is placed where the matching between the modes occurs.

electric field, $k_{y,v}$ is the y-component of the waveguide mode wave vector in vacuum, and k_z corresponds to the z-component of the same wave vector. Note that the 2D material flake ranges from $z = 0$ to $z = L_z$. The properties of the guiding modes have been calculated by using standard dielectric waveguide theory [164]. Indeed, in the limit of very thin slabs, it is possible to find analytical expressions for the different wave vectors [159]

$$k_{y,\mathrm{v}} = \left(\frac{\omega}{c}\right)^2 \frac{ih(\epsilon_\mathrm{p}-1)}{2}, \quad k_z = \frac{\omega}{c}\sqrt{1+\left(\frac{\omega h(\epsilon_\mathrm{p}-1)}{2c}\right)^2} \tag{7.6}$$

where ϵ_p is the dielectric constant of the parallelepiped. The expression of Eq. (7.5) for the electric field $E_{x,\mathrm{wm}}(y,z)$ is only valid outside of the parallelepiped. However, since h is very small compared to the total extension of the mode, we can neglect the fraction of the field that propagates inside the material for a minimal model. To calculate the absorption cross section ($Q_{\mathrm{TE}}^{\mathrm{an}}$) of our system, we have to calculate the overlapping integral (Ω) between the intensity of the incident plane wave (I_{inc}) and that of the slab

mode ($I_{\rm wm}$), normalized to $|I_{\rm inc}|^2$:

$$\Omega = \frac{\int I_{\rm inc} I_{\rm wm}(y, z=0) dy}{|I_{\rm inc}|^2} = \frac{\int |E_{x,\rm inc}|^2 |E_{x,\rm wm}(y, z=0)|^2 dy}{|E_{x,\rm inc}|^4} = \frac{1}{\mathrm{Im}\{k_{y,\rm v}\}}. \tag{7.7}$$

Since the incident plane wave and the waveguide mode have very similar electric fields, Ω is proportional to the extension of the guiding mode along the y-direction. Once we have calculated Ω, we have to consider which fraction of the power is then absorbed along the parallelepiped length L_z. Therefore, $Q_{\rm TE}^{\rm an}$ is given by

$$Q_{\rm TE}^{\rm an} = \frac{\Omega}{\delta} \frac{I_{wm}(y, z=0) - I_{\rm wm}(y, z=Lz)}{I_{\rm wm}(y, z=0)} = \frac{1 - e^{-2\mathrm{Im}\{k_z\} L_z}}{\delta \mathrm{Im}\{k_{y,\rm v}\}}. \tag{7.8}$$

Let us stress that as our parallelepiped is infinite along the x-direction, we just have to divide by the geometrical thickness of our 2D material (δ) to obtain $Q_{\rm TE}^{\rm an}$. In Fig. 7.1(c) we show the analytical results for the absorption efficiency $Q_{\rm TE}^{an}(\omega)$ (dashed lines) and, as one can see, there is an excellent agreement with the exact numerical simulations. This agreement allows us to conclude that the extraordinary absorption efficiency of a graphene flake in this configuration is due to the fact that it behaves as a lossy waveguide that absorbs the radiation via the excitation of guided TE modes. In particular, because of the low impedance mismatch, the incident radiation is efficiently coupled into guided modes and is eventually absorbed.

Once $Q_{\rm TE}(\omega)$ is known, we can use Eq. (7.3) to calculate the FFRHT between two graphene flakes in the coplanar configuration (see Fig. 7.1(a)). We shall characterize the FFRHT in terms of the room-temperature linear heat conductance per unit of length, $G_{\rm th} = P/(L_x \Delta T)$, in the limit $\Delta T = (T_2 - T_1) \to 0$. Before presenting our results, let us show a test simulation that demonstrates that Eq. (7.3) yields accurate results for the FFRHT between 2D materials

Figure 7.3 shows the spectral $G_{\rm th}$ at room temperature between two graphene sheets of dimensions $L_x = 640$ μm, $L_z = 1$ μm, $\mathcal{E}_{\rm s} = 0.01$ eV and separated by a gap of 5 mm. The reason for choosing such a large L_x is to make the graphene flake quasi-infinite in that direction, since the $Q_{\rm TE}(\omega)$ has been calculated considering that the graphene layer is semi-infinite. Besides, the reason why the gap between both objects is so large is to be in the far-field limit where Eq. (7.3) is strictly valid. The red solid line in Fig. 7.3 represents the exact result, obtained with the code SCUFF-EM [39, 82], while the black dashed line shows the one obtained with Eq. (7.3). On the other hand, the $Q_{\rm TE}(\omega)$ used in the analytical approach was computed using COMSOL MULTIPHYSICS. As it can

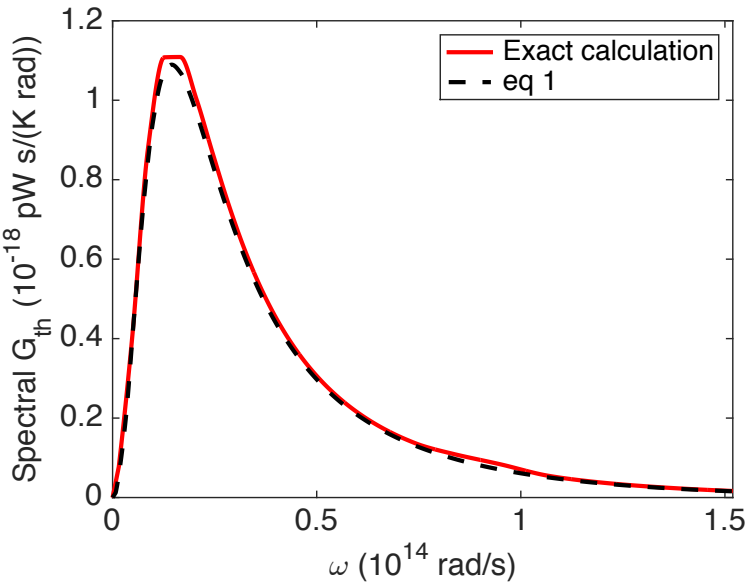

Figure 7.3: Spectral $G_{\rm th}$ as a function of ω for a system composed of two graphene flakes of dimensions $L_x = 640$ μm, $L_z = 1$ μm, $\mathcal{E}_{\rm s} = 0.01$ eV and separated by a gap d=5 mm. The red line shows the exact calculations while the dashed black line corresponds to the results obtained with Eq. 7.3.

be observed in Fig. 7.3, there is an excellent agreement between both approaches, which demonstrates the validity of Eq. (7.3) to calculate the FFRHT between 2D materials.

In Figure 7.4(a) we show the spectral $G_{\rm th}$, i.e., the conductance per unit of frequency, for two graphene sheets of length $L_z = 10$ μm, $\mathcal{E}_{\rm s} = 10^{-4}$ eV, and a gap $d = 1$ mm. It can be observed that the system exhibits a broad-band FFRHT spectrum, similar to the FFRHT between metals [11]. The conductance peak appears at $\omega = 9 \times 10^{10}$ rad/s for all chemical potentials. This maximum originates from the convolution of the Planck's distribution function ($I_{\rm BB}$) and $Q_{\rm TE}(\omega)$, see Eq. (7.3). Notice, however, that the magnitude of $G_{\rm th}$ does increase with μ and can be tuned by a factor of 2.5 between $\mu = 0.2$ eV and $\mu = 0.5$ eV.

Let us turn now to the analysis of the total thermal conductance and its comparison with the predictions of Planck's law for blackbodies. Fig. 7.4(b) shows $G_{\rm th}$ normalized by the corresponding blackbody result ($G_{\rm BB} = 4\sigma\delta F_{12}T^3$) as a function of the flake's length L_z. As it can be observed, the power exchanged by the two graphene flakes overcomes Planck's results by up to 4 orders of magnitude for a length of 100 μm. The reason for this huge enhancement can be understood with the help of Fig. 7.1(c), where it is shown that the absorption efficiency of a graphene sheet reaches values much larger than 1 for a broad range of infrared frequencies, accesible at room temperature. Besides, the

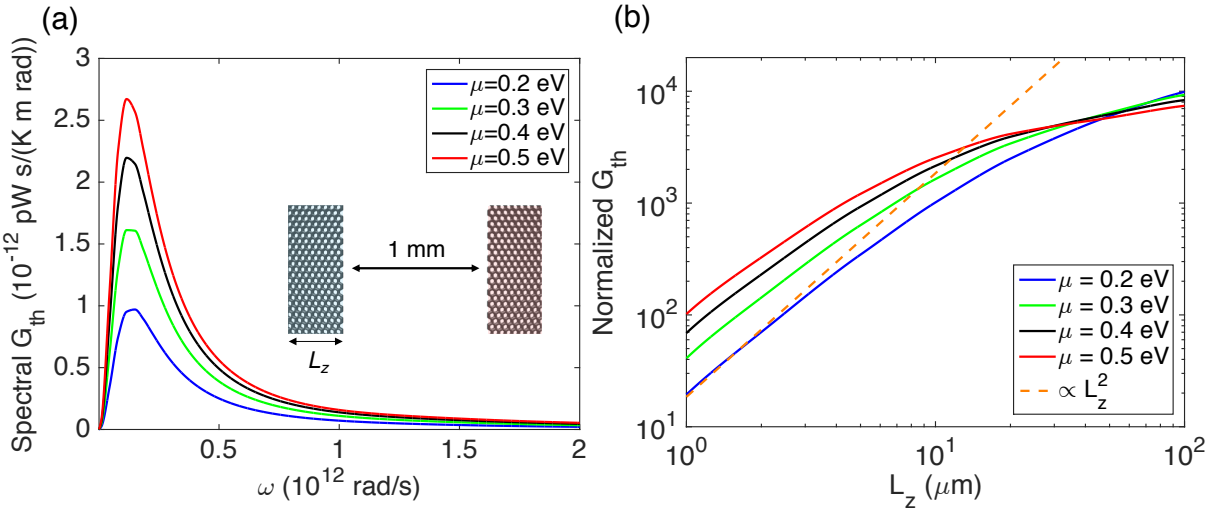

Figure 7.4: (a) Spectral thermal conductance as a function of the radiation frequency for a system composed of two graphene flakes of length $L_z = 10$ μm, $\mathcal{E}_s = 10^{-4}$ eV, and a gap $d = 1$ mm (see inset). The temperature is 300 K. (b) The total thermal conductance $G_{\rm th}$, normalized by the blackbody results, for the same system as in panel (a) and plotted as a function of L_z for different chemical potentials. The dashed orange line is proportional to L_z^2. Let us stress that these normalized results do not depend on the gap as long as d is much larger than the thermal wavelength.

normalized $G_{\rm th}$ increases with L_z simply because the absorption and emission of radiation in the graphene flakes increases with this length. It can be also seen in Fig. 7.4(b) that for small lengths, the normalized $G_{\rm th}$ is proportional to L_z^2, which can be understood as follows. The efficiency $Q_{\rm TE}(\omega)$ is proportional to $(1-e^{-2{\rm Im}\{k_z\}L_z})$, according to Eq. (7.8). In the limit in which ${\rm Im}\{k_z\}L_z \ll 1$, $Q_{\rm TE}(\omega)$ is simply proportional to L_z. Thus, from Eq. (7.3), it is obvious that $G_{\rm th} \propto L_z^2$ for short graphene flakes, as it is verified in Fig. 7.4(b).

We have shown that the FFRHT between graphene sheets can overcome the Planckian limit by more than 4 orders of magnitude. However, our analysis also suggests that the thermal conductance could be further enhanced by increasing the intrinsic losses in the graphene sheets. To test this idea, we have calculated the FFRHT for these graphene sheets assuming a larger value for the scattering energy $\mathcal{E}_s$. Fig. 7.5(a) shows the normalized 2D conductivity of graphene for $\mathcal{E}_s = 0.01$ eV, i.e., two orders of magnitude larger than in the examples above. The corresponding results for the absorption efficiency $Q_{\rm TE}(\omega)$ are displayed in Fig. 7.5(b). The absorption cross section is again orders of magnitude larger than the geometrical one and, more importantly, it is also higher than in the previous case. Fig. 7.5(c) shows the spectral $G_{\rm th}$ for $L_z = 10$ μm, $\mathcal{E}_s = 0.01$ eV, and a gap $d = 1$ mm. In this case the maximum of the spectral $G_{\rm th}$ is strongly

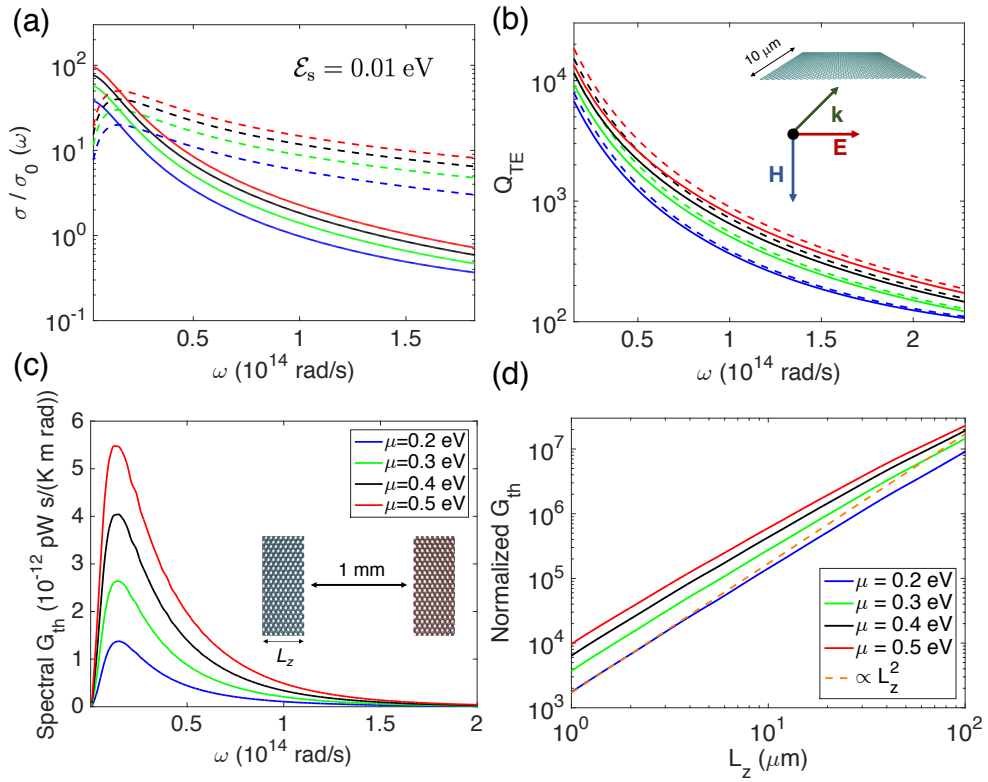

Figure 7.5: (a) Real (solid lines) and imaginary (dashed lines) part of the normalized conductivity of graphene for $T = 300$ K and $\mathcal{E}_s = 0.01$ eV, for different chemical potentials (μ). (b) Frequency-dependent absorption efficiency for a plane wave with TE polarization ($Q_{TE}(\omega)$) and normal incidence into a graphene sheet with length $L_z = 10$ μm and infinite width (see inset), for different values of μ. The solid lines correspond to the exact numerical results, while the dashed lines were obtained with Eq. (7.8). (c) Spectral G_{th} as a function of ω for a system composed of two graphene flakes of length $L_z = 10$ μm, $\mathcal{E}_s = 0.01$ eV, and a gap $d = 1$ mm (see inset). (d) G_{th}, normalized by the blackbody results, for the same system and plotted as a function of L_z for different chemical potentials. The dashed orange line is proportional to L_z^2.

blueshifted ($\omega = 1.3 \times 10^{13}$ rad/s), and the relevant frequencies for the FFRHT are also higher. The reason for this blueshift is that $Q_{TE}(\omega)$ adopts larger values at frequencies which have a better overlap with Planck distribution function at room temperature. As a consequence, the total thermal conductance G_{th} is much higher in this case, as we illustrate in Fig. 7.5(d). Notice that in this case the Planckian limit can be overcome by more than 7 orders of magnitude. Thus, we see here that the graphene with a high density of impurities (i.e., with low mobility), which is normally dismissed for optoelectronic and plasmonic applications, is more efficient regarding thermal emission and absorption.

For the sake of comparison, we have also analyzed the FFRHT between two graphene sheets of the same dimensions as those of Fig. 7.5(c) ($\mu = 0.3$ eV) now parallel to each other and separated by a distance d along the normal direction. In that case,

the geometrical cross section is 27000 times larger than in the coplanar configuration and Planck's law would thus predict 27000^2 higher heat transfer efficiency than in the coplanar case. However, the FFRHT between the graphene sheets in this case is only 4 times larger and it does not exhibit an enhancement over Planck's law. Indeed, the ratio with the blackbody results is 1.5×10^{-3}. This confirms that the FFRHT between coplanar sheets is truly remarkable and that its absolute value is comparable with other setups that have a much higher geometrical cross section. Moreover, we have performed additional simulations to verify if such FFRHT could be measured in a realistic experimental setup. We have calculated the FFRHT between two graphene sheets with $L_x = 20$ μm, $L_z = 60$ μm, $\mu = 0.5$ eV, $\mathcal{E}_s = 0.01$ eV and separated by a gap of 20 μm, where the thermal radiation is already dominated by the far-field contribution [15]. The dimensions chosen for both the graphene sheets and the gap are within reach of state-of-the-art calorimetric techniques[70, 158]. In order to compute the FFRHT, we have again made use of the code SCUFF-EM [39, 82]. The room-temperature linear heat conductance between the flakes is in this case 1.62 pW/K, which is within the sensitivity of existent calorimetric techniques [70, 158].

7.3. Results for single-layer black phosphorus

At this point one may wonder whether the dramatic violation of Planck's law discussed above for the case of graphene may also occur in other 2D materials. To show that this is actually the case, we now turn to analyze the case of single-layer black phosphorus (SLBP). We have computed the FFRHT between two coplanar SLBP sheets (see Fig. 7.1(a)). The distinctive steps of the atomic structure of SLBP are in our case placed along the z-direction. We have modeled the dielectric properties of a black phosphorus monolayer in an analogous way to graphene and its 2D conductivity has been taken from previous studies [181]. Let us mention that we have modeled black phosphorous (BP) as an isotropic body. As there are only electric fields oscillating in the x-direction ($Q_{TM}(\omega) = 0$, see Figs. 7.1 and 7.6(b)), we can model our BP monolayer as having an isotropic conductivity. Both the real (solid line) and the imaginary (dashed line) part of the conductivity of SLBP along the x-direction are plotted in Fig. 7.6(a) for $T = 300$ K, $\mathcal{E}_s = 0.01$ eV, and two different electron dopings $n = 5\times10^{13}$ cm^{-2} and $n = 10^{14}$ cm^{-2}. The parameters chosen represent realistic SLBP samples [182]. Fig. 7.6(b) shows $Q_{\mathrm{TE}}(\omega)$

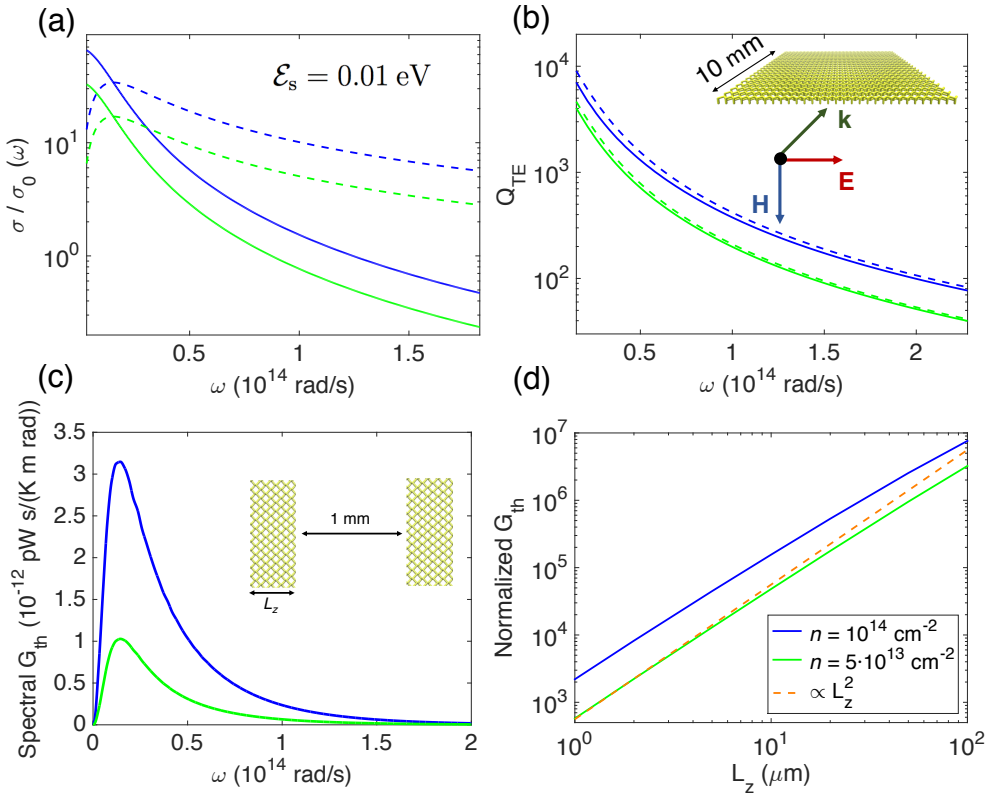

Figure 7.6: (a) Real (solid lines) and imaginary (dashed lines) part of the normalized conductivity of single-layer black phosphorus for $T = 300$ K and $\mathcal{E}_s = 0.01$ eV, for two different dopings (n). (b) Frequency-dependent absorption efficiency for a plane wave with TE polarization ($Q_{TE}(\omega)$) and normal incidence into a SLBP sheet with length $L_z = 10$ μm and infinite width (see inset). The solid lines correspond to the exact numerical results, while the dashed lines were obtained with Eq. (7.8). (c) Spectral G_{th} as a function of ω for a system composed of two SLBP flakes of length $L_z = 10$ μm separated by a gap $d = 1$ mm (see inset). (d) Thermal conductance G_{th}, normalized by the blackbody results, for the same system as in panel (c) and plotted as a function of L_z, for two different dopings. The dashed orange line is proportional to L_z^2.

calculated numerically (solid lines) with COMSOL MULTIPHYSICS (see Supporting Information) for a SLBP sheet with $L_z = 10$ μm (see inset of Fig. 7.6(b)) and both doping values. The SLBP absorption efficiency exhibits very similar characteristics to those of low-quality graphene, as both of them have similar dielectric functions for infrared frequencies. Moreover, $Q_{TE}^{an}(\omega)$ (dashed lines) shows again an excellent agreement with the exact numerical simulations. As for graphene, we have used the results for $Q_{TE}(\omega)$ in combination with Eq. (7.3) to describe the FFRHT. The spectral conductance of black phosphorus monolayers separated by 1 mm is plotted in Fig. 7.6(c), while the normalized total thermal conductance as a function of the length L_z is shown in Fig. 7.6(d). Notice that in this case the FFRHT can be larger than the corresponding result calculated

from Planck's law by almost 7 orders of magnitude, showing that this enhancement is not exclusive of graphene, but can also occur in other 2D materials such as SLBP.

7.4. Conclusions

In summary, we have presented a theoretical analysis of the FFRHT between 2D materials, graphene and single-layer black phosphorus, in a coplanar configuration. We have shown that the relevant absorption cross section of flakes of these materials can be orders of magnitude larger than their atomic-sized geometrical cross section. We have also shown that this extraordinary absorption efficiency makes the FFRHT between flakes of these materials more than 7 orders of magnitude larger than the limit set by Planck's law, which constitutes the ultimate violation of this law in the far-field regime. Finally, we have shown that the novel mechanism responsible for this FFRHT involves the propagation properties of TE-polarized guiding modes in these materials, modes that are usually irrelevant in the context of plasmonic or optoelectronic applications.

8 | General conclusions and outlook

8.1. English

In this thesis we have tackled some of the open problems in the field of radiative heat transfer (RHT). In Chapters 2-5, we have analyzed the near-field radiative heat transfer (NFRHT) between two objects in a variety of scenarios. On the other hand, we have studied in Chapters 6-7 the far-field radiative energy exchange between subwavelength objects. In this last chapter, we present the general conclusions of the thesis together with an outlook about the future perspectives in the field of RHT.

8.1.1. Near-field radiative heat transfer

Let us start by summarizing the main conclusions obtained of Chapter 2-5, which have analyzed NFRHT in different situations. We have explained in the General Introduction (Chapter 1) that the RHT can be greatly enhanced in the near-field due to the contribution of evanescent waves. However, whether this enhancement can be obtained with thin films remained unanswered. In Chapter 2 we have demonstrated a dramatic increase in NFRHT, comparable to that obtained between bulk materials, even for very thin dielectric films (50-100 nm) when the spatial separation between the hot and cold surfaces is comparable to the film thickness. This study was performed in collaboration with the experimental group of Professors Pramod Reddy and Edgar Meyhofer of the University of Michigan. We have explained our results by analyzing the spectral characteristics and mode shapes of surface phonon-polaritons, which dominate near-field radiative heat transport in polar dielectric thin films. We have shown that in the limit of small gaps, the penetration depth of these modes is of the order of the gap size and it is independent of the coating thickness. Therefore, for gaps smaller than the film thickness, a SiO_2 coating

film exchanges the same radiative energy than a bulk SiO_2 sample.

NFRHT is a physical phenomenon which could have deep implications in the development of novel thermal technologies. To this goal, it would be convenient to actively tune the radiative heat flow in the near-field. This was the motivation to analyze theoretically in Chapter 3 the magnetic field dependence of the NFRHT between two parallel plates. We have shown that when the plates are made of doped semiconductors, the near-field thermal radiation can be greatly affected by the application of a static magnetic field. We have found that irrespective of its direction, the presence of a magnetic field reduces the radiative heat conductance, and dramatic reductions up to a factor of 7 can be found with fields of a few Teslas at room temperature. We have explained that this striking behavior is due to the fact that the magnetic field radically changes the nature of the NFRHT. The field not only affects the electromagnetic surface modes (both plasmons and phonon-polaritons) that normally dominate the near-field radiation in doped semiconductors, but it also induces hyperbolic modes that progressively dominate the heat transfer as the field increases. In particular, we have shown that when the field is perpendicular to the plates, the semiconductors become ideal hyperbolic near-field emitters. Our study paves the way for an active control of NFRHT and it opens the possibility to study unique hyperbolic thermal emitters without the need to resort to complicated metamaterials.

As commented above, the energy exchanged by radiation between two bodies can be enhanced by orders of magnitude in the near-field. Until recently, the extended materials which exhibited the highest thermal conductance in this regime were polar dielectrics, in which the NFRHT is dominated by surface phonon polaritons. In Chapter 4 we have demonstrated that the use of metasurfaces provides a viable strategy to largely tune and enhance NFRHT between extended structures. In particular, using a rigorous coupled wave analysis, we have predicted that Si-based metasurfaces featuring two-dimensional periodic arrays of holes can exhibit a room-temperature near-field radiative heat conductance much larger than any unstructured material to date. We have shown that this enhancement, which takes place in a broad range of separations, relies on the existence of broadband surface plasmon-polaritons (SPPs) in doped Si and the possibility to largely tune the properties of these modes that dominate the radiative heat transfer in the near-field regime. By introducing holes in the Si metasurfaces, one can reduce both the effective plasma frequency and the losses in the material. Therefore, these SPPs are redshifted and can be more easily occupied at room temperature, leading to a larger radiative heat flow in the near-field.

The physical mechanisms which dominate NFRHT were well understood down to sep-

aration distances of 10 nm between two bodies. However, for smaller gap distances, it was still unclear if fluctuational electrodynamics (FE) was able to describe the radiative heat flow exchange. To better understand this phenomenon, we have studied in Chapter 5 from both theoretical and experimental points of view the NFRHT in the extreme near field (gaps smaller than 10 nm) between metals and polar dielectrics. From the experimental side, our colleagues of the University of Michigan have developed custom-fabricated scanning probes with embedded thermocouples, in conjunction with new microdevices capable of periodic temperature modulation, to measure RHT down to gaps as small as two nanometers. To theoretically simulate this process, we have used the fluctuating-surface-current formulation of the RHT combined with the boundary element method, as implemented in the SCUFF-EM solver. Using this approach, we have computed the NFRHT between the exact geometries involved in the experiments, considering even the nanometric-roughness at the devices. In order to obtain accurate results for the radiative heat flow between micro-sized objects separated by single-nanometer distances, we have employed a non-uniform grid that was finer at both the tip apex and at the center of the simulated samples. We have found that our state-of-the-art calculations of RHT, performed within the framework of FE, are in excellent agreement with the experimental measurements, providing unambiguous evidence that confirms the validity of this theory down to gap distances of $\sim$ 2-3 nm, for both metals and dielectrics. Moreover, our work suggests that the giant thermal conductances found by previous experiments in this regime are originated by the existence of contaminants between the scanning thermal tip and the substrate.

8.1.2. Far-field radiative heat transfer

The two last chapters are devoted to analyze the far-field radiative heat transfer (FFRHT) between two subwavelength objects. In Chapter 6, we have presented a theoretical analysis that demonstrates that the FFRHT between objects with dimensions smaller than the thermal wavelength can overcome the Planckian limit by orders of magnitude. To guide the search for super-Planckian FFRHT, we have considered the theory of FE to derive a relation between the FFRHT and the directional absorption efficiency of the objects involved. Guided by this relation, and making use of state-of-the-art numerical simulations, we have shown that the far-field radiative energy exchange between highly anisotropic objects can largely overcome the black-body limit when some of their dimensions are smaller than the thermal wavelength. In particular, we have illustrated this phenomenon in the case of suspended pads made of polar dielectrics like SiN or SiO_2.

These structures are widely used to measure the thermal transport through nanowires and low-dimensional systems and can be employed to test our predictions. We have shown that the standard theories of thermal radiation are unable to predict the FFRHT between micro- and nanodevices.

Finally, in Chapter 7 we have explored the ultimate limit of the far-field violation of Planck's law. We have presented a theoretical study of the RHT between two-dimensional (2D) materials. We have shown that the far-field thermal radiation exchanged by two coplanar systems with a one-atom-thick geometrical cross section can be more than 7 orders of magnitude larger than the theoretical limit set by Planck's law for blackbodies and can be comparable to the heat transfer of two parallel sheets at the same distance. In particular, we have illustrated this phenomenon with different materials such as graphene, where the radiation can also be tuned by a external gate, and single-layer black phosphorus. In both cases the FFRHT is dominated by TE-polarized guiding modes, which are normally irrelevant for plasmonic and optoelectronic applications. Our predictions provide a new insight into the thermal radiation exchange mechanisms between 2D materials.

8.1.3. Outlook

The research field of radiative heat transfer has experienced a significant advance in the last years. However, there are still multiple open questions which will keep the activity and interest in the field in the future.

From a fundamental point of view, one of the main challenges is to understand the mechanisms that govern the energy exchange in the crossover regime between conduction and radiation, *i.e.*, when the gap between two objects is subnanometric. In dielectrics, it has been predicted that the heat conductance can be further enhanced in subnanometer gaps due to the tunneling of acoustic phonons [19]. In metals, however, it is still not clear at which distances the electronic contribution to the heat flow dominates over the photonic one [183]. New theoretical microscopic models must go beyond FE in order to analyze how two objects exchange energy in this very interesting regime [19], where electrons, photons and phonons can transport energy between two bodies.

Another research line which can be very promising is the study of radiative heat exchange between objects at cryogenic temperatures. In that case, the thermal wavelength can be increased up to ~ 1 mm, so near-field effects would arise at macroscopic distances. Moreover, the radiative heat transfer between superconducting materials at temperatures below their critical temperature could be analyzed. In this regime, the ra-

diative heat flow would be dominated by very different mechanisms and new interesting phenomena could arise.

From the experimental point of view, many advances could be performed to further increase the measured heat flows. The current experimental techniques show a trade off between heat conductance intensity and gap distance. The highest radiative heat flows have been obtained in the plate-plate configuration, where all the setup has a subwavelength gap distance. However, because of alignment issues, it is not possible to reach gaps smaller than $\sim$ 70 nm [44]. In order to reach nanometer gaps, scanning thermal probes are needed, but their nanometer size imply that the obtained radiative thermal conductances are approximately $\sim$ 1-10 nW K^{-1} [140], depending on the size of the scanning tip. New experimental advances are needed in order to develop setups where the radiative heat flow enhancement is exploited to its maximum level.

Besides, there are several interesting predictions for the heat flow in the nanoscale which have not been measured yet, such as the tuning of NFRHT by a magnetic field (Chapter 3) or the extraordinary heat conductance between doped-Si metasurfaces (Chapter 4). In order to realize these interesting proposals, it will be necessary to combine the novel setups able to quantify NFRHT [44, 140] together with the current developments in nanofabrication. There are also several existing proposals of technological applications for the enhancement of radiative heat transfer in the near-field, such as the fabrication of near-field thermophotovoltaic cells [58–60] and the realization of high-resolution thermal lithography [16]. So far, these ideas have not been realized due to technical difficulties. In the next years, new efforts should be made to improve the experimental systems and finally build these setups which will for sure improve the performance of multiple devices.

On the other hand, the new insights that we provide for the far-field radiative heat transfer should be considered in the fabrication of new nanodevices, where the dimensions of the different components are smaller than the thermal wavelength. In those cases, the radiative heat transfer between the parts of the system are estimated using the upper limit given by Planck's law for blackbodies. We have shown that the radiative heat flow can be orders of magnitude larger than this limit, so exact numerical calculations should be performed to characterize the thermal properties of these systems.

Thermal radiation is a universal phenomenon which is present in numerous aspects of our daily life: from the light coming from the sun to the radiation of a fireplace. Improving the knowledge of this process will generate new ways of controlling the radiative energy, and, therefore, will increase the quality of life of the society. We hope that this thesis is a small step towards this direction.

8.2. Español

En esta tesis hemos resuelto algunos de los problemas abiertos en el campo de la transferencia radiativa de calor (TRC). En los Capítulos 2-5, hemos analizado la transferencia radiativa de calor en el campo cercano (TRCCC) en distintas situaciones. Por otro lado, hemos estudiado en los Capítulos 6-7 el intercambio radiativo de energía en el campo lejano entre objetos cuyas dimensiones son más pequeñas que la longitud de onda. En este último capítulo presentamos las conclusiones generales de la tesis junto a una perspectiva sobre el futuro del campo de la TRC.

8.2.1. Transferencia radiativa de calor en el campo cercano

Comenzaremos resumiendo las conclusiones principales obtenidas en los Capítulos 2-5, en los que se ha analizado la TRCCC en distintos casos. Hemos explicado en la Introducción general (Capítulo 1) que la TRC puede aumentar notablemente en el campo cercano debido a la contribución de ondas evanescentes. Sin embargo, todavía no se sabía si este aumento podía obtenerse con láminas delgadas de materiales polares como el sílice (SiO_2). En el Capítulo 2 hemos demostrado un aumento dramático en la transferencia de calor, comparable al que se obtiene entre muestras de materiales en volumen, en láminas nanométricas de dieléctricos (50-100 nm) cuando la distancia de separación entre las superficies fría y caliente es comparable al grosor de la lámina. Este estudio fue realizado en colaboración con el grupo experimental de los profesores Pramod Reddy y Edgar Meyhofer de la Universidad de Míchigan. Hemos explicado nuestros resultados analizando las características de los fonones-polaritones de superficie. En concreto, hemos mostrado que en el límite de separaciones pequeñas entre dos cuerpos, la longitud de penetración de estos modos es del orden de la distancia de separación e independiente del grosor de la lámina. Por tanto, para separaciones más pequeñas que el grosor de la lámina, una fina película de SiO_2 intercambia la misma energía radiativa que una muestra del material en volumen.

La TRCCC es un fenómeno físico que podría tener profundas implicaciones en el desarrollo de nuevas tecnologías térmicas. Para ello, sería conveniente poder modificar externamente el flujo de calor en el campo cercano. Esta fue la motivación para analizar teóricamente en el Capítulo 3 la dependencia con el campo magnético de la transferencia radiativa de calor en el campo cercano. Hemos mostrado que la radiación térmica en el campo cercano entre dos superficies de semiconductores dopados puede ser sensiblemente afectada por la aplicación de un campo magnético estático. Hemos encontrado que para

cualquier dirección del campo magnético, éste reduce la conductancia radiativa y grandes reducciones de hasta un factor 7 pueden producirse empleando campos magnéticos de unos pocos Teslas a temperatura ambiente. El campo magnético no sólo afecta a los modos electromagnéticos de superficie (tanto plasmones como fonones-polaritones) que normalmente dominan la radiación en el campo cercano en semiconductores dopados, sino que también induce modos hiperbólicos que dominan progresivamente la transferencia de calor según aumenta el campo. En particular, hemos demostrado que cuando el campo es perpendicular a la superficies, los semiconductores se convierten emisores hiperbólicos ideales en el campo cercano. Nuestro estudio allana el camino para un control activo de la TRCCC y abre la posibilidad de estudiar emisores térmicos hiperbólicos sin la necesidad de recurrir a metamateriales complejos.

Como hemos visto anteriormente, la energía intercambiada por radiación entre dos cuerpos puede aumentar en órdenes de magnitud en el campo cercano. Hasta hace poco, los materiales que exhibían una mayor conductancia térmica en este régimen eran los dieléctricos polares, en los que la TRCCC está dominada por fonones-polaritones de superficie. En el Capítulo 4 hemos demostrado que el uso de metasuperficies es una estrategia plausible para modificar y aumentar notablemente la TRCCC entre estructuras planas. En concreto, expresando los campo eléctricos como suma de ondas planas y utilizando el formalismo de la matriz de scattering, hemos predicho que metasuperficies de silicio dopado que contienen una red periódica de agujeros exhiben en el campo cercano una conductancia térmica a temperatura ambiente mayor que la de cualquier otro material sin estructurar. Hemos mostrado que este aumento de la TRCCC, que ocurre en un amplio rango de distancias de separación, se debe a la existencia de plasmones-polaritones de superficie (PPS) en silicio dopado y a la posibilidad de modificar las propiedades de estos modos, que son los que dominan la TRCCC. En concreto, introduciendo agujeros en las metasuperficies de silicio, es posible reducir tanto la frecuencia de plasma efectiva como las pérdidas en el material. Por tanto, estos PPS se desplazan hacia frecuencias menores y pueden ser ocupados más fácilmente a temperatura ambiente, produciendo un mayor flujo radiativo de calor en el campo cercano.

Los mecanismos físicos que dominan la TRCCC se conocían bien hasta distancias de separación entre dos cuerpos de 10 nm. Sin embargo, para distancias menores, no estaba claro si la teoría denominada "fluctuational electrodynamics" (FE) era capaz de describir correctamente el flujo de calor radiativo. Para conocer mejor este fenómeno, hemos estudiado en el Capítulo 5 desde un punto vista tanto teórico como experimental la TRCCC en el régimen de campo cercano extremo (distancias menores a 10 nm) entre tanto metales como dieléctricos polares. Desde el punto de vista experimental, nuestros

colaboradores de la Universidad de Míchigan han desarrollado una nueva tecnología que incluye unas puntas AFM que incorporan un termopar y unos nuevos microdispositivos capaces de modular periódicamente su temperatura. Empleando estos dispositivos, han sido capaces de medir la TRC hasta distancias de separación de 2 nm. Para simular teóricamente este proceso, hemos empleado la formulación de la TRC basada en corrientes fluctuantes de superficie combinada con el "boundary element method", tal y como está implementada en SCUFF-EM. Utilizando este enfoque, hemos calculado la TRCCC entre las geometrías exactas empleadas en el sistema experimental, teniendo en cuenta hasta la rugosidad nanométrica existente en los dispositivos. Para obtener resultados correctos del flujo de calor radiativo entre objetos de tamaño micrométrico separados por distancias de hasta 1 nm, hemos utilizado mallados no uniformes que eran más precisos tanto en el final de la punta como en el centro de la muestra simulada. Hemos mostrado que nuestros cálculos de la TRC, realizados en el marco teórico de la teoría FE, muestran un acuerdo excelente con los resultados experimentales. Por tanto, hemos demostrado la validez de esta teoría para describir la TRC hasta distancias de separación entre los cuerpos de $\sim$ 2-3 nm, tanto en metales como en dieléctricos. Además, los resultados mostrados en el Capítulo 5 sugieren que las enormes conductancias térmicas medidas en experimentos previos en este mismo régimen están debidas a la existencia de contaminantes entre la punta y la muestra.

8.2.2. Transferencia radiativa de calor en el campo lejano

Los últimos dos capítulos están dedicados a analizar la transferencia radiativa de calor en el campo lejano (TRCCL) entre objetos cuyas dimensiones son menores a la longitud de onda. En el Capítulo 6, hemos presentado un análisis teórico que demuestra que la TRCCL entre objetos pequeños puede superar el límite Planckiano en órdenes de magnitud. Para guíar la búsqueda de la TRCCL super-Planckiana, hemos utilizado la teoría FE para derivar una relación entre la TRCCL y la eficiencia de absorción direccional de los objetos involucrados. Guiados por esta relación y empleando simulaciones numéricas, hemos mostrado que el intercambio radiativo de calor en el campo lejano entre objetos asimétricos puede sobrepasar notablemente el límite para cuerpos negros cuando algunas de las dimensiones del objeto son menores que la longitud de onda térmica. En concreto, hemos ilustrado este fenómeno con micro-dispositivos de dieléctricos polares como el SiN y el SiO_2. Estas estructuras son ampliamente empleadas para medir el transporte térmico a través de nanocables y sistemas bidimensionales y pueden ser utilizadas para comprobar nuestras predicciones teóricas. Hemos demostrado también

que las teorías estándar de radiación térmica son incapaces de predecir la TRCCL entre micro- y nanodispositivos.

Finalmente, en el Capítulo 7 hemos explorados los límites de la TRC súper Planckiana en el campo lejano. Hemos presentado un estudio teórico de la TRC entre materiales bidimensionales (2D). Hemos mostrado que la radiación térmica intercambiada en el campo lejano entre dos sistemas coplanares con una sección eficaz geométrica de un átomo de grosor puede ser más de 7 órdenes de magnitud mayor que el límite teórico establecido por la ley de Planck para cuerpos negros. Hemos illustrado este fenómeno con distintos materiales como el grafeno, en el que la radiación intercambiada puede modificarse con un voltaje externo, y las monocapas de fósforo negro. En ambos casos, la TRCCL está dominada por modos guiados con polarización TE, que son normalmente irrelevantes en aplicaciones plasmónicas y optoelectrónicas. Los resultados mostrados en este capítulo mejoran el conocimiento de los mecanismos de intercambio de radiación térmica entre materiales 2D.

8.3. Perspectiva futura del campo

El campo de investigación de la transfencia radiativa de calor ha experimentado un avance significante en los últimos años. Sin embargo, todavía hay muchas preguntas abiertas que mantendrán la actividad y el interés en el campo durante los próximos años.

Desde un punto de vista fundamental, uno de los restos principales es comprender los mecanismos que dominan el intercambio de energía en el régimen intermedio entre conducción y radiación, es decir, cuando el gap entre dos objetos es subnanométrico. En materiales dieléctricos, algunos trabajos han predicho que la conductancia térmica puede ser aumentada todavía más en el régimen subnanométrico debido al túnel de fonones acústicos [19]. En metales, en cambio, todavía no está claro a qué distancias la contribución electrónica al flujo de calor domina sobre la fotónica [183]. Nuevos modelos teóricos microscópicos deben ir más allá de la teoría FE para analizar cómo intercambian energía dos objetos en este régimen tan interesante [19], en el que electrones, fotones y fonones pueden transportar energía entre dos cuerpos.

Otra línea de investigación que podría ser muy prometedora es el estudio de la TRC entre objetos a temperaturas criogénicas. En este caso, la longitud de onda térmica puede llegar a ser de hasta $\sim$ 1 mm, por lo que los efectos del campo cercano podrían aparecer a distancias macroscópicas. Además, la TRC entre materiales superconductores

a temperaturas menores que su temperatura crítica podría ser analizada. En este régimen, el flujo radiativo de calor estaría dominado por mecanismos completamente nuevos y podrían aparecer nuevos fenómenos físicos.

Desde el punto de vista experimental, podrían llevarse a cabo numerosos avances para mejorar la medida del flujo de calor en el campo cercano. Las técnicas experimentales actuales no son capaces de medir un alto flujo de radiación a distancias de separación nanométricas. Las TRCCC más altas han sido obtenidos en la configuración plano-plano, en el que todo el sistema experimental está situado a una distancia menor que la longitud de onda térmica. Sin embargo, debido a problemas de alineamiento, no es posible alcanzar gaps menores a $\sim$ 70 nm con este sistema [44]. Para alcanzar distancias de separación menores, es necesario utilizar puntas de AFM o STM, pero su tamaño nanométrico implica que las conductancias radiativas obtenidas son mucho menores y del orden de $\sim 1 - 10$ nWK^{-1} [140], dependiendo del tamaño de la punta. Se necesitan por tanto nuevos avances experimentales para desarrollar sistemas en los que el aumento de flujo radiativo de calor sea explotado al máximo.

Además, hay muchas predicciones teóricas interesantes sobre el flujo de calor en la nanoescala que todavía no se han medido, como la modificación de la TRCCC con campos magnéticos (Capítulo 3) o la conductancia térmica extraordinaria entre metasuperficies de Si dopado (Capítulo 4). Para llevar a cabo estas propuestas, será necesario combinar los experimentos actuales capaces de cuantificar la TRCCC [44, 140] con los últimos avances en nanofabricación. Hay también varias propuestas teóricas de aplicaciones tecnológicas para el aumento de la radiación térmica en el campo cercano, como la fabricación de células termofotovoltaicas de campo cercano [58–60] y el desarrollo de litografía térmica de alta resolución [16]. Hasta ahora, estas ideas no se han llevado a cabo debido a dificultades técnicas. En los próximos años, nuevos proyectos deben llevarse a cabo para mejorar los sistemas experimentales actuales y construir finalmente estas propuestas que sin duda mejorarán el funcionamiento de múltiples dispositivos.

Por otro lado, el nuevo conocimiento que hemos aportado sobre la TRCCL debe ser considerado en la fabricación de nuevos nanodispositivos, en los que las dimensiones de los distintos componentes son más pequeñas que la longitud de onda térmica. En este caso, la TRC entre las partes del sistema se estima actualmente utilizando la cota superior dada por la ley de Planck para cuerpos negros. Hemos demostrado que el flujo radiativo de calor puede ser órdenes de magnitud mayor que este límite, por lo que deben llevarse a cabo simulaciones numéricas exactas para caracterizar las propiedades térmicas de estos sistemas.

La radiación térmica es un fenómeno universal que está presente en numerosas ac-

tividades de nuestro día a día: desde la luz que viene del sol hasta la radiación de una chimenea. Mejorar el conocimiento de este fenómeno generará nuevas formas de controlar la energía radiativa, y, por tanto, aumentará la calidad de vida de la sociedad. Esperamos que esta tesis sea un pequeño paso en esta dirección.

A | Scattering matrix approach for anisotropic multilayer systems.

Our analysis of the radiative heat transfer is based on the combination of Rytov's fluctuational electrodynamics (FE) and a scattering matrix formalism that describes the propagation of electromagnetic waves in multilayer systems made of optically anisotropic materials. As we show in Appendix B, the radiative heat transfer can be expressed in terms of the scattering matrix of our system. Thus, it is convenient to first discuss in this appendix the scattering matrix approach employed in this work ignoring for the moment the fluctuating currents that generate the thermal radiation. Later in Appendix B, we show how this approach can be combined with FE. We follow here Ref. [108], which presents a generalization of the formalism introduced by Whittaker and Culshaw in Ref. [80] for isotropic systems.

Let us first describe the Maxwell's equations to be solved. Assuming a harmonic time dependence $\exp(-i\omega t)$, the Maxwell's equations for non-magnetic materials and in the absence of currents adopt the following form: $\nabla\cdot\epsilon_0\hat{\epsilon}\mathbf{E}=0$, $\nabla\cdot\mathbf{H}=0$, $\nabla\times\mathbf{H}=-i\omega\epsilon_0\hat{\epsilon}\mathbf{E}$, and $\nabla\times\mathbf{E}=i\omega\mu_0\mathbf{H}$, where the permittivity is in general a tensor given by Eq. (3.1). The first Maxwell's equation is automatically satisfied if the third one is fulfilled, and the second one can be satisfied by expanding the magnetic field in terms of basis functions with zero divergence. Following Ref. [80], it is convenient to introduce the rescaling: $\omega\epsilon_0\mathbf{E}\rightarrow\mathbf{E}$ and $\sqrt{\mu_0\epsilon_0}\omega=\omega/c\rightarrow\omega$. Thus, the final two equations to be solved are

$$\nabla\times\mathbf{H} = -i\hat{\epsilon}\mathbf{E}, \tag{A.1}$$

$$\nabla\times\mathbf{E} = i\omega^2\mathbf{H}. \tag{A.2}$$

We consider here a planar multilayer system grown along the z-direction in which the

tensor $\hat{\epsilon}$ is constant inside every layer, *i.e.* it is independent of the in-plane coordinates $\mathbf{r} \equiv (x, y)$. Thus, for an in-plane wave vector $\mathbf{k} \equiv (k_x, k_y)$, we can write the fields as

$$\mathbf{H}(\mathbf{r}, z) = \boldsymbol{h}(z) e^{i\mathbf{k}\cdot\mathbf{r}} \text{ and } \mathbf{E}(\mathbf{r}, z) = \boldsymbol{e}(z) e^{i\mathbf{k}\cdot\mathbf{r}}. \tag{A.3}$$

With this notation, Eqs. (A.1) and (A.2) can be rewritten as

$$ik_y h_z(z) - h_y'(z) = -i \sum_j \epsilon_{xj} e_j(z) \tag{A.4}$$

$$h_x'(z) - ik_x h_z(z) = -i \sum_j \epsilon_{yj} e_j(z) \tag{A.5}$$

$$ik_x h_y(z) - ik_y h_x(z) = -i \sum_j \epsilon_{zj} e_j(z), \tag{A.6}$$

and

$$ik_y e_z(z) - e_y'(z) = i\omega^2 h_x(z) \tag{A.7}$$

$$e_x'(z) - ik_x e_z(z) = i\omega^2 h_y(z) \tag{A.8}$$

$$ik_x e_y(z) - ik_y e_x(z) = i\omega^2 h_z(z), \tag{A.9}$$

where the primes stand for ∂_z. Now our task is to solve the Maxwell's equations for an unbounded layer. For this purpose, we write the magnetic field $\boldsymbol{h}(z)$ as follows

$$\boldsymbol{h}(z) = e^{iqz} \left\{ \phi_x \hat{\mathbf{x}} + \phi_y \hat{\mathbf{y}} - \frac{1}{q}(k_x \phi_x + k_y \phi_y) \hat{\mathbf{z}} \right\}, \tag{A.10}$$

where $\hat{\mathbf{x}}$, $\hat{\mathbf{y}}$, and $\hat{\mathbf{z}}$ are the Cartesian unit vectors and q is the z-component of the wave vector. Here, ϕ_x and ϕ_y are the expansion coefficients to be determined by substituting into Maxwell's equations. Notice that this expression satisfies $\nabla \cdot \mathbf{H} = 0$. Now, it is convenient to rewrite the previous expression in the vector notation:

$$\boldsymbol{h}(z) = e^{iqz} \left(\phi_x, \phi_y, -\frac{1}{q}(k_x \phi_x + k_y \phi_y) \right)^T. \tag{A.11}$$

With this notation, Eqs. (A.4-A.6) can be written as

$$\hat{\mathcal{C}} \boldsymbol{h}(z) = \hat{\epsilon} \boldsymbol{e}(z), \text{ where } \hat{\mathcal{C}} = \begin{pmatrix} 0 & q & -k_y \\ -q & 0 & k_x \\ k_y & -k_x & 0 \end{pmatrix}. \tag{A.12}$$

On the other hand, Eqs. (A.7-A.9) adopt now the form

$$\hat{\mathcal{C}}^T \boldsymbol{e}(z) = \omega^2 \boldsymbol{h}(z). \tag{A.13}$$

From Eq. (A.12) we obtain the following expression for the electric field

$$\boldsymbol{e}(z) = \hat{\eta}\hat{\mathcal{C}}\boldsymbol{h}(z), \tag{A.14}$$

where $\hat{\eta} = \hat{\epsilon}^{-1}$. Substituting this expression in Eq. (A.13) we obtain the following equation for the magnetic field

$$\hat{\mathcal{C}}^T \hat{\eta}\hat{\mathcal{C}}\boldsymbol{h}(z) = \omega^2 \boldsymbol{h}(z), \tag{A.15}$$

which defines an eigenvalue problem for ω^2. Indeed, only two of the three identities obtained from this equation, one for each $\hat{\mathbf{x}}$, $\hat{\mathbf{y}}$, and $\hat{\mathbf{z}}$, are independent. From the first two identities, and using Eq. (A.11), we obtain the following equations determining the allowed values for q

$$\left(\hat{\mathcal{A}}_2 q^2 + \hat{\mathcal{A}}_1 q + \hat{\mathcal{A}}_0 + \hat{\mathcal{A}}_{-1}\frac{1}{q}\right)\phi = 0, \tag{A.16}$$

where $\phi = (\phi_x, \phi_y)^T$ and the 2×2 matrices $\hat{\mathcal{A}}_n$ are defined by

$$\begin{aligned}
\hat{\mathcal{A}}_2 &= \begin{pmatrix} \eta_{yy} & -\eta_{yx} \\ -\eta_{xy} & \eta_{xx} \end{pmatrix}, \\
\hat{\mathcal{A}}_1 &= \hat{\mathcal{A}}_1^{(a)} + \hat{\mathcal{A}}_1^{(b)} = \begin{pmatrix} -k_y\eta_{zy} & k_y\eta_{zx} \\ k_x\eta_{zy} & -k_x\eta_{zx} \end{pmatrix} + \begin{pmatrix} -k_y\eta_{yz} & k_x\eta_{yz} \\ k_y\eta_{xz} & -k_x\eta_{xz} \end{pmatrix}, \\
\hat{\mathcal{A}}_0 &= \hat{\mathcal{A}}_0^{(a)} + \hat{\mathcal{A}}_0^{(b)} - \omega^2\hat{1} = \\
&= \begin{pmatrix} k_y^2\eta_{zz} & -k_xk_y\eta_{zz} \\ -k_xk_y\eta_{zz} & k_x^2\eta_{zz} \end{pmatrix} + \begin{pmatrix} k_x^2\eta_{yy} - k_xk_y\eta_{yx} & k_xk_y\eta_{yy} - k_y^2\eta_{yx} \\ k_xk_y\eta_{xx} - k_x^2\eta_{xy} & k_y^2\eta_{xx} - k_xk_y\eta_{xy} \end{pmatrix} - \omega^2\begin{pmatrix} 1 & 0 \\ 0 & 1 \end{pmatrix}, \\
\hat{\mathcal{A}}_{-1} &= \begin{pmatrix} k_y^2k_x\eta_{zx} - k_x^2k_y\eta_{zy} & k_y^3\eta_{zx} - k_y^2k_x\eta_{zy} \\ k_x^3\eta_{zy} - k_x^2k_y\eta_{zx} & k_x^2k_y\eta_{zy} - k_y^2k_x\eta_{zx} \end{pmatrix}.
\end{aligned} \tag{A.17}$$

This eigenvalue problem leads to the following quartic secular equation: $\sum_{n=0}^{4} D_n q^n = 0$,

where the coefficients are given by

$$
\begin{aligned}
D_4 &= \eta_{xx}\eta_{yy} - \eta_{xy}\eta_{yx}, \\
D_3 &= k_x\left[\eta_{xy}\eta_{yz} + \eta_{yx}\eta_{zy} - \eta_{yy}(\eta_{xz}+\eta_{zx})\right] + k_y\left[\eta_{yx}\eta_{xz} + \eta_{xy}\eta_{zx} - \eta_{xx}(\eta_{yz}+\eta_{zy})\right], \\
D_2 &= k_x^2\left[\eta_{yy}(\eta_{xx}+\eta_{zz}) - \eta_{xy}\eta_{yx} - \eta_{yz}\eta_{zy}\right] + k_y^2\left[\eta_{xx}(\eta_{yy}+\eta_{zz}) - \eta_{xy}\eta_{yx} - \eta_{xz}\eta_{zx}\right] \\
&\quad + k_xk_y\left[\eta_{xz}(\eta_{yz}+\eta_{zy}) + \eta_{yz}(\eta_{zx}-\eta_{xz}) - \eta_{zz}(\eta_{xy}+\eta_{yx})\right] - \omega^2(\eta_{xx}+\eta_{yy}), \\
D_1 &= k_x^3\left[\eta_{xy}\eta_{yz} + \eta_{yx}\eta_{zy} - \eta_{yy}(\eta_{xz}+\eta_{zx})\right] + k_y^3\left[\eta_{yx}\eta_{xz} + \eta_{xy}\eta_{zx} - \eta_{xx}(\eta_{yz}+\eta_{zy})\right] \\
&\quad + k_x^2k_y\left[\eta_{xy}\eta_{zx} + \eta_{xz}\eta_{yx} - \eta_{xx}(\eta_{yz}+\eta_{zy})\right] + k_y^2k_x\left[\eta_{yx}\eta_{zy} + \eta_{yz}\eta_{xy} - \eta_{yy}(\eta_{xz}+\eta_{zx})\right] \\
&\quad + \omega^2\left[k_x(\eta_{xz}+\eta_{zx}) + k_y(\eta_{yz}+\eta_{zy})\right], \\
D_0 &= k_x^4(\eta_{yy}\eta_{zz} - \eta_{yz}\eta_{zy}) + k_y^4(\eta_{xx}\eta_{zz} - \eta_{xz}\eta_{zx}) + k_x^3k_y\left[\eta_{xz}\eta_{zy} + \eta_{yz}\eta_{zx} - \eta_{zz}(\eta_{xy}+\eta_{yx})\right] \\
&\quad + k_y^3k_x\left[\eta_{yz}\eta_{zx} + \eta_{xz}\eta_{zy} - \eta_{zz}(\eta_{yx}+\eta_{xy})\right] + k_x^2k_y^2\left[\eta_{zz}(\eta_{xx}+\eta_{yy}) - \eta_{xz}\eta_{zx} - \eta_{yz}\eta_{zy}\right] \\
&\quad + \omega^2\left[\omega^2 - k_x^2(\eta_{yy}+\eta_{zz}) - k_y^2(\eta_{xx}+\eta_{zz}) + k_xk_y(\eta_{xy}+\eta_{yx})\right]. \qquad \text{(A.18)}
\end{aligned}
$$

In general, this secular equation has to be solved numerically, but in many situations of interest the allowed values for q can be obtained analytically (see Appendix C). The solution of Eq. (A.16) provides four complex eigenvalues for q, two lie in the upper half of the complex plane and the other two in the lower half.

The next step toward the solution of the Maxwell's equations in a multilayer structure is the determination of the fields in the different layers. This can be done by expressing the fields as a combination of forward and backward propagating waves with wave numbers q_n (with $n = 1, 2$), and complex amplitudes a_n and b_n, respectively. These amplitudes will be determined later by using the boundary conditions at the interfaces and surfaces of the multilayer structure. Since the boundary conditions are simply the continuity of the in-plane field components, we focus here on the analysis of the field components e_x, e_y, h_x, and h_y. From Eq. (A.11), the in-plane components of $\boldsymbol{h}$ can be expanded in terms of propagating waves as follows

$$
\begin{pmatrix} h_x(z) \\ h_y(z) \end{pmatrix} = \sum_{n=1}^{2} \left\{ \begin{pmatrix} \phi_{x_n} \\ \phi_{y_n} \end{pmatrix} e^{iq_nz} a_n + \begin{pmatrix} \varphi_{x_n} \\ \varphi_{y_n} \end{pmatrix} e^{-ip_n(d-z)} b_n \right\}, \qquad \text{(A.19)}
$$

where d is the thickness of the layer. Here, a_n is the coefficient of the forward going wave at the $z = 0$ interface, and b_n is the backward going wave at $z = d$. On the other hand, q_n correspond to the eigenvalues of Eq. (A.16) with $\mathrm{Im}\{q_n\} > 0$ and p_n are the eigenvalues with $\mathrm{Im}\{p_n\} < 0$.

To simplify the notation, we now define two 2×2 matrices $\hat{\Phi}_+$ and $\hat{\Phi}_-$ whose columns

are the vectors ϕ_n and φ_n, respectively. Moreover, we define the diagonal 2×2 matrices $\hat{\mathrm{f}}_+(z)$ and $\hat{\mathrm{f}}_-(d-z)$, such that $[\hat{\mathrm{f}}_+(z)]_{nn} = e^{iq_n z}$ and $[\hat{\mathrm{f}}_-(d-z)]_{nn} = e^{-ip_n(d-z)}$, and the 2-dimensional vectors $\boldsymbol{h}_\parallel(z) = (h_x(z), h_y(z))^T$, $\boldsymbol{a} = (a_1, a_2)^T$, and $\boldsymbol{b} = (b_1, b_2)^T$. In terms of these quantities, the in-plane magnetic-field components become

$$\boldsymbol{h}_\parallel(z) = \hat{\Phi}_+\hat{\mathrm{f}}_+(z)\boldsymbol{a} + \hat{\Phi}_-\hat{\mathrm{f}}_-(d-z)\boldsymbol{b}. \tag{A.20}$$

Similarly, from Eq. (A.14) it is straightforward to show that the in-plane components of the electric field, $\boldsymbol{e}_\parallel(z) = (-e_y(z), e_x(z))^T$, are given by

$$\begin{aligned}\boldsymbol{e}_\parallel(z) &= \left(\hat{\mathcal{A}}_0^{(b)}\hat{\Phi}_+\hat{q}^{-1} + \hat{\mathcal{A}}_1^{(b)}\hat{\Phi}_+ + \hat{\mathcal{A}}_2\hat{\Phi}_+\hat{q}\right)\hat{\mathrm{f}}_+(z)\boldsymbol{a} \\ &+ \left(\hat{\mathcal{A}}_0^{(b)}\hat{\Phi}_-\hat{p}^{-1} + \hat{\mathcal{A}}_1^{(b)}\hat{\Phi}_- + \hat{\mathcal{A}}_2\hat{\Phi}_-\hat{p}\right)\hat{\mathrm{f}}_-(d-z)\boldsymbol{b},\end{aligned} \tag{A.21}$$

where the $\hat{\mathcal{A}}$'s are defined in Eq. (A.17) and we have defined the 2×2 diagonal matrices $\hat{q}$ and $\hat{p}$ such that $\hat{q}_{nn} = q_n$ and $\hat{p}_{nn} = p_n$.

We can now combine Eq. (A.20) and (A.21) into a single expression as follows

$$\begin{pmatrix} \boldsymbol{e}_\parallel(z) \\ \boldsymbol{h}_\parallel(z) \end{pmatrix} = \hat{M}\begin{pmatrix} \hat{\mathrm{f}}_+(z)\boldsymbol{a} \\ \hat{\mathrm{f}}_-(d-z)\boldsymbol{b} \end{pmatrix} = \begin{pmatrix} \hat{M}_{11} & \hat{M}_{12} \\ \hat{M}_{21} & \hat{M}_{22} \end{pmatrix}\begin{pmatrix} \hat{\mathrm{f}}_+(z)\boldsymbol{a} \\ \hat{\mathrm{f}}_-(d-z)\boldsymbol{b} \end{pmatrix},$$

where the 2×2 matrices M_{ij} are defined as

$$\begin{aligned}\hat{M}_{11} &= \hat{\mathcal{A}}_0^{(b)}\hat{\Phi}_+\hat{q}^{-1} + \hat{\mathcal{A}}_1^{(b)}\hat{\Phi}_+ + \hat{\mathcal{A}}_2\hat{\Phi}_+\hat{q}, \\ \hat{M}_{12} &= \hat{\mathcal{A}}_0^{(b)}\hat{\Phi}_-\hat{p}^{-1} + \hat{\mathcal{A}}_1^{(b)}\hat{\Phi}_- + \hat{\mathcal{A}}_2\hat{\Phi}_-\hat{p}, \\ \hat{M}_{21} &= \hat{\Phi}_+, \quad \hat{M}_{22} = \hat{\Phi}_-.\end{aligned} \tag{A.22}$$

The final step in our calculation is to use the scattering matrix (S-matrix) to compute the field amplitudes needed to describe the different relevant physical quantities. By definition, the S-matrix relates the vectors of the amplitudes of forward and backward going waves, $\boldsymbol{a}_l$ and $\boldsymbol{b}_l$, where l now denotes the layer, in the different layers of the structure as follows

$$\begin{pmatrix} \boldsymbol{a}_l \\ \boldsymbol{b}_{l'} \end{pmatrix} = \hat{S}(l', l)\begin{pmatrix} \boldsymbol{a}_{l'} \\ \boldsymbol{b}_l \end{pmatrix} = \begin{pmatrix} \hat{S}_{11} & \hat{S}_{12} \\ \hat{S}_{21} & \hat{S}_{22} \end{pmatrix}\begin{pmatrix} \boldsymbol{a}_{l'} \\ \boldsymbol{b}_l \end{pmatrix}. \tag{A.23}$$

The field amplitudes in two consecutive layers are related via the continuity of the in-plane components of the fields in every interface and surface. If we consider the interface

between the layer l and the layer $l+1$, this continuity leads to

$$\begin{pmatrix} \boldsymbol{e}_{\parallel}(d_l) \\ \boldsymbol{h}_{\parallel}(d_l) \end{pmatrix}_l = \begin{pmatrix} \boldsymbol{e}_{\parallel}(0) \\ \boldsymbol{h}_{\parallel}(0) \end{pmatrix}_{l+1}, \tag{A.24}$$

where d_l is the thickness of layer l. From this condition, together with Eq. (A.22), it is easy to show that the amplitudes in layers l and $l+1$ are related by the interface matrix $\hat{I}(l,l+1) = \hat{M}_l^{-1}\hat{M}_{l+1}$ in the following way

$$\begin{pmatrix} \hat{f}_l^+ \boldsymbol{a}_l \\ \boldsymbol{b}_l \end{pmatrix} = \hat{I}(l,l+1) \begin{pmatrix} \boldsymbol{a}_{l+1} \\ \hat{f}_{l+1}^- \boldsymbol{b}_{l+1} \end{pmatrix} = \begin{pmatrix} \hat{I}_{11} & \hat{I}_{12} \\ \hat{I}_{21} & \hat{I}_{22} \end{pmatrix} \begin{pmatrix} \boldsymbol{a}_{l+1} \\ \hat{f}_{l+1}^- \boldsymbol{b}_{l+1} \end{pmatrix}, \tag{A.25}$$

where $\hat{f}_l^+ = \hat{\mathrm{f}}_{l,+}(d_l)$ and $\hat{f}_{l+1}^- = \hat{\mathrm{f}}_{l+1,-}(d_{l+1})$.

Now, with the help of the interface matrices, the S-matrix can be calculated in an iterative way as follows. The matrix $\hat{S}(l',l+1)$ can be calculated from $\hat{S}(l',l)$ using the definition of $\hat{S}(l',l)$ in Eq. (A.23) and the interface matrix $\hat{I}(l,l+1)$. Eliminating $\boldsymbol{a}_l$ and $\boldsymbol{b}_l$ we obtain the relation between $\boldsymbol{a}_{l'}$, $\boldsymbol{b}_{l'}$ and $\boldsymbol{a}_{l+1}$, $\boldsymbol{b}_{l+1}$, from which $\hat{S}(l',l+1)$ can be constructed. This reasoning leads to the following iterative relations

$$\begin{aligned}
\hat{S}_{11}(l',l+1) &= \left[\hat{I}_{11} - \hat{f}_l^+ \hat{S}_{12}(l',l)\hat{I}_{21}\right]^{-1} \hat{f}_l^+ \hat{S}_{11}(l',l) \\
\hat{S}_{12}(l',l+1) &= \left[\hat{I}_{11} - \hat{f}_l^+ \hat{S}_{12}(l',l)\hat{I}_{21}\right]^{-1} \left(\hat{f}_l^+ \hat{S}_{12}(l',l)\hat{I}_{22} - \hat{I}_{12}\right) \hat{f}_{l+1}^- \\
\hat{S}_{21}(l',l+1) &= \hat{S}_{22}(l',l)\hat{I}_{21}\hat{S}_{11}(l',l+1) + \hat{S}_{21}(l',l) \\
\hat{S}_{22}(l',l+1) &= \hat{S}_{22}(l',l)\hat{I}_{21}\hat{S}_{12}(l',l+1) + \hat{S}_{22}(l',l)\hat{I}_{22}\hat{f}_{l+1}^-.
\end{aligned} \tag{A.26}$$

Starting from $\hat{S}(l',l') = 1$, one can apply the previous recursive relations to a layer at a time to build up $\hat{S}(l',l)$. Let us conclude this appendix by saying that from the knowledge of the S-matrix one can easily compute the field amplitudes in every layer and, in turn, the fields everywhere in the system [80].

B | Thermal radiation in multilayer anisotropic systems.

In this appendix we show how the scattering matrix approach of Appendix A can be used to describe the thermal radiation between planar multilayer systems made of anisotropic materials. For this purpose, we first discuss how a generic emission problem can be formulated in the framework of the S-matrix formalism and then, we show how such a formulation can be used to describe the thermal emission of a multilayer system.

B.1. Emission in the scattering matrix approach

For concreteness, let us assume that there is a set of oscillating point sources, with harmonic time dependence, occupying the whole plane defined by $z = z'$. The corresponding electric current density $\mathbf{J}$ is given by

$$\mathbf{J}(\mathbf{r}, z) = \mathbf{J}_0 \delta(z - z') = \boldsymbol{j}_0 e^{i\mathbf{k}\cdot\mathbf{r}} \delta(z - z'), \tag{B.1}$$

where $\boldsymbol{j}_0(\mathbf{k}) = \mathbf{J}_0 e^{-i\mathbf{k}\cdot\mathbf{r}}$. This current density enters as a source term in Ampère's law, Eq. (A.1), which now becomes $\nabla \times \mathbf{H} = \mathbf{J} - i\hat{\epsilon}\mathbf{E}$, while Eq. (A.2) (Faraday's law) remains unchanged. Thus, Eqs. (A.4-A.6) adopt now the following form

$$ik_y h_z(z) - h_y'(z) = j_{0x}\delta(z - z') - i\sum_j \epsilon_{xj} e_j(z) \tag{B.2}$$

$$h_x'(z) - ik_x h_z(z) = j_{0y}\delta(z - z') - i\sum_j \epsilon_{yj} e_j(z) \tag{B.3}$$

$$ik_x h_y(z) - ik_y h_x(z) = j_{0z}\delta(z - z') - i\sum_j \epsilon_{zj} e_j(z). \tag{B.4}$$

The presence of the source term induces discontinuities in the fields across the plane $z = z'$, as we proceed to show. First, let us consider the effect of the in-plane components of the current density by putting $j_z = 0$. To cancel the singular term due to the source in Eqs. (B.2) and (B.3), there must be discontinuities in h_x and h_y at $z = z'$ equal to j_{0y} and $-j_{0x}$, respectively. All the other field components are continuous, except for e_z that exhibits a discontinuity equal to $(k_x j_{0x} + k_y j_{0y})/\epsilon_{zz}$ in virtue of Eq. (B.4). Let us analyze now the role of the perpendicular component of $\mathbf{J}$ by putting $j_{0x} = j_{0y} = 0$. From Eq. (B.4), it is clear that in this case e_z must contain a singularity to cancel the singular term associated to the current source, that is $e_z(z) = -i(j_{0z}/\epsilon_{zz})\delta(z - z')+$ non-singular parts. This introduces singular terms in the left-hand side of the Maxwell Eqs. (A.7) and (A.8), which are cancelled by discontinuities in e_x and e_y equal to $k_x j_{0z}/\epsilon_{zz}$ and $k_y j_{0z}/\epsilon_{zz}$, respectively. Additionally, it is obvious from Eqs. (B.2) and (B.3) that h_x and h_y acquired discontinuities equal to $-\epsilon_{yz} j_{0z}/\epsilon_{zz}$ and $\epsilon_{xz} j_{0z}/\epsilon_{zz}$, respectively. Defining the following vectors

$$\boldsymbol{p}_{\parallel} = (j_{0y} - \epsilon_{yz} j_{0z}/\epsilon_{zz}, -j_{0x} + \epsilon_{xz} j_{0z}/\epsilon_{zz})^T \tag{B.5}$$

$$\boldsymbol{p}_z = (-k_y j_{0z}/\epsilon_{zz}, k_x j_{0z}/\epsilon_{zz})^T, \tag{B.6}$$

the boundary conditions on the in-plane components of the fields are thus

$$\begin{aligned} \boldsymbol{e}_{\parallel}(z'^{+}) - \boldsymbol{e}_{\parallel}(z'^{-}) &= \boldsymbol{p}_z \\ \boldsymbol{h}_{\parallel}(z'^{+}) - \boldsymbol{h}_{\parallel}(z'^{-}) &= \boldsymbol{p}_{\parallel}. \end{aligned} \tag{B.7}$$

These discontinuity conditions can now be combined with the S-matrix formalism of the previous appendix to calculate the emission throughout the system. Let us consider that the emission plane defines the interface between layers l and $l+1$ in our multilayer structure. Thus, the boundary conditions in this interface become

$$\begin{pmatrix} \boldsymbol{e}_{\parallel}(0) \\ \boldsymbol{h}_{\parallel}(0) \end{pmatrix}_{l+1} - \begin{pmatrix} \boldsymbol{e}_{\parallel}(d_l) \\ \boldsymbol{h}_{\parallel}(d_l) \end{pmatrix}_{l} = \begin{pmatrix} \boldsymbol{p}_z \\ \boldsymbol{p}_{\parallel} \end{pmatrix}. \tag{B.8}$$

Using now the expression of the fields in terms of the layer matrices ($\hat{M}$'s), see Eq. (A.22), we can write

$$\hat{M}_{l+1} \begin{pmatrix} \boldsymbol{a}_{l+1} \\ \hat{f}^{-}_{l+1} \boldsymbol{b}_{l+1} \end{pmatrix} - \hat{M}_l \begin{pmatrix} \hat{f}^{+}_{l} \boldsymbol{a}_l \\ \boldsymbol{b}_l \end{pmatrix} = \begin{pmatrix} \boldsymbol{p}_z \\ \boldsymbol{p}_{\parallel} \end{pmatrix}. \tag{B.9}$$

The external boundary conditions for an emission problem is that there should be only outgoing waves, that is $\boldsymbol{a}_0 = \boldsymbol{b}_N = \mathbf{0}$, where 0 denotes here the first layer of the structure and N the last one. Using the definitions of the S-matrices $\hat{S}(0,l)$ and $\hat{S}(l+1,N)$ from Eq. (A.23), it follows that

$$\boldsymbol{a}_l = \hat{S}_{12}(0,l)\boldsymbol{b}_l \tag{B.10}$$

$$\boldsymbol{b}_{l+1} = \hat{S}_{21}(l+1,N)\boldsymbol{a}_{l+1}. \tag{B.11}$$

Substituting for $\boldsymbol{a}_l$ and $\boldsymbol{b}_{l+1}$ from Eqs. (B.10) and (B.11) in Eq. (B.9) and rearranging things, we arrive at the following central result

$$\begin{pmatrix} \hat{M}_{11,l+1} + \hat{M}_{12,l+1}\hat{f}^-_{l+1}\hat{S}_{21}(l+1,N) & -[\hat{M}_{12,l} + \hat{M}_{11,l}\hat{f}^+_l\hat{S}_{12}(0,l)] \\ \hat{M}_{21,l+1} + \hat{M}_{22,l+1}\hat{f}^-_{l+1}\hat{S}_{21}(l+1,N) & -[\hat{M}_{22,l} + \hat{M}_{21,l}\hat{f}^+_l\hat{S}_{12}(0,l)] \end{pmatrix} \begin{pmatrix} \boldsymbol{a}_{l+1} \\ \boldsymbol{b}_l \end{pmatrix} = \begin{pmatrix} \boldsymbol{p}_z \\ \boldsymbol{p}_\parallel \end{pmatrix}, \tag{B.12}$$

which allows us to compute the field amplitudes on the left and on the right-hand side of the emitting plane. From the solution of this matrix equation we can compute the field amplitude everywhere inside and outside the multilayer structure from the knowledge of the scattering matrix.

B.2. Radiative heat transfer

Let us now show that the previous results can be used to describe the radiative heat transfer. First of all, we need to specify the properties of the electric currents that generate the thermal radiation. In the framework of fluctuational electrodynamics [6], the thermal emission is generated by random currents $\mathbf{J}$ inside the material. While the statistical average of these currents vanishes, *i.e.* $\langle \mathbf{J} \rangle = 0$, their correlations are given by the fluctuation-dissipation theorem [12, 13]

$$\langle J_k(\mathbf{R},\omega) J_l^*(\mathbf{R}',\omega') \rangle = \frac{4\epsilon_0 \omega c}{\pi} \Theta(\omega,T)\delta(\mathbf{R}-\mathbf{R}')\delta(\omega-\omega') \left[\epsilon_{kl}(\mathbf{R},\omega) - \epsilon^*_{lk}(\mathbf{R},\omega)\right]/(2i), \tag{B.13}$$

where $\mathbf{R} = (\mathbf{r}, z)$ and $\Theta(\omega,T) = \hbar\omega c/[\exp(\hbar\omega c/k_\mathrm{B}T) - 1]$, T being the absolute temperature. Let us remind the reader that with the rescaling introduced at the beginning of Appendix A, ω has dimensions of wave vector in our notation. Notice that in the expression of $\Theta(\omega,T)$ a term equal to $\hbar\omega c/2$ that accounts for vacuum fluctuations has been omitted since it does not affect the neat radiation heat flux. Notice also that we are using here the most general form of this theorem that is suitable for non-reciprocal systems.

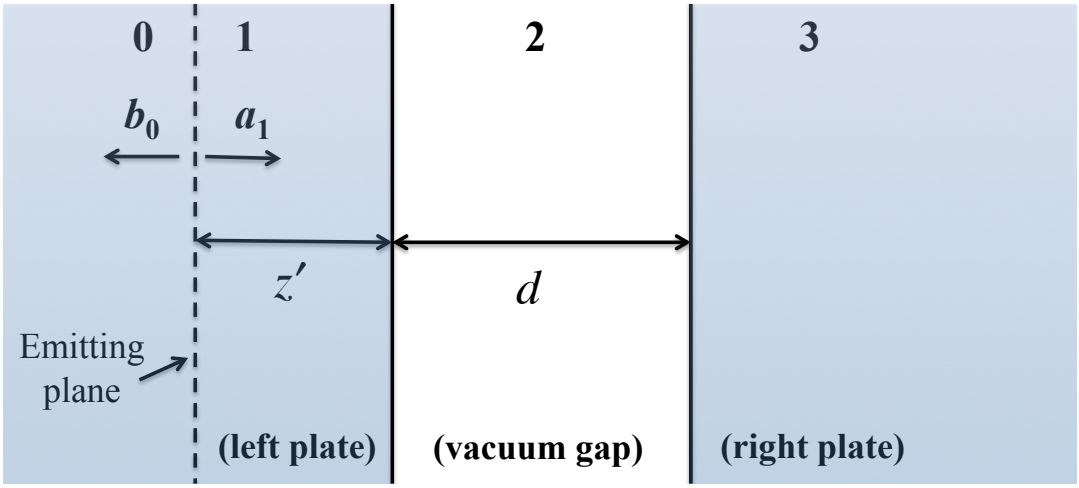

Figure B.1: Two parallel plates separated by a vacuum gap of width d. The vertical dashed line inside the left plate indicates the position of an emitting plane that contains the radiation sources that generate the field amplitudes $\boldsymbol{b}_0$ and $\boldsymbol{a}_1$.

The fact that the current correlations are local in space and diagonal in frequency space reduces the problem of the thermal radiation to the description of the emission by point sources for a given frequency, parallel wave vector, and position inside the structure. Thus, we can directly apply the results derived in the previous section.

Let us now consider our system of study, namely two parallel plates at temperatures T_1 and T_3 separated by a vacuum gap of width d, see Fig. B.1. Our strategy to compute the net radiative heat transfer between the two plates follows closely that of the seminal work by Polder and Van Hove [11]. First, we compute the radiation power per unit of area transferred from the left plate to the right one, $Q_{1\to3}$. For this purpose, we first compute the statistical average of the z-component of the Poynting vector describing the power emitted from a plane located at $z = z'$ inside the left plate for a given frequency and parallel wave vector and then, we integrate integrate the result over all possible values of z', ω, and $\mathbf{k}$, *i.e.*

$$Q_{1\to3}(d, T_1) = \int_0^\infty d\omega \int d\mathbf{k} \int_0^\infty dz' \langle S_z(\omega, \mathbf{k}, z') \rangle. \tag{B.14}$$

A similar calculation for the power $Q_{3\to1}$ transferred from the right plate to the left one completes the computation of the net transferred power per unit of area.

Let us focus now on the analysis of the power emitted by a plane inside the left plate, see Fig. B.1. This emitting plane defines a fictitious interface between layers 0 and 1, which are both inside the left plate. To determine the power emitted to the right plate

we first compute the field amplitudes $\boldsymbol{a}_1$ on the right hand side of the plane. For this purpose we make of use of Eq. (B.12), where in this case $l = 0$ and $N = 3$. Taking into account that $\hat{S}_{12}(0,0) = 0$, it is straightforward to show that

$$\begin{aligned} \boldsymbol{a}_1 &= [\hat{M}_{11,1} - \hat{M}_{12,1}\hat{M}_{22,1}^{-1}\hat{M}_{21,1}]^{-1}\boldsymbol{p}_z + [\hat{M}_{21,1} - \hat{M}_{22,1}\hat{M}_{12,1}^{-1}\hat{M}_{11,1}]^{-1}\boldsymbol{p}_{\parallel} \\ &= [\hat{M}_1^{-1}]_{11}\boldsymbol{p}_z + [\hat{M}_1^{-1}]_{12}\boldsymbol{p}_{\parallel}. \end{aligned} \tag{B.15}$$

To compute $Q_{1\to 3}$, it is convenient to calculate the Poynting vector in the vacuum gap. For this purpose, we need the field amplitudes in that layer. From Eq. (A.23), it is easy to deduce that these amplitudes are given in terms of $\boldsymbol{a}_1$ as follows

$$\boldsymbol{a}_2 = \hat{D}\hat{S}_{11}(1,2)\boldsymbol{a}_1, \tag{B.16}$$

where $\hat{D} \equiv [\hat{1} - \hat{S}_{12}(1,2)\hat{S}_{21}(2,3)]^{-1}$ and

$$\boldsymbol{b}_2 = \left[\hat{1} - \hat{S}_{21}(2,3)\hat{S}_{12}(1,2)\right]^{-1}\hat{S}_{21}(2,3)\hat{S}_{11}(1,2)\boldsymbol{a}_1 = \hat{S}_{21}(2,3)\boldsymbol{a}_2. \tag{B.17}$$

It is worth stressing that the different elements of the scattering matrix that appear in the previous expressions can be factorized into scattering matrices $\tilde{S}$ containing only information about the interfaces of the layered system, which are basically the Fresnel coefficients of the structure, and phase factors describing the propagation between these interfaces. In particular, from Eq. (A.26) it is easy to show that

$$\hat{S}_{11}(1,2) = \tilde{S}_{11}(1,2)\hat{f}_1^+(z') \tag{B.18}$$

$$\hat{S}_{12}(1,2) = \tilde{S}_{12}(1,2)e^{iq_2 d} \tag{B.19}$$

$$\hat{S}_{21}(2,3) = \tilde{S}_{21}(2,3)e^{iq_2 d}, \tag{B.20}$$

where $q_2 = \sqrt{\omega^2 - k^2}$ is the z-component of the wave vector in the vacuum gap and

$$\hat{f}_1^+(z') = \begin{pmatrix} e^{iq_{1,1}z'} & 0 \\ 0 & e^{iq_{2,1}z'} \end{pmatrix}. \tag{B.21}$$

Here, $q_{i,1}$ (with $i = 1, 2$) are the z-components of the two allowed wave vectors in the medium 1. On the other hand, the $\tilde{S}$-matrices can be computed directly from the

interface matrices as follows [see Eq. (A.26)]

$$\tilde{S}_{11}(1,2) = \hat{I}_{11}^{-1}(1,2) \tag{B.22}$$
$$\tilde{S}_{12}(1,2) = -\hat{I}_{11}^{-1}(1,2)\hat{I}_{12}(1,2) \tag{B.23}$$
$$\tilde{S}_{21}(2,3) = \hat{I}_{21}(2,3)\hat{I}_{11}^{-1}(2,3). \tag{B.24}$$

In terms of the amplitudes $\boldsymbol{a}_2$ and $\boldsymbol{b}_2$, the fields in the vacuum gap at $z = 0$ are given by [see Eq. (A.22)]

$$\begin{pmatrix} \boldsymbol{e}_\parallel(0) \\ \boldsymbol{h}_\parallel(0) \end{pmatrix}_2 = \begin{pmatrix} \hat{M}_{11,2}\left[\boldsymbol{a}_2 - e^{iq_2 d}\boldsymbol{b}_2\right] \\ \boldsymbol{a}_2 + e^{iq_2 d}\boldsymbol{b}_2 \end{pmatrix}, \tag{B.25}$$

where we have used that $\hat{M}_{12,2} = -\hat{M}_{11,2}$, valid for any isotropic system. Thus, the z-component of the Poynting vector evaluated at $z = 0$ in the vacuum gap reads

$$\begin{aligned} S_z(\omega, \mathbf{k}, z') = {} & \frac{1}{4\omega}\sqrt{\frac{\mu_0}{\epsilon_0}}\left\{\boldsymbol{h}_\parallel^\dagger(0)\boldsymbol{e}_\parallel(0) + \boldsymbol{e}_\parallel^\dagger(0)\boldsymbol{h}_\parallel(0)\right\}_2 = \frac{1}{4\omega}\sqrt{\frac{\mu_0}{\epsilon_0}}\left\{\boldsymbol{a}_2^\dagger\left(\hat{M}_{11,2} + \hat{M}_{11,2}^\dagger\right)\boldsymbol{a}_2 - \right. \\ & e^{i(q_2 - q_2^*)d}\boldsymbol{b}_2^\dagger\left(\hat{M}_{11,2} + \hat{M}_{11,2}^\dagger\right)\boldsymbol{b}_2 + e^{-iq_2^* d}\boldsymbol{b}_2^\dagger\left(\hat{M}_{11,2} - \hat{M}_{11,2}^\dagger\right)\boldsymbol{a}_2 - \\ & \left. e^{iq_2 d}\boldsymbol{a}_2^\dagger\left(\hat{M}_{11,2} - \hat{M}_{11,2}^\dagger\right)\boldsymbol{b}_2\right\}. \end{aligned} \tag{B.26}$$

Moreover, since

$$\hat{M}_{11,2} = \frac{1}{q_2}\begin{pmatrix} \omega^2 - k_y^2 & k_x k_y \\ k_x k_y & \omega^2 - k_x^2 \end{pmatrix} \equiv \frac{1}{q_2}\hat{A} \tag{B.27}$$

and q_2 is either real (for $k < \omega$) or purely imaginary (for $k > \omega$), Eq. (B.26) reduces to

$$S_z(\omega, \mathbf{k}, z') = \frac{1}{2q_2\omega}\sqrt{\frac{\mu_0}{\epsilon_0}}\begin{cases} \boldsymbol{a}_2^\dagger\hat{A}\boldsymbol{a}_2 - \boldsymbol{b}_2^\dagger\hat{A}\boldsymbol{b}_2, & k < \omega \\ e^{-iq_2^* d}\boldsymbol{b}_2^\dagger\hat{A}\boldsymbol{a}_2 - e^{iq_2 d}\boldsymbol{a}_2^\dagger\hat{A}\boldsymbol{b}_2, & k > \omega, \end{cases}$$

where the first term provides the contribution of propagating waves and the second one corresponds to the contribution of evanescent waves.

From this point on, the rest of the calculation is pure algebra and we will not describe it here in detail. Let us simply say that the basic idea is to use Eqs. (B.16) and (B.17) to express the Poynting vector in Eq. (B.28) in terms of the field amplitude $\boldsymbol{a}_1$. Then, using Eq. (B.15) and the fluctuation-dissipation theorem of Eq. (B.13) one can calculate the statistical average of the Poynting vector. Let us mention that the calculation can be greatly simplified by rotating every 2×2 matrix appearing in the problem from the Cartesian basis (x-y) to the basis of s- and p-polarized waves. This can be done via the

unitary matrix

$$\hat{R} \equiv \frac{1}{k} \begin{pmatrix} k_x & k_y \\ k_y & -k_x \end{pmatrix}, \tag{B.28}$$

which is the matrix that defines the transformation that diagonalizes the matrix $\hat{A}$, *i.e.*

$$\hat{A}_d \equiv \hat{R}\hat{A}\hat{R} = \begin{pmatrix} \omega^2 & 0 \\ 0 & q_2^2 \end{pmatrix}. \tag{B.29}$$

Finally, after integrating over all possible values of ω, $\mathbf{k}$, and z', see Eq. (B.14), one arrives at the following result for the power per unit of area transferred from the left plate to the right one

$$Q_{1\to 3}(d, T_1) = \int_0^\infty \frac{d\omega}{2\pi} \Theta(\omega, T_1) \int \frac{d\mathbf{k}}{(2\pi)^2} \tau(\omega, \mathbf{k}, d), \tag{B.30}$$

where $\tau(\omega, \mathbf{k}, d)$ is the total transmission coefficient of the electromagnetic modes and it is given by

$$\tau(\omega, \mathbf{k}, d) = \begin{cases} \mathrm{Tr}\left\{[\hat{1} - \bar{S}_{12}(1,2)\bar{S}_{12}^\dagger(1,2)]\bar{D}^\dagger[\hat{1} - \bar{S}_{21}^\dagger(2,3)\bar{S}_{21}(2,3)]\bar{D}\right\}, & k < \omega, \\ \mathrm{Tr}\left\{[\bar{S}_{12}(1,2) - \bar{S}_{12}^\dagger(1,2)]\bar{D}^\dagger[\bar{S}_{21}^\dagger(2,3) - \bar{S}_{21}(2,3)]\bar{D}\right\} e^{-2|q_2|d}, & k > \omega. \end{cases} \tag{B.31}$$

Here, the 2×2 matrices indicated by a bar are defined as follows

$$\bar{D} \equiv \hat{A}_d^{1/2}\hat{R}\hat{D}\hat{R}\hat{A}_d^{-1/2} \tag{B.32}$$

$$\bar{D}^\dagger \equiv \hat{A}_d^{-1/2}\hat{R}\hat{D}^\dagger\hat{R}\hat{A}_d^{1/2}. \tag{B.33}$$

Following a similar reasoning, one can compute the power per unit of area transfer from the right plate to the left one and the final result reads

$$Q_{3\to 1}(d, T_3) = \int_0^\infty \frac{d\omega}{2\pi} \Theta(\omega, T_3) \int \frac{d\mathbf{k}}{(2\pi)^2} \tau(\omega, \mathbf{k}, d), \tag{B.34}$$

where $\tau(\omega, \mathbf{k}, d)$ is also given by Eq. (B.31). Thus, the net power per unit of area exchanged by the plates is given by Eqs. (3.8) and (3.9) in Section 3.2. To conclude, let us stress that in the manuscript ω is meant to be an angular frequency.

C | Dispersion relations and surface electromagnetic modes.

C.1. Dispersion relations

In this appendix we provide the solution of the eigenvalue problem of Eqs. (A.16) and (A.17) that give the dispersion relations of the electromagnetic modes that can exist inside the materials considered in this work. In particular, we focus here on three cases of special interest for our discussions in Chapter 3.

Case 1: $\hat{\epsilon} = diag[\epsilon_{xx}, \epsilon_{xx}, \epsilon_{zz}]$. This situation is of relevance for the case in which the magnetic field is perpendicular to the plate surfaces, see section 3.3.1. In this case, the allowed q-values are given by

$$q_{\mathrm{o}}^2 = \epsilon_{xx}\omega^2 - k^2, \;\; q_{\mathrm{e}}^2 = \epsilon_{xx}\omega^2 - k^2\epsilon_{xx}/\epsilon_{zz}. \tag{C.1}$$

Case 2: $\hat{\epsilon} = diag[\epsilon_{xx}, \epsilon_{zz}, \epsilon_{zz}]$. This situation is relevant for the case in which the magnetic field is parallel to the plate surfaces, see section 3.3.2, and the allowed q-values are given by

$$q_{\mathrm{o}}^2 = \epsilon_{zz}\omega^2 - k^2, \;\; q_{\mathrm{e}}^2 = \epsilon_{xx}\omega^2 - k^2\epsilon_{xx}/\epsilon_{zz}. \tag{C.2}$$

Case 3: the diagonal elements of $\hat{\epsilon}$ are ϵ_{xx} and $\epsilon_{yy} = \epsilon_{zz}$, while the only non-vanishing off-diagonal elements are $\epsilon_{yz} = -\epsilon_{zy}$. This situation is relevant for the case in which the magnetic field is parallel to the plate surfaces, see section 3.3.2. In this case, the allowed q-values adopt the following form

$$q_{\mathrm{o},1}^2 = \epsilon_{xx}\omega^2 - k^2, \;\; q_{\mathrm{o},2}^2 = (\epsilon_{yy}^2 + \epsilon_{yz}^2)\omega^2/\epsilon_{yy} - k^2. \tag{C.3}$$

C.2. Surface electromagnetic modes

We briefly describe here how we determine the dispersion relation of the surface electromagnetic modes in our system and we also provide the results for some configurations of special interest.

Let us consider a structure containing N planar layers. From Eq. (A.25), it is easy to show that the field amplitudes in layers l and $l+1$ are related as follows

$$\begin{aligned}\begin{pmatrix} \boldsymbol{a}_l \\ \boldsymbol{b}_l \end{pmatrix} &= \begin{pmatrix} \hat{f}_l^+ & \hat{0} \\ \hat{0} & \hat{1} \end{pmatrix}^{-1} \hat{I}(l,l+1) \begin{pmatrix} \hat{1} & \hat{0} \\ \hat{0} & \hat{f}_{l+1}^- \end{pmatrix} \begin{pmatrix} \boldsymbol{a}_{l+1} \\ \boldsymbol{b}_{l+1} \end{pmatrix} \\ &\equiv \hat{I}'(l,l+1) \begin{pmatrix} \boldsymbol{a}_{l+1} \\ \boldsymbol{b}_{l+1} \end{pmatrix}. \end{aligned} \tag{C.4}$$

Now, using this relation recursively we can relate the field amplitudes in the first and last layers as follows

$$\begin{pmatrix} \boldsymbol{a}_1 \\ \boldsymbol{b}_1 \end{pmatrix} = \left[\prod_{l=1}^{N-1} \hat{I}'(l,l+1)\right] \begin{pmatrix} \boldsymbol{a}_N \\ \boldsymbol{b}_N \end{pmatrix} \equiv \hat{I}^S \begin{pmatrix} \boldsymbol{a}_N \\ \boldsymbol{b}_N \end{pmatrix}. \tag{C.5}$$

The condition for an eigenmode of the system is that $\boldsymbol{a}_1 = \boldsymbol{b}_N = \boldsymbol{0}$, which from the previous equation implies that $\hat{I}_{11}^S \boldsymbol{a}_N = \boldsymbol{0}$. The condition for having a non-trivial solution of this equation is that $\det \hat{I}_{11}^S = 0$, which is the condition that surface electromagnetic modes must satisfy. In our plate-plate geometry, the 4×4 matrix $\hat{I}^S$ is simply given by

$$\hat{I}^S = \hat{I}(1,2) \begin{pmatrix} e^{-iq_2 d}\hat{1} & \hat{0} \\ \hat{0} & e^{iq_2 d}\hat{1} \end{pmatrix} \hat{I}(2,3), \tag{C.6}$$

where let us recall that $q_2 = \sqrt{\omega^2 - k^2}$. Thus, the condition for an eigenmode of the system reads

$$\det[\hat{I}_{11}(1,2)\hat{I}_{11}(2,3)e^{-iq_2 d} + \hat{I}_{12}(1,2)\hat{I}_{21}(2,3)e^{iq_2 d}] = 0. \tag{C.7}$$

In what follows, we provide the explicit equations satisfied by the dispersion relation of the surface waves in the three cases considered above.

Case 1: In this case, Eq. (C.7) leads to

$$e^{-iq_2 d} = \pm \left(\frac{q_\mathrm{e} - \epsilon_{xx} q_2}{q_\mathrm{e} + \epsilon_{xx} q_2}\right), \tag{C.8}$$

where $q_{\rm e}$ is given in Eq. (C.1). This equations reduces to Eq. (3.15) in the electrostatic limit $k \gg \omega/c$.

Case 2: Here, assuming that the surface wave propagates along the x-direction, its dispersion relation satisfies the following relation

$$e^{-iq_2 d} = \pm \left(\frac{q_{\rm e} - \epsilon_{xx} q_2}{q_{\rm e} + \epsilon_{xx} q_2} \right), \tag{C.9}$$

where $q_{\rm e}$ is given in Eq. (C.2). In the electrostatic limit, this equation reduces to Eq. (3.15).

Case 3: In this case, and assuming that the surface waves propagate along the y-direction, its dispersion relation is given by the solution of the following equation

$$e^{-2iq_2 d} = \frac{(\eta_{yy} q_{\rm o,2} - q_2 + \eta_{yz} k)(\eta_{yy} q_{\rm o,2} - q_2 - \eta_{yz} k)}{(\eta_{yy} q_{\rm o,2} + q_2 + \eta_{yz} k)(\eta_{yy} q_{\rm o,2} + q_2 - \eta_{yz} k)}, \tag{C.10}$$

where $\eta_{yy} = \epsilon_{yy}/(\epsilon_{yy}^2 + \epsilon_{yz}^2)$, $\eta_{yz} = -\epsilon_{yz}/(\epsilon_{yy}^2 + \epsilon_{yz}^2)$, and $q_{\rm o,2}$ is given in Eq. (C.3). In the electrostatic limit this equation reduces to Eq. (3.20).

Bibliography

[1] M. F. Modest, *Radiative Heat Transfer* (Academic Press, New York, 2013). (cited on pages 1, 2, 112, 113, and 114)

[2] M. Planck, *The Theory of Heat Radiation* (P. Blakiston's Son & Co., Philadelphia, 1914). (cited on pages 3, 4, 5, and 22)

[3] T. L. Bergman, A. S. Lavine, F. P. Incropera, and D. P. DeWitt, *Fundamentals of Heat and Mass Transfer* (John Wiley & Sons, Inc., New Jersey, 2011). (cited on pages 4 and 134)

[4] D. Bijl, *Note on Thermal Radiation at Low Temperatures*, Philos. Mag. **43**, 1342 (1952). (cited on p. 5)

[5] S. M. Rytov, *Theory of Electric Fluctuations and Thermal Radiation*, (Air Force Cambridge Research Center, Bedford, MA, 1953). (cited on pages 6, 7, and 49)

[6] S. M. Rytov, Y. A. Kravtsov, and V. I. Tatarskii, *Principles of Statistical Radiophysics* (Springer-Verlag, Berlin, 1989), Vol. 3. (cited on pages 6, 7, 49, 85, 110, 113, and 165)

[7] E. G. Cravalho, G. A. Domoto, and C. L. Tien, *Measurements of thermal radiation of solids at liquid-helium temperatures*, AIAA 3rd Thermophysics Conference (Los Angeles, CA, 1968). (cited on p. 6)

[8] G. A. Domoto, R. F. Boehm, and C. L. Tien, *Experimental Investigation of Radiative Transfer Between Metallic Surfaces at Cryogenic Temperatures*, J. Heat Transfer **92** (3), 412 (1970). (cited on p. 6)

[9] C.M. Hargreaves, *Anomalous radiative transfer between closely-spaced bodies*, Phys. Lett. A **30** (9), 491 (1969). (cited on p. 7)

[10] C.M. Hargreaves, *Radiative transfer between closely-spaced bodies*, Philips Res. Rep. **5**, 1 (1973). (cited on p. 7)

[11] D. Polder and M. Van Hove, *Theory of Radiative Heat Transfer between Closely Spaced Bodies*, Phys. Rev. B **4**, 3303 (1971). (cited on pages 7, 9, 14, 50, 138, and 166)

[12] L. Landau, E. Lifshitz, and L. Pitaevskii, *Course of Theoretical Physics* (Pergamon, New York, 1980), Vol. 9, Part 2. (cited on pages 7, 50, and 165)

[13] Yu. A. Il'inskii and L. V. Keldysh, *Electromagnetic Response of Material Media* (Plenum Press, New York, 1994). (cited on pages 7, 50, and 165)

[14] D. Dalvit, P. Milonni, D. Roberts, F. da Rosa (eds.), *Casimir Physics*, (Springer-Verlag, Berlin Heidelberg, 2011), Lecture Notes in Physics 834. (cited on p. 8)

[15] B. Song, A. Fiorino, E. Meyhofer, and P. Reddy, *Near-Field Radiative Thermal Transport: From Theory to Experiment*, AIP Advances **5**, 053503 (2015). (cited on pages 10, 17, and 141)

[16] J. B. Pendry, *Radiative Exchange of Heat between Nanostructures*, J. Phys. Condens. Matter **11**, 6621 (1999). (cited on pages 11, 21, 45, 86, 149, and 154)

[17] J. P. Mulet, K. Joulain, R. Carminati, and J. J. Greffet, *Nanoscale Radiative Heat Transfer between a Small Particle and a Plane Surface* Appl. Phys. Lett. **78**, 2931 (2001). (cited on p. 12)

[18] J. P. Mulet, K. Joulain, R. Carminati, and J. J. Greffet, *Enhanced Radiative Heat Transfer at Nanometric Distances*, Microscale Therm. Eng. **6**, 209 (2002). (cited on pages 12, 37, 71, and 81)

[19] V. Chiloyan, J. Garg, K. Esfarjani, and G. Chen, *Transition from Near-Field Thermal Radiation to Phonon Heat Conduction at Sub-Nanometre Gaps*, Nat. Commun. **6**, 6755 (2015). (cited on pages 13, 86, 148, and 153)

[20] M. T. H. Reid, A. W. Rodriguez, and S. G. Johnson, *Fluctuation-Induced Phenomena in Nanoscale Systems: Harnessing the Power of Noise*, Proc. IEEE **101**, 531 (2013). (cited on pages 14 and 15)

[21] R. Messina, and M. Antezza, *Scattering-Matrix Approach to Casimir-Lifshitz Force and Heat Transfer out of Thermal Equilibrium between Arbitrary Bodies*, Phys. Rev. A **84**, 042102 (2011). (cited on pages 14 and 91)

[22] M. Krüger, T. Emig, and M. Kardar, *Non-equilibrium Electromagnetic Fluctuations: Heat Transfer and Interactions*, Phys. Rev. Lett. **106**, 210404 (2011). (cited on pages 14 and 91)

[23] M. Krüger, G. Bimonte, T. Emig, and M. Kardar *Trace formulas for nonequilibrium Casimir interactions, heat radiation and heat transfer for arbitrary objects*, Phys. Rev. B **86**, 115423 (2012). (cited on pages 14 and 91)

[24] G. Bimonte, *Scattering Approach to Casimir Forces and Radiative Heat Transfer for Nanostructured Surfaces out of Thermal Equilibrium*, Phys. Rev. A **80**, 042102 (2009). (cited on pages 14 and 74)

[25] A. Pryamikov, K. Joulain, P. Ben-Abdallah, and J. Drevillon, *Role of Confined Bloch Waves in the Near-Field Heat Transfer between Two Photonic Crystals*, J. Quant. Spectrosc. Radiat. Transfer **112**, 1314 (2011). (cited on p. 14)

[26] J. Lussange, R. Guérout, F. S. S. Rosa, J. J. Greffet, A. Lambrecht, and S. Reyanud, *Radiative Heat Transfer between Two Dielectric Nanogratings in the Scattering Approach*, Phys. Rev. B **86**, 085432 (2012). (cited on pages 14 and 15)

[27] R. Guérout, J. Lussange, F. S. S. Rosa, J.-P. Hugonin, D. A. R. Dalvit, J. J. Greffet, A. Lambrecht, and S. Reyanud, *Enhanced Radiative Heat Transfer between Nanostructured Gold Plates*, Phys. Rev. B **85**, 180301(R) (2012). (cited on pages 14 and 72)

[28] J. Dai, S. A. Dyakov and M. Yan, *Enhanced Near-Field Radiative Heat Transfer between Corrugated Metal Plates: Role of Spoof Surface Plasmon Polaritons*, Phys. Rev. B **92**, 035419 (2015). (cited on pages 14 and 72)

[29] X. Liu and Z. M. Zhang, *Enhanced Near-Field Thermal Radiation and Reduced Casimir Stiction between Doped-Si Gratings*, Phys. Rev. A **91**, 062510 (2015). (cited on pages 14 and 72)

[30] X. Liu, B. Zhao, and Z. M. Zhang, *Near-Field Thermal Radiation between Metasurfaces*, ACS Photonics **91**, 062510 (2015). (cited on pages 14 and 72)

[31] J. Dai, S. A. Dyakov and M. Yan, *Radiative Heat Transfer between Two Dielectric-Filled Metal Gratings*, Phys. Rev. B **93**, 155403 (2016). (cited on pages 14 and 72)

[32] J. Dai, S. A. Dyakov, S. I. Bozhevolnyi and M. Yan, *Near-Field Radiative Heat Transfer between Metasurfaces: A Full-Wave Study Based on Two-Dimensional Grooved Metal Plates*, Phys. Rev. B **94**, 125431 (2016). (cited on pages 14 and 72)

[33] C. Otey and S. Fan, *Numerically Exact Calculation of Electromagnetic Heat Transfer between a Dielectric Sphere and Plate*, Phys. Rev. B **84**, 245431 (2011). (cited on pages 15 and 42)

[34] A. Narayanaswamy, S. Shen, and G. Chen, *Thermal Near-Field Radiative Transfer between Two Spheres*, Phys. Rev. B **77**, 075125 (2008). (cited on p. 15)

[35] A. W. Rodriguez, O. Ilic, P. Bermel, I. Celanovic, J. D. Joannopoulos, M. Soljačić, and S. G. Johnson, *Frequency-Selective Near-Field Radiative Heat Transfer between Photonic Crystal Slabs: A Computational Approach for Arbitrary Geometries and Materials*, Phys. Rev. Lett. **107**, 114302 (2011). (cited on pages 15, 16, 72, and 91)

[36] C. Luo, A. Narayanaswamy, G. Chen, and J.D. Joannopoulos, *Thermal Radiation from Photonic Crystals: A Direct Calculation*, Phys. Rev. Lett. **93**, 213905 (2004). (cited on p. 16)

[37] A. P. McCauley, M. T. H. Reid, M. Krüger, and S. G. Johnson, *Modeling Near-Field Radiative Heat Transfer from Sharp Objects Using a General Three-Dimensional Numerical Scattering Technique*, Phys. Rev. B **85**, 165104 (2012). (cited on p. 16)

[38] A. W. Rodriguez, M. T. H. Reid, and S. G. Johnson, *Fluctuating-Surface-Current Formulation of Radiative Heat Transfer for Arbitrary Geometries*, Phys. Rev. B **86**, 220302(R) (2012). (cited on pages 15, 16, and 93)

[39] A. W. Rodriguez, M. T. H. Reid, and S. G. Johnson, *Fluctuating-Surface-Current Formulation of Radiative Heat Transfer: Theory and Applications*, Phys. Rev. B **88**, 054305 (2013). (cited on pages 16, 43, 85, 91, 92, 93, 113, 116, 137, and 141)

[40] L. Hu, A. Narayanaswamy, X. Y. Chen, and G. Chen, *Near-Field Thermal Radiation between Two Closely Spaced Glass Plates Exceeding Planck's Blackbody Radiation Law*, Appl. Phys. Lett. **92**, 133106 (2008). (cited on pages 17 and 85)

[41] R. S. Ottens, V. Quetschke, S. Wise, A. A. Alemi, R. Lundock, G. Mueller, D. H. Reitze, D. B. Tanner, and B. F. Whiting, *Near-Field Radiative Heat Transfer between Macroscopic Planar Surfaces*, Phys. Rev. Lett. **107**, 014301 (2011). (cited on p. 17)

[42] T. Kralik, P. Hanzelka, M. Zobac, V. Musilova, T. Fort, and M. Horak, *Strong Near-Field Enhancement of Radiative Heat Transfer between Metallic Surfaces*, Phys. Rev. Lett. **109**, 224302 (2012). (cited on p. 17)

[43] R. St-Gelais, L. Zhu, S. H. Fan, and M. Lipson, *Near-Field Radiative Heat Transfer between Parallel Structures in the Deep Subwavelength Regime*, Nat. Nanotechnol. **11**, 515 (2016). (cited on pages 19 and 85)

[44] B. Song, D. Thompson, A. Fiorino, Y. Ganjeh, P. Reddy, E. Meyhofer, *Radiative Heat*

Conductances between Dielectric and Metallic Parallel Plates with Nanoscale Gaps, Nat. Nanotechnol. **11**, 509 (2016). (cited on pages 18, 19, 72, 83, 85, 149, and 154)

[45] E. Rousseau, A. Siria, G. Jourdan, S. Volz, F. Comin, J. Chevrier, and J.-J, Greffet, *Radiative Heat Transfer at the Nanoscale*, Nat. Photonics **3**, 514 (2009). (cited on pages 19, 29, 32, and 85)

[46] P. J. van Zwol, L. Ranno, and J. Chevrier, *Tuning Near Field Radiative Heat Flux through Surface Excitations with a Metal Insulator Transition*, Phys. Rev. Lett. **108**, 234301 (2012) (cited on p. 19)

[47] P. J. van Zwol, S. Thiele, C. Berger, W. A. de Heer, and J. Chevrier, *Nanoscale Radiative Heat Flow due to Surface Plasmons in Graphene and Doped Silicon*, Phys. Rev. Lett. **109**, 264301 (2012). (cited on pages 19 and 131)

[48] A. Narayanaswamy, S. Shen, and G. Chen, *Near-Field Radiative Heat Transfer between a Sphere and a Substrate*, Phys. Rev. B **78**, 115303 (2008). (cited on pages 19 and 32)

[49] S. Shen, A. Narayanaswamy, and G. Chen, *Surface Phonon Polaritons Mediated Energy Transfer between Nanoscale Gaps*, Nano Lett. **9**, 2909 (2009). (cited on pages 18, 19, 29, 32, and 85)

[50] A. Kittel, W. Müller-Hirsch, J. Parisi, S.-A. Biehs, D. Reddig, and M. Holthaus, *Near-field Heat Transfer in a Scanning Thermal Microscope*, Phys. Rev. Lett. **95**, 224301 (2005). (cited on pages 20, 23, 85, 86, 96, 97, 99, 101, 103, 104, and 107)

[51] L. Worbes, D. Hellmann, and A. Kittel, *Enhanced Near-Field Heat Flow of a Monolayer Dielectric Island*, Phys. Rev. Lett. **110**, 134302 (2013). (cited on pages 20, 23, 85, 86, 99, 101, 102, 103, 104, and 107)

[52] K. Kloppstech, N. Könnne, S. A. Biehs, A. W. Rodriguez, L. Worbes, D. Hellmann, and A. Kittel, *Giant Heat Transfer in the Crossover Regime between Conduction and Radiation*, Nat. Commun. **8**, 14475 (2017). (cited on pages 18, 20, 85, 86, 101, 102, 103, 104, and 107)

[53] K. Park, S. Basu, W. P. King, and Z. M. Zhang, *Performance Analysis of Near-Field Thermophotovoltaic Devices Considering Absorption Distribution*, J. Quant. Spectrosc. Radiat. Transfer **109**, 305 (2008). (cited on p. 20)

[54] A. Lenert, D. M. Bierman, Y. Nam, W. R. Chan, I. Celanovic, M. Soljačić, and E. N. Wang, *A Nanophotonic Solar Thermophotovoltaic Device*, Nat. Nanotechnol. **9**, 126

(2014). (cited on pages 20 and 45)

[55] W. Shockley, and J. J. Queisser, *Detailed Balance Limit of Efficiency of* p-n *Junction Solar Cells*, J. Appl. Phys. **32**, 510 (1961). (cited on p. 20)

[56] S. Fan, *An alternative 'Sun' for solar cells*, Nat. Nanotechnol. **9**, 92 (2014). (cited on pages 20 and 21)

[57] N. P. Harder, and P. Würfel, *Theoretical limits of thermophotovoltaic solar energy conversion*, Semiconductor Sci. Technol. **18**, S151 (2003). (cited on p. 20)

[58] A. Narayanaswamy, and G. Chen, *Surface modes for near field thermophotovoltaics*, Appl. Phys. Lett. **82**, 3544 (2003). (cited on pages 21, 149, and 154)

[59] M. Laroche, R. Carminati, and J. J. Greffet, *Near-field thermophotovoltaic energy conversion*, J. Appl. Phys. **100**, 063704 (2006). (cited on pages 21, 149, and 154)

[60] R. Messina, and P. Ben-Abdallah, *Graphene-Based Photovoltaic Cells for Near-Field Thermal Energy Conversion*, Sci. Rep. **3**, 1383 (2013). (cited on pages 21, 149, and 154)

[61] W. A. Challener, C. B. Peng, A. V. Itagi, D. Karns, W. Peng, Y. Y. Peng, X. M. Yang, X. B. Zhu, N. J. Gokemeijer, Y. T. Hsia, G. Ju, R. E. Rottmayer, M. A. Seigler, and E. C. Gage, *Heat-assisted Magnetic Recording by a Near-field Transducer with Efficient Optical Energy Transfer*, Nat. Photonics **3**, 220 (2009). (cited on pages 21 and 86)

[62] B. C. Stipe, T. C. Strand, C. C. Poon, H. Balamane, T. D. Boone, J. A. Katine, J. L. Li, V. Rawat, H. Nemoto, A. Hirotsune, O. Hellwig, R. Ruiz, E. Dobisz, D. S. Kercher, N. Robertson, T. R. Albrecht, and B. D. Terris, *Magnetic Recording at 1.5 Pb* m^2 *Using an Integrated Plasmonic Antenna*, Nat. Photon. **4**, 484 (2010). (cited on p. 21)

[63] S.-A. Biehs and P. Ben-Abdallah, *Revisiting Super-Planckian Thermal Emission in the Far-Field Regime*, Phys. Rev. B **93**, 165405 (2016). (cited on p. 22)

[64] C. F. Bohren and D. R. Huffman, *Absorption and Scattering of Light by Small Particles* (Wiley, New York, 1998). (cited on pages 22, 110, 113, 115, and 116)

[65] J. A. Schuller, T. Taubner, and M. L. Brongersma, *Optical Antenna Thermal Emitters*, Nat. Photon. **3**, 658 (2009). (cited on p. 22)

[66] G. W. Kattawar and M. Eisner, *Radiation from a Homogeneous Isothermal Sphere*, Appl. Opt. **9**, 2685 (1970). (cited on pages 22 and 113)

[67] V. A. Golyk, M. Krüger, and M. Kardar, *Heat Radiation from Long Cylindrical Objects*, Phys. Rev. E **85**, 046603 (2012). (cited on p. 22)

[68] C. Wuttke and A. Rauschenbeutel, *Thermalization Via Heat Radiation of an Individual Object Thinner than the Thermal Wavelength*, Phys. Rev. Lett. **111**, 024301 (2013). (cited on pages 22 and 130)

[69] B. Song, Y. Ganjeh, S. Sadat, D. Thompson, A. Fiorino, V. Fernández-Hurtado, J. Feist, F. J. Garcia-Vidal, J. C. Cuevas, P. Reddy, and E. Meyhofer, *Enhancement of Near-Field Radiative Heat Transfer Using Polar Dielectric Thin Films*, Nat. Nanotechnol. **10**, 253 (2015). (cited on pages 27, 58, 68, 81, 85, and 89)

[70] S. Sadat, E. Meyhofer, and P. Pramod, *Resistance Thermometry-Based Picowatt-Resolution Heat-Flow Calorimeters*, Appl. Phys. Lett. **102**, 163110 (2013). (cited on pages 28, 30, 89, 110, 122, 130, and 141)

[71] D. G. Cahill, P. V. Braun, G. Chen, D. R. Clarke, S. H. Fan, K. E. Goodson, P. Keblinski, W. P. King, G. D. Mahan, A. Majumdar, H. J. Maris, S. R. Phillpot, E. Pop, and L. Shi, *Nanoscale Thermal Transport. II. 2003-2012*, Appl. Phys. Rev. **1**, 011305 (2014). (cited on p. 30)

[72] *Thermal heat radiation, near-field energy density and near-field radiative heat transfer of coated materials*, S. A. Biehs, Eur. Phys. J. B **58**, 423 (2007). (cited on p. 31)

[73] C.J. Fu, W. C. Tan, *Near-field radiative heat transfer between two plane surfaces with one having a dielectric coating*, J. Quant. Spectrosc. Radiat. Transfer **110**, 1027 (2009). (cited on p. 31)

[74] E. D. Palik, *Handbook of Optical Constants of Solids* (Academic Press, London, 1985). (cited on pages 31 and 116)

[75] M. A. Ordal, L. L. Long, R. J. Bell, S. E. Bell, R. R. Bell, R. W. Alexander and C. A. Ward, *Optical-Properties of the Metals Al, Co, Cu, Au, Fe, Pb, Ni, Pd, Pt, Ag, Ti, and W in the Infrared and Far Infrared* Appl. Opt. **22**,1099 (1983). (cited on pages 31, 106, and 116)

[76] B. V. Derjaguin, I. I. Abrikosova and E. M. Lifshitz, *Direct Measurement of Molecular Attraction between Solids Separated by a Narrow Gap* Quart. Rev. Chem. Soc. **10**, 295 (1956). (cited on pages 30 and 32)

[77] G. Cataldo, J. A. Beall, H.-M. Cho, B. McAndrew, M. D. Niemack, and E. L. Wollack,

Infrared Dielectric Properties of Low-Stress Silicon Nitride, Opt. Lett. **37**, 4200 (2012). (cited on pages 34 and 116)

[78] S. Basu and Z.M. Zhang, *Ultrasmall penetration depth in nanoscale thermal radiation*, Appl. Phys. Lett. **95**, 133104 (2009). (cited on p. 39)

[79] J. A. Dionne, L. A. Sweatlock and H. A. Atwater, *Plasmon Slot Waveguides: Towards Chip-Scale Propagation with Subwavelength-Scale Localization*, Phys. Rev. B, **73**, 035407 (2007). (cited on p. 41)

[80] D. M. Whittaker and I. S. Culshaw, *Scattering-Matrix Treatment of Patterned Multilayer Photonic Structures*, Phys. Rev. B **60**, 2610 (1999). (cited on pages 41, 157, and 162)

[81] K. Sasihithlu and A. Narayanaswamy, *Proximity effects in radiative heat transfer*, Phys. Rev. B **83**, 161406 (2011). (cited on p. 42)

[82] M. T. H. Reid and S. G. Johnson, *Efficient Computation of Power, Force and Torque in BEM Scattering Calculations*, IEEE T. Antenn. Propag. **63**, 3588 (2015). (cited on pages 43, 93, 113, 116, 137, and 141)

[83] http://homerreid.com/scuff-em. (cited on pages 43 and 93)

[84] B. Guha, C. Otey, C. B. Poitras, S. H. Fan, and M. Lipson, *Near-Field Radiative Cooling of Nanostructures*, Nano Lett. **12**, 4546 (2012). (cited on p. 45)

[85] I. S. Nefedov and C. R. Simovski, *Giant Radiation Heat Transfer Through Micron Gaps*, Phys. Rev. B **84**, 195459 (2011). (cited on p. 47)

[86] S. A. Biehs, M. Tschikin, and P. Ben-Abdallah, *Hyperbolic Metamaterials as an Analog of a Blackbody in the Near Field*, Phys. Rev. Lett. **109**, 104301 (2012). (cited on pages 47, 48, 59, and 72)

[87] Y. Guo, C. L. Cortes, S. Molesky, and Z. Jacob, *Broadband super-Planckian Thermal Emission from Hyperbolic Metamaterials*, Appl. Phys. Lett. **101**, 131106 (2012). (cited on p. 47)

[88] D. R. Smith and D. Schurig, *Electromagnetic Wave Propagation in Media with Indefinite Permittivity and Permeability Tensors*, Phys. Rev. Lett. **90**, 077405 (2003). (cited on pages 47 and 58)

[89] A. Poddubny, I. Iorsh, P. Belov, and Y. Kivshar, *Hyperbolic Metamaterials*, Nat. Photonics **7**, 958 (2013). (cited on pages 47 and 68)

[90] P. Shekhar, J. Atkinson, and Z. Jacob, *Hyperbolic Metamaterials: Fundamentals and Applications*, Nano Convergence **1**, 14 (2014). (cited on pages 47 and 68)

[91] S. A. Biehs, M. Tschikin, R. Messina, and P. Ben-Abdallah, *Super-Planckian Near-Field Thermal Emission with Phonon-Polaritonic Hyperbolic Metamaterials*, Appl. Phys. Lett. **102**, 131106 (2013). (cited on p. 48)

[92] M. Tschikin, S. A. Biehs, R. Messina, P. Ben-Abdallah, *On the Limits of the Effective Description of Hyperbolic Materials in Presence of Surface Waves*, J. Opt. **15**, 105101 (2013). (cited on p. 48)

[93] Y. Guo and Z. B. Jacob, *Thermal Hyperbolic Metamaterials*, Opt. Express **21**, 15014 (2013). (cited on p. 48)

[94] C. Simovski, S. Maslovski, I. Nefedov, and S. Tretyakov, *Optimization of Radiative Heat Transfer in Hyperbolic Metamaterials for Thermophotovoltaic Applications*, Opt. Express **21**, 14988 (2013). (cited on p. 48)

[95] X. L. Liu, R. Z. Zhang, and Z. M. Zhang, *Near-Field Thermal Radiation between Hyperbolic Metamaterials: Graphite and Carbon Nanotubes*, Appl. Phys. Lett. **103**, 213102 (2013). (cited on p. 48)

[96] Y. Guo and Z. Jacob, *Fluctuational Electrodynamics of Hyperbolic Metamaterials*, J. Appl. Phys. **115**, 234306 (2014). (cited on p. 48)

[97] O. D. Miller, S. G. Johnson, and A. W. Rodriguez, *Effectiveness of Thin Films in Lieu of Hyperbolic Metamaterials in the Near Field*, Phys. Rev. Lett. **112**, 157402 (2014). (cited on pages 48 and 72)

[98] S. Lang, M. Tschikin, S. A. Biehs, A. Yu. Petrov, and M. Eich, *Large Penetration Depth of Near-Field Heat Flux in Hyperbolic Media*, Appl. Phys. Lett. **104**, 121903 (2014). (cited on p. 48)

[99] I. S. Nefedov and L. A. Melnikov, *Super-Planckian Far-Zone Thermal Emission from Asymmetric Hyperbolic Metamaterials*, Appl. Phys. Lett. **105**, 161902 (2014). (cited on p. 48)

[100] M. Tschikin, S. A. Biehs, P. Ben-Abdallah, S. Lang, A. Yu. Petrov, and M. Eich, *Radiative Heat Flux Predictions in Hyperbolic Metamaterials*, J. Quant. Spectrosc. Radiat. Transf. **158**, 17 (2015). (cited on p. 48)

[101] P. J. van Zwol, K. Joulain, P. Ben-Abdallah, and J. Chevrier, *Phonon Polaritons*

Enhance Near-Field Thermal Transfer Across the Phase Transition of VO_2, Phys. Rev. B **84**, 161413(R) (2011). (cited on p. 48)

[102] P. J. van Zwol, K. Joulain, P. Ben-Abdallah, J. J. Greffet, and J. Chevrier, *Fast Nanoscale Heat-Flux Modulation with Phase-Change Materials*, Phys. Rev. B **83**, 201404(R) (2011). (cited on p. 48)

[103] L. J. Cui, Y. Huang, and J. Wang, *Near-Field Radiative Heat Transfer between Chiral Metamaterials*, J. Appl. Phys. **112**, 084309 (2012). (cited on p. 48)

[104] Y. Huang, S. V. Boriskina, and G. Chen, *Electrically Tunable Near-Field Radiative Heat Transfer via Ferroelectric Materials*, Appl. Phys. Lett. **105**, 244102 (2014). (cited on p. 48)

[105] K. Chen, P. Santhanam, S. Sandhu, L. Zhu, and S. Fan, *Heat-Flux Control and Solid-State Cooling by Regulating Chemical Potential of Photons in Near-Field Electromagnetic Heat Transfer*, Phys. Rev. B **91**, 134301 (2015). (cited on p. 48)

[106] E. Moncada-Villa, V. Fernández-Hurtado, F. J. García-Vidal, A. García-Martín and J. C. Cuevas, *Magnetic Field Control of Near-Field Heat Transfer and the Realization of Highly Tunable Hyperbolic Thermal Emitters.*, Phys. Rev. B **92**, 125418 (2015). (cited on pages 48, 81, and 82)

[107] A. Zvezdin and V. Kotov, *Modern Magnetooptics and Magnetooptical Materials* (IOP, Bristol, 1997). (cited on p. 50)

[108] B. Caballero, A. García-Martín, and J. C. Cuevas, *Generalized Scattering-Matrix Approach for Magneto-Optics in Periodically Patterned Multilayer Systems*, Phys. Rev. B **85**, 245103 (2012). (cited on pages 51, 53, 74, 75, and 157)

[109] S. A. Biehs, P. Ben-Abdallah, F. S. S. Rosa, K. Joulain, and J.-J. Greffet, *Nanoscale Heat Flux between Nanoporous Materials*, Opt. Express **19**, A1088 (2011). (cited on p. 53)

[110] M. S. Kushwaha, *Plasmons and Magnetoplasmons in Semiconductor Heterostructures*, Surf. Sci. Rep. **41**, 1 (2001). (cited on pages 53 and 64)

[111] R. F. Wallis, in A.D. Boardman (Ed.), *Electromagnetic Surface Modes*, (Wiley, New York, 1982), p. 575. (cited on pages 53 and 64)

[112] E. D. Palik, B. Kaplan, B. W. Gammon, H. Kaplan, J. J. Quinn, and B. F. Wallis, *Surface Magnetoplasmon-Optic Phonon Modes in InSb*, Phys. Lett. A **45**, 143 (1973).

(cited on p. 54)

[113] A. Hartstein, E. Burstein, E. D. Palik, R. W. Gammon, and B. W. Henvis, *Investigation of Optic-Phonon-Magnetoplasmon-Type Surface Polaritons on n-Insb*, Phys. Rev. B **12**, 3186 (1975). (cited on p. 54)

[114] E. D. Palik, R. Kaplan, R. W. Gammon, H. Kaplan, R. F. Wallis, and J. J. Quinn, *Coupled Surface Magnetoplasmon-Optic-Phonon Polariton Modes on InSb*, Phys. Rev. B **13**, 2497 (1976). (cited on pages 54 and 55)

[115] L. Remer, E. Mohler, W. Grill, and B. Lüthi, *Nonreciprocity in the Optical Reflection of Magnetoplasmas*, Phys. Rev. B **30**, 3277 (1984). (cited on p. 54)

[116] C. J. Fu and Z. M. Zhang, *Nanoscale Radiation Heat Transfer for Silicon at Different Doping Levels*, Int. J. Heat Mass Transfer **49**, 1703 (2006). (cited on pages 64 and 65)

[117] E. Rousseau, M. Laroche, and J. J. Greffet, *Radiative Heat Transfer at Nanoscale Mediated by Surface Plasmons for Highly Doped Silicon*, Appl. Phys. Lett. **95**, 231913 (2009). (cited on p. 64)

[118] J. Shi, P. Li, B. Liu, and S. Shen, *Tuning Near Field Radiation by Doped Silicon*, Appl. Phys. Lett. **102**, 183114 (2013). (cited on p. 64)

[119] M. Lim, S. S. Lee, and B. J. Lee, *Near-Field Thermal Radiation between Doped Silicon Plates at Nanoscale Gaps*, Phys. Rev. B **91**, 195136 (2015). (cited on p. 64)

[120] P. O. Chapuis, S. Volz, C. Henkel, K. Joulain, and J. J. Greffet, *Effects of Spatial Dispersion in Near-Field Radiative Heat Transfer between Two Parallel Metallic Surfaces*, Phys. Rev. B **77**, 035431 (2008). (cited on pages 68, 85, 99, and 106)

[121] H. Iizuka and S. Fan, *Analytical Treatment of Near-Field Electromagnetic Heat Transfer at the Nanoscale*, Phys. Rev. B **92**, 144307 (2015). (cited on p. 71)

[122] O. D. Miller, S. G. Johnson, and A. W. Rodriguez, *Shape-Independent Limits to Near-Field Radiative Heat Transfer*, Phys. Rev. Lett. **115**, 204302 (2015). (cited on p. 71)

[123] R. Messina, *Sharing Heat in the Near Field*, Physics **8**, 109 (2015). (cited on p. 71)

[124] R. Messina, A. Noto, B. Guizal and M. Antezza, *Radiative Heat Transfer between Metallic Gratings Using Adaptive Spatial Resolution*, Phys. Rev. B **95**, 125404 (2017). (cited on p. 72)

[125] S. Basu, B. J. Lee, Z. M. Zhang, *Infrared Radiative Properties of Heavily Doped Silicon at Room Temperature*, J. Heat Transfer **132**, 023301 (2010). (cited on p. 73)

[126] L. Li, *Use of Fourier Series in the Analysis of Discontinuous Periodic Structures*, J. Opt. Soc. Am. A **13**, 1870 (1996). (cited on pages 74 and 75)

[127] A. David, H. Benisty and C. Weisbuch, *Fast factorization rule and plane-wave expansion method for two-dimensional photonic crystals with arbitrary hole-shape*, Phys. Rev. B **73**, 075107 (2006). (cited on pages 75 and 76)

[128] X. L. Liu, L. P. Wang and Z. M. Zhang, *Wideband Tunable Omnidirectional Infrared Absorbers Based on Doped Silicon Nanowire Arrays*, J. Heat Transfer **135**, 061602 (2013). (cited on pages 80 and 81)

[129] V. R. Manfrinato, L. Zhang, D. Zu, H. Duan, R. G. Hobbs, E. A. Stachand, and K. K. Berggren, *Resolution Limits of Electron-Beam Lithography toward the Atomic Scale*, Nano Lett. **13**, 1555 (2013). (cited on p. 83)

[130] R. St-Gelais, B. Guha, L. X. Zhu, S. H. Fan, and M. Lipson, *Demonstration of Strong Near-Field Radiative Heat Transfer between Integrated Nanostructures*, Nano Lett. **14**, 6971 (2014). (cited on p. 85)

[131] M. P. Bernardi, D. Milovich, and M. Francoeur, *Radiative Heat Transfer Exceeding the Blackbody Limit between Macroscale Planar Surfaces Separated by a Nanosize Vacuum Gap*, Nat. Comm. **7**, 12900 (2016). (cited on p. 85)

[132] K. Joulain, J.-P. Mulet, F. Marquier, R. Carminati, and J.-J. Greffet, *Surface Electromagnetic Waves Thermally Excited: Radiative Heat Transfer, Coherence Properties and Casimir Forces Revisited in the Near Field*, Surf. Sci. Rep. **57**, 59 (2005). (cited on p. 85)

[133] F. Singer, Y. Ezzahri and K. Joulain, *Near Field Radiative Heat Transfer between Two Nonlocal Dielectrics*, J. Quant. Spectros. Radiat. Transfer **154**, 55 (2015). (cited on p. 85)

[134] B. N. J. Persson, A. I. Volokitin and H. Ueba, *Phononic Heat Transfer across an Interface: Thermal Boundary Resistance*, J. Phys. Condens. Matter **23**, 045009 (2011). (cited on p. 85)

[135] B. V. Budaev, and D. B. Bogy, *On the Role of Acoustic Waves (Phonons) in Equilibrium Heat Exchange across a Vacuum Gap*, Appl. Phys. Lett. **99**, 053109 (2011). (cited on p. 85)

[136] D. P. Sellan, E. S. Landry, K. Sasihithlu, A. Narayanaswamy, A. J. H. McGaughey, and C. H. Amon, *Phonon Transport across a Vacuum Gap*, Phys. Rev. B **85**, 024118 (2012). (cited on p. 85)

[137] Y. Ezzahri and K. Joulain, *Vacuum-Induced Phonon Transfer between Two Solid Dielectric Materials: Illustrating the Case of Casimir Force Coupling*, Phys. Rev. B **90**, 115433 (2014). (cited on p. 85)

[138] J. B. Pendry, K. Sasihithlu, and R. V. Craster, *Phonon-Assisted Heat Transfer between Vacuum-Separated Surfaces*, Phys. Rev. B **94**, 075414 (2016). (cited on p. 85)

[139] S. Basu, Z. M. Zhang, C. J. Fu, *Review of Near-Field Thermal Radiation and its Application to Energy Conversion*, Int. J. Energy Res. **33**, 1203 (2009). (cited on p. 86)

[140] K. Kim, B. Song, V. Fernández-Hurtado, W. Lee, W. Jeong, L. Cui, D. Thompson, J. Feist, M. T. H. Reid, F. J. Garcia-Vidal, J. C. Cuevas, E. Meyhofer, and P. Reddy, *Radiative Heat Transfer in the Extreme Near Field*, Nature **528**, 387 (2015). (cited on pages 86, 101, 106, 149, and 154)

[141] L. Cui, W. Jeong, V. Fernández-Hurtado, J. Feist, F. J. Garcia-Vidal, J. C. Cuevas, E. Meyhofer, and P. Reddy, *Study of Radiative Heat Transfer in Ångström- and Nanometre-Sized Gaps*, Nat. Commun. **8**, 14479 (2017). (cited on pages 86, 101, and 106)

[142] K. Kim, W. Jeong, W. Lee, and P. Reddy, *Ultra-High Vacuum Scanning Thermal Microscopy for Nanometer Resolution Quantitative Thermometry*, ACS Nano **6**, 4248 (2012). (cited on pages 86 and 87)

[143] W. Lee, K. Kim, W. Jeong, L. A. Zotti, F. Pauly, J. C. Cuevas, and P. Reddy, *Heat Dissipation in Atomic-Scale Junctions*, Nature **498**, 209 (2013). (cited on p. 86)

[144] K. Kim, W. Jeong, W. Lee, S. Sadat, D. Thompson, E. Meyhofer, and P. Reddy, *Quantification of Thermal and Contact Resistances of Scanning Thermal Probes*, Appl. Phys. Lett. **105**, 203107 (2014). (cited on p. 87)

[145] A. E. H. Love, *The Integration of the Equations of Propagation of Electric Waves*, Phi. Trans. Roy. Soc. London **197**, 1 (1901). (cited on p. 92)

[146] R. F. Harringston, *Boundary Integral Formulations for Homogeneous Material Bodies*, J. Electromagn. Waves. Appl. **3**, 1 (1989). (cited on p. 92)

[147] K.-M. Chen, *A Mathematical Formulation of the Equivalence Principle*, IEEE Trans. Microwave Theory Tech. **37**, 1576 (1989). (cited on p. 92)

[148] S. M. Rao and D. R. Glisson, *Electromagnetic scattering by surfaces of arbitrary shape*, IEEE T. Antenn. Propag. **30**, 409 (1982). (cited on p. 93)

[149] V. B. Svetovoy, P. J. van Zwol, G. Palasantzas, and J. T. M. De Hosson, *Optical Properties of Gold Films and the Casimir Force*, Phys. Rev. B **77**, 035439 (2008). (cited on p. 90)

[150] J. Zenneck, *Breeding of Even Electromagnetic Waves along an Even Conducting Surface and its Relation to Radiotelegraphy*, Ann. Phys-Berlin **23**, 846 (1907). (cited on p. 99)

[151] L. Olesen, M. Brandbyge, M. R. Sørensen, K. W. Jacobsen, E. Lægsgaard, I. Stensgaard, and F. Besenbacher, *Apparent Barrier Height in Scanning Tunneling Microscopy Revisited*, Phys. Rev. Lett. **76**, 1485 (1996). (cited on pages 102 and 103)

[152] C. J. Chen, *Introduction to Scanning Tunneling Microscopy* (Oxford University Press, Oxford, 2008) (cited on pages 102 and 103)

[153] K. Raiber, A. Terfort, C. Benndorf, N. Krings, and H. H. Strehblow, *Removal of Self-Assembled Monolayers of Alkanethiolates on Gold by Plasma Cleaning*, Surf. Sci. **595**, 56 (2005). (cited on p. 103)

[154] P. Kim, L. Shi, A. Majumdar, and P. L. McEuen, *Thermal Transport Measurements of Individual Multiwall Carbon Nanotubes*, Phys. Rev. Lett. **87**, 215502 (2001). (cited on pages 110, 122, and 130)

[155] L. Shi *et al. Measuring Thermal and Thermoelectric Properties of One-Dimensional Nanostructures Using a Microfabricated Device*, J. Heat Transfer **125**, 881 (2003). (cited on pages 110, 122, and 130)

[156] S. Lee, F. Yang, J. Suh, S. Yang, Y. Lee, G. Li, H. S. Choe, A. Suslu, Y. Chen, C. Ko, J. Park, K. Liu, J. Li, K. Hippalgaonkar, J. L. Urban, S. Tongay, and J. Wu, *Anisotropic In-Plane Thermal Conductivity of Black Phosphorus Nanoribbons at Temperatures Higher than 100 K*, Nat. Commun. **6**, 8573 (2015). (cited on pages 110, 122, and 130)

[157] S. Lee, K. Hippalgaonkar, F. Yang, J. Hong, C. Ko, J. Suh, K. Liu, K. Wang, J. J. Urban, X. Zhang, C. Dames, S. A. Hartnoll, O. Delaire, and J. Wu *Anomalously Low Electronic Thermal Conductivity in Metallic Vanadium Dioxide*, Science **355**, 371 (2017). (cited on pages 110, 122, and 130)

[158] J. Zheng, M. C. Wingert, E. Dechaumphai, and R. Chen, *Sub-Picowatt/Kelvin Resistive Thermometry for Probing Nanoscale Thermal Transport*, Rev. Sci. Instrum. **84**, 114901

(2013). (cited on pages 110, 122, 130, and 141)

[159] V. Fernández-Hurtado, A. I. Fernández-Domínguez, J. Feist, F. J. García-Vidal, and J. C. Cuevas, *Super-Planckian Far-Field Radiative Heat Transfer*, Phys. Rev. B **97**, 045408 (2018). (cited on pages 109, 131, 134, and 136)

[160] R. M. Abraham Ekeroth, A. García-Martín, and J. C. Cuevas, *Thermal Discrete Dipole Approximation for the Description of Thermal Emission and Radiative Heat Transfer of Magneto-Optical Systems*, Phys. Rev. B **95**, 235428 (2017).
(cited on pages 111, 112, 113, 116, 118, 120, 121, and 134)

[161] S. Edalatpour, M. Cuma, T. Trueax, R. Backman, and M. Francoeur, *Convergence Analysis of the Thermal Discrete Dipole Approximation*, Phys. Rev. E **91**, 063307 (2015). (cited on p. 111)

[162] S. Edalatpour and M. Francoeur, *Near-field Radiative Heat Transfer between Arbitrarily Shaped Objects and a Surface*, Phys. Rev. B **94**, 045406 (2016). (cited on p. 111)

[163] N. Juul, *Investigation of Approximate Methods for Calculation of the Diffuse Radiation Configuration View Factor Between two Spheres*, Lett. Heat Mass Transfer **3**, 513 (1976). (cited on pages 113 and 114)

[164] D. Marcuse, *Theory of Dielectric Optical Waveguides* (Academic Press, London, 1991). (cited on pages 128 and 136)

[165] D. E. Chang, C. A. Regal, S. B. Papp, D. J. Wilson, J. Ye, O. Painter, H. J. Kimble, and P. Zoller, *Cavity Opto-Mechanics Using an Optically Levitated Nanosphere*, Proc. Natl. Acad. Sci. U.S.A. **107**, 1005 (2010). (cited on p. 130)

[166] B. T. Draine, *Physics of the Interstellar and Intergalactic Medium* (Princeton University Press, Princeton, 2011). (cited on p. 130)

[167] A. I. Volokitin, and B. N. J. Persson, *Near-Field Radiative Heat Transfer between Closely-Spaced Graphene and Amorphous SiO_2*, Phys. Rev. B **83**, 241407 (2011). (cited on p. 131)

[168] O. Ilic, J. Marinko, J. D. Joannopoulos, I. Celanovic, H. Buljan, and M. Soljačić, *Near-Field Thermal Radiation Transfer Controlled by Plasmons in Graphene*, Phys. Rev. B **85**, 155422 (2012). (cited on p. 131)

[169] V. B. Stetovoy, P. J. van Zwol, and J. Chevrier, *Plasmon Enhanced Near-Field Radiative Heat Transfer for Graphene Covered Dielectrics*, Phys. Rev. B **85**, 155418

(2012). (cited on p. 131)

[170] X. L. Liu, and Z. M. Zhang, *Graphene-Assisted Near-Field Radiative Heat Transfer between Corrugated Polar Materials*, Appl. Phys. Lett. **104**, 251911 (2014). (cited on p. 131)

[171] R. Messina, P. Ben-Abdallah, B. Guizal, and M. Antezza, *Graphene-Based Amplification and Tuning of Near-Field Radiative Heat Transfer between Dissimilar Polar Materials*, Phys. Rev. B **96**, 045402 (2017). (cited on p. 131)

[172] X. L. Liu, and Z. M. Zhang, *Giant Enhancement of Nanoscale Thermal Radiation Based on Hyperbolic Graphene Plasmons*, Appl. Phys. Lett. **107**, 143114 (2015). (cited on p. 132)

[173] F. V. Ramirez, S. Shen, and A. J. H. McGaughey, *Near-Field Radiative Heat Transfer in Graphene Plasmonic Nanodisk Dimers*, Phys. Rev. B **96**, 165427 (2017). (cited on p. 132)

[174] Y. Renwen, A. Manjavacas, and F. J. García de Abajo, *Ultrafast Radiative Heat Transfer*, Nat. Comm. **8**, 2 (2017). (cited on p. 132)

[175] P. Rodriguez-Lopez, W. K. Tse, and D. A. R. Dalvit, *Radiative Heat Transfer in 2D Dirac Materials*, J. Phys. Condens. Matter. **27**, 214019 (2015). (cited on p. 132)

[176] R. Mas-Bastellé, C. Gómez-Navarro, J. Gómez-Herrero, and F. Zamora, *2D Materials: to Graphene and Beyond*, Nanoscale **3**, 20 (2011). (cited on p. 132)

[177] L. A. Falkovsky, *Optical Properties of Graphene*, J. Phys.: Conf. Ser. **129**, 012004 (2008). (cited on p. 133)

[178] A. Y. Nikitin, F. J. Garcia-Vidal, and L. Martin-Moreno, *Analytical Expressions for the Electromagnetic Dyadic Green's Function in Graphene and Thin Layers*, IEEE J. Select. Topics Quantum Electron. **19**, 4600611 (2013). (cited on pages 133 and 135)

[179] T. Low, A. Chaves, J. D. Caldwell, A. Kumar, N. X. Fang, P. Avouris, T. F. Heinz, F. Guinea, L. Martin-Moreno, and F. Koppens, *Polaritons in Layered Two-Dimensional Materials*, Nat. Mater. **16**, 182 (2016). (cited on p. 134)

[180] Y. K. Koh, M.-H. Bae, D. G. Cahill, and E. Pop, *Reliably Counting Atomic Planes of Few-Layer Graphene (n>4)*, ACS Nano **5**, 269 (2011). (cited on p. 135)

[181] T. Low, R. Roldán, H. Wang, F. Xia, P. Avouris, L. Martín-Moreno, and F. Guinea, *Plasmons and Screening in Monolayer and Multilayer Black Phosphorus*, Phys. Rev. Lett.

113, 106802 (2014). (cited on p. 141)

[182] Y. Saito, and Y. Iwasa, *Ambipolar insulator-to-metal transition in black phosphorus by ionic-liquid gating*, ACS Nano **9**, 3192 (2015). (cited on p. 141)

[183] L. Cui, W. Jeong, S. Hur, M. Matt, J. C. Kl´ockner, F. Pauly, P. Nielaba, J. C. Cuevas, E. Meyhofer, and P. Reddy, *Quantized Thermal Transport in Single-Atom Junctions*, Science **355**, 1192 (2017). (cited on pages 148 and 153)

List of Figures

List of publications

Publications related to the content of this Thesis

1. *Exploring the limits of super-Planckian far-field radiative heat transfer using 2D materials.*
   V. Fernández-Hurtado, A. I. Fernández-Domínguez, J. Feist, F. J. García-Vidal, and J. C. Cuevas,
   arXiv:1802.09463 (2018) (Submitted).

2. *Super-Planckian far-field radiative heat transfer.*
   V. Fernández-Hurtado, A. I. Fernández-Domínguez, J. Feist, F. J. García-Vidal, and J. C. Cuevas,
   Physical Review B 97, 045408 (2018).

3. *Enhancing near-field radiative heat transfer with Si-based metasurfaces.*
   V. Fernández-Hurtado, F. J. García-Vidal, S.Fan, and J. C. Cuevas,
   Physical Review Letters 118, 203901 (2017).

4. *Study of radiative heat transfer in Ångström-and nanometre-sized gaps.*
   L. Cui, W. Jeong, **V. Fernández-Hurtado**, J. Feist, F. J. García-Vidal, J. C. Cuevas, E. Meyhofer, and P. Reddy,
   Nature Communications 8, 14479 (2017).

5. *Radiative heat transfer in the extreme near field.*
   K. Kim*, B. Song*, **V. Fernández-Hurtado***, W. Lee, W. Jeong, L. Cui, D. Thompson, J. Feist, M. T. H. Reid, F. J. García-Vidal, J. C. Cuevas, E. Meyhofer, and P. Reddy, (*Equal contributors)
   Nature 528, 387 (2015).

6. *Magnetic field control of near-field radiative heat transfer and the realization of highly tunable hyperbolic thermal emitters.*
   E. Moncada-Villa, **V. Fernández-Hurtado**, F. J. García-Vidal, A. García-Martín and J. C. Cuevas,
   Physical Review B 92, 125418 (2015).

7. *Enhancement of near-field radiative heat transfer using polar dielectric thin films.*
   B. Song, Y. Ganjeh, S. Sadat, D. Thompson, A. Fiorino, **V. Fernández-Hurtado**, J. Feist, F. J. Garcia-Vidal, J. C. Cuevas, P. Reddy, and E. Meyhofer,
   Nature Nanotechnology 10, 253 (2015).

Other publications

Lattice scars: surviving in an open discrete billiard.
V. Fernández-Hurtado, J. Mur-Petit, J. J. García-Ripoll, and R. A. Molina,
New Journal of Physics 16, 035005 (2014).